Cranfield University

Naveed ur Rahman

Propulsion and Flight Controls Integration for the Blended Wing Body Aircraft

School of Engineering

PhD Thesis

Cranfield University

Department of Aerospace Sciences
School of Engineering

PhD Thesis

Academic Year 2008-09

Naveed ur Rahman

Propulsion and Flight Controls Integration for the Blended Wing Body Aircraft

Supervisor: Dr James F. Whidborne

May 2009

Abstract

The Blended Wing Body (BWB) aircraft offers a number of aerodynamic performance advantages when compared with conventional configurations. However, while operating at low airspeeds with nominal static margins, the controls on the BWB aircraft begin to saturate and the dynamic performance gets sluggish. Augmentation of aerodynamic controls with the propulsion system is therefore considered in this research. Two aspects were of interest, namely thrust vectoring (TVC) and flap blowing. An aerodynamic model for the BWB aircraft with blown flap effects was formulated using empirical and vortex lattice methods and then integrated with a three spool Trent 500 turbofan engine model. The objectives were to estimate the effect of vectored thrust and engine bleed on its performance and to ascertain the corresponding gains in aerodynamic control effectiveness.

To enhance control effectiveness, both internally and external blown flaps were simulated. For a full span internally blown flap (IBF) arrangement using IPC flow, the amount of bleed mass flow and consequently the achievable blowing coefficients are limited. For IBF, the pitch control effectiveness was shown to increase by 18% at low airspeeds. The associated detoriation in engine performance due to compressor bleed could be avoided either by bleeding the compressor at an earlier station along its axial length or matching the engine for permanent bleed extraction. For an externally blown flap (EBF) arrangement using bypass air, high blowing coefficients are shown to be achieved at 100% Fan RPM. This results in a 44% increase in pitch control authority at landing and take-off speeds. The main benefit occurs at take-off, where both TVC and flap blowing help in achieving early pitch rotation, reducing take-off field lengths and lift-off speeds considerably. With central flap blowing and a limited TVC of 10°, the lift-off range reduces by 48% and lift-off velocity by almost 26%.

For the lateral-directional axis it was shown that both aileron and rudder control powers can be almost doubled at a blowing coefficient of $C_u = 0.2$. Increased roll authority greatly helps in achieving better roll response at low speeds, whereas the increased rudder power helps in maintaining flight path in presence of asymmetric thrust or engine failure, otherwise not possible using the conventional winglet rudder.

Acknowledgments

I would like to dedicate this thesis to my parents who worked tirelessely throughout their lives and are still making all efforts to support me and my family in every possible way. I am here at this stage of my carrier only because of them. It would be very hard for me to pay them back for what they have done, probably the best way would be to try and match what they did for us, for our children.

My deepest acknowledgments to my supervisor and mentor Dr. James F. Whidborne who guided me throughout my research and made this thesis possible. I am greatly indebted to him. In addition, it would not be fair not to mention Dr. Alastair K. Cooke whom I bothered many a times to seek guidance with regards to flight dynamics and aerodynamic model building. I found his NFLC Jetstream model very valuable in understanding flight dynamics in an entirely new perspective.

Last but not the least, I would like to thank my wife, Zahra, and my kids, Sarah and Saad, for their patience, understanding and support during the last three years. I hope I would be able to give more time to them after my studies.

My time here at Cranfield has been memorable, except for the cold British weather I have enjoyed every aspect of this country. Once again, I would like to thank, everybody who helped me finish this work and made this Cranfield experience a most pleasurable one.

Naveed ur Rahman.
May, 2009

Contents

List of Tables

List of Figures

Abbreviations and symbols

Aircraft Notation

a_f	Lift curve slope for vertical fin
a_t	Lift curve slope for horizontal tail
a_w	Lift curve slope for wing
b	Reference, Wing span
$\overline{c}$	Mean aerodynamic chord
c_f	Flap chord
C_L	Lift coefficient, $L/(\bar{q}S)$
C_{L_f}	Lift coefficient of vertical fin
C_{L_t}	Lift coefficient of horizontal tail
C_{L_w}	Lift coefficient of wing
C_l	Rolling moment coefficient, $l/(\bar{q}Sb)$
$C_{l\beta}$	Variation of rolling moment coefficient with side slip, $(\partial C_l/\partial\beta)$
$C_{l\delta a}$	Variation in roll moment coefficient with aileron deflection, $(\partial C_l/\partial\delta_a)$
$C_{l\delta r}$	Variation in roll moment coefficient with rudder deflection, $(\partial C_l/\partial\delta_r)$
C_{lp}	Variation in roll moment coefficient with roll rate, $(\partial C_l/\partial p)/(b/V_t)$
C_{lr}	Variation in roll moment coefficient with yaw rate, $(\partial C_l/\partial r)/(b/V_t)$
C_m	Pitching moment coefficient, $M/(\bar{q}S\bar{c})$
C_{mac}	Pitching moment coefficient about aerodynamic center
C_{m0}	Pitching moment at CG for zero total lift
$C_{m\alpha}$	Variation in pitch moment coefficient with angle of attack, $(\partial C_m/\partial\alpha)$
C_{mq}	Pitch damping derivative, $(\partial C_m/\partial q)/(\bar{c}/V_t)$
$C_{m\delta e}$	Variation in pitch moment coefficient with elevator deflection, $(\partial C_m/\partial\delta_e)$
C_n	Yawing moment coefficient, $N/(\bar{q}Sb)$
$C_{n\beta}$	Variation of yawing moment coefficient with side slip,$(\partial C_n/\partial\beta)$
$C_{n\delta a}$	Variation in yawing moment coefficient with aileron deflection, $(\partial C_n/\partial\delta_a)$
$C_{n\delta r}$	Variation in yawing moment coefficient with rudder deflection, $(\partial C_n/\partial\delta_r)$
C_{np}	Variation in yawing moment coefficient with roll rate, $(\partial C_n/\partial p)/(b/V_t)$
C_{nr}	Variation in yawing moment coefficient with yaw rate, $(\partial C_n/\partial r)/(b/V_t)$
C_Y	Side force coefficient, $Y/(\bar{q}S)$
$C_{Y\beta}$	Variation of side force coefficient with side slip, $(\partial C_Y/\partial\beta)$
$C_{Y\delta a}$	Variation in side force coefficient with aileron deflection, $(\partial C_Y/\partial\delta_a)$

$C_{Y\delta r}$	Variation in side force coefficient with rudder deflection, $(\partial C_Y/\partial \delta_r)$
C_{Yp}	Variation in side force coefficient with roll rate, $(\partial C_Y/\partial p)/(b/V_t)$
C_{Yr}	Variation in side force coefficient with yaw rate, $(\partial C_Y/\partial r)/(b/V_t)$
C_u	Blowing momentum coefficient, $(\dot{m}_{jet}V_{jet}/(\bar{q}S))$
C_X	Body X aerodynamic force coefficient, $(X/(\bar{q}S))$
C_{x_i}	Polynomial coefficient for C_X
C_Z	Z aerodynamic force coefficient, $Z/(\bar{q}S)$
$C_{Z\alpha}$	Variation in Z force coefficient with alpha, $(\partial C_Z/\partial \alpha)$
$C_{Z\delta e}$	Variation in Z force coefficient with elevator, $(\partial C_Z/\partial \delta_e)$
C_{Z0}	Z force coefficient at zero alpha
C_{Zq}	Variation in Z force coefficient with pitch rate, $(\partial C_Z/\partial q)/(\bar{c}/V_t)$
C_{Zu}	Variation in Z force coefficient with forward velocity, $(\partial C_Z/\partial u)/(\bar{c}/V_t)$
g	Acceleration due to gravity, (m/sec^2)
I_{xx}	Inertia about X Body axis, (kg.m^2)
I_{yy}	Inertia about Y Body axis, (kg.m^2)
I_{zz}	Inertia about Z Body axis, (kg.m^2)
h	Altitude
h	Non-dimensional distance b/w CG and tip of mean aerodynamic chord
h_0	Non-dimensional distance b/w wing AC and tip of mean aerodynamic chord
h_t	Non-dimensional distance b/w tail AC and tip of mean aerodynamic chord
i_t	Horizontal tail incidence w.r.t to fuselage reference line
K_n	Static margin, $(h - h_0)$
l	Rolling moment about CG
L_w	Lift generated by wing
L_{fin}	Lift generated by vertical fin
L_t	Lift generated by horizontal tail
M	Mach number
m	Aircraft mass, (kg)
M_{cg}	Pitching moment about center of gravity
$\overset{\circ}{M}_u$	Pitch moment variation with forward velocity, $\bar{q}S\bar{c}(2C_m - C_{m\alpha}\alpha)$
$\overset{\circ}{M}_w$	Pitch moment variation with downward velocity, $\bar{q}S\bar{c}C_{m\alpha}$
$\overset{\circ}{M}_q$	Pitch moment variation with pitch rate, $\bar{q}S\bar{c}C_{mq}/(V_t/\bar{c})$
$\overset{\circ}{M}_{\delta_e}$	Pitch moment variation with elevator deflection, $\bar{q}S\bar{c}C_{m\delta_e}$
N	Yaw moment about CG
$\overset{\circ}{N}_v$	Yaw moment variation with side velocity, $\bar{q}SbC_{n_\beta}/V_t$
$\overset{\circ}{N}_p$	Yaw moment variation with roll rate, $\bar{q}SbC_{n_p}/(V_t/b)$
$\overset{\circ}{N}_r$	Yaw moment variation with yaw rate, $\bar{q}SbC_{n_r}/(V_t/b)$
$\overset{\circ}{N}_{\delta_a}$	Yaw moment variation with aileron deflection, $\bar{q}SbC_{n_{\delta_a}}$

$\overset{\circ}{N}_{\delta_r}$	Yaw moment variation with rudder deflection, $\bar{q}SbC_{n_{\delta_r}}$
p	Roll rate
p_n	Position north
p_e	Position east
q	Pitch rate
$\bar{q}$	Dynamic pressure, $(1/2\rho V_t^2)$
r	Yaw rate
S	Wing reference area
T_{θ_2}	Time constant of numerator zero of (q/δ_e) transfer function
T_γ	Flight path angle delay
V_t	True Airspeed
U, u	X body Velocity, perturbation velocity
V, v	Y body Velocity, perturbation velocity
W, w	Z body Velocity, perturbation velocity
W	Aircraft Weight
S	Wing reference area
S_t	Tail reference area
S_f	Vertical fin reference area
X	X body force
$\overset{\circ}{X}_u$	X force variation with forward velocity, $\rho USC_X + (\bar{q}S/U)(2C_{x2}C_Z - C_{x1})C_{Z\alpha}\alpha$
$\overset{\circ}{X}_w$	X force variation with downward velocity, -$(\bar{q}S/U)[2C_{x2}C_Z - C_{x1}]C_{Z_\alpha}$
$\overset{\circ}{X}_q$	X force variation with pitch rate, $-\bar{q}S[2C_{x2}C_Z - C_{x1}]C_{Z_q}$
$\overset{\circ}{X}_{\delta_e}$	X force variation with elevator deflection, $-\bar{q}S[2C_{x2}C_Z - C_{x1}]C_{Z_{\delta_e}}$
Y	Y body force
$\overset{\circ}{Y}_v$	Y force variation with side velocity
$\overset{\circ}{Y}_p$	Y force variation with roll rate, $\bar{q}SC_{Y_p}/(V_t/b)$
$\overset{\circ}{Y}_r$	Y force variation with yaw rate, $\bar{q}SC_{Y_r}/(V_t/b)$
$\overset{\circ}{Y}_{\delta_a}$	Y force variation with aileron deflection, $\bar{q}SC_{Y_{\delta_a}}$
$\overset{\circ}{Y}_{\delta_r}$	Y force variation with rudder deflection, $\bar{q}SC_{Y_{\delta_r}}$
Z	Z body force
$\overset{\circ}{Z}_u$	Z force variation with forward velocity, $\rho SC_Z U - (\bar{q}SC_{Z_\alpha}\alpha/U)$
$\overset{\circ}{Z}_w$	Z force variation with downward velocity, $\rho SC_Z W + (\bar{q}SC_{Z_\alpha}/U)$
$\overset{\circ}{Z}_q$	Z force variation with pitch rate,$\bar{q}SC_{Z_q}/(V_t/\bar{c})$
$\overset{\circ}{Z}_{\delta_e}$	Z force variation with elevator deflection, $\bar{q}SC_{Z_{\delta_e}}$
L	Roll moment about CG
$\overset{\circ}{L}_v$	Roll moment variation with side velocity, $\bar{q}SbC_{l_\beta}/(V_t)$
$\overset{\circ}{L}_p$	Roll moment variation with roll rate, $\bar{q}SbC_{l_p}/(V_t/b)$

$\overset{\circ}{L}_r$	Roll moment variation with yaw rate, $\bar{q}SbC_{l_r}/(V_t/b)$
$\overset{\circ}{L}_{\delta_a}$	Roll moment variation with aileron deflection, $\bar{q}SbC_{l_{\delta_a}}$
$\overset{\circ}{L}_{\delta_r}$	Roll moment variation with rudder deflection, $\bar{q}SbC_{l_{\delta_r}}$
α	Angle of attack
β	Angle of side slip
γ	Flight path angle
Λ	Wing Sweep back angle
ω_{sp}	Short period mode natural frequency
ω_{ph}	Phugoid mode natural frequency
ω_D	Dutch roll mode natural frequency
τ_R	Roll mode time constant
τ_S	Spiral mode time constant
ϵ	Downwash angle on horizontal tail
ϕ, θ, ψ	Aircraft roll, pitch and yaw angles
θ_n	Nozzle pitch deflection angle
ρ	Air density
δ_a	Aileron deflection
δ_e	Elevator deflection
δ_r	Rudder deflection
δ_t	Throttle deflection

Engine Notation

A_9	Core Nozzle exit area
A_{19}	Bypass nozzle exit area
c_p	Specific heat at constant pressure
g_c	Proportionality constant, $g_c = 1$ in SI Units
h_i	Specific enthalpy at i_{th} station, (J.Kg/K)
I_s	Spool inertia, (kg.m^2)
HV_{fuel}	Heating value of fuel
$\dot{m}_i$	Mass storage rate at i_{th} volume, (kg/s)
N	Shaft rotational speed, RPM
N_L	Physical, Low pressure compressor shaft rotational speed
N_I	Physical, Intermediate compressor shaft rotational speed
N_H	Physical, High pressure compressor shaft rotational speed
N_c^*	Corrected, compressor speed, $(N/\sqrt{T_{in}/T_{std}})$
N_t^*	Corrected, turbine speed, $(N/\sqrt{T_{in}})$
P_a	Ambient pressure
P_i	Total pressure at station number i
P_r	Pressure ratio
P_d	Total pressure in bleed duct
P_{std}	Standard pressure at sea level
R	Gas constant, (J/Kg/K)
S_i	Entropy at i_{th} station
T_d	Total temperature in bleed duct
T_i	Total temperature at station number i
T_{std}	Standard temperature at sea Level
T_C	Core or main nozzle thrust
T_B	Bypass nozzle thrust
T_x	X component of vectored thrust
T_z	Z component of vectored thrust
u	Engine control vector, $[w_f, A_9]$
V_i	Inter-component volume of i_{th} station
w	Mass flow rate (kg/s)
w_a	Mass flow rate of air
w_f	Mass flow rate of fuel
w_{cl}	Mass flow rate from LPC/Fan exit
w_{ci}	Mass flow rate from IPC exit

w_{ch}	Mass flow rate from HPC exit
w_{tl}	Mass flow rate from LPT exit
w_{ti}	Mass flow rate from IPT exit
w_{th}	Mass flow rate from HPT exit
w_{LP}	Mass flow rate at LPC/Fan Entry
w_{IP}	Mass flow rate at IPC Entry
w_{HP}	Mass flow rate at HPC Entry
w_c^*	Corrected mass flow through compressor, $(w_{in}\sqrt{T_{in}/T_{std}})/(P_{in}/P_{std})$
w_t^*	Corrected mass flow through turbine , $w_{in}\sqrt{T_{in}/P_{in}}$
w_{core}	Main Nozzle exit mass flow rate
w_{wing}	Wing Nozzle exit mass flow rate
w_{bypass}	Bypass Nozzle exit mass flow rate
X	Engine state vector
x/l	Non-dimensional bleed location along compressor length, l
η_b	Combustor burning efficiency
η_c	Compressor isentropic efficiency
η_I	Intake efficiency
η_m	Mechanical transmission efficiency
η_t	Turbine isentropic efficiency
Δh	Specific enthalpy change
ΔT	Temperature change
γ	Ratio of specific heats
ϕ_{HP}	Fraction of bleed from HPC mass flow rate
ϕ_{IP}	Fraction of bleed from IPC mass flow rate
τ_{turb}	Torque generated by the turbine
τ_{comp}	Torque required by the compressor

Abbreviations

AC	Aerodynamic Center
AFC	Aerodynamic Flight Control
BWB	Blended Wing Body
CFD	Computational Fluid Dynamics
CG	Center of Gravity
FCS	Flight Control System
PCA	Propulsion Controlled Aircraft
EBF	Externally Blown Flaps
EGT	Exhaust Gas Temperature
HP	High Pressure
HPC	High Pressure Compressor
HPT	High Pressure Turbine
IBF	Internally Blown Flaps
IP	Intermediate Pressure
IPC	Intermediate Pressure Compressor
ICV	Inter-component Volume
IPT	Intermediate Pressure Turbine
LP	Low Pressure
LPC	Low Pressure Compressor or Fan
LPT	Low Pressure Turbine
TET	Turbine Entry Temperature
TVC	Thrust Vector Control

Chapter 1

Introduction

1.1 Introduction

The flying wing design is a very attractive configuration due to the aerodynamic performance advantages it offers over its conventional counterpart [1]. However, the omission of horizontal and vertical stabilizers leads to stability and control authority issues. Consequently very few tailless aircraft have been designed and flown successfully. This is especially true for the civil aerospace sector where the technical advantages associated with this design are easily outweighed by the requirements on safety and degradation in handling qualities.

The blended wing body (BWB) is a special kind of tailless aircraft which has gained renewed interest despite the stability and control deficiencies inherent in its design [2]. This aircraft has been aimed towards the more challenging civil aerospace sector with the following benefits in mind.

- Absence of a horizontal stabilizer and a cylindrical fuselage implies lesser wetted area and therefore less drag. From the aerodynamics point of view this means lesser power required at cruise condition and therefore potentially fewer engines for the same payload. From an environmental perspective, it means lesser emissions per passenger or a greener aircraft.
- Low landing speeds are desirable for all types of aircraft. In the blended wing body concept, the fuselage also produces a significant amount of lift in addition to the outboard wings. Therefore at low airspeeds it might not be necessary to use high lift devices which add weight and complexity in the system.
- Another concept that has been gaining interest is to mount the engines above the Fuselage Reference Line (FRL). The blended fuselage could then act as

a noise shield, reflecting most of the energy away from ground [3]. This has led to a revolutionary new BWB design developed under the *Silent Aircraft Initiative* [4], a joint project between MIT & Cambridge. Although still in its infancy, it is already considering new control strategies such as thrust vectoring to provide additional pitch control authority to this aircraft [5].

Despite these benefits, the BWB concept has many technical challenges [6] which have to be overcome before it becomes a reality.

1.2 Problem Description

Some of the challenges faced by the BWB aircraft designers are,

- Optimization of the planform for attainment of a significantly higher lift to drag ratio than conventional configurations.
- Structural design of a non-cylindrical pressurized fuselage.
- Provision of adequate control authority over the full flight envelope.
- A low emission, low noise propulsion system.

This particular thesis however will focus just on the stability and control aspects, the aim being to see if they can be modified/improved by help from the propulsion system.

1.3 Objectives

The research objectives were grouped as, (i) to quantify the flight control system performance of a representative BWB aircraft [7] and (ii) to augment it by means of propulsion and aerodynamic controls integration. This extends the role of the propulsion system in providing control in addition to provision of thrust. The research methodology was therefore set so as to model both the aerodynamics and the propulsion system as accurately as possible and achieve optimum stability margins/handling qualities, without significantly compromising the efficiency of the propulsion system. In this context, the following candidate concepts for controls and propulsion system integration were evaluated,

- **Use of Jet-Flaps -** Conventional trailing edge flaps on the aerodynamic surfaces are used to generate a force that can be applied about a given axis to generate a control moment. This provides an efficient mechanism to control the aircraft in all three axes. With an increase in flap deflection, the flap efficiency decreases due to boundary layer growth and adverse pressure gradient on the upper trailing edge of the airfoil. At higher flap deflections, the flow may eventually separate and the flap efficiency is drastically reduced. If a certain amount of air from a pressure source such as the engine compressor is blown onto the upper trailing edge of the airfoil, it re-energizes the boundary layer and the airfoil has the potential to be used at much larger deflection angles [8]. If the amount of blown air is increased to an extent that the thin film of jet sheet extends beyond the physical flap limits then the system behaves as pneumatic or air flap, more commonly called the jet-flap. Englar [9] states that this concept has the potential of generating lift comparable to that of the mechanically complex high lift configurations. Since the BWB aircraft has limited moment arms for both the pitch and yaw axis, a problem of control authority exists. The jet-flap concept can be applied here, making the flaps more effective and hence provide better control authority to the aircraft.

- **Thrust Vectoring -** An alternate option is the use of thrust vectoring by the limited motion of the jet exhaust of the engine. Thrust vectoring provides the necessary control force by deflection of the exhaust jet but with a corresponding loss in net axial thrust.

- **Control Allocation -** The third concept is that of control allocation which is based on the proper utilization of control surfaces that span the entire extent of the trailing edge for the BWB. By means of control allocation it may be possible to allocate a control surface to more than one axis without knowledge to the pilot. This would be done automatically by the flight management system, translating pilot commands to appropriate control surfaces depending on the flight condition.

- **Circulation Control -** In the circulation control concept [10], the mechanical flaps are omitted altogether and the thin jet sheet of air is deflected by means of a special arrangement from the trailing edge of the airfoil. In this research, the flapless circulation control concept is not considered as it will be shown later that controls/propulsion augmentation is necessary only under low speed flight conditions. Under high speed flight the control force from mechanical flaps is adequate to control the aircraft in all three axis.

The final solution however may be a hybrid or a combination of the above.

1.4 Methodology

The BWB planform used in this research has been derived from a previous PhD work by Castro [7] at Cranfield University. This research therefore may be considered as a continuation of earlier efforts. The BWB aircraft has been the subject of active research in the industry and academia and therefore an adequate aerodynamic database exists. The methodology adopted for the implementation of propulsion and flight control systems integration on this aircraft was analytical and was broken down into the following aspects.

- **Identification of Control Problems -** As a first step, it was considered necessary to ascertain the longitudinal and lateral-directional stability and control properties for this aircraft. This included, (i) trim and linear analysis under different flight conditions, (ii) evaluation of handling qualities for all three axis and (iii) the design of a stability augmentation system. This exercise clearly identified the areas where controls/propulsion integration could be applied and found useful.

- **Turbofan Transient Performance Modeling -** Two key elements that form the building blocks of any propulsion/controls integration concept are the propulsion system and the airframe. Propulsion system transient performance modeling was therefore considered an important aspect of this work. The requirement was to evaluate the performance of a turbofan engine under variable bleed conditions, effect/extent of thrust vectoring necessary and interaction of aerodynamic controls with engine dynamics. Variable engine bleed was required to cater for an internally blown flap arrangement whereas thrust vectoring was considered for pitch control. In the literature, two approaches have been traditionally considered for transient performance modeling of engine dynamics, namely, (i) an iterative approach and (ii) the inter-component volume approach. The iterative approach is accurate but not well suited for real-time applications whereas the inter-component volume approach is simpler to implement, is therefore faster but less accurate. After a detailed assessment of both the methods, a novel hybrid approach was adopted to model a three spool turbofan engine in a real-time environment. The benefits incurred were both speed and accuracy. The model was validated against the Cranfield University's gas turbine simulation program, TURBOMATCH [11], and the NASA's DYNGEN [12] iterative engine simulation code.

- **Development of a BWB Model with Blown Flaps -** The next logical step was to develop an aircraft model in which the effects of an internally or

externally blown flaps could be simulated. The BWB planform that has been considered had variable twist along the span and different sweep back angles for the inboard and outboard wing sections. In addition, it had an aerodynamic camber section profile which varied from reflexed camber for the inboard sections, nearly symmetric for the mid span and super-critical for the outboard wing. The aerodynamic model for this BWB configuration was developed using a combination of Engineering Sciences Data Units (ESDUs) and a vortex lattice code called TORNADO [13]. The model was then validated against a reference BWB aircraft [7], of similar planform. The effect of blown flaps was included using the jet-flap theory as initially developed by Spence [14] and Williams [15] and later on extended/validated by many other researchers.

- **Controls and Propulsion Integration -** With the propulsion and aerodynamic models in place, it was now possible to incorporate the aerodynamic influence of blown flaps and its effect on engine performance. Slot widths of appropriate dimensions were allocated above the trailing edge of the flaps and then a bleed source selected from either the LP, IP or HP compressor stages of the three spool turbofan. Each of the slots now acted as nozzles to supply a mass flow at a certain jet velocity. The primary aerodynamics effects were an increased sectional lift curve slope, C_{L_α}, and a greater flap effectiveness. The blown flap arrangement was also implemented for the vertical fins which was later found to be crucial for an asymmetric thrust or engine failure condition.

- **Integrated Model Evaluation -** The propulsion and airframe models were implemented in a full six degree of freedom non-linear flight simulation. Lateral and longitudinal flight control systems were designed and implemented to simulate various flight conditions including take-off, approach and landing. Control modes included, pure thrust vector control (TVC), pure aerodynamic flight control (AFC) , AFC + TVC and blown flap arrangements at different blowing momentum coefficients (C_u). The detrimental effect of engine blowing and thrust vectoring was assessed whereas the advantages gained in aerodynamics were recorded. These are presented in the results and conclusions section.

1.5 Thesis Outline

Following this introduction, a detailed literature review is presented in Chapter 2. The literature review section covers aspects such as the development of tailless

aircraft and their generic stability problems. It also includes a discussion of the jet-flap concept and mentions of some aircraft that have attempted to use propulsion and flight control systems integration. Chapter 3 presents in detail the stability, control and handling qualities aspects of the considered airframe and identifies the major problem areas. Chapter 4 and 5 cover the hybrid engine and the BWB aircraft model with blown flaps respectively. Chapter 6 discusses the propulsion and controls integration aspects of the above models, whereas Chapter 7 presents the results of various flight conditions with propulsion and controls model integrated in a non-linear flight simulation environment. Chapter 8 concludes this research, identifies limitations and sets directions for further research work on the subject.

Chapter 2

Literature Review

By virtue of the nature of the research topic involving both tailless aircraft and propulsion/flight control systems integration, the literature review is sub-divided into the following sections, (i) tailless aircraft and their stability analysis, (ii) jet-flaps and their applications and (iii) a brief review of a few propulsion controlled aircraft that have used either thrust vectoring or jet-flaps or a combination thereof.

2.1 Literature Review - Tailless Aircraft

In this section, tailless aircraft are first considered in general, their historical development in the UK, US and Europe along with some of the recent developments. The longitudinal and lateral-directional aerodynamic properties of the tailless designs are then highlighted to emphasize upon the underlying reasons related to poor controls and handling qualities performance.

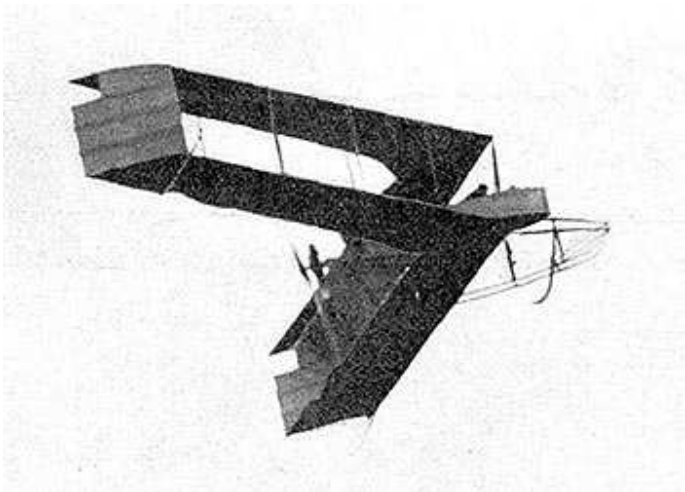

Figure 2.1: Lt. John W. Dunne in his flying wing [16]

2.1.1 A Historical Perspective

Developments in the UK and Germany - Some of the earliest contributions to flying wings came from Lt. John W. Dunne [17] of UK between the period 1907-1914. He started his work from a tailless glider and followed it up by a series of powered bi-planes. Even at this early stage of development, he had realized the advantage of wing sweep to increase the effective tail length. He also incorporated wash out or twist at the wing tips to counteract the premature tip stall characteristics, that are inherent in swept wing designs. One of his many works is shown in Figure 2.1.

Figure 2.2: Horten IX [18]

Reimar and Walter Horten [18] were two brothers who served in the German army during the second world war. There extensive work on tailless airplanes finally culminated in the design of a twin turbojet bomber named the Horton IX (Figure 2.2). The design was in certain aspects similar to the Northrop [19] designs of the same period. It was flight tested in the year 1945. In its first flight test, Horton IX achieved a maximum level speed of 497 mph. Unfortunately this aircraft crashed during landing and was totally destroyed.

Developments in the US - In the US, the most significant contributions toward the design of tailless aircraft came from Northrop [19]. One of his earlier designs the Northrop N-1M flew in 1940s. After the war, Northrop built a piston powered flying wing bomber called the YB-35. With the advent of turbojet engines, Northrop converted this to the jet-powered YB-49. The YB-49 aircraft flew well initially but the prototype also crashed during landing. The pilot, Glen Edwards was killed. The Edwards Air force Base was then named after him. The Northrop YB-49 flying wing bomber never went into production. Figure 2.3 shows a YB-49 at take-off.

Figure 2.3: YB-49 at take-off [20]

With the advent of modern fly-by-wire technology, the flying wing bomber B-2 was built and finally brought into production by Northrop Grumman in the late 1980s. The primary benefit offered by the flying wing design was that of stealth and better payload carrying capability. The flight handling characteristics were much improved by the fly-by-wire system. The flight control system of B-2 is developed by General Electric and is quadruple redundant with a set of primary and back up control laws. By virtue of its flight controls technology the Northrop B-2 shows Level 1 flying qualities throughout its flight envelope.

Figure 2.4: Northrop B2 Spirit [20]

Since the 1990s, renewed interest in a special type of tailless aircraft has emerged. Named as the Blended Wing Body (BWB) it has a wing that blends smoothly into a wide flat tailless fuselage. With the marked increase of composite use in aircraft structures such non-cylindrical shapes are now considered feasible. Significant benefits in terms of speed, range and internal volume are envisaged. Designed by Boeing Phantom Works and manufactured at Cranfield Aerospace England, the X-

48B blended wing body went through extensive wind tunnel tests at NASA Langley and the first flight test was carried out in July 2007.

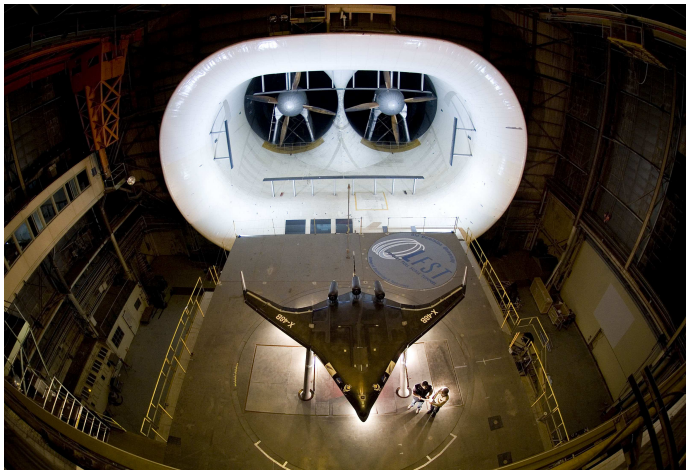

Figure 2.5: X-48B undergoing wind tunnel testing at NASA [21]

Another development that has gained momentum is the *Silent Aircraft Initiative* [4] (Figure 2.6). The aircraft has a blended wing type airframe and a distributed propulsion system [22]. The design objectives include reduced aircraft noise and low emissions [23]. In order to meet these objectives, the design of the planform and the placement of the engines is a radical departure from the conventional. From this initial design it seems apparent that this design will not fly without some level of thrust vectoring incorporated in the pitch axis. The development team at MIT and Cambridge predicts that first prototype is expected to be in service in a 20 to 30 years time frame. This estimate is not unrealistic keeping in view the technical challenges that need to be overcome in addition to convincing the aircraft manufacturers about the advantages associated with such a design. Considering the fact that the Boeing-747 aircraft first flew in the 1970's, the next generation of large civil air transport is already long overdue.

Figure 2.6: Silent Aircraft experimental design SAX-40 [4]

2.1.2 Tailless Aircraft and Longitudinal Stability

This section presents a review on some of the important longitudinal stability parameters as applicable to tailless designs. These include the pitch stiffness parameter, C_{m_α}, the pitch damping derivative, C_{m_q} and the elevator control power, $C_{m_{\delta_e}}$. It also includes a brief review of the influence of static margin, K_n, and wing sweep, Λ, on the longitudinal stability of such aircraft.

2.1.2.1 Tailless Aircraft and Static Pitch Stability (C_{m_α})

A discussion on the underlying equations that govern the longitudinal stability of tailless designs is considered. An appreciation of this aspect is important as it leads the aircraft designer to shape the wing so that it provides both lift and control at the same time. McCormick [24] suggests that for static pitch stability,

$$C_{m\alpha} < 0 \tag{2.1}$$

$$C_{m0} > 0 \tag{2.2}$$

Here angle of attack (α) is referenced from the zero lift line of the aircraft. Equation (2.1) states that for the aircraft to be statically stable in pitch, the variation in pitching moment with alpha must be negative. Therefore an increase in angle of attack will generate a negative pitching moment about the CG, bringing the aircraft back to its trim condition. From the second condition (2.2), it is evident that for $\alpha = 0$, the value of pitching moment about CG (M_{cg}) must be positive. The aircraft will then need to generate a certain value of $\alpha > 0$ to sustain the weight of the aircraft. It is assumed that for the normal range of angle of attack the variation in M_{cg} is linear, therefore the aircraft can only trim at positive α if $M_{cg} > 0$ at $\alpha = 0$.

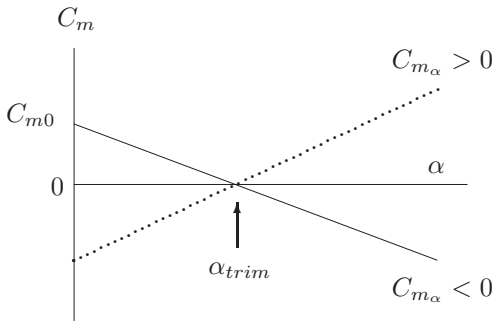

Figure 2.7: Variation of pitching moment with angle of attack

In Figure 2.7 the aircraft is in trim at a certain positive value of angle of attack, where the total pitching moment about the centre of gravity is zero. If the angle of attack is now slightly increased from its trim value, the pitching moment about CG varies almost linearly with alpha. For the line marked $C_{m\alpha} < 0$, the increment in pitching moment is negative. Thus a nose down moment is introduced which for a given elevator setting, δ_e, brings the aircraft back to α_{trim}. In contrast, if the variation of pitching moment marked with line $C_{m\alpha} > 0$ is considered, the increment in pitching moment with angle of attack is positive. This shall further increase the angle of attack and the aircraft would quickly diverge in the pitch axis.

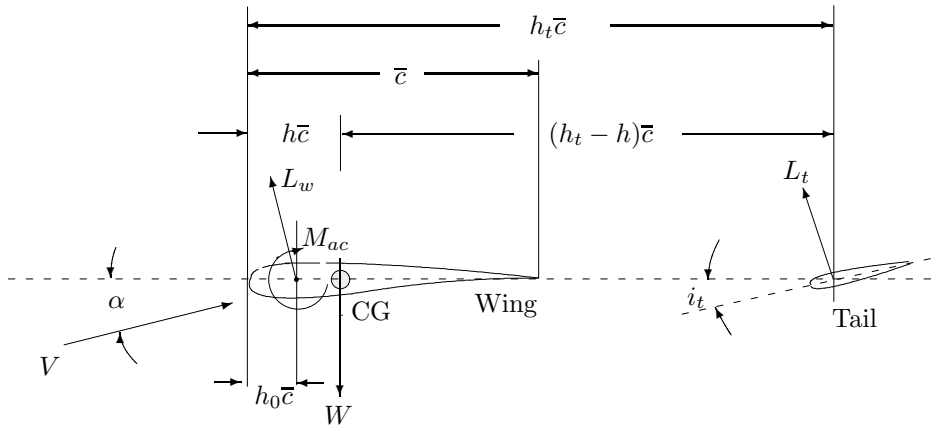

Figure 2.8: Forces and moments on wing and horizontal tail

Now consider the case of static moment balance for a conventional aircraft as shown in Figure 2.8. The pitching moment about the CG can be written as the sum of individual moments due to wing lift, tail lift and the moment about the aerodynamic centre of the wing. For this simple analysis, the moments generated by the propulsion system and that due to the drag on the tail have been neglected. It is also assumed that angle of attack is small so that $\cos(\alpha) \approx 1$. The pitching moment about CG is given as,

$$M_{cg} = M_{ac} + (h - h_0)\overline{c}L_w - (h_t - h)\overline{c}L_t \tag{2.3}$$

Non-dimensionalizing the above equation by $qS\overline{c}$ gives,

$$C_{mcg} = C_{mac} + (h - h_0)C_{Lw} - (h_t - h)\frac{S_t}{S}C_{Lt} \tag{2.4}$$

Defining a linear variation of tail lift coefficient, C_{Lt}, as below

$$C_{Lt} = a_t[\alpha\left(1 - \frac{d\epsilon}{d\alpha}\right) - i_t] \tag{2.5}$$

where a_t is the tail plane lift curve slope and the remaining term is the effective angle of attack seen by the tail. It is less than the wing angle of attack, α, by the wing down-wash effect, $d\epsilon/d\alpha$, and the tail incidence angle, i_t. The wing lift coefficient can also be expressed by a linear relationship

$$C_{Lw} = a_w\alpha \tag{2.6}$$

where a_w is the lift curve slope of the wing. Equation (2.4) can now be written as

$$C_{mcg} = C_{mac} + (h - h_0)a_w\alpha - (h_t - h)\frac{S_t}{S}a_t\left[\alpha\left(1 - \frac{d\epsilon}{d\alpha}\right) - i_t\right] \tag{2.7}$$

Equation (2.7) is the basic relationship for the pitching moment about CG for an aircraft with a tail. Defining the following,

$$C_{m0} = C_{mac} + (h_t - h)\frac{S_t}{S}a_t i_t \tag{2.8}$$

$$C_{m\alpha} = (h - h_0)a_w - (h_t - h)\frac{S_t}{S}a_t\left(1 - \frac{d\epsilon}{d\alpha}\right) \tag{2.9}$$

Equation (2.7) can be re-written as

$$C_{mcg} = C_{m0} + C_{m\alpha}\alpha \tag{2.10}$$

From Equation (2.2) we have argued that for positive pitch stability $C_{m0} > 0$. Examining Equation (2.8) it can be seen that for a tailed aircraft, C_{m0} has two parts. One due to wing, C_{mac}, and other due to the fixed incidence of the tail. For positively cambered airfoils, C_{mac} is invariant with α and is negative. Overall C_{m0} is then made positive by the second term (due to the tail) on the right hand side of Equation (2.8). The tail setting angle, i_t, is defined positive downwards and the distance between the tail aerodynamic centre and the CG, $h_t - h$, is also positive. So the contribution of the tail towards C_{m0} is positive and helps to achieve the desired condition of $C_{m0} > 0$. For a tailless aircraft, Equation (2.8) reduces to

$$C_{m0} = C_{mac} \tag{2.11}$$

The C_{m0} is then made positive by incorporating a reflex at the trailing edge of the wing (Figure 2.9). This however comes at the cost of a reduction in the value of

achievable lift coefficient.

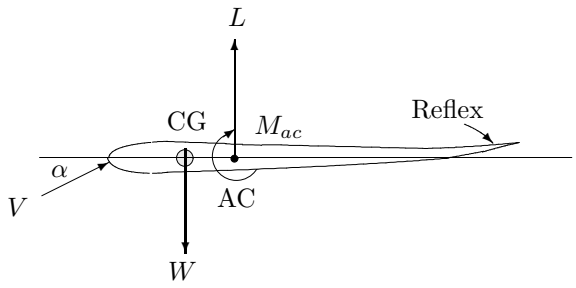

Figure 2.9: Trailing edge reflex for tailless airplanes

Referring to the expression for $C_{m\alpha}$ as given by Equation (2.9), it can be seen that it also has two parts, one given by the wing and the other by the tail. From Equation (2.1) it is known that for positive pitch stability, $C_{m\alpha} < 0$. The second part (due to the tail) on right hand side of Equation (2.9) provides most of the negative component of $C_{m\alpha}$. The first part $(h - h_0)a_w$, which is due to the wing is usually positive with $(h - h_0)$ being positive. This means that the CG can be located aft of the aerodynamic centre of the wing. For a tailless aircraft however, Equation (2.9) reduces to

$$C_{m\alpha} = (h - h_0)a_w \tag{2.12}$$

The only way in which $C_{m\alpha}$ can now be be made negative is by setting $(h - h_0) < 0$. That is by locating the CG ahead of the aerodynamic centre of the wing. This severely restricts the available CG range for tailless aircraft as compared to a conventional configuration.

2.1.2.2 Tailless Aircraft and Pitch Damping (C_{mq})

For aircraft with horizontal stabilizers, most of the pitch damping is contributed by the horizontal stabilizer. However Jones [25] points out that as long as the aircraft has a positive static margin, a lower value of C_{mq} associated with tailless airplanes is not a serious disadvantage. Northrop [19] further explains that although the value of C_{mq} is low for tailless airplanes, the short period oscillation is well damped. This is due to the vertical damping parameter, C_{Zw}, that absorbs most of the energy of oscillation.

Donlan [26] further suggests that a reduced or a negative static margin for tailless aircraft may result in an uncontrolled dynamic instability called **tumbling**. Tumbling consists of a continuous pitching rotation about the lateral axis of the airplane. Conventional control surfaces are almost rendered useless once the tumbling motion is initiated. Donlan [26] continues to state that to avoid this tumbling dynamic mode, the centre of gravity of a tailless airplane should never be permitted under any condition to reach a position behind the aerodynamic centre of the wing. Fremaux [27] however argues that a positive static margin is not a guarantee against the tumbling phenomenon for tailless aircraft. The absence of the horizontal stabilizer and thus reduced pitch damping, C_{mq}, is a big drawback in this context.

2.1.2.3 Tailless Aircraft and Elevator Control Power ($C_{m_{\delta e}}$)

The type of longitudinal control usually employed for tailless aircraft consists of an elevator (or flap) placed at the trailing edge of the wing. For the same static margin, the elevator of a tailless airplane usually must be deflected considerably more than that of a conventional airplane to produce the same change in pitching moment coefficient C_m. Donlan [26] also analyzes the control power required for take-off conditions. At take-off, the longitudinal control besides supplying a pitching moment to trim the aircraft, must also be able to provide the additional pitching moment necessary to counteract:

- Pitching moment of the weight of airplane about the point of ground contact.
- Pitching moment created by friction force on wheels.

It appears likely that if some scheme of enhancing the elevator control power ($C_{m_{\delta e}}$) is not provided the nose wheel would not lift off, especially for tailless aircrafts with large static margins.

2.1.2.4 Tailless Aircraft and Static Margin (K_n)

For a tailless aircraft, the static margin is simply the non-dimensional distance between the aerodynamic centre (AC) of the wing and the CG location. It is positive if CG is ahead of AC toward nose. The longitudinal control power and dynamic stability problems severely restrict the CG range for tailless airplanes. Donlan [26] suggests an ultimate static margin range of 0.02 to 0.08 for such aircraft. Castro [7] also states that due to the limited control power the positive static margin has to be limited to lower values than those of conventional aircraft. Northrop [19] however

argues that an unstable configuration augmented with the power of a digital fly-by-wire flight control system provides the best design option for a tailless aircraft. The final range of static margin for any aircraft can however only be ascertained after a full dynamic and static stability analysis throughout its flight envelope.

2.1.2.5 Effect of Wing Sweep (Λ) on Tailless Aircraft

It was noted by Thorpe [28] that sweep-back gives the wing an effective tail length and is therefore especially adaptable for tailless airplanes. High lift flaps can then be placed at the centre of the wing where their lift increments produce only minor changes in pitching moment about the centre of gravity. Flaps for longitudinal control can be located near the wing tips to produce the requisite pitching moment for trim. Furthermore, he adds that sweep-back introduces the undesirable effect of premature tip stall, which can be avoided by use of wash out or wing twist. This lowers the angle of attack of the tip section.

Another effective method advocated by Donlan [26] to overcome tip stall was the use of leading edge slats. He states that if this method is properly implemented, it could delay tip stall by 10°. Thorpe [28] further states that use of wing sweep enhances the elevator control power but introduces a worse problem of tip stall due to lateral growth of boundary layer over the swept wing. This, if left untreated, may result in wing drop and loss of control due to lack of flow over the control surface. Northrop [19] also concludes that sweep back provides probably the best way to enhance longitudinal control power for tailless designs.

2.1.3 Tailless Aircraft and Lateral-Directional Stability

The review on lateral directional stability includes discussion on some of the important stability parameters as applicable to tailless designs. These are the directional stiffness, C_{n_β}, roll stiffness, C_{l_β}, rudder control power, $C_{n_{\delta_r}}$ and adverse yaw, $C_{n_{\delta_a}}$.

2.1.3.1 Tailless Aircraft and Directional Stability (C_{n_β})

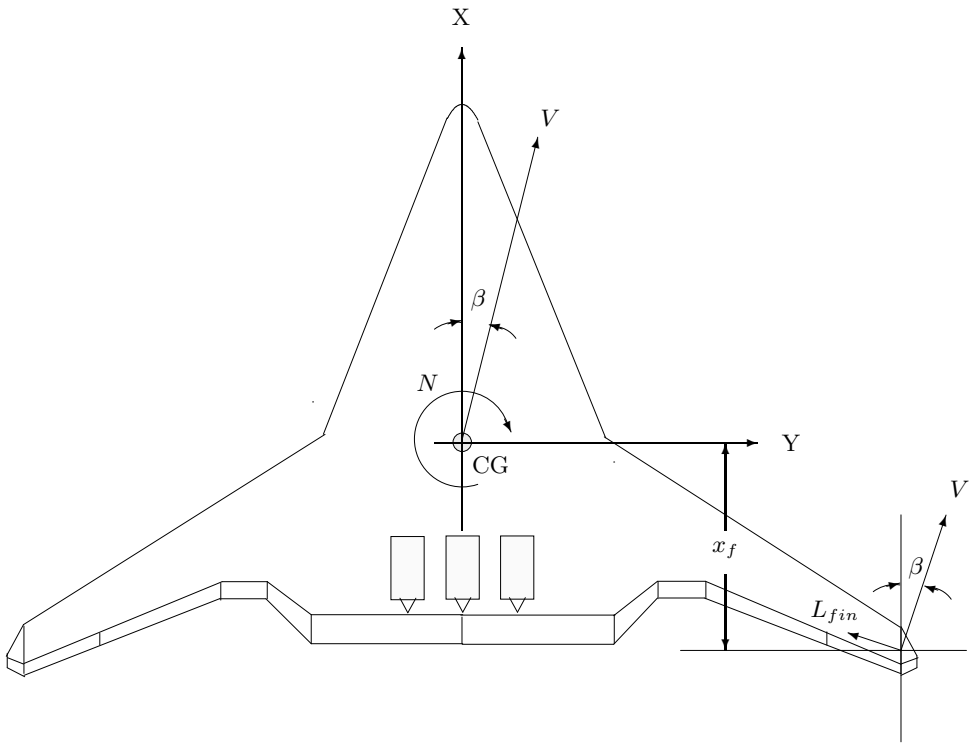

Figure 2.10: A tailless aircraft in positive sideslip

Consider a tailless aircraft with vertical side fins as shown in Figure 2.10. The airplane is undergoing positive sideslip, β. The velocity component along the y body axis is non-zero and positive. Since the velocity vector, V, does not lie in the plane of symmetry a yawing moment, N, is produced by the fuselage and the vertical fin. By definition, the airplane will possess positive directional stability if,

$$\frac{\partial N}{\partial \beta} = N_\beta > 0 \tag{2.13}$$

With the controls fixed, a positive sideslip, β, generates a yawing moment N. For positive yaw stiffness, this yawing moment will be restoring ($N > 0$) and causes the aircraft's nose to turn into the wind, minimizing sideslip. Generally the yawing

moment from the fuselage is de-stabilizing however the contribution from an aft-placed vertical fin is stabilizing. This yawing moment may be expressed as

$$N = \overline{q}SbC_n \tag{2.14}$$

where C_n is the yawing moment coefficient, S is the reference area, b is the characteristic length and $\overline{q}$ is the free stream dynamic pressure. The lift from the vertical fin is

$$L_{fin} = \frac{1}{2}\rho {V_t}^2 S_f C_{Lf} \tag{2.15}$$

If the distance of the mean aerodynamic centre of the vertical fin and the centre of gravity of aircraft is x_f, then the yawing moment generated by the fin is

$$N_f = L_{fin}x_f = \frac{1}{2}\rho {V_t}^2 S_f C_{Lf} x_f \tag{2.16}$$

But $C_{Lf} = a_f(1 - \frac{d\epsilon}{d\beta})\beta$, where a_f is the vertical fin lift curve slope and $d\epsilon/d\beta$ is the down wash factor of fuselage and wing on the vertical fin. Therefore (2.15) becomes,

$$N_f = \frac{1}{2}\rho {V_t}^2 S_f a_f x_f (1 - \frac{d\epsilon}{d\beta})\beta \tag{2.17}$$

Non-dimensionalizing by $\bar{q}Sb$ and taking partial derivative w.r.t β gives,

$$C_{n\beta_{fin}} = \frac{S_f}{S}\frac{x_f}{b}a_f(1 - \frac{d\epsilon}{d\beta}) \tag{2.18}$$

From the above equation, it is evident that directional stiffness parameter $C_{n\beta}$ is a function of the vertical fin area S_f and fin moment arm x_f. For flying wings it is usual practice to place the vertical fins at the wing tips. Structurally it becomes difficult to provide a large fin area using such an arrangement. The fin moment arm, x_f, is also reduced significantly. Directional stability will thus start depending upon on the contribution from the wing/fuselage combination. This may be difficult to calculate theoretically but can be measured quite accurately in a wind tunnel.

Donlan [26] in his report has mentioned about the difficulty in achieving the acceptable values of $C_{n\beta}$ for flying wings. During a series of wind tunnel tests conducted at NASA Langley it was noted that achievable values of $C_{n\beta}$ are less than one third to that of airplanes with tails. This poses a significant challenge in achieving the desired value of weather-cock stability for flying wings.

It is further stated that swept-back wings provide a certain degree of directional stiffness which increases at higher angles of attack. However at high speeds or low values of angle of attack, the directional stiffness provided by the swept-back wing alone seemed inadequate. Fuselage and nacelles have a destabilizing effect comparable in magnitude to the stabilizing effect of the wing alone. It is therefore necessary for tailless airplanes to provide some alternate method of supplying directional stiffness.

2.1.3.2 Tailless Aircraft and Lateral Stability (C_{l_β})

Unlike the restoring moments generated in the pitch and yaw axis, there is no similar mechanism in the roll axis to keep wings level. If the gravity vector is omitted, the aircraft will fly equally well into any roll orientation into the direction of the incoming airflow. In a generic sense it can be said that aircraft possess neutral static stability in roll.

Mclean [29] states that although airplanes have no first order aerodynamic roll stiffness, stable airplanes do have an inherent tendency to fly with wings level. They do so because of the dihedral effect. This is due to interaction of gravity and derivative $C_{l\beta}$ (rolling moment due to sideslip) which exists primarily because of the wing dihedral. When the aircraft rolls to an angle, ϕ, there is a weight component $mg\sin(\phi)$ in the y-body axis. This induces a sideslip velocity, v, to the right and sideslip $\beta > 0$. If the value of $C_{l\beta} < 0$, a restoring rolling moment $\Delta l = C_{l\beta}\beta$ is generated which brings the aircraft back to wings level. The value of $C_{l\beta}$ may be positive or negative depending upon the aircraft configuration, however it is usually kept small otherwise strong yaw-roll coupling exists. The lateral static stability for tailless aircraft is not much different to that of a conventional configuration and good roll damping and stiffness can be achieved using standard design practice.

2.1.3.3 Tailless Aircraft and Yaw Control Power ($C_{n_{\delta r}}$)

Castro [7] states that the yaw control power requirement is determined by one of the following,

- Asymmetric thrust due to engine failure
- Crosswind

Engine Failure - An off-axis engine failure will result in a yaw disturbance moment, ΔN. Under steady state flight conditions the yaw and roll moment balance is given

as,

$$\Delta N = \bar{q}Sb(C_{n_\beta}\beta + C_{n_{\delta a}}\delta a + C_{n_{\delta r}}\delta r) \tag{2.19}$$

$$C_l = 0 = C_{l_\beta}\beta + C_{l_{\delta a}}\delta a + C_{l_{\delta r}}\delta r \tag{2.20}$$

The cross derivatives namely yawing moment due to aileron deflection, $C_{n\delta a}$, (adverse yaw) and rolling moment due to rudder deflection (adverse roll), $C_{l\delta r}$, also appear in the above equations. Assuming zero sideslip ($\beta = 0$), the above reduces to a system of two equations and can be solved analytically for two unknowns ($\delta a, \delta r$). The rudder deflection will be required to counteract the disturbance in yaw and the aileron deflection will be required to counteract adverse roll generated by the rudder.

Cross wind - For the cross wind case, the sideslip is not zero and the equations can be simply re-written as

$$\tan\beta = \frac{v}{V_t} \tag{2.21}$$

$$C_n = 0 = C_{n_\beta}\beta + C_{n_{\delta a}}\delta a + C_{n_{\delta r}}\delta r \tag{2.22}$$

$$C_l = 0 = C_{l_\beta}\beta + C_{l_{\delta a}}\delta a + C_{l_{\delta r}}\delta r \tag{2.23}$$

where v is the wind component in the y-body axis. The net rolling and yawing moment coefficients are considered zero. The above equations can be solved analytically for the aileron and rudder deflections required for steady state side slipping flight.

Castro [7] analyzes four blended wing configurations for assessment of rudder power under these conditions. For the engine failed case with $\beta = 0$ it was found that the aircraft with maximum control power, $C_{n\delta r}$, required the minimum amount of rudder deflection to trim the engine moment. This was as expected. However under cross-wind conditions ($\beta \neq 0$) the same aircraft had the maximum deflection required to trim since directional stiffness, $C_{n\beta}$, was also large for that aircraft. High directional stiffness though desirable therefore becomes a problem under severe cross wind conditions especially at landing.

Various kinds of rudders were tested by Northrop [19] in his early designs. The most successful design was that of the double split flap drag rudder shown in Figure 2.11. Split flaps generate yawing moment by the differential drag on the split flaps and by virtue of their long moment arm (approximately half span) from the centre of

gravity. By the use of a flight control system it is possible to sense sideslip or lateral acceleration and apply the stabilizing yawing moment by use of split flaps. This is an ingenious method of providing directional stiffness to the airplane at the cost of increased drag.

Figure 2.11: B-2 split flap rudders deployed on ground [20]

2.1.3.4 Tailless Aircraft and Adverse Yaw ($C_{n_{\delta_a}}$)

Both conventional and tailless airplanes suffer from adverse yaw. Adverse yaw is due to the yawing moment produced by the differential drag on the ailerons. When ailerons are deflected differentially the drag on them is not equal. The down going aileron sees more drag than the up going one. When the pilot deflects the ailerons to initiate a turn he also applies a bit of rudder to counteract the adverse yaw. This maintains the turn direction as desired. Autopilots incorporate this feature by employing a so-called *ARI : Aileron to Rudder Interconnect* between the lateral and directional axis.

Donlan [26] suggests that while designing ailerons for flying wings special care must be taken to minimize the differential drag upon aileron deflection. In addition it is also suggested to keep the thrust line as close as possible to the centreline, so as to minimize the control power requirement in asymmetric thrust conditions.

2.2 A Literature Review on Jet-Flaps

This section will review the jet-flap concept. The focus will be on the mechanism of lift generation through such an arrangement and a description of its theoretical principles. An application of this technology to aircraft for control purposes will be covered in the next section. Figure 2.12 shows the concept.

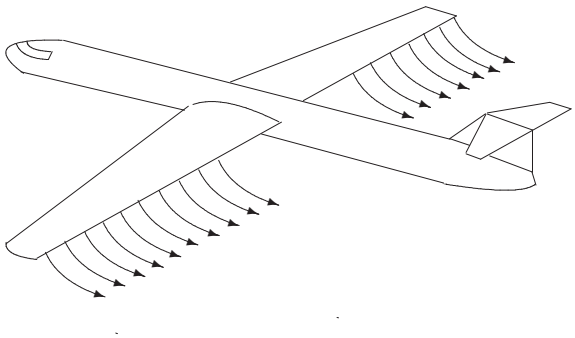

Figure 2.12: The jet-flap concept

2.2.1 Past and the Present

In the UK, jet-flap studies started as early as 1953 at the National Gas Turbine Establishment (N.G.T.E). This included exploration of the basic jet-flap concept by Davidson [30] and Stratford [31] and two-dimensional pressure plot experiments by Dimmock [32]. Williams [15] extended these to three-dimensional sections to include the effects of finite aspect ratio of wings. In 1958, Spence [14] at the Royal Aircraft Establishment (RAE) presented his pioneering work on the theoretical derivation of lift coefficient (C_L) of a jet-flapped wing. Spence derived the expressions for lift coefficient as a function of flap deflection, angle of attack and blowing momentum coefficient (C_u). Many of these experiments were used to support the design of a jet-flap research aircraft called Hunting H-126 [33], unfortunately this aircraft never went into production. Lately, re-newed interest in flapless unmanned vehicles have stirred up research in this area and the work of Frith and Wood [34] on using circulation control for flight control is an example in point.

Similar experiments were conducted in the US and many references could be made. One such example is Englar [9], who at the Georgia Tech Research Institute conducted a series of experiments on jet-flaps and circulation control trailing and leading edge devices for lift enhancement. $\Delta C_L/C_u > 80$ have been reported resulting in

lift coefficients comparable to or better than most complex mechanical flap systems. Englar further analyzes the application of these concepts to a representative model of Boeing 737-100 during take-off and landing. Take-off performance was verified against a 50 ft obstacle. Using analytical studies it was shown that the take-off distance could reduced by more than 50% and the landing speed be reduced up to 40% due to blowing from the trailing edge of the airfoil. The bleed mass flow from the engine was restricted to 5% of the overall fan inflow resulting in a appoximately 5% loss in thrust. For cruise, climb or descent, jet-flaps were not used.

2.2.2 Jet-Flaps and Mechanism of High Lift

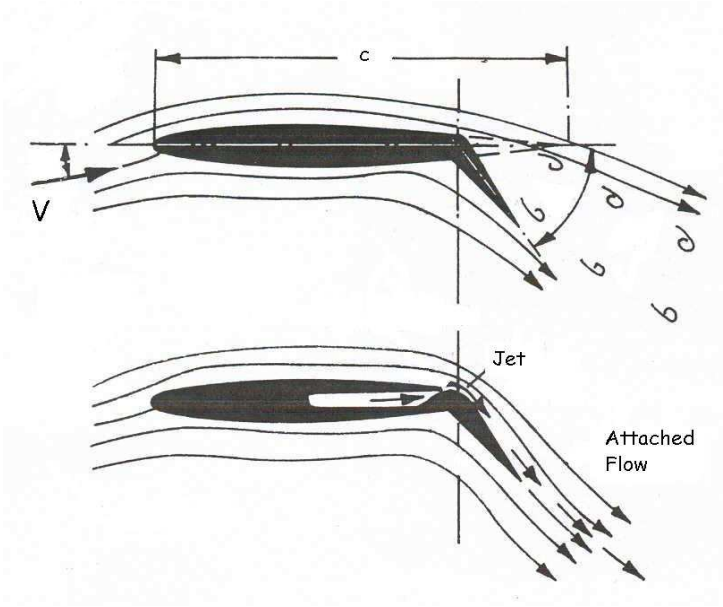

Figure 2.13: Flow control through a trailing edge blown flap [8]

There are two fundamental methods to change the lift coefficient of the airfoil. These are, (i) to adjust the angle of attack of the airfoil relative to the incoming airflow or (ii) to deflect the trailing edge flap i-e change its geometry. As the angle of attack is increased or the flaps are deflected to higher values, flow separation sets in. This occurs either at the wing tip or close to flap hinge. The frictional losses in the boundary layer causes the flow to loose much of its kinetic energy and in the presence of adverse pressure gradient it eventually separates. This puts an upper limit on the achievable lift coefficients [8]. The flow separation can be overcome by either

- Removing the low energy fluid from boundary layer through suction
- Re-energizing the boundary layer through blowing

This particular work uses the later approach for its application to the blended wing body. The blown flap arrangement for boundary layer control/lift enhancement is shown in Figure 2.13.

The blown flap causes the flow to remain attached with the upper trailing edge of the airfoil, however the blowing intensity needs to be increased up to a certain minimum ($C_{u_{crit}}$) level to avoid flow separation completely [8] and achieve the theoretical limit of lift as predicted by potential theory [35]. However after a certain upper limit of angle of attack, the flow starts to separate from the leading edge of the airfoil and trailing edge blowing is not effective.

Within nominal limits of angle of attack, increased blowing above the minimum level required for boundary layer control causes the jet of high velocity to extend beyond the physical flap limits, behaving like an extended flap. This phenomenon has been named as super-circulation or the jet-flap effect. Thus for low values of blowing momentum, the lift is produced by boundary layer control and for high values it is produced by super-circulation. The increase in lift coefficient (C_L) as a function of blowing coefficient (C_u) is shown in Figure 2.14. The reduction in slope ($\Delta C_L/C_u$) after the critical momentum coefficient can be noted, indicating the change in mechanism of lift generation at higher blowing coefficients.

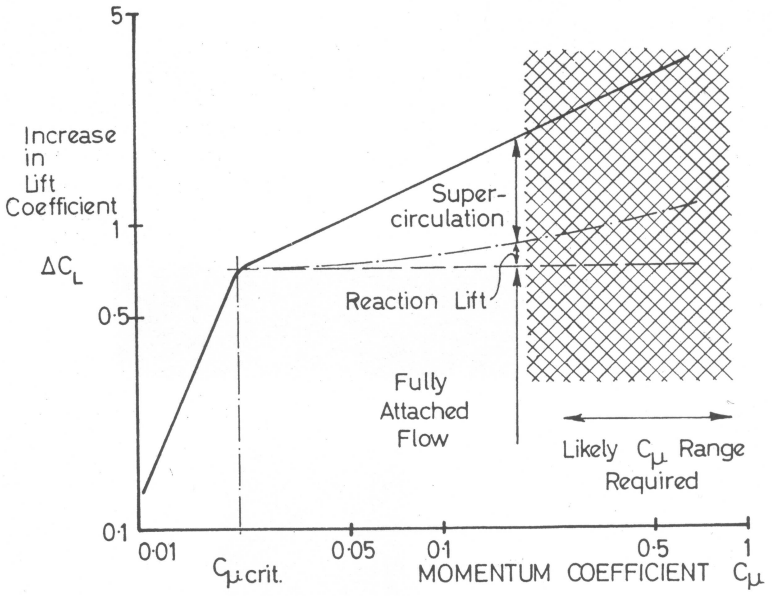

Figure 2.14: Lift increment vs blowing momentum [36]

Many researchers have shown jet-flaps to be a mechanism for producing high lift by blowing air from the trailing edge of an airfoil. By controlling the direction of

the exitting mass flow, it is theoretically possible to produce control moments in all three axes of the aircraft. Englar [9] applied this idea to a Boeing B737-100, he however dispensed with the conventional controls completely in favor of differential blowing for control on all three axis.

The jet-flap is a prime example of integrated aerodynamics and propulsion system, since it can provide the necessary high lift at low speed flight and can meet the flight requirements by optimum selection of required jet momentum flux and jet deflection. Its disadvantage lies in the bleed necessary from the engine or the requirement for a separate gas generator. A non-dimensional parameter, the blowing momentum coefficient, C_u, is generally used to express the strength of momentum flux on the blown flap. It is given as,

$$C_u = \frac{\dot{m}_j V_j}{\overline{q} S} \tag{2.24}$$

where $\dot{m}_j$ is the jet mass flow, V_j is the jet velocity, $\overline{q}$ is the free stream dynamic pressure and S is the reference area . Defining exit area and air density as A_j and ρ_j respectively, (2.24) becomes

$$C_u = \frac{(\rho_j A_j V_j) V_j}{\frac{1}{2}\rho_\infty V_\infty^2 S} \tag{2.25}$$

The jet velocity V_j and density ρ_j can be calculated using isentropic expansion calculations. Englar [9] gives an expression for jet velocity V_j,

$$V_j^2 = \frac{2\gamma R T_d}{(\gamma - 1)}[1 - (\frac{P_\infty}{P_d})^{\frac{\gamma-1}{\gamma}}] \tag{2.26}$$

where T_d and P_d represent total conditions in the blowing duct. Englar [9] further states that a jet expansion to actual static pressure just outside the jet slot would yield higher jet velocities V_j and therefore C_u. Nothing prevents the exitting jet velocity to be supersonic unless the down-shock causes flow interference on the blown surface.

2.2.3 Achievable Lift Coefficients

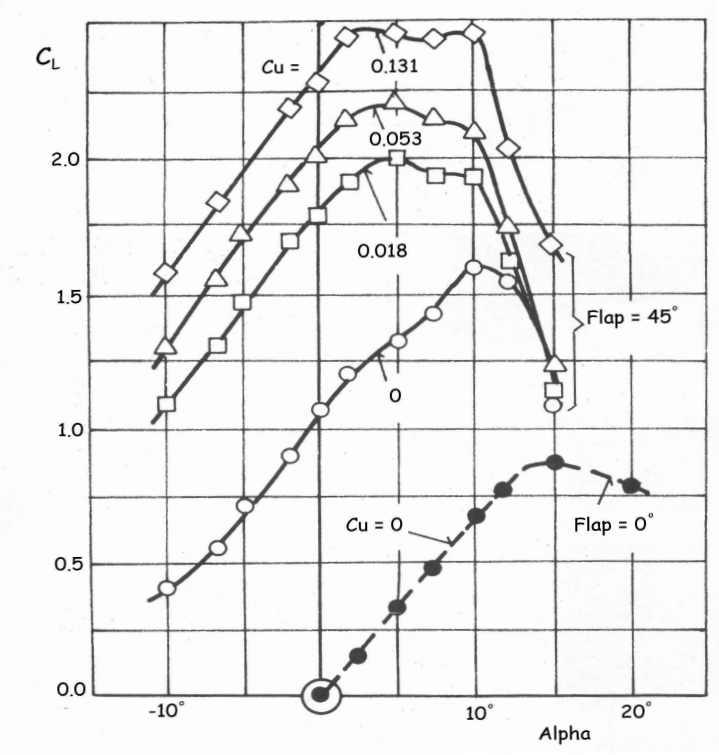

Figure 2.15: Lift coefficients with trailing edge flap blowing [8]

Based on his experimental results, Williams [15] gives an expression of lift coefficient for a two dimensional thin airfoil as,

$$C_L = \tau \left(\frac{\partial C_L}{\partial \tau} \right) + \alpha \left(\frac{\partial C_L}{\partial \alpha} \right) \tag{2.27}$$

where τ is the flap deflection and α is the angle of attack. For the trailing edge blowing case ($c_f/c \to 0$), where c_f/c is flap chord to main chord ratio, the derivatives on the right hand side of Equation (2.27) are expressed as,

$$\frac{\partial C_L}{\partial \tau} = \left[4\pi C_u (1.0 + 0.151 {C_u}^{1/2} + 0.139 C_u) \right]^{1/2} \tag{2.28}$$

$$\frac{\partial C_L}{\partial \alpha} = 2\pi (1.0 + 0.151 {C_u}^{1/2} + 0.219 C_u) \tag{2.29}$$

Similar results were achieved by Spence [14] theoretically. Figure 2.15 shows some of the results from Williams [15] experiments indicating lift coefficients in excess of 2.0 with blowing coefficients (C_u) of the order 0.05. The effect of high $\Delta C_L/C_u$ at low values of blowing coefficient is evident. The above results are further discussed in Chapter 5 where these equations are applied to the case of a BWB aircraft.

2.2.4 Some Blown Flap Arrangements

Figure 2.16 shows some of the possible blown flap arrangements. They can broadly be categorized as,

- Internally blown flaps, or
- Externally blown flaps

In Figure 2.16, the two arrangements shown on the left are examples of internally blown flaps. The ducting for the air has to be made either part of the fixed wing or the movable flap. If the supply source is the compressor of the propulsive system then the amount of air that can be bled from it is limited. This limits the achievable blowing momentum coefficient with such an arrangement. On the right side of Figure 2.16, two externally blown flap arrangements are shown. With such an arrangement very high blowing momentum coefficients can be achieved as all the engine mass flow can be made to impinge upon the blown flap externally, either above or below the wing. The other advantage is that the compressor is not bled so the engine operating point does not change. Both these approaches have been explored for the BWB, as discussed in later chapters.

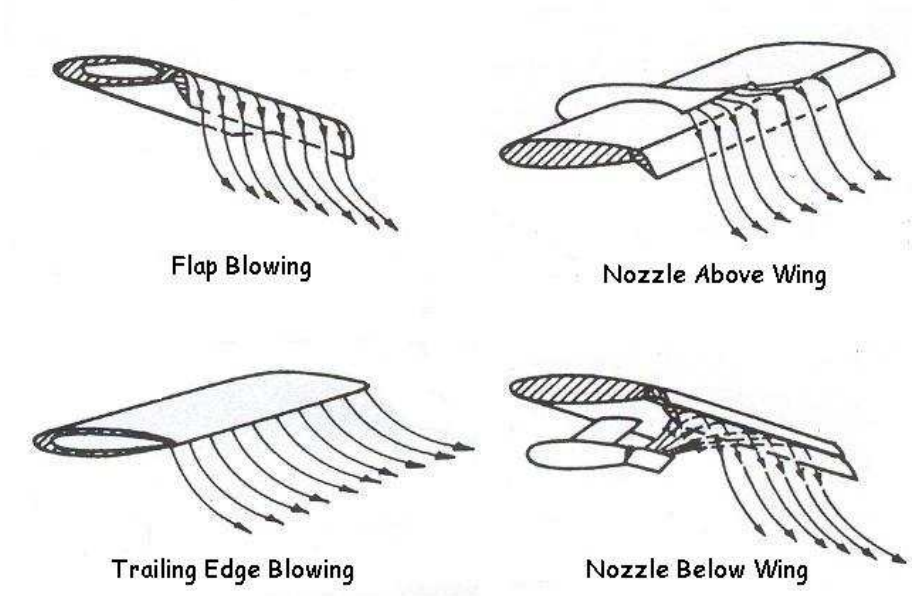

Figure 2.16: Internal and external blown flap arrangements [37]

2.3 A Review on Propulsion/Controls Integration

In this section, efforts made by various researchers to use the propulsion system for flight control purposes is reviewed. This can broadly be categorized as,

- Use of propulsion system for emergency/secondary control
- Use of propulsion system as primary controls

Historically various aircraft designers have attempted to use the propulsion system for control force generation in addition to its normal function of providing thrust. Such aircraft in which the propulsion system is used directly to generate control moments are called *Propulsion Controlled Aircraft* or PCA. PCA may use the propulsion system as secondary control in the event of primary aerodynamic controls failure or as primary controls in the form of thrust vectoring or jet-flaps. Although jet-flaps are a mechanism for providing high lift in absence of complex multi-element flaps, it holds a special significance for the blended wing body. In the absence of a horizontal stabilizer and reduced moments arms for the pitch and yaw axis, the blown/jet-flap concept can make the controls more effective and prevent control saturation. Not many studies are available for propulsion/controls integration for the BWB aircraft, however this literature review includes a preliminary study conducted by NASA on an embedded wing propulsion (EWP) concept which considers distributed propulsion for an 800 passenger BWB aircraft. A discussion on some of the propulsion controlled aircraft follows.

2.3.1 MD-11 Propulsion Controlled Transport Aircraft

Burken et al. [38] did extensive work on the use of propulsion system to control a multi-engine transport aircraft MD-11 (Figure 2.17). Control of both the longitudinal and the lateral-directional axis was considered. The MD-11 airplane is a long range, three engine, wide body transport. The airplane is 202 feet long and has a wing span of 170 feet. The focus of his work was to control the airplane in the event of partial or complete loss of primary control surfaces. Based on his research, Burken [38] proposed the following control strategy,

- **MD-11 - Longitudinal Control**

  For the longitudinal axis, the magnitude and the direction of the velocity vector was to be controlled. This means control of the flight path angle and

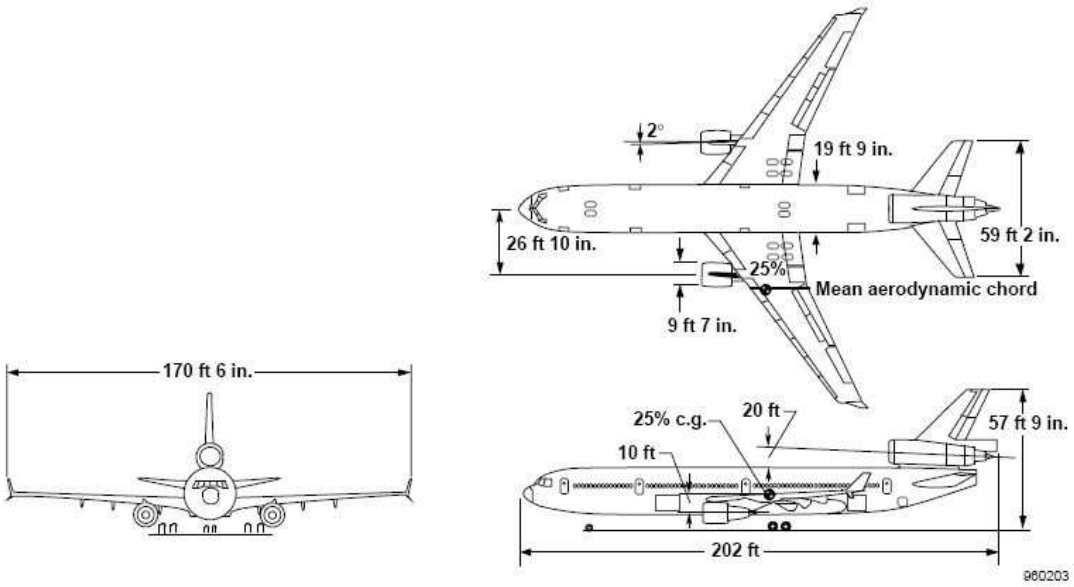

Figure 2.17: Mcdonald Douglas MD-11 transport aircraft [38]

airspeed. Burken [38] allocated individual control tasks to separate engines available on the aircraft. Collective thrust changes on the wing engines were used to implement flight path angle control and the tail engine was used to implement speed control. A flight path error was formed which was passed through a limited P+I network to generate a pitch angle demand. Pitch angle and pitch rate feedback was then used to form collective commands for the left and right engines. The use of pitch angle and pitch rate feedback ensured adequate phugoid and short period damping. For speed control, Burken [38] used the tail engine and a conventional auto-throttle speed control system.

- **MD-11 - Lateral-directional Control**

  Lateral-directional control was obtained by using differential throttle inputs to generate yaw, resulting in roll caused by the dihedral term, $C_{l\beta}$. The primary parameter to be controlled was aircraft heading. A heading error was generated, which was used to generate a bank angle demand. Roll angle, roll and yaw rates were used in the inner loops to control and damp the roll angle. The differential thrust command was then transmitted to the left and right wing engines. This was an intelligent way of obtaining roll control by use of the dihedral effect.

This control strategy was later flight tested on an actual airplane. The aircraft was successfully landed with the primary control surfaces locked at the neutral position.

2.3.2 Boeing - Propulsion/Flight Control System

Various studies have been carried out for propulsion and controls integration on the Boeing aircraft. Two of these are presented here for the Boeing-747 and the Boeing-737 aircraft respectively.

- **Boeing-747 - Thrust Vectoring Control (TVC)**

  Hareförs [39] at the University of Leicester recently conducted a study in collaboration with Volvo Aero Corporation on the design of an integrated propulsion and flight control system for a Boeing-747 aircraft. Both differential thrust management and thrust vectoring control (TVC) were considered. The study concludes that such aircraft can be effectively controlled by use of differential and collective thrust only. To obtain control in all three axes, thrust vectoring was implemented along y and z axes of the aircraft. The vectoring angles $(\delta y, \delta z)$ were limited to 45° and the slew rate limit on the nozzle actuators was set at 60°/s. The thrust components in the x, y and z aircraft axes are given as

$$T_x = T \cos \delta y \cos \delta z$$
$$T_y = T \sin \delta y \cos \delta z$$
$$T_z = T \cos \delta y \sin \delta z$$

  In this study, thrust vectoring was used on all four engines of the Boeing-747 to obtain control moments in three axes. Deflection in the x-z plane generates a T_z force. This force, when used differentially on outboard engines, is most effective in producing roll moment. The motion of the nozzle in the x-y plane produces a T_y force which can be used to generate a yawing moment. The pitching moment is generated by a contribution from the T_x force and that of a T_z force due to the collective thrust vectoring in the x-z plane. Hareförs [39] concludes that effective control can be achieved with differential thrust for lateral control and collective thrust for longitudinal control. The flying qualities however using PCA alone are not as good as those obtained by use of aerodynamic control surfaces, but when PCA and TVC are combined, excellent flying qualities were achieved for the lateral axis. For the longitudinal axis, the TVC+PCA combination still falls short of the flying qualities achieved by use of the horizontal stabilizer.

- **Boeing-737 : Jet-Flaps/Circulation Control for High Lift**

  An analytical/experimental research program was conducted by Englar [9] and his research team in order to conduct a feasibility study of circulation control devices for application to advanced subsonic transport aircraft. The experimental part of the program was concerned with testing two-dimensional airfoils/wing section with an internally blown flap and circulation control arrangements. In the circulation control concept, the movable flap is omitted altogether and the exiting mass flow is made to follow a rounded trailing edge in a manner analogous to a pure trailing edge flap by using the so called *Coanda Effect*. The aerodynamic benefits incurred are a significant increase in sectional lift coefficient as a function of blowing momentum coefficient (C_u). In the absence of a full 3D model with blowing arrangements, the 2D sectional data was corrected for wing sweep, taper and finite aspect ratio. The bleed mass flow was limited to 5% of Fan flow and accounted for almost 5% loss in axial thrust assuming zero thrust recovery after blowing. Analytical studies indicated a 70-80% reduction in take-off and landing distances and 2.5 to 3.0 times increase in the maximum achievable lift coefficient.

2.3.3 Propulsion Control for F-15 Aircraft

Burcham [40] developed and flight tested a propulsion based flight control system for an F-15 airplane at the NASA Dryden Flight Research Centre. The principles used were as follows,

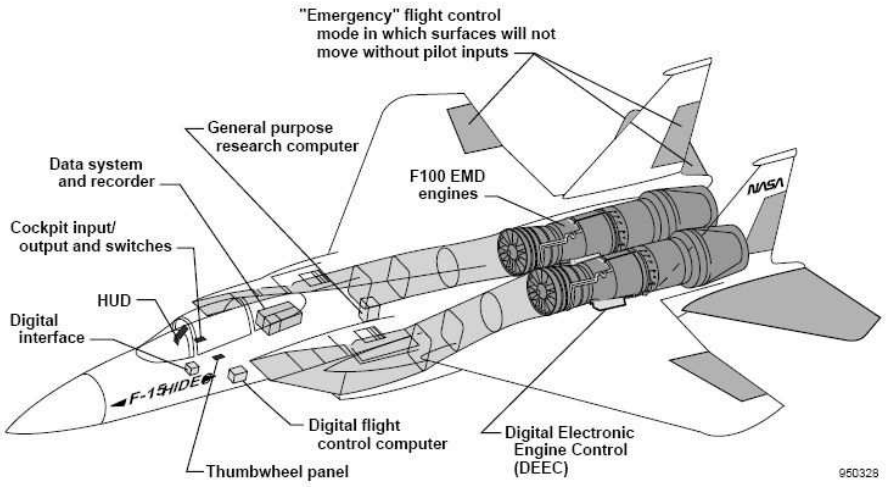

Figure 2.18: F-15 aircraft modified for propulsion control [40]

- **Roll Control using Differential Thrust**

  Differential thrust generates sideslip that through the dihedral effect results in roll rate. Roll rate is controlled to establish a bank angle that results in a turn and a change in aircraft heading. Full differential thrust for the F-15 airplane yields a roll rate of approximately 15°/sec at a speed of 170 kts. With throttles-only flight control, bank is controlled by yaw and the turns were typically not coordinated.

- **Longitudinal Control using Collective Thrust**

  Burcham [40] states that a thrust increase will cause an increase in speed that results in greater lift. With the lift being more than the weight, the flightpath angle will increase, causing the airplane to climb. If allowed to continue, this effect will be oscillatory (phugoid mode). The degree of change to the flightpath angle is proportional to the difference between the initial trim airspeed and the current airspeed. Hence, the flightpath angle tends to increase as speed or throttle increases.

  If the thrust line is inclined nose up to the flightpath, an increase in thrust will increase the vertical component of thrust. This increased vertical component of thrust will cause a direct increase in vertical velocity (that is, rate of climb) and a resulting increase in flightpath angle. For a given aircraft configuration, this effect will increase as angle of attack is increased or the speed is lowered. Burcham [40] states that for the F-15 airplane, the combination of the above thrust effects is to produce a nose up flightpath angle rate response. This rate response peaks at approximately 2°/sec for an increase in throttle for level flight to intermediate power on both engines at 170 kts.

Burcham [40] concludes that the PCA pitch and roll control provided adequate up-and-away flight control. In addition, PCA system was used for landings and was found adequate for safe runway landings in good weather. Pitch control was sluggish but very stable. Approximately 10 seconds were required to achieve a commanded flight path change. Bank angle control was positive but lagged inputs by approximately 3 seconds. On approaches, the pilots spent most of their time making bank angle corrections.

2.3.4 Hunting H-126 - Jet Flap Research Aircraft

The Hunting H-126 jet-flap research aircraft [33] was clearly ahead of its time. It was built by Hunting Corporation under a contract with British Ministry of Aviation for jet-flap research at the Royal Aircraft Establishment (RAE). The primary aims for building such an aircraft were, (i) to complement the wind tunnel [15] and theoretical [14] studies done at that time and (ii) also to investigate the handling qualities for such an arrangement. Figure 2.19 shows the aircraft with its internal ducting. A general description of the aircraft along with some its stability and control features are discussed here briefly.

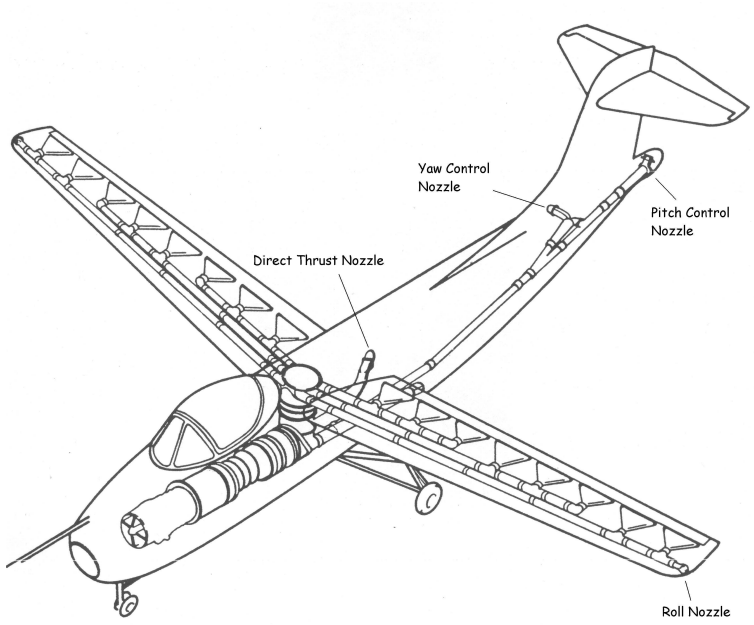

Figure 2.19: Hunting corporation H-126 jet-flap research aircraft [33]

- **Jet Efflux Distribution**

  At that time a decision was made to use the Orpheus turbojet engine as bypass engines were not yet developed. Instead of bleeding the compressor stages, the main jet efflux was used. The engine was de-rated from 5000 to 4300 lbf to keep the exhaust/duct metal temperature below 620° C. The distribution of jet efflux was as follows,

  - 50% for jet-flaps on the wings
  - 35% for direct thrust nozzles
  - 5% respectively for each of the pitch/roll/yaw control nozzles

- **Stability and Control Problems**

  Early in the design stage, it was revealed that the jet-flapped wing in addition to producing large values of lift-coefficients (in excess of 6.0) also produced a large nose down pitching moment. This resulted in a loss of trim lift coefficient due to large trim elevator deflections. This problem was alleviated by using direct thrust nozzles (using approximately 35% of jet efflux) which were placed so as to generate a positive pitching moment that compensated for the jet-flap negative pitching moment. This problem was also noted in this work for the BWB aircraft, even more so due to the absence of a horizontal stabilizer.

  The H-126 aircraft project gave valuable information with regards to achievable lift coefficients with a jet-flap arrangement. In addition, novel ways of controlling pitch, roll and yaw axis with TVC nozzles were actually tested in flight. The project however was discontinued due to financial restrictions and lack of interest in the jet-flap scheme at that time.

2.3.5 UAV Flight Control through Circulation Control

Recent interest in designing flapless unmanned aircraft, primarily for maximizing stealth characteristics has resurrected the jet-flap/circulation concepts for flight control purposes. Frith et. al. [34] at the University of Manchester recently performed an experimental investigation on a totally flapless aircraft by use of circulation control technology. Lift augmentation ($\Delta C_L/C_u$) of approximately 20 was achieved by use of trailing edge blowing only. Experiments were also conducted to achieve roll control by differential blowing on the wings. Rolling moments comparable to that of conventional flaps were reported. In the pitch axis it was further verified that the aircraft could be trimmed adequately well by use of blown air. Increased blowing moment coefficient, C_u, resulted in greater pitching moment about the centre of gravity. Frith further reports that useful lift increments ($\Delta C_L > 0.1$) can be achieved with C_u values of the order of 0.005, equivalent to those of existing flaps. Frith concludes that more experimental/theoretical work is needed to realize the full potential of circulation control for application to this new class of aircraft. Pulsed jets may also be used to provide similar increments yet at a lower mass flow rate [41].

2.3.6 Embedded Wing Propulsion (EWP)

This last part of the literature review briefly discusses the distributed propulsion work done at NASA. The propulsion-airframe integration efforts have culminated into the so called Embedded Wing Propulsion (EWP) [42] concept. EWP is based on a blended wing body and utilizes a large number of relatively smaller engines embedded within the inboard wing structure. The leading edge forms the intake and the trailing edge as the exit for the engine mass flow. The trailing and the leading edge could be deflected to achieve high lift coefficients for take-off and landing. Thrust vectoring was also considered for a 2D case using computational fluid dynamics. The author concludes that EWP concept can be adapted for a variety of missions with aerodynamics performance advantages. Figure 2.20 shows a notional concept for the EWP.

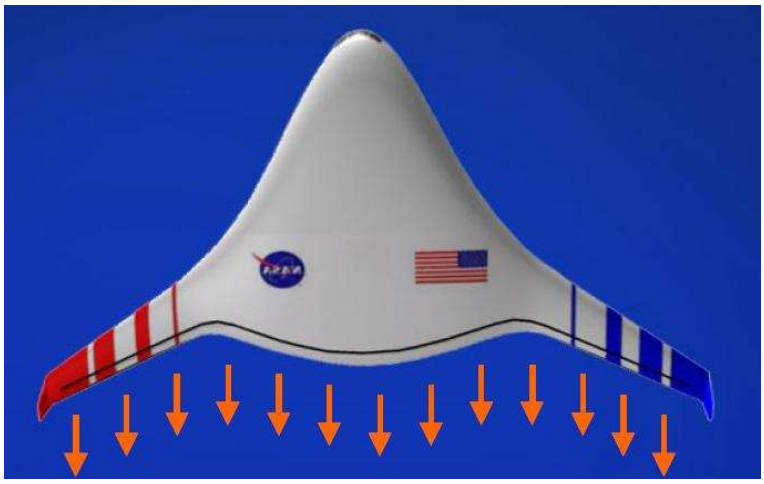

Figure 2.20: The EWP concept for an 800 passenger BWB [42]

2.4 Conclusions - Literature Review

The literature review section has discussed at some length the tailless aircraft, jet-flaps and some propulsion/controls integration concepts. Many more examples could be given but have been omitted due to space limitations. Important conclusions can be made from this review,

- Propulsion and flight control systems integration has been done on a number of aircraft, more so for the conventional configuration. Tailless aircraft in service are few and those with propulsion and controls integrated even less.

With emerging new configurations such as the blended wing body, the jet-flap/blowing concepts for lift generation and flight control has gained renewed interest.

- Large increments in lift coefficients can be achieved using the jet-flap scheme, however it is accompanied by a significant nose down pitch moment. This pitch moment has to be countered without a loss in trim lift coefficient before the full potential of a blown flap arrangement can be utilized.

- Last but not the least, the supply of compressed air from any engine would be limited and would result in a loss of thrust depending upon the percentage bleed. Any mechanism that utilizes the jet efflux directly without the use of internal ducting and accompanying pressure losses would be therefore preferred.

Chapter 3

Identification of Control Problems

It is important to identify the control problems of the baseline BWB configuration [7], before attempting to solve them. The following aspects are considered,

- Estimation of control authority.
- Dynamical analysis of the linear airframe model.
- Evaluation of longitudinal and lateral-directional handling qualities.

Design of a stability/command augmentation system was *a priori* requirement to carry out the above tasks. At the end, this exercise clearly identified the areas where controls/propulsion integration could be applied and found useful.

3.1 Control Authority Analysis

The purpose of the control authority analysis was to identify if the roll, pitch and yaw axis control powers are adequate, especially for low speed flight conditions. The analysis was done separately for the longitudinal and lateral-directional axis. The flap deflection ranges and the aerodynamic data is based on a previous BWB aerodynamic model [7], which will be referred to as the baseline. Details of this aerodynamic model can be found in Appendix A.

3.1.1 Longitudinal Control Power and Trim

The longitudinal control power for steady state non-manoeuvring flight was assessed through longitudinal trim analysis. For a straight and level flight ($\gamma = 0$) all the state derivatives are assumed zero except the north and east position derivatives,

$(\dot{p}_n, \dot{p}_e)$, which are allowed to vary. The MATLAB trim utility was then used to solve the equations of motion with the above constraints. The body rates (p, q, r) and the side slip angle, β, were also set to zero, this decouples the longitudinal and lateral-directional dynamics. From reference [43], the equations of motion for the longitudinal axis are,

$$\begin{bmatrix} \dot{U} \\ \dot{W} \\ \dot{q} \\ \dot{\theta} \\ \dot{h} \end{bmatrix} = \begin{bmatrix} (X + T_x)/m + (rV - qW)/m - g\sin\theta \\ (Z + T_z)/m + (qU - pV)/m + g\cos\theta \\ M/I_{yy} - pr(I_{xx} - I_{zz})/I_{yy} - (p^2 - r^2)I_{xz}/I_{yy} \\ q\cos\phi - r\sin\phi \\ U\sin\theta - V\cos\theta\sin\phi - W\cos\theta\cos\phi \end{bmatrix} \tag{3.1}$$

With the addition of the gravity components, the body axis accelerations $(\dot{U}, \dot{W})$ are simple expressions for Newtons second law of motion with addition of acceleration terms due to body rates (rV, qW, qU, pV). If the roll and yaw rates are zero $(p, r = 0)$, as a for steady wings level flight, the pitch acceleration term $(\dot{q})$ becomes a rotational equivalent of Newtons second law with, $\dot{q} = M/I_{yy}$. With zero bank angle $(\phi = 0)$, the rate of climb derivative $(\dot{h}_n)$ is a transformation of the body axis velocities (U, W) on to the inertial axis. The terms T_x and T_z represent the components of the thrust vector along the X and Z body axis respectively.

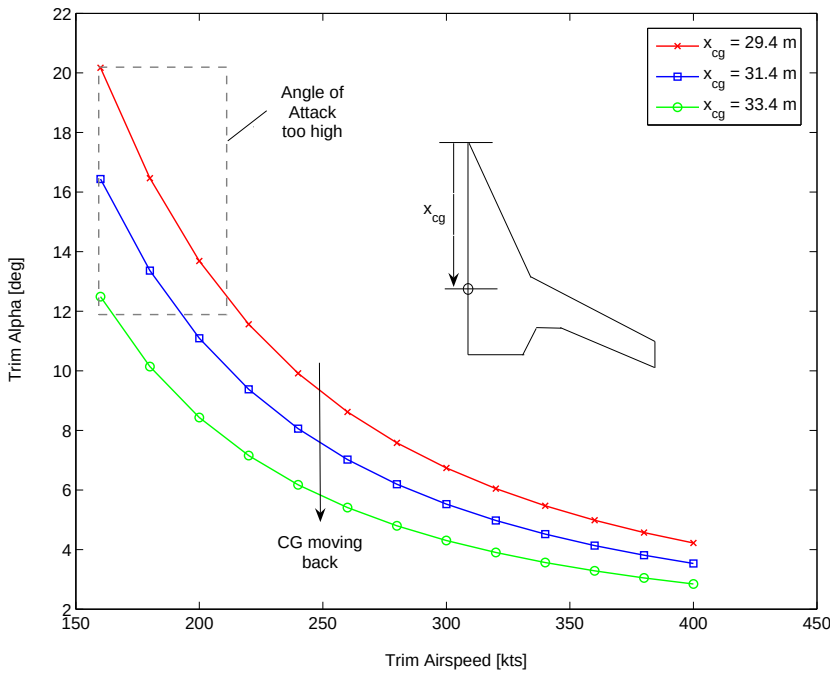

Figure 3.1: Variation in trim alpha with airspeed and CG position

Figure 3.1 shows that in order to sustain the weight of aircraft, the trim angle of

attack increases as the flight speed is reduced. However in the absence of a high lift configuration for the BWB, the increase in angle of attack with decrease in airspeed is significant. In addition to this, and contrary to the conventional tailed aircraft configurations, the BWB aircraft shows a strong influence of CG position on trim angle of attack. At an airspeed of 160 kts, as the CG is moved back by 4 m, the trim angle of attack decreases by almost 8°.

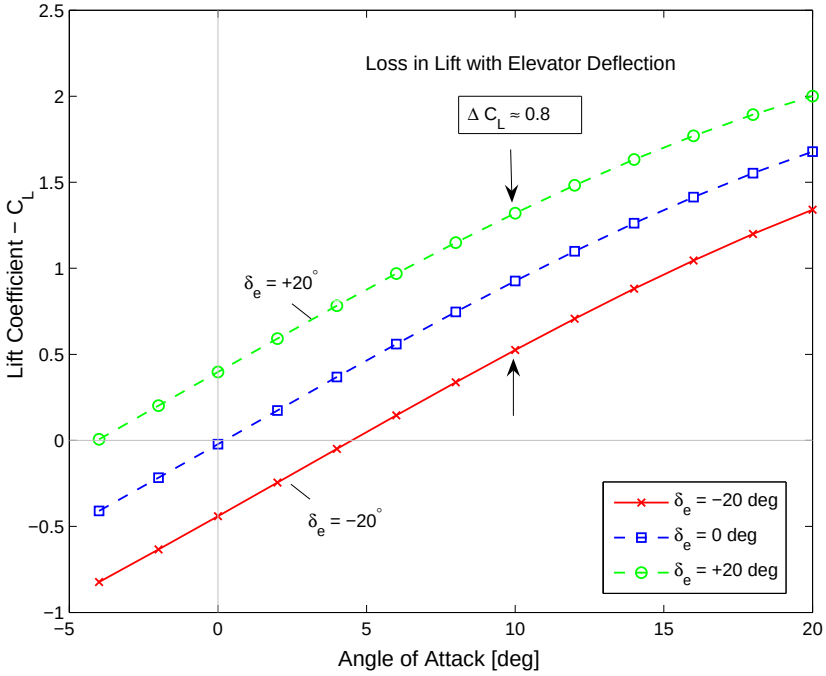

Figure 3.2: Variation in lift coefficient with alpha and elevator deflection

Figure 3.2 further elucidates this point. The graph shows the variation in lift coefficient with angle of attack and elevator deflection. To a close approximation,

$$C_L = C_{L0} + \left(\frac{\partial C_L}{\partial \alpha}\right)\alpha + \left(\frac{\partial C_L}{\partial \delta e}\right)\delta e \tag{3.2}$$

The influence of the elevator, $(\partial C_L/\partial \delta e)$, on lift coefficient is both significant and detrimental. For instance from Figure 3.2, it can be seen that at an angle of attack of 10°, the wing looses almost 40% of its lift generation capability when the elevator deflects by -20°. This loss of lift is undesirable. In a tailless configuration such as the BWB, the elevators are incorporated on the main lifting surface and for nominal CG locations, they deflect in the negative direction to trim the aircraft, resulting in a significant loss of lift.

Figure 3.3 illustrates the trim elevator requirement. The required elevator deflection increases at lower airspeeds and increasing static margin. Again the CG position

strongly influences the trim elevator deflection, which gets close to saturation for nominal/forward CG locations and lower airspeeds. Figure 3.4 shows the corresponding trim throttle requirement. At lower airspeeds the trim throttle is higher due to higher values of induced drag. The trim throttle plot shows that due to its unique configuration, the BWB aircraft operates on the back side of the power required curve even for significantly higher values of airspeeds.

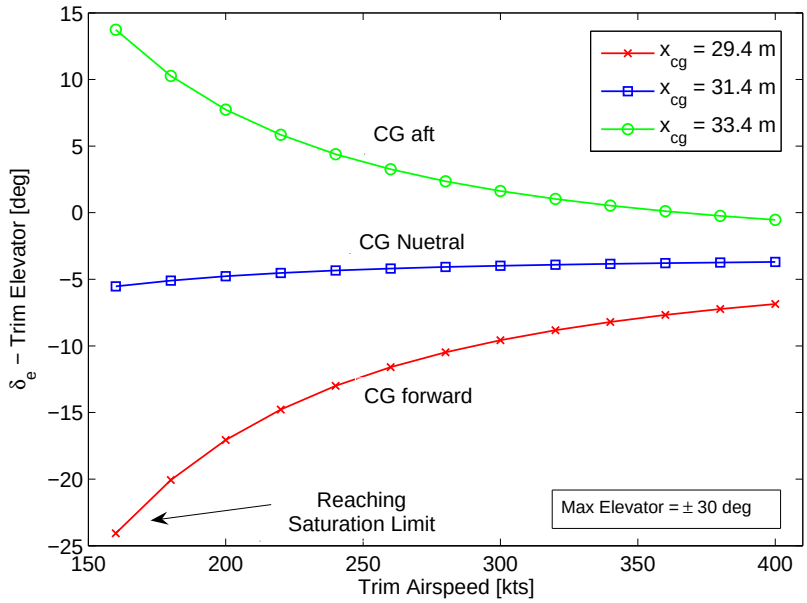

Figure 3.3: Variation in trim elevator with airspeed and CG position

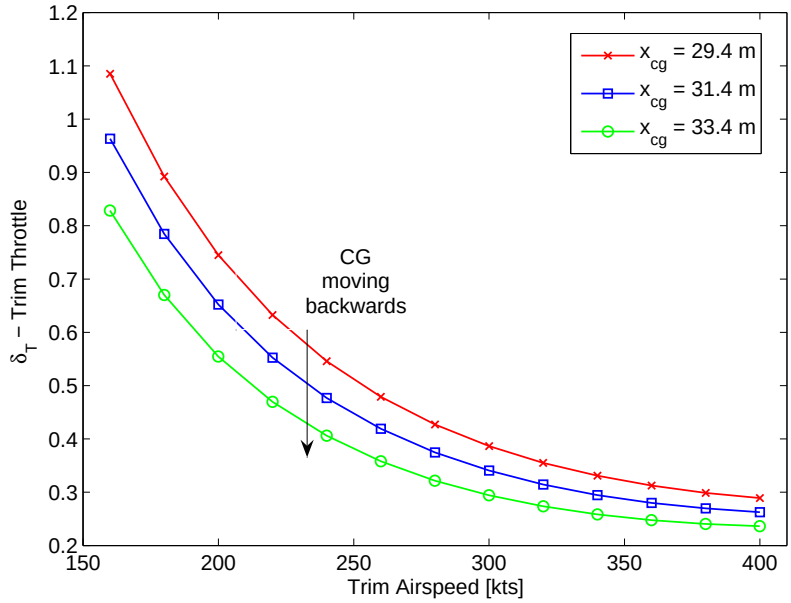

Figure 3.4: Variation in trim throttle with airspeed and CG position

3.1.2 Lateral-Directional Control Power and Trim

The purpose of this analysis is to estimate the amount of aileron and rudder $(\delta a, \delta r)$ deflections necessary to trim the aircraft under asymmetric flight conditions. In a straight and level zero sideslip flight, the parameters that usually effect the trim state are aircraft speed, altitude and CG position. If the aircraft is symmetric and there are no moments generated by propulsion system, the variation of trim parameters such as speed and altitude effects the longitudinal controls $(\delta e, \delta t)$ only. Trim lateral controls, i-e aileron and rudder $(\delta a, \delta r)$, shall nominally be zero. However rudder/aileron deflections are necessary under asymmetric flight conditions, such as port/starboard engine failure, crosswinds or if any roll/yaw moments are generated by the propulsion system in normal operation. The lateral-directional trim analysis was based on the following equations of motion from reference [43],

$$\begin{bmatrix} \dot{V} \\ \dot{p} \\ \dot{r} \\ \dot{\phi} \end{bmatrix} = \begin{bmatrix} Y/m + (pW - rU)/m - g\cos\theta\sin\phi \\ L/I_{xx} + qr(I_{yy} - I_{zz})/I_{xx} + I_{xz}(pq + \dot{r})/I_{xx} \\ (N + N_E)/I_{zz} + pq(I_{xx} - I_{yy})/I_{zz} - I_{xz}(qr - \dot{p})/I_{zz} \\ p + (q\sin\phi + r\cos\phi)\tan\theta \end{bmatrix}. \tag{3.3}$$

The equation for the lateral body acceleration $(\dot{V})$ is an expression for Newtons second law with addition of gravity and acceleration terms (pW, rU). These terms exist due to the angular rotation rate of the body in the inertial frame. The expression for body axis roll acceleration $(\dot{p})$ includes the additional rotational acceleration term (qr) which couples pitch rate into roll axis on account of yaw rate. Similarly for yaw acceleration $(\dot{r})$, the acceleration term (pq) couples roll rate into yaw axis on account of pitch rate. Thus the roll and yaw equations of motion are coupled. The Euler rotation rate $(\dot{\phi})$ is a simple projection of body rates (p, q, r) on the $(\dot{\phi})$ axis and is a kinematic relationship. The east position and heading states (p_e, ψ) are not presented as they do not effect the lateral-directional dynamics.

The term N_E represents the yawing moment produced by the engine about the CG position in case of asymmetric thrust. Nominally if all the three engines are operating at the same thrust level this yawing moment component should be zero. However in the event of a starboard or port engine failure, a significant yawing moment will be generated, which will have to be catered for by the rudder deflection. To estimate the rudder control power requirements, two trim cases were considered

- Engine failure (asymmetric thrust)
- Engine failure with crosswinds

The engine failure case will first be considered independently and then in combination with cross winds. Presence of strong cross winds and asymmetric thrust can put severe demands on both lateral (roll) and directional (yaw) controls.

Rudder Requirements for Starboard/Port Engine Failure - For the present analysis it is assumed that three engines are used and they are mounted on top of the centre body. In case of a port or starboard engine failure, rudder deflection will be necessary to maintain direction and zero out any sideslip. The amount of rudder deflection will further depend on the throttle setting and the aircraft speed.

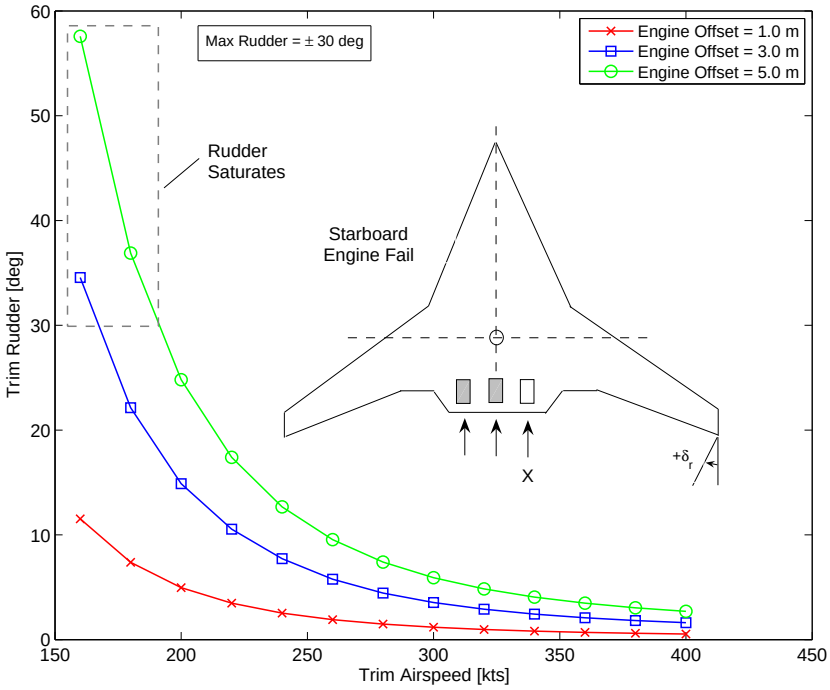

Figure 3.5: Trim rudder with starboard engine fail

Figure 3.5 illustrates that at lower airspeeds and for a lateral engine offset of 5 m, the rudder deflection to achieve zero sideslip reaches very high values. Clearly the rudder control power of the baseline BWB configuration is inadequate. Also shown in Figure 3.6 are the required trim aileron deflections to counter the adverse rolling moment generated by the rudder. At lower airspeeds, the aileron requirement just to counteract this adverse roll is also excessive.

Trimming under Cross Winds and Engine Failure - A similar trim analysis was performed for the cross wind case. Depending upon the direction of crosswind, the amount of rudder deflection can increase or decrease. If both the yawing moment generated by the asymmetric thrust and the cross wind act in the same direction the

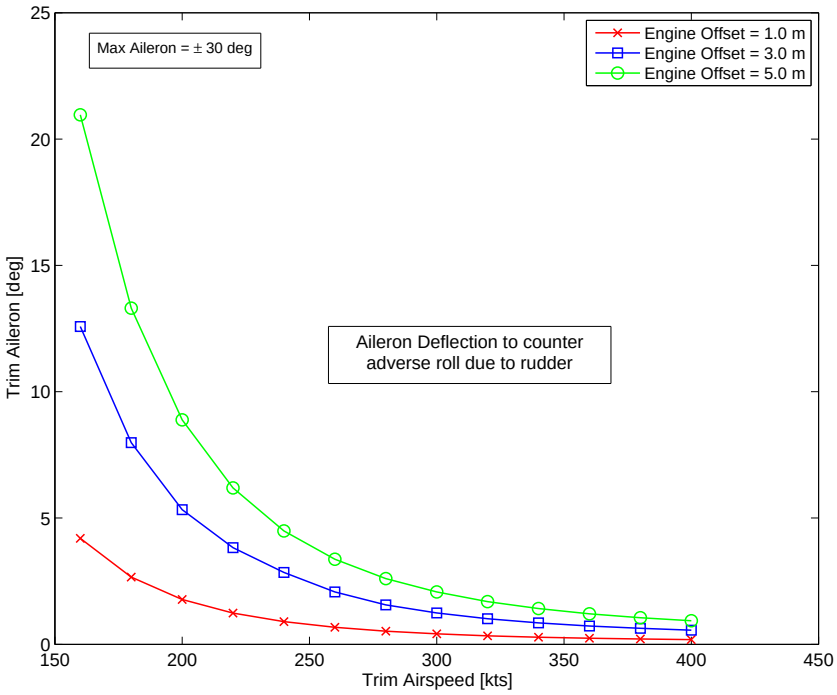

Figure 3.6: Trim aileron with starboard engine fail

amount of rudder deflection will increase and vice versa. This is shown in Figure 3.7. As per MILSTD 8785C [44] both Easterly and Westerly cross winds of 30 kts under an asymmetric thrust condition were simulated.

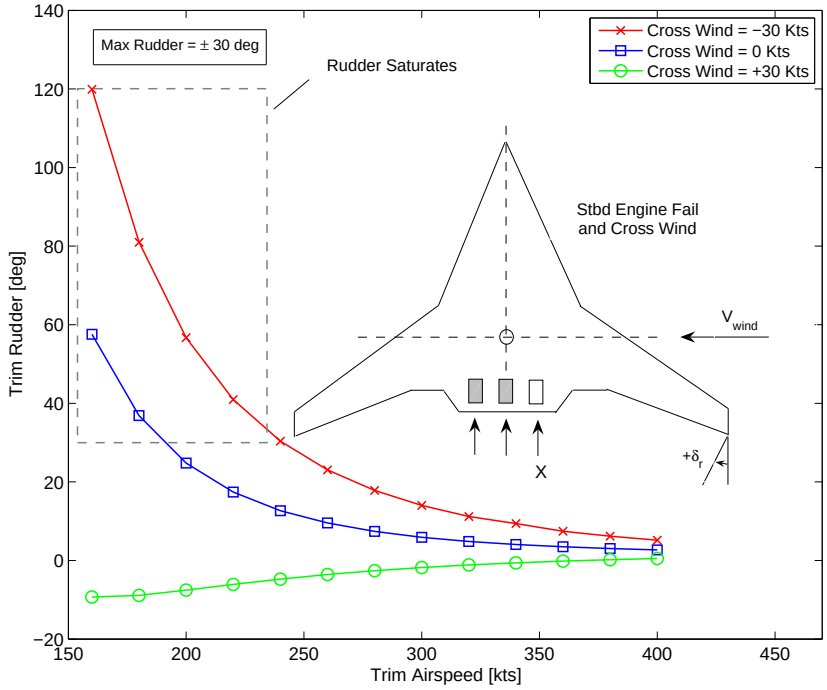

Figure 3.7: Trim rudder with starboard engine fail and crosswinds

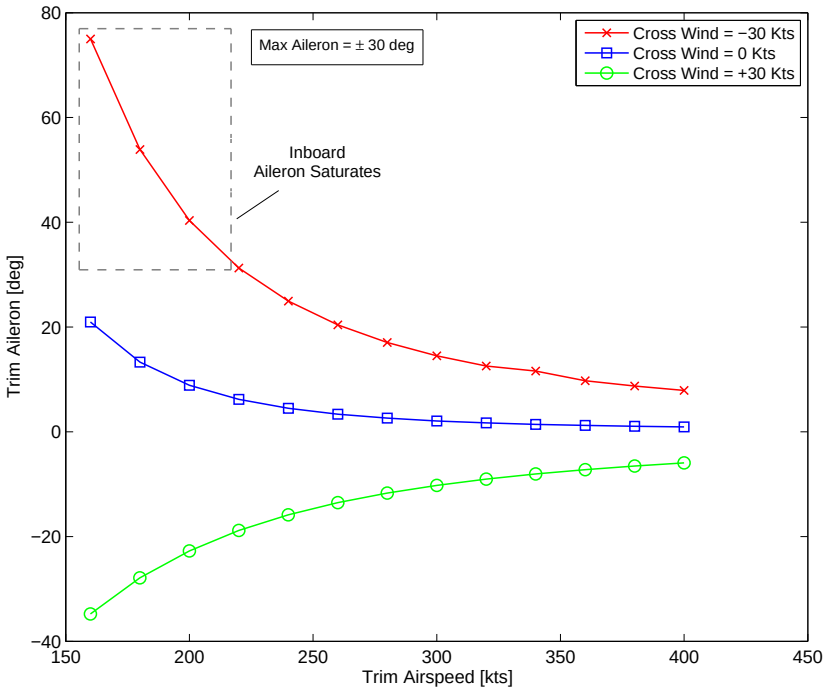

Figure 3.8: Trim aileron with starboard engine fail and crosswinds

Also shown in Figure 3.8 is the trim aileron deflection. In the presence of crosswinds the rolling moment due to sideslip, $C_{l\beta}$, also comes into play and may adversely effect the aileron deflection depending on wind direction.

To summarize, the presence of crosswinds and a starboard/port engine failure, puts severe demands on the winglet rudder. The winglet rudders as shown in Figure 3.9 are not powerful enough to maintain the desired aircraft direction. It seems that the rudder control authority has to be increased at least 3 to 4 times than the current design or an alternate source of yaw control such as drag flaps or lateral thrust vectoring may be used.

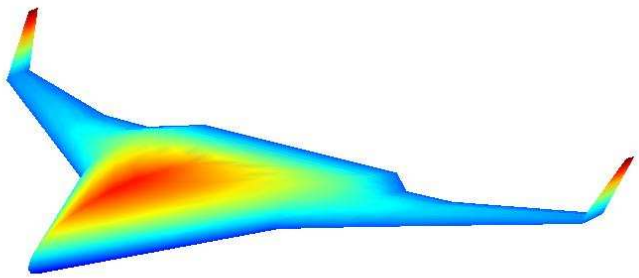

Figure 3.9: A CAD model of baseline BWB configuration with winglet rudders

3.2 Variation in Dynamic Modes

The purpose of this section is to estimate the effect of airspeed and static margin on the longitudinal and lateral-directional dynamics of the BWB aircraft. A derivation of linear dynamics for the BWB aircraft is considered in Appendix B. The relationship of CG position and static margin for the BWB is considered first.

Static Margin and CG Position for the Baseline BWB - Reference [43] gives an expression for the static margin, K_n, as the ratio of the slope of the pitching moment and lift coefficient with angle of attack.

$$K_n = -\frac{C_{m\alpha}}{C_{L\alpha}} \tag{3.4}$$

Whereas the lift curve slope, $C_{L\alpha}$, is positive within normal limits of angle of attack, the parameter, $C_{m\alpha}$, which is a strong function of CG position must be negative for positive static margins ($K_n > 0$).

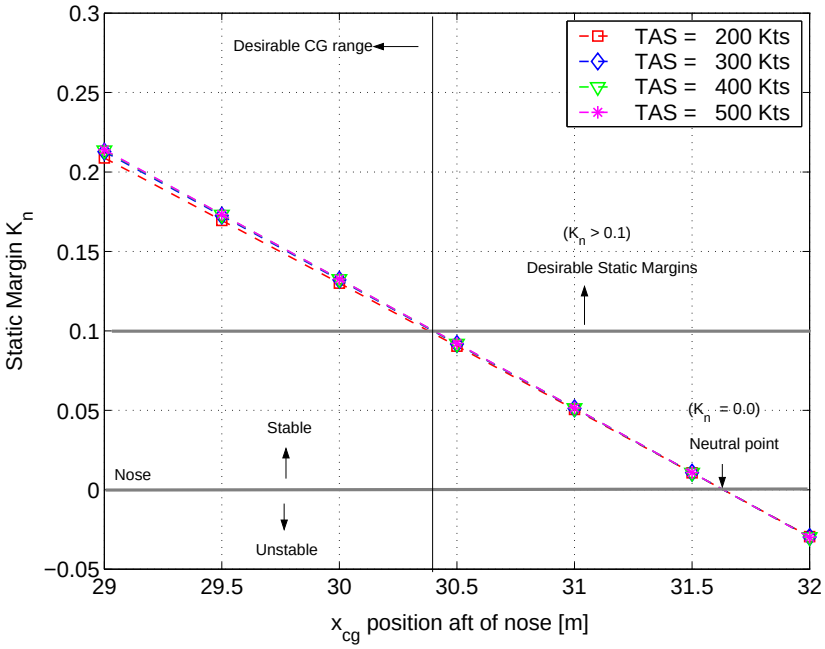

Figure 3.10: Variation in static margin,K_n with x_{cg} position

Figure 3.10 shows the variation in static margin with CG position for the baseline BWB. The static margin decreases as the CG moves aft and goes negative at $x_{cg} =$ 31.65 m, which is the neutral point. Due to the limitations of available aerodynamic data, the neutral point and also the static margin plot are shown to be relatively insensitive to variations in airspeed. In practice however, the neutral point does shift aft at higher Mach numbers.

3.2.1 Variation in Dynamic Modes - Longitudinal Axis

Figure 3.11 shows the pole locations for longitudinal axis for an x_{cg} variation of 29.0 to 32.0 m and up to a speed of 500 kts. The short period and the phugoid poles are marked. The phugoid poles being slow are clustered near the origin while the short period dynamics show significant variation. Following points can be observed.

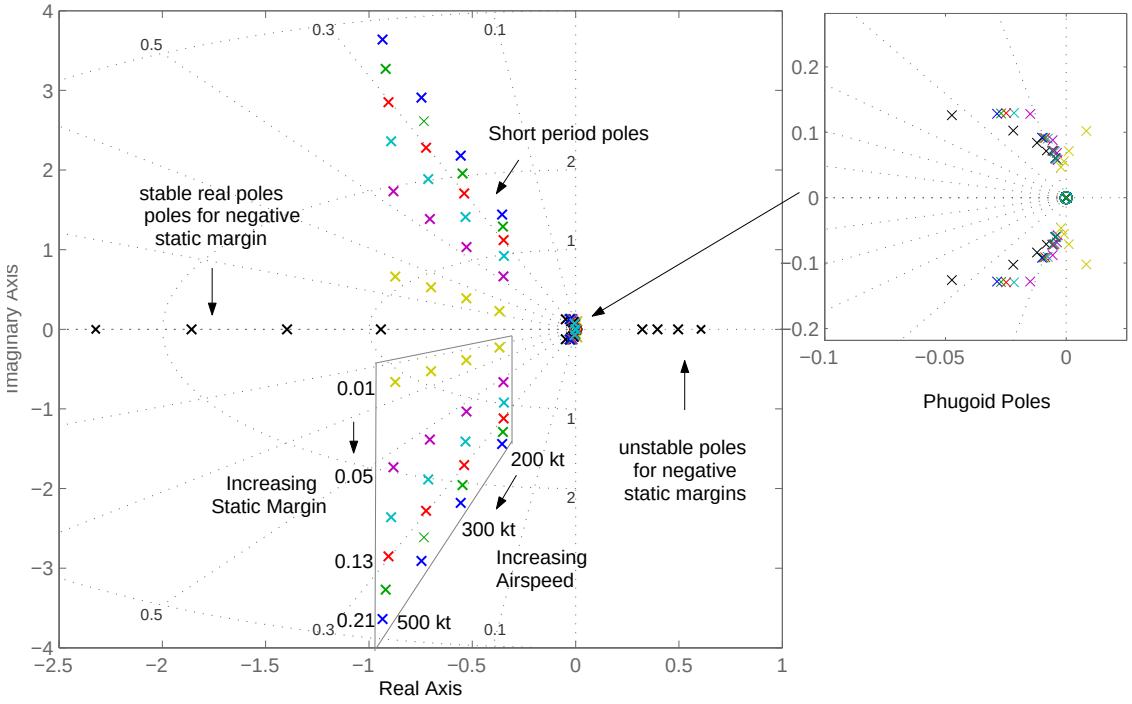

Figure 3.11: Variation in Longitudinal Modes with Static margin and Airspeed

- The short period frequency (ω_{sp}) increases with airspeed and forward CG positions. Thus at higher speeds and stable CG positions the short period dynamics will be fast which is desirable from handling qualities point of view.
- The short period damping (ζ_{sp}) decreases with increasing static margin and is almost insensitive to airspeed.
- Short period mode goes unstable at negative static margins.
- The phugoid poles also go unstable for negative static margins specially at lower airspeeds. At higher airspeeds the phugoid mode remains stable but poorly damped.

The effect of airspeed/CG position on natural frequency and damping for the short period and phugoid mode will now be considered.

Variation in Short Period Mode - Figures 3.12 and 3.13 show the variation in short period mode with static margin and airspeed. At a fixed airspeed, the short period natural frequency, ω_{sp}, shows an almost linear variation with static margin. The effect of increased airspeed is to increase the frequency of the short period mode and vice versa. The short period damping, ζ_{sp}, is unaffected by changes in airspeed but increases with decreasing static margin. Based on this variation in short period dynamics, a static margin ($K_n > 0.1$) is considerd desirable, however it is possible to operate at lower static margins with a well designed stability augmentation system.

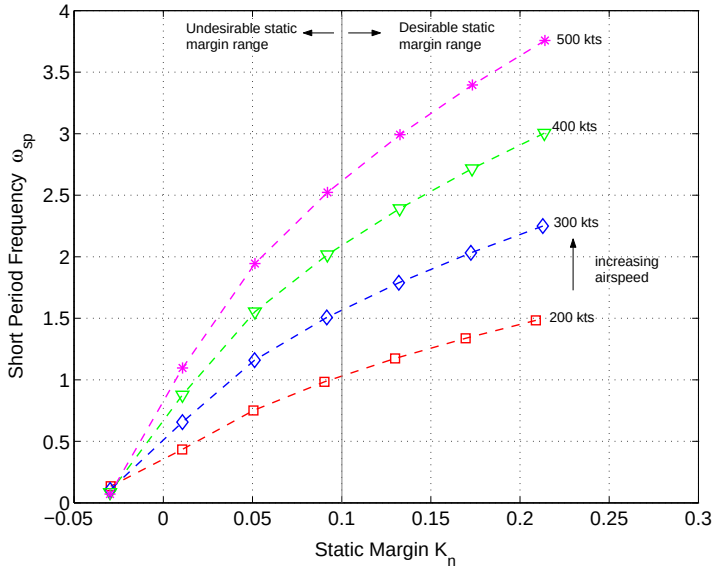

Figure 3.12: Short period frequency (ω_{sp}) variation with static margin and airspeed

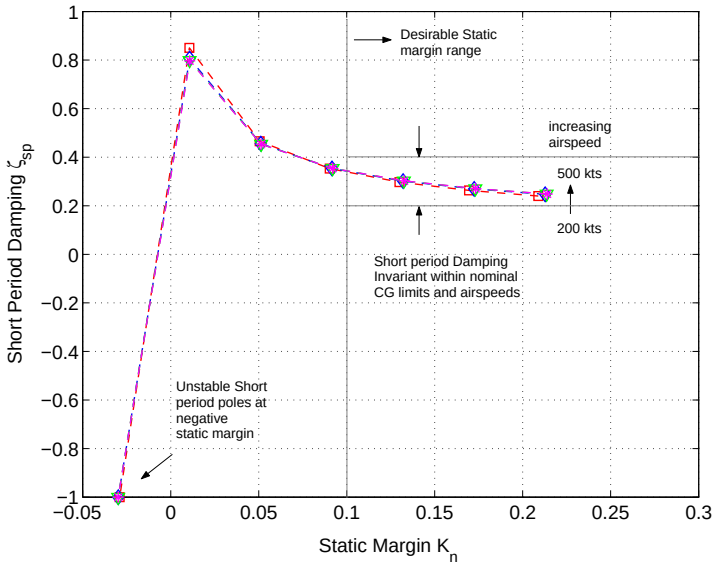

Figure 3.13: Short period damping (ζ_{sp}) variation with static margin and airspeed

Variation in Phugoid Mode - Figures 3.14 and 3.15 show the variation in phugoid mode with static margin and airspeed. The phugoid frequency, ω_{ph}, is not sensitive to variations in static margin, however it decreases with increase in airspeed. The phugoid damping, ζ_{ph}, is however relatively less sensitive to static margin but decreases with increase in airspeed. Thus at higher airspeeds, the phugoid will be less damped and slower. At airspeeds of less than 200 kts and low static margins, the phugoid mode goes unstable and the damping is negative.

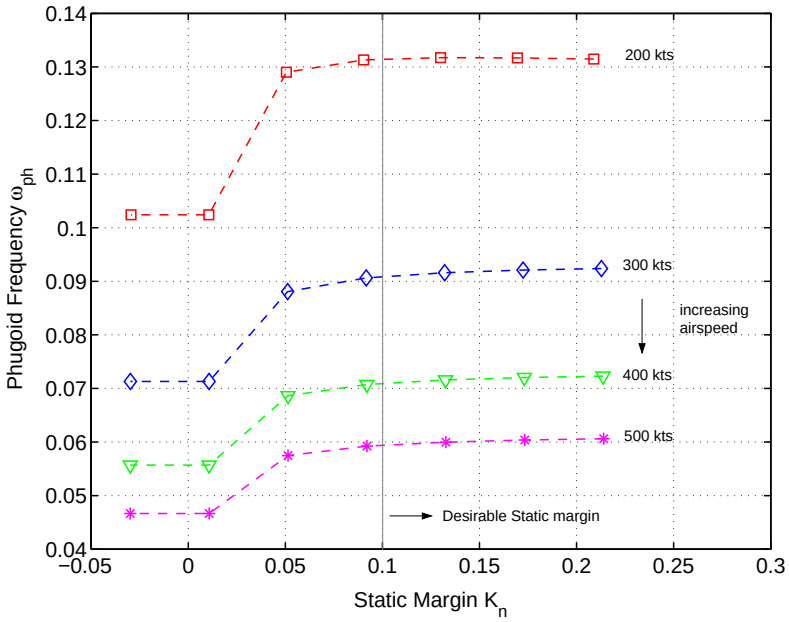

Figure 3.14: Phugoid frequency (ω_{ph}) variation with static margin and airspeed

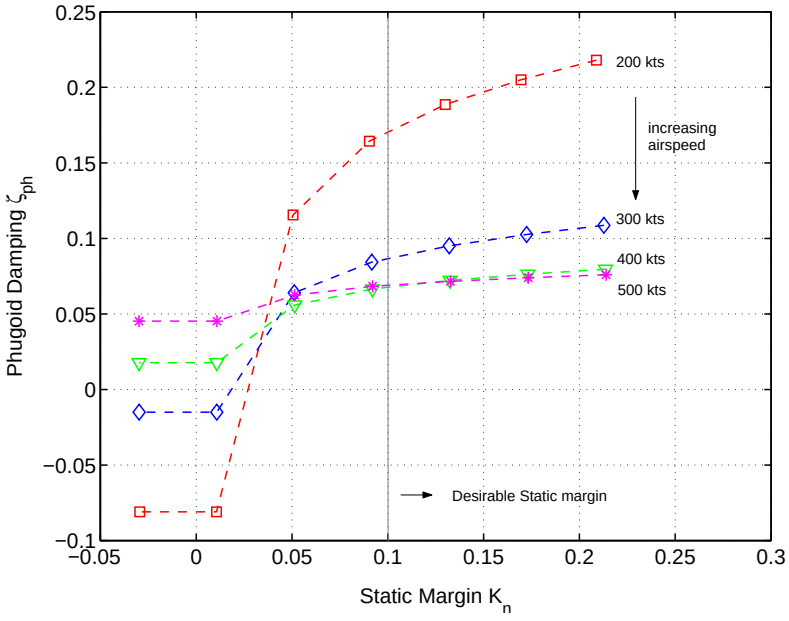

Figure 3.15: Phugoid damping (ζ_{ph}) variation with static margin and airspeed

3.2.2 Varition in Dyanmic Modes - Lateral Directional Axis

Figure 3.16 shows the open loop pole zero map for lateral dynamics for an x_{cg} variation of 29.0 to 32.0 m and upto a speed of 500 kts. The roll subsidence, spiral and dutch roll poles are marked. Following points may be observed.

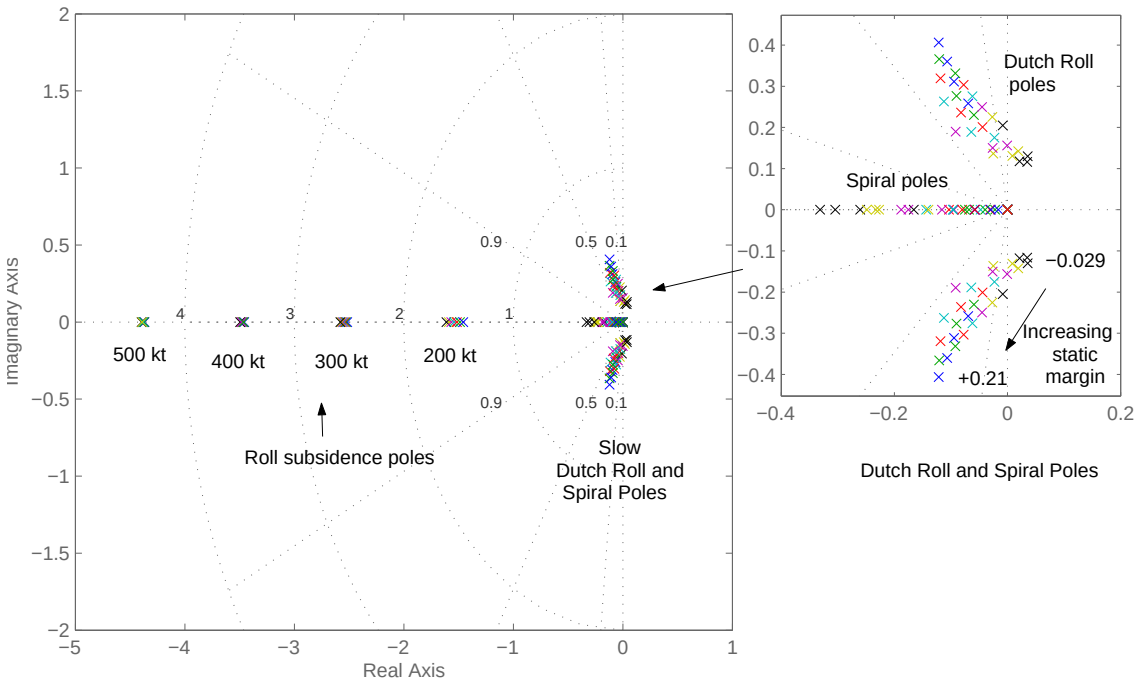

Figure 3.16: Variation in Lat-Dir Modes with Static margin and Airspeed

- The roll subsidence pole is fast and varies with airspeed. It determines the speed of response for the roll motion to aileron controls . As the airspeed is increased the dimensional derivative L_{δ_a} i-e roll moment due to aileron deflection increases. For a constant roll axis inertia (I_{xx}), the roll acceleration increases with airspeed and hence a faster roll subsidence mode. However the roll mode is relatively insensitive to variation in x_{cg} position.
- The spiral mode remains stable but gets faster at slower airspeeds. A fast and divergent spiral mode is undesirable from handling qualities perspective.
- The dutch roll mode remains slow for all airspeeds and gets unstable at a certain combination of low airspeeds and negative static margins.

The effect of airspeed/CG position on natural frequency or damping for each the roll subsidence, spiral and dutch roll mode is discussed next.

Variation in Roll and Spiral Modes - Figures 3.17 and 3.18 show the variation in roll and spiral modes with static margin and airspeed. The roll time constant, τ_r, is less sensitive to CG position, but gets slower as the airspeed is reduced. The roll mode is within the MIL-STD-8785C [44] Level 1 requirements up to a speed of 200 kts. The spiral mode time constant, τ_s, on the other hand shows strong influence of both CG position and airspeed. For static margins ($K_n > 0.1$), the spiral time constant is high, however it gets unfavourably faster at lower airspeeds.

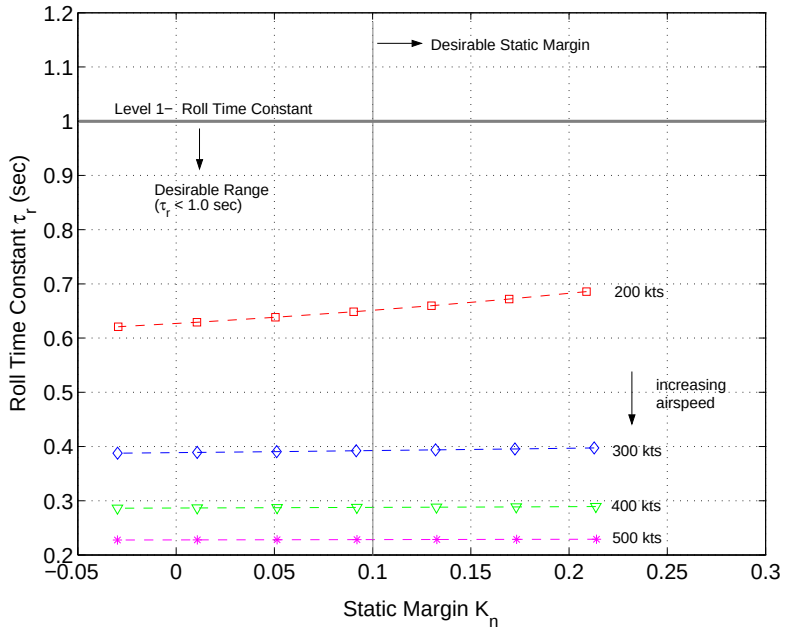

Figure 3.17: Roll mode time constant (τ_r) variation with static margin and airspeed

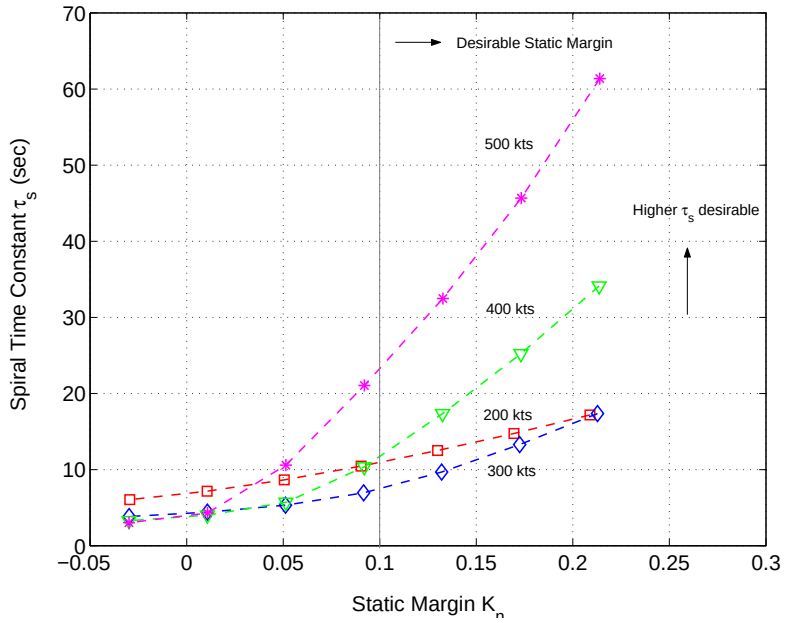

Figure 3.18: Spiral time constant (τ_s) variation with static margin and airspeed

Variation in Dutch Roll Mode - Figure 3.19 shows the variation in dutch roll frequency with static margin and airspeed. Although higher airspeeds and static margins tend to increase the dutch roll natural frequency, ω_{dr}, but it still falls short of acceptable limits. For all combinations of speeds and CG positions the dutch roll mode is slower than the Level 1 requirements. The dutch roll damping, ζ_{dr}, in Figure 3.20 remains within Level 1 limits when the static margin $K_n > 0.1$, however it deteriorates rapidly as the static margin is reduced any further.

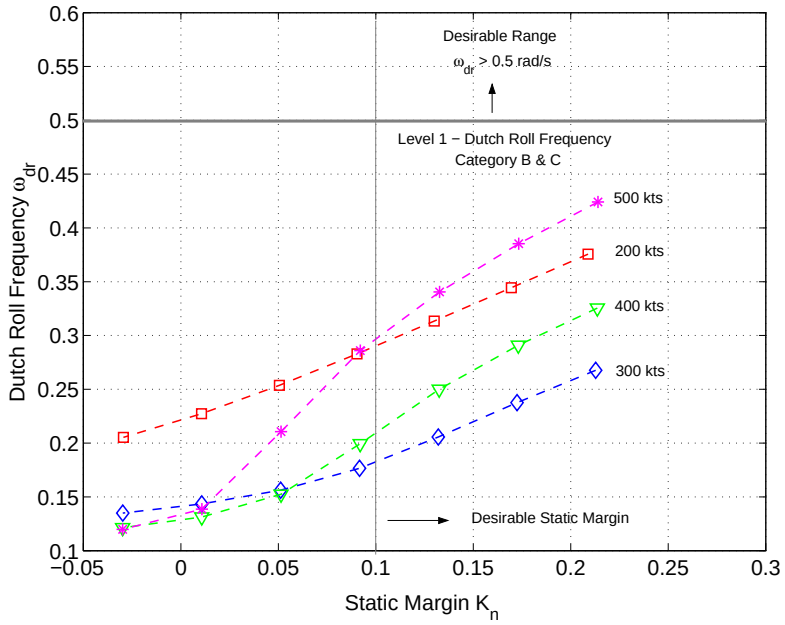

Figure 3.19: Dutch roll frequency (ω_{dr}) variation with static margin and airspeed

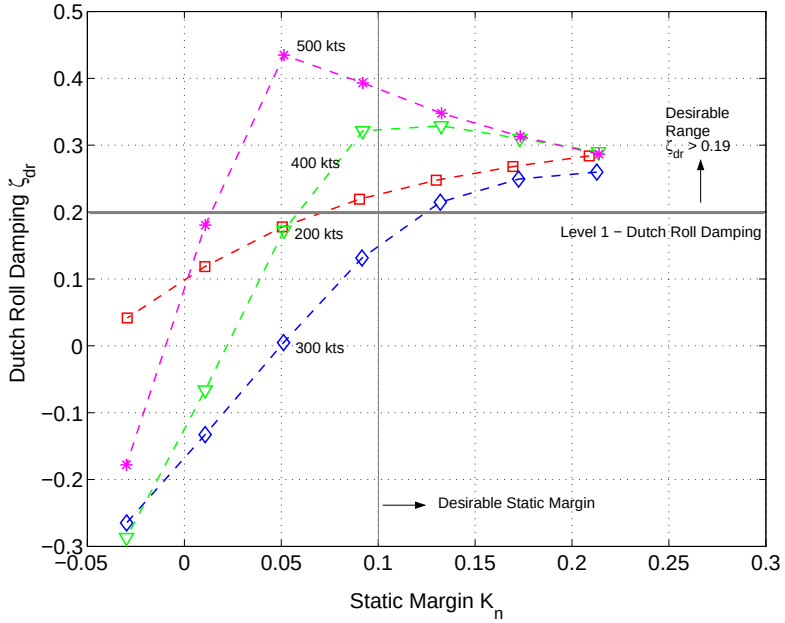

Figure 3.20: Dutch roll damping (ζ_{dr}) variation with static margin and airspeed

3.3 BWB - Handling Qualities Assessment

In this section, the handling qualities of the baseline BWB configuration both with and without a stability augmentation system (SAS) are considered, the purpose being to identify controls related handling qualities limitations if any.

3.3.1 Longitudinal Handling Qualities (BWB)

Many criteria exist to assess the longitudinal handling qualities of aircraft. The following two will be used for the baseline BWB to see if they give consistent results.

- The Control Anticipation Parameter (CAP) criteria [45].
- The Neil Smith criteria [46].

3.3.1.1 CAP Assessment - Open Loop

CAP may be defined in terms of short period natural frequency (ω_{sp}) and the normal acceleration derivative w.r.t angle of attack (N_α) or as the ratio of instantaneous pitch acceleration to steady state normal acceleration [43],

$$\text{CAP} = \frac{\dot{q}(0)}{N_{z(\infty)}} = \frac{\omega_{sp}^2}{N_\alpha} \tag{3.5}$$

where

$$\omega_{sp} = \sqrt{M_q Z_w - M_w(Z_q + U_e)} \tag{3.6}$$

$$N_\alpha = -Z_w U_e / g \tag{3.7}$$

where U_e is the steady state speed in x-body axis. CAP may be evaluated graphically or through the evaluation of the parameters (ω_{sp}, N_α). Step responses were obtained for $[N_z, \dot{q}, q, \theta, \gamma]$ using reduced order models for short period dynamics and are shown in Figure 3.21. The corresponding CAP parameters are,

Parameter	Value	Units
Control Anticipation Parameter (CAP)	0.216	-
Short period frequency (ω_{sp})	1.139	rad/s
G's per alpha (N_α)	5.986	g/rad

Table 3.1: CAP parameters at (V = 200 kts, Alt = 5000 ft, $K_n = 0.1$)

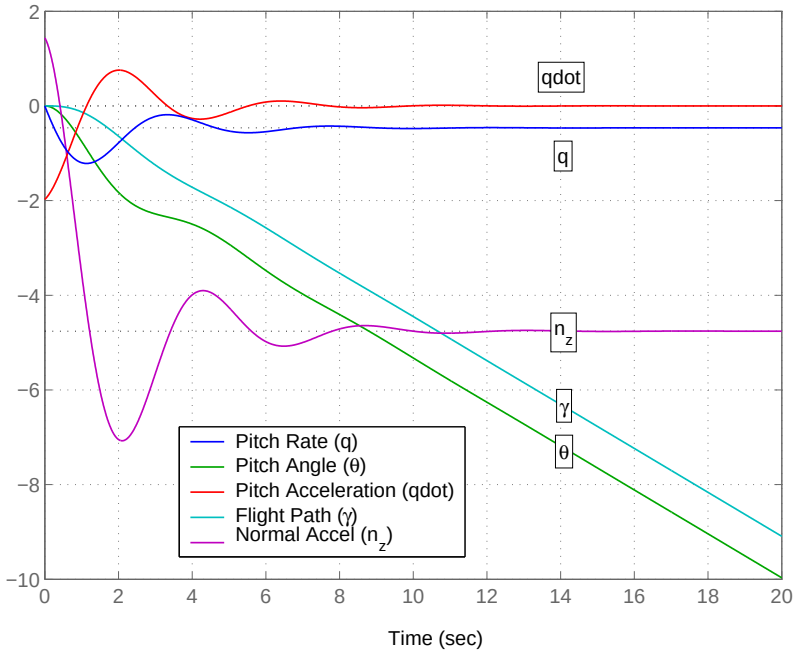

Figure 3.21: CAP Assessment - Longitudinal response to step elevator

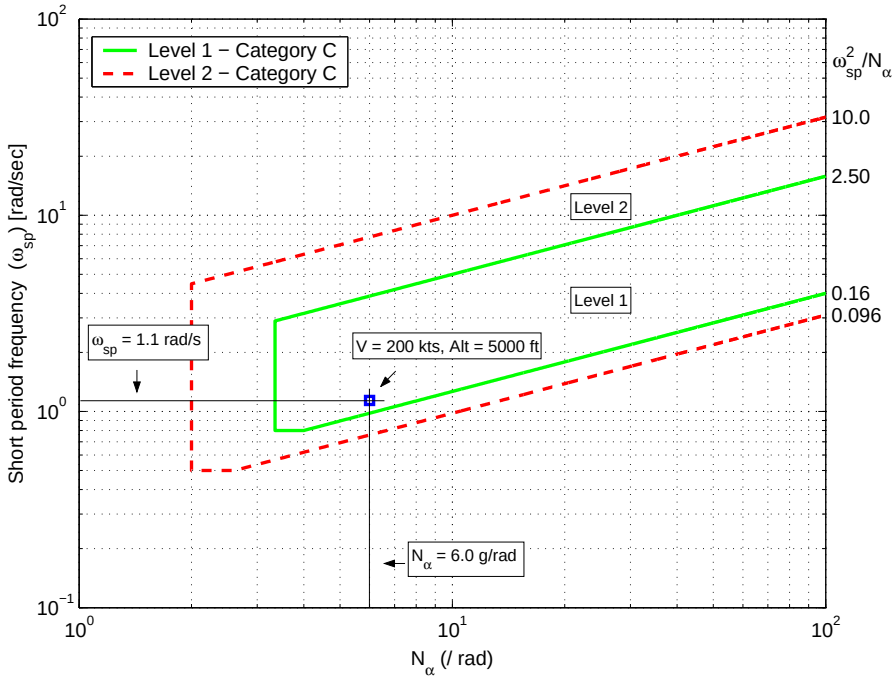

Figure 3.22: CAP Assessment - Short period characteristics

Figure 3.22 shows the location of the CAP parameter on a log-log plot. Level 1 and Level 2 regions are shown for a category C (Take-off/Landing) flight phase. For the airspeed and altitude combination under consideration, the BWB aircraft shows marginal Level 1 flying qualities. The short period frequency ($\omega_{sp} = 1.1$ rad/s) is still however at the lower limit. A higher short period frequency ($\omega_{sp} = 2.0$ rad/s) would have been desirable.

3.3.1.2 Neil Smith Assessment - Open Loop

The Neil Smith criteria [46], includes the pilot in evaluation of the pitch response. It assumes that to accomplish a given task, a pilot acts as a controller thus introducing pilot gain and phase in the forward path. The amount of gain and phase (lead/lag) needed by the pilot to achieve a certain close loop bandwidth (ω_{BW}) determines the handling qualities of the aircraft. The criteria requires that the close loop phase lag at the bandwidth frequency be -90° and the close loop low frequency droop be -3 dB. For this analysis the pilot's neuromuscular delay is assumed fixed at 0.3 seconds.

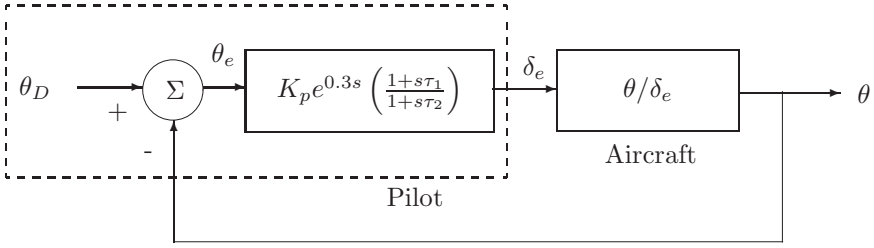

Figure 3.23: Pilot and aircraft close loop system model

Using the linearization procedure as outlined in Appendix B, a reduced order θ/δ_e transfer function is obtained at V=200 kts, Alt = 5000 ft and $K_n = 0.1$,

$$\frac{\theta}{\delta_e} = \frac{1.7676(s + 0.5813)}{s(s^2 + 0.8747s + 1.296)} \tag{3.8}$$

It now remains to find the pilot transfer function which gives a close loop phase lag of -90.0° at bandwidth frequency of $\omega_{BW} = 3.0$ rad/s and in addition a close loop low frequency droop of -3.0 dB. The pilot's transfer function is represented by

$$G_p(s) = K_p \exp^{-\tau s}\left(\frac{1 + s\tau_1}{1 + s\tau_2}\right) = K_p D_p(s) P_p(s) \tag{3.9}$$

where K_p is the pilot gain, $D_p(s)$ is the pilot time delay of τ seconds and $P_p(s)$ is the pilot's phase compensation. The resulting Neil Smith parameters are

Neil Smith Parameters	Value	Units
Pilot gain K_p	0.565	-
Pilot phase [+ve for lead]	+74.05	deg
Phase at ω_{BW} of 3.05 rad/s	-90.11	deg
Low frequency Droop	-3.103	dB
Close loop resonance	5.045	dB

Table 3.2: Neil Smith parameters at (V = 200 kts, Alt = 5000 ft, $K_n = 0.1$)

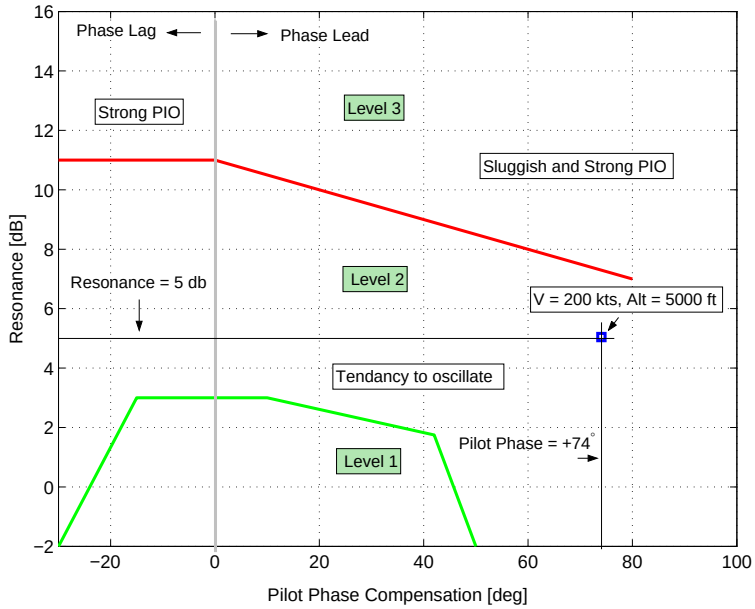

Figure 3.24: Neil Smith Assessment at [V = 200 kts, Alt = 5000 ft]

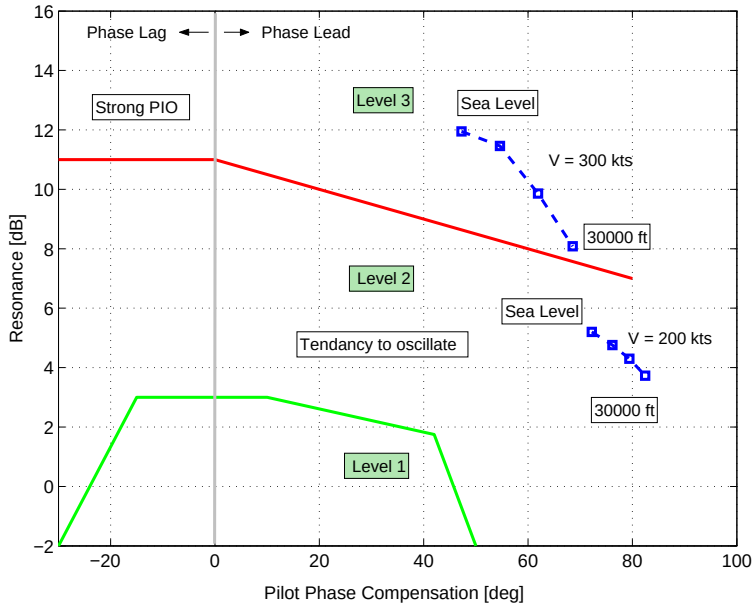

Figure 3.25: Neil Smith Assessment at [V = 200, 300 kts, Alt = 0 to 30000 ft]

Figure 3.24 shows Level 2 flying qualities for the current flight condition of V = 200 kts and Alt = 5000 ft. Figure 3.25 shows the variation in Neil Smith parameters with changes in altitude and airspeed. At constant speed and with increase in altitude, the aircraft tends to get more sluggish, hence requiring greater pilot compensation. However the resonance peak drops indicating greater damping in pitch oscillations. At a lower airspeed of V=200 kts, the system is sluggish with Level 2 flying qualities. For a higher speed of V=300 kts, the system is less sluggish but more oscillatory with a strong PIO tendency. Hence Level 3 flying qualities.

3.3.1.3 Longitudinal Handling Qualities - SAS Engaged

A longitudinal stability augmentation system (SAS) with alpha and pitch rate feedback was designed as per MILSPEC 8785C requirements on short period dynamics. The design of the SAS is detailed in Appendix C. Figure 3.26 shows the CAP assessment both with and without the SAS engaged. With an increased short period frequency by use of alpha feedback, the system is now well inside the CAP Level 1 handling qualities requirements.

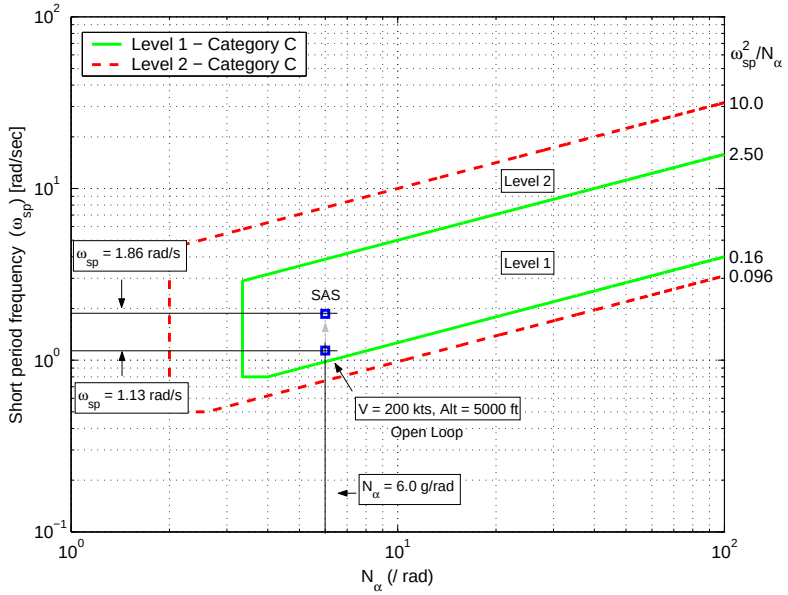

Figure 3.26: CAP Assessment with SAS

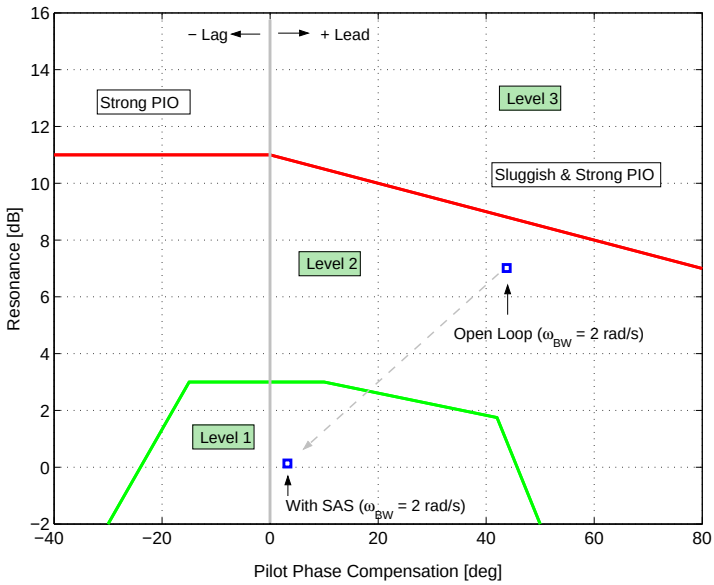

Figure 3.27: Neil Smith Assessment with SAS

Figure 3.27 shows the Neil Smith assessment with SAS engaged. The improvement

in short period frequency from 1.13 to 1.86 rad/s (due to SAS) causes a reduction in the pilot compensation to achieve a close loop bandwidth of $\omega_{BW} = 2.0$ rad/s and the improved damping reduces the close resonance peak.

3.3.2 Lateral-Directional Handling Qualities (BWB)

MILSPEC 8785C [44] conveniently expresses the lateral-directional handling qualities requirements in terms of lateral-directional pole positions. In addition, reference [45] specifies the manoeuvre requirements. Table 3.3 summarizes the Level 1 lateral-directional requirements for a Class III (Heavy Transport) aircraft.

Parameter	Cat. A	Cat. B	Cat. C	Units
Roll mode time constant (τ_R)	1.40	1.40	1.40	sec
Dutch roll frequency (ω_{dr})	0.50	0.50	0.50	rad/s
Dutch roll damping (ζ_{dr})	0.19	0.08	0.08	-
Dutch roll parameter ($\zeta_{dr}\omega_{dr}$)	0.35	0.15	0.1	-
Spiral (time to double bank angle) (t_2)	12	20	12	sec
Time to reach 30° bank angle	1.5	2.0	3.0	sec
Adverse sideslip β_{adv}	$6k$	$10k$	$10k$	-
Proverse sideslip β_{pro}	$2k$	$3k$	$3k$	-
Roll rate (p) limit at first minimum	60	25	60	% of p_{max}
Change in bank Angle	-	-	-	as control

Table 3.3: MILSTD 8785C - Class III - Level 1 - Lateral-directional requirements

p_{max}	Maximum roll rate for a given control deflection
β_{adv}	Adverse sideslip (right roll command causes right(+) sideslip)
β_{pro}	Proverse sideslip (right roll command causes left(-) sideslip)
k	Time taken to reach 30° bank/time specified (above) to reach 30° bank

3.3.2.1 Handling Qualities Assessment - Open Loop

The roll mode time constant, the dutch roll mode and the spiral modes have already been considered earlier in Section 3.2. It was shown that the dutch roll frequency, ω_{dr}, is very low due to poor directional stiffness, C_{n_β}, and does not meet the Level 1 requirements stated above. The dutch roll damping, ζ_{dr}, however meets these requirements as long as the static margin $K_n > 0.1$. This section will now focus on the lateral-directional manoeuvre requirements.

Roll rate (p) and Roll Angle (ϕ) Manoeuvre - The Level 1 requirement on roll rate is that the second roll rate peak should be of the same sign and not less than a

certain percentage of the first peak. Figure 3.28 shows the roll rate response due to step aileron at various airspeeds. Since there is a very strong roll/yaw coupling, the second roll rate peak is of opposite sign from the initial or intended direction. The open loop response is clearly not Level 1. Figure 3.29 shows the corresponding roll angle, which also settles in the opposite direction. Due to this dynamic behavior, the adverse/proverse yaw measurements were made after engagement of a lateral-directional SAS system. The SAS system is of conventional design with washed out yaw rate feedback for dutch roll damping, sideslip feedback for increasing the dutch roll frequency, roll rate feedback to speed up the roll mode and an aileron to rudder inter-connect (ARI) for turn co-ordination.

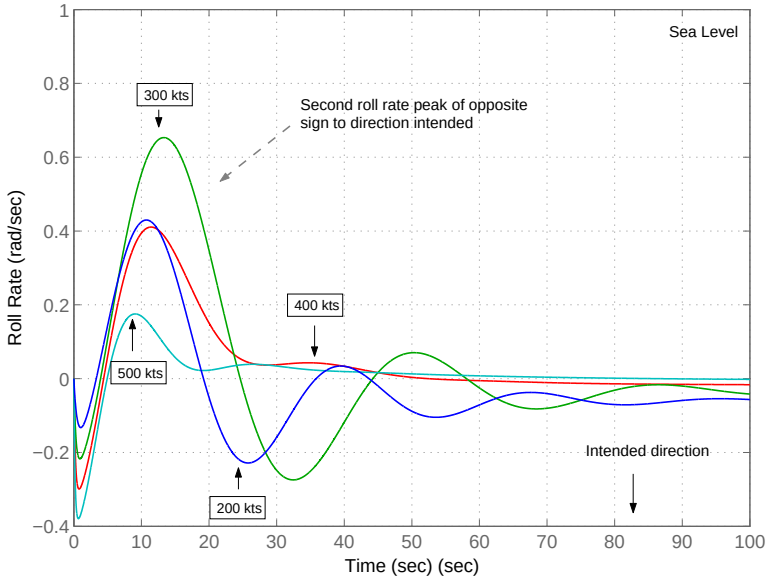

Figure 3.28: Roll rate (p/δ_a) step response - Open loop

3.3.2.2 Handling Qualities Assessment - SAS Engaged

The design of the lateral-directional employing washed-out yaw rate, roll rate feedback, sideslip suppression and an aileron to rudder interconnect is discussed in Appendix C. The lateral-directional handling qualities are now considered with the stability augmentation system operating, these include, (i) roll rate manoeuvre, (ii) time to reach 30° bank angle and (iii) Adverse yaw.

Roll Rate Manoeuvre - SAS Engaged - Figure 3.30 shows the close loop roll rate to aileron (p/δ_a) step response. The first peak and the first minimum after it are highlighted. With the SAS, the BWB aircraft meets the Level 1 requirements

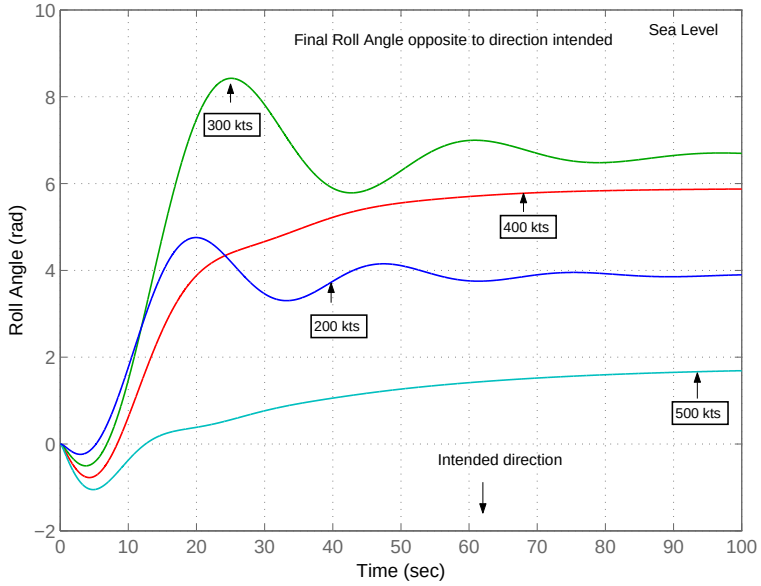

Figure 3.29: Roll angle (ϕ/δ_a) step response - Open loop

above speeds of 200 kts. The results for the roll rate manoeuvre are summarized in Table 3.4. Note that k is the ratio of first minimum to first peak in roll rate.

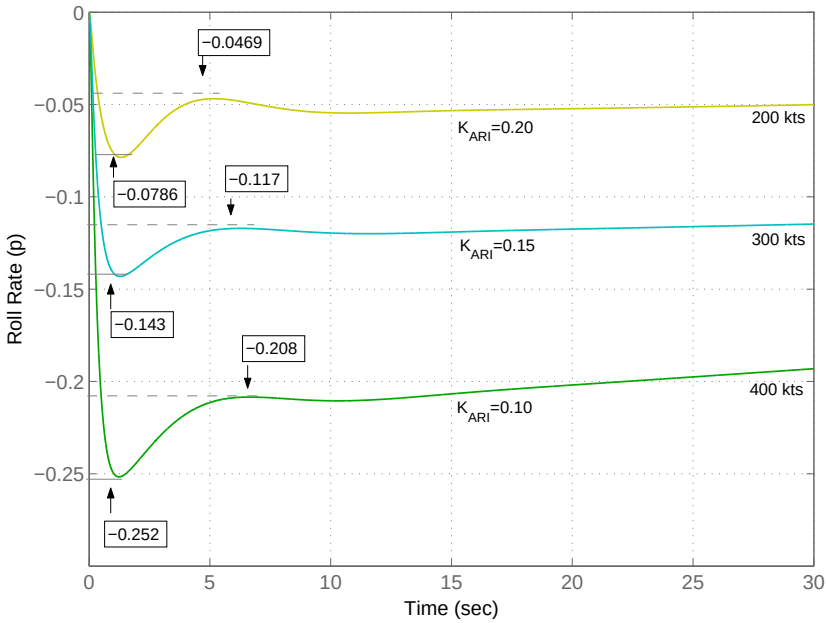

Figure 3.30: Comparison - roll rate/angle response with SAS

Roll Angle Manoeuvre (Time for 30° Bank) - SAS Engaged - This requirement varies according to the phases of flight (Category A/B/C). Figure 3.31 shows that the system does not meet the minimum Level 1 requirements of reaching the re-

Airspeed kts	First peak	First min.	Ratio (k)	Level 1 req.	Level 2 req.
400	-0.252	-0.2080	0.825	0.60	0.25
300	-0.143	-0.1170	0.818	0.60	0.25
200	-0.0786	-0.0469	0.596	0.60	0.25

Table 3.4: Roll rate at first minimum as percentage of roll rate at first peak (k)

quired bank angle of 30° for both category B and C flight phases. Table 3.5 presents the data numerically against the requirements. Clearly it can be inferred that roll angle performance deteriorates with airspeed. In fact at 200 kts, the time to reach 30° bank with full control deflection is 18.4 seconds. Comparing this with a category C flight phase requirement of 3.0 seconds, it seems that either the control power is too less or the roll inertia is too high. The roll subsidence mode frequency cannot be improved further as it would saturate the controls. The roll control power needs to be enhanced especially at low airspeeds in order to meet Level 1 requirements.

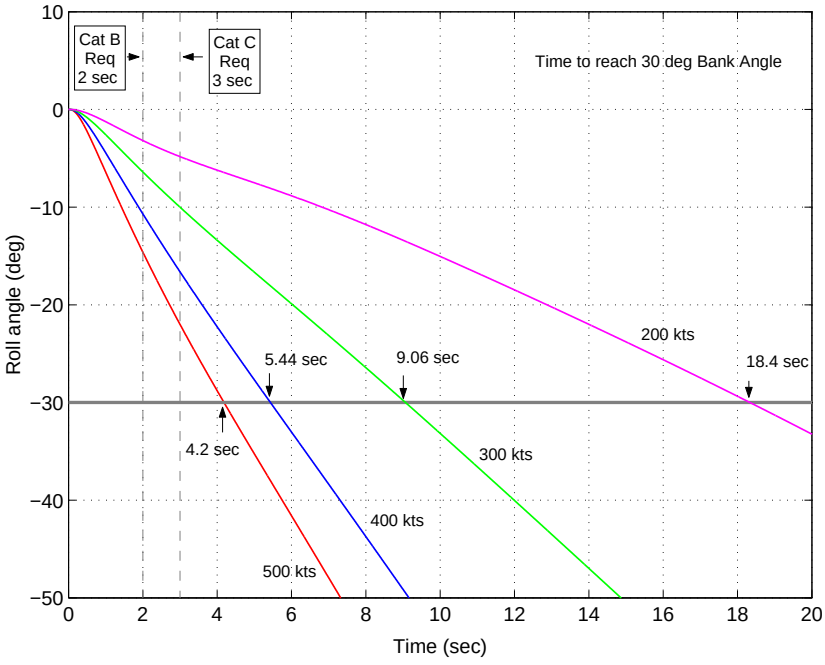

Figure 3.31: Roll angle response - SAS engaged

Airspeed (kts)	Cat. A	Cat. B	Cat. C	Time for 30° bank	Units
500	1.50	2.00	3.00	4.20	sec
400	1.50	2.00	3.00	5.44	sec
300	1.50	2.00	3.00	9.06	sec
200	1.50	2.00	3.00	18.4	sec

Table 3.5: Time to reach 30° bank angle - SAS engaged

Adverse Yaw - SAS Engaged - McLaughlin [47] suggests that the level of aileron cross coupling can be estimated by the parameter $(\omega_\phi/\omega_{dr})^2$. This is the ratio of the squares of natural frequencies appearing in the roll angle to aileron (ϕ/δ_a) transfer function. If $(\omega_\phi/\omega_{dr})^2 = 1$, the yaw or sideslip disturbance is minimal. If $(\omega_\phi/\omega_{dr})^2 > 1$, the induced yaw is in the proverse direction and if $(\omega_\phi/\omega_{dr})^2 < 1$, it is in the adverse direction. In the following analysis this parameter is considered both with and without the aileron to rudder inter-connect (ARI).

Figure 3.32 shows the sideslip generated for a -25.0° step aileron input. Flight speeds were from 400 to 200 kts at an altitude of 10,000 ft. The figure shows that positive slip is generated in all three cases hence the sideslip/yaw angle are adverse. Table 3.6 presents a summary. The parameter k as defined in Section 3.3.2 is also listed. Only category C flight phase requirements are considered. Table 3.6 shows that sideslip is reduced significantly with the aileron to rudder interconnect. The system still has residual slip which can be of annoyance to the pilot especially at lower airspeeds.

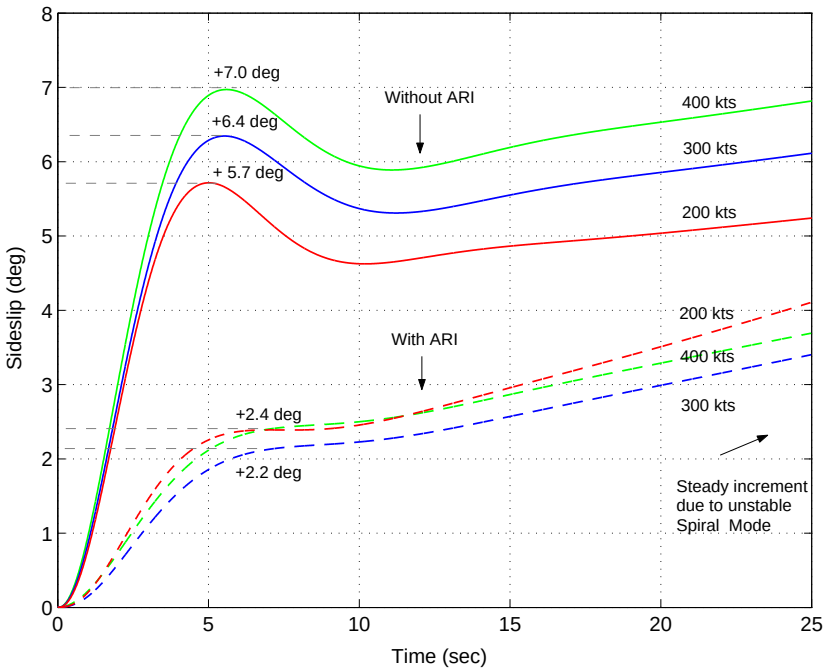

Figure 3.32: Adverse yaw due to aileron deflection - SAS engaged

Airspd kts	k	Cat C $(10k)$	β	β_{ARI}	$(\omega_\phi/\omega_{dr})^2$	$(\omega_\phi/\omega_{dr})^2_{ARI}$
400	5.44/3 = 1.81	18.1	+7.0	+2.4	0.40	0.81
300	9.06/3 = 3.02	30.2	+6.4	+2.2	0.31	0.75
200	18.4/3 = 6.13	60.1	+5.7	+2.4	0.07	0.47

Table 3.6: Adverse/proverse yaw measurements

3.4 Chapter Summary

A summary of control problems for the baseline BWB is presented in Table 3.7.

No	Parameter	Remarks
1.0	Pitch Control	At lower airspeeds (V < 200 kts) and nominal static margins ($K_n > 0.15$) the baseline BWB aircraft shows limited pitch control power. As shown later this proves to be a serious limitation during the take-off rotation phase. However for lower static margins ($K_n < 0.1$) the actuator limits are not exceeded.
2.0	Yaw Control	A trim analysis was carried out for asymmetric flight conditions with starboard/port engine fail and crosswinds. For asymmetric thrust, the small rudders on the winglets saturate very quickly at landing and take-off speeds. If cross winds are added, it may further exacerbate the situation depending on wind direction. It seems that rudder power needs to be enhanced 3 to 4 times to make this a practical design.
3.0	Roll Control	The roll control power was assessed by the time required to reach 30° bank angle. By virtue of the planform shape, the roll axis inertia is large and with only inboard ailerons operating, the BWB aircraft fails to meet Level 1 requirements at airspeeds below 300 kts. Control allocation may be used at low airspeeds by assigning outboard flaps for additional roll control, but this will be done at the expense of a further reduction in pitch control authority.
4.0	Longitudinal Dynamics	To assess the longitudinal dynamics, both linear airframe and handling qualities analysis were conducted. Below static margins of $K_n < 0.1$, the short period mode gets slower and eventually becomes unstable at $K_n = 0.0$. A stability augmentation system (SAS) with alpha and pitch rate feedback was necessary to bring the system to Level 1 requirements. Without the SAS the baseline BWB barely meets CAP or Neil Smith handling qualities requirements but with SAS engaged both criteria are satisfied. The longitudinal dynamics were found to be satisfactory with a gain scheduled SAS.
5.0	Lateral Dynamics	The lateral-directional dynamics were very poor. The dutch roll mode is too slow at all combinations of airspeeds and CG positions. Sideslip feedback was necessary to speed up the dutch roll and high gain values had to be used, straining the already weak rudder. An aileron to rudder inter-connect (ARI) was required to counteract adverse sideslip. However even after the full SAS engaged there is considerable residual sideslip. A weak rudder and poor directional stiffness are considered to be the main causes. The system will be very difficult to fly without a well designed lateral-directional SAS.

Table 3.7: Summary of BWB stability and control problems

Chapter 4

Transient Engine Model and Effects of Controls Integration

In the previous chapter, the BWB aircraft was analyzed from a stability and controls point of view and certain problem areas were identified. In this context, various control methodologies were highlighted in Chapter 1, where the propulsion system could be used to augment the control characteristics of the BWB aircraft. These included, (i) thrust vectoring to supplement the aerodynamic flight controls for the longitudinal and lateral-directional axis and (ii) the use of blown flaps to improve flap effectiveness and hence provide better control authority.

Thrust vectoring on its own does not directly affect the engine operating point or the steady state running line. The loss in axial thrust due to vectored thrust can be reclaimed by adjustment of throttle position. However in a blown flap arrangement, if the bleed mass flow is taken from an engine compressor stage, then this disrupts the mass flow for engine components downstream. The engine operating point shifts and may adversely affect critical engine parameters such as the turbine entry temperature (TET), the specific fuel consumption (SFC) and thrust. It is therefore considered necessary to a have a real-time transient model of the propulsion system that could be integrated with a BWB aircraft with a blown flap controls arrangement. In this context this chapter will cover,

- The development of a transient engine model.
- Model validation.
- Engine performance under variable bleed conditions.
- Engine performance under thrust vectoring.

Various techniques have been used in the literature for propulsion system modeling. The usual approach is to represent different engine subsystems using performance maps and then interlink each individual component to get an overall engine model. These can further be categorized as,

- **The Inter-component Volume Method**

  This method assumes that during a transient operation, flow mismatch occurs. The amount of mismatch is used to calculate pressure derivatives at various stages (volumes) inside the engine. The pressure derivatives can then be integrated to get pressures using numerical integration techniques. Fawke [48] used this approach to model single and two spool turbojet engines and verified his results to a reasonable accuracy with experimental data. Behbahani [49] at the Air force Research Laboratory (Wright Patterson Air force Base) has reported to develop a two spool turbofan engine model using the component volume approach in Matlab/Simulink.

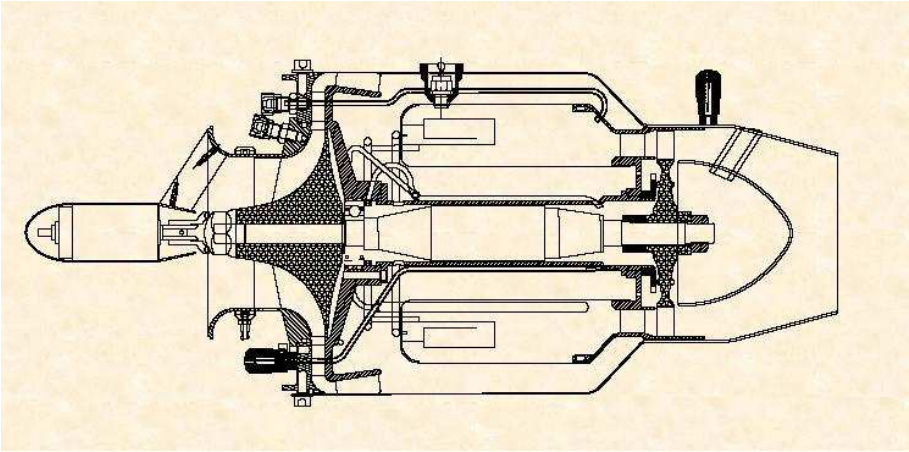

Figure 4.1: The AMT Olympus single spool turbojet [50]

During the initial part of this research, the inter-component volume method was used to simulate a small single spool turbojet called the AMT Olympus [50]. This engine is shown in Figure 4.1 and can generate a thrust of up to 180 N. Experimental bleed data for this engine was also available which was used to validate the simulation results. Since later on for the BWB, a three spool turbofan engine was to be used, therefore the details of the single spool turbojet are not presented here, however this engine model forms the basis of the more complicated three spool turbofan, discussed next. Results for the single spool turbojet were published [51] and are provided in Appendix F for future reference.

- **The Iterative Method**

  This method uses an iterative approach such as the Newton Raphson method [52] to satisfy or minimize a set of error variables given certain engine parameters as inputs. The method starts with an initial guess of the engine state vector and computes error variables that need to satisfy steady state constraints. A pass through the engine calculations is made and the errors or mismatch across engine components are calculated. The error values are used to calculate a new and improved guess for the state vector. The process is repeated till the error variables are less than a specified tolerance.

  Sellers [12] used the iterative approach to model the transient performance of various engine configurations. An engine simulation program by the name of DYNGEN was written by Sellers and later updated it by DYGABCD. The DYGABCD was also capable of producing A,B,C,D matrices (linear model) at a given engine operating point. Lately, Parker [53] at the NASA's Glenn Research centre has developed a turbofan engine simulation in Matlab/Simulink. The program is called MAPSS (Modular Aero Propulsion Simulation Software) and is based on an iterative procedure.

  The DYNGEN program had transient capability and could simulate a three spool turbofan with inter-stage bleeds. It was accurate and could easily handle design point calculations. It was used extensively for the initial assessment of the three spool turbofan. Its only draw back was that it used an iterative approach, a three spool turbofan would require nine state variables and as many iterations to reach a converged solution. Thus it was not suitable for real-time implementation. On the other hand, the non-iterative inter-component volume approach when expanded to a three spool turbofan started giving increasing errors across high pressure engine stages. To solve this problem a hybrid approach was adopted which combined the two methods thus providing both speed and accuracy. This approach was applied to the three spool turbofan and shall form the subject for the rest of this chapter.

4.1 A Hybrid 3 Spool Turbofan Engine Model

This section presents a transient three spool turbofan engine simulation model that was developed as an integral part of this research work. It uses a combination of inter-component volume and iterative techniques, or the so called hybrid approach. The engine model runs in real time and has been implemented in MATLAB/Simulink environment. The main advantage of the hybrid approach is that it preserves the accuracy of the iterative method while maintaining the simplicity of the inter-component volume method. The inter-component volume method is used to calculate the mass flow accumulation inside each volume and the iterative approach is used to solve the thermodynamic algebraic equations associated with each engine component. The rate of change of mass flow in the volume is used to calculate pressure derivatives which are integrated to get pressures. With a knowledge of instantaneous spool speeds in addition to these pressures, the compressor/turbine mass flows and efficiencies are calculated using static component maps. This allows the engine state vector to be updated at each pass through the engine calculations.

This technique was applied on the Rolls Royce Trent 500 three spool turbofan engine and the results were compared with an iterative method such as the DYNGEN [12].

4.1.1 Engine Stations and State Vector

A simplified schematic for a three spool turbofan is shown in Figure 4.2. Various engine stations have been designated by following aerospace standard AS755D [54].

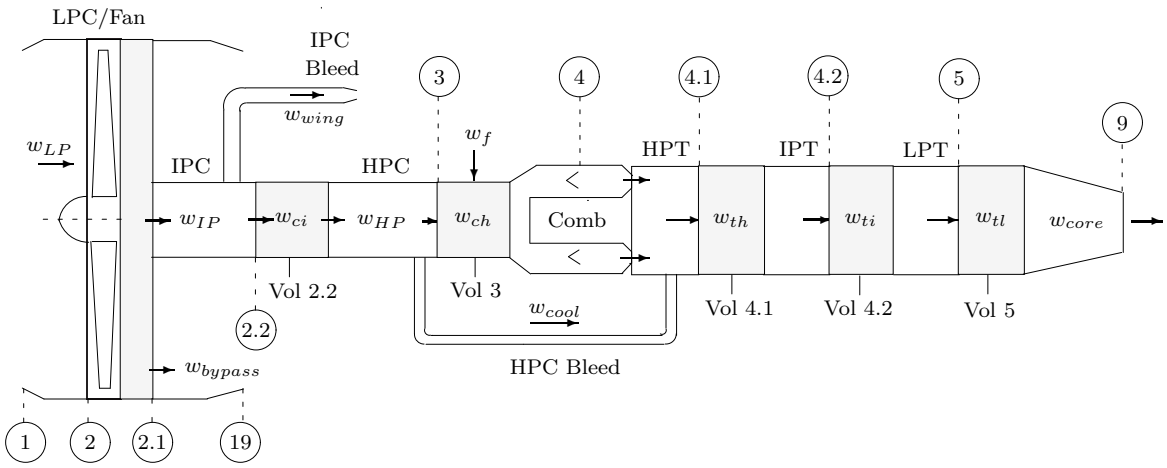

Figure 4.2: Three-spool turbofan schematic

Station Description

1	Inlet	- Entry
2	Inlet	- Exit
2.1	LPC	- Low pressure compressor outlet
2.2	IPC	- Intermediate pressure compressor outlet
3	HPC	- High pressure compressor outlet
4	CMB	- Combustor outlet
4.1	HPT	- High pressure turbine outlet
4.2	IPT	- Intermediate pressure turbine outlet
5	LPT	- Low pressure turbine outlet
9	Nozzle	- Main outlet
19	Nozzle	- Bypass outlet

With reference to Figure 4.2, the mass flow into the system is from the low pressure compressor, w_{LP}, and the main burner fuel flow input, w_f. The mass flow exits from the three exhaust nozzles, these are the core exhaust nozzle mass flow, w_{core}, the bypass nozzle mass flow, w_{bypass}, and the bleed mass flow from the intermediate compressor to the wing duct, w_{wing}. To simulate the turbofan, the following choice of state vector, X, and control vector, u, was made,

$$X = [P_{2.1}, P_{2.2}, P_3, P_{4.1}, P_{4.2}, P_5, N_L, N_I, N_H]$$
$$u = [w_f]$$

where P_i are the total pressures at the i_{th} station, N_L, N_I, N_H are the physical shaft speeds of the low pressure, the intermediate pressure and the high pressure rotors respectively and w_f is the main burner fuel flow rate.

4.1.2 Calculation of Pressure Derivatives - $(\dot{P}_i)$

The three-spool engine was simulated by calculation of the state derivatives, $\dot{X}$. The estimation of these state derivatives for pressures and spool speeds will therefore be considered. When the engine is running in a steady state condition, the net mass flow into the system equals the net mass flow out of the system. However as the engine accelerates or decelerates a transient state occurs and there will be accumulation or depletion of mass at various stages/volumes inside the engine. From the gas law, the rate of change of mass is proportional to rate of change of pressure and temperature,

$$\dot{P} = \frac{R}{V}(T\dot{m} + m\dot{T}) \tag{4.1}$$

The above equation has two derivatives, the terms $\dot{m}T$ and $m\dot{T}$. Bates and Fawke [48] have shown that the temperature derivative can be neglected in comparison to the mass derivative term. Thus to calculate the pressure derivatives, the mass flow errors inside the control volumes are required. The pressure derivatives are based on engine component maps as outlined in Appendix E and have been obtained as follows,

4.1.2.1 Mass Flow Error at LPC/Fan exit - ($\dot{m}_{2.1}$)

With reference to Figure 4.4, an inter-component volume, $V_{2.1}$, is placed at the fan exit and the entry of the intermediate compressor and the bypass duct. The mass flow, w_{cl}, entering into this volume is from the low pressure (LP) compressor which is a function of LPC corrected shaft speed, ${N_{L_C}}^* = N_L/\sqrt{T_2/T_{std}}$, and fan pressure ratio, $P_{2.1}/P_2$. With the assumption of zero bleed from the LPC stage we have,

$$w_{LP} = w_{cl} = f(\frac{P_{2.1}}{P_2}, {N_{L_C}}^*)_{MAP} \tag{4.2}$$

where w_{LP} is obtained using an LP compressor map given in Appendix E, with LPC pressure ratio, $P_{2.1}/P_2$, and corrected LPC shaft speed, ${N_{L_C}}^*$, as inputs.

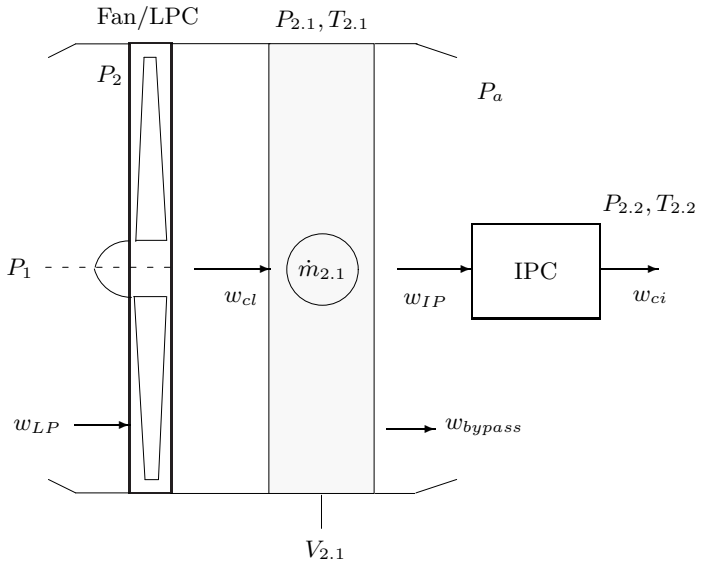

Figure 4.3: Inter-component volume, $V_{2.1}$, between Fan and IPC/bypass nozzle

The mass flow exiting from the control volume, $V_{2.1}$, goes into the intermediate pressure (IP) compressor and the bypass nozzle. The mass flow ingested by the intermediate compressor, w_{IP}, is a function of the intermediate compressor pressure ratio, $P_{2.2}/P_{2.1}$, and the IPC corrected shaft speed, ${N_{I_C}}^* = N_I/\sqrt{T_{2.1}/T_{std}}$. A

certain percentage of IP compressor mass flow, ϕ_{IP}, may be drawn for flow control or turbine cooling purposes and the reduced mass flow at IP compressor exit is w_{ci}. The mass flow ingested by the IP compressor in terms of percentage bleed and IPC exit mass flow is given as,

$$w_{IP} = \frac{w_{ci}}{1 - \phi_{IP}} = f(\frac{P_{2.2}}{P_{2.1}}, {N_{I_C}}^*)_{MAP} \tag{4.3}$$

The bypass nozzle mass flow is a function of the bypass nozzle pressure ratio, $P_{2.1}/P_a$, and the bypass nozzle area, A_{19}, besides some other gas parameters,

$$w_{bypass} = \frac{A_{19}P_{2.1}}{R}\left(\frac{P_{2.1}}{P_a}\right)^{-1/\gamma}\sqrt{\frac{2g_c c_p}{T_{2.1}}\left(1 - \left(\frac{P_{2.1}}{P_a}\right)^{-R/c_p}\right)} \tag{4.4}$$

The mass flow error inside the control volume is therefore,

$$\dot{m}_{2.1} = w_{cl} - w_{IP} - w_{bypass} \tag{4.5}$$

In this analysis, it is assumed that there is no bleed off-take from the LP compressor. Further in Equation 4.4, the pressure ratio $(P_{2.1}/P_a)$ is limited to the choking pressure ratio if the bypass nozzle operates choked.

4.1.2.2 Mass Flow Error at IPC Exit - $(\dot{m}_{2.2})$

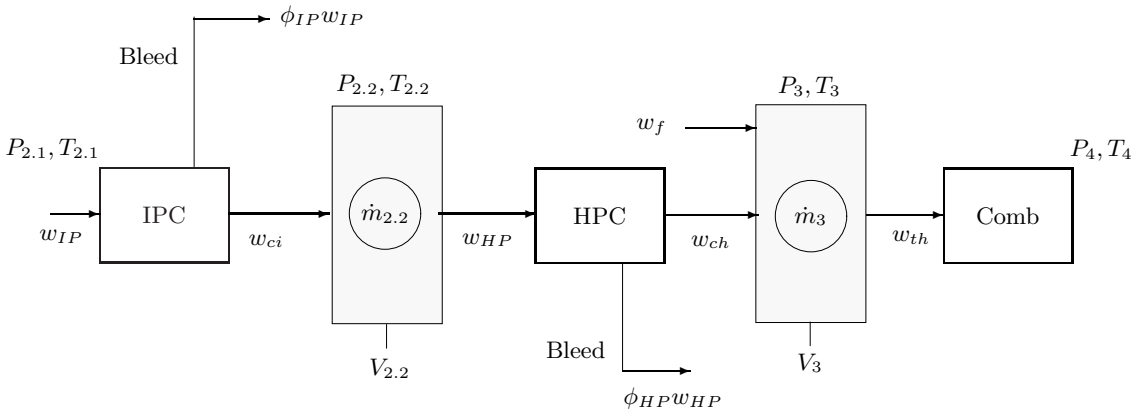

Figure 4.4: Inter-component volumes, $V_{2.2}$ and V_3

With reference to Figure 4.4, an inter-component volume, $V_{2.2}$, is placed between IP compressor exit and the high pressure (HP) compressor entry. The mass flow entering this volume is the reduced mass flow after bleed extraction from the IPC

stage and is referenced as w_{ci}. The mass flow, w_{HP}, exiting from this volume is that ingested by the HP compressor. A certain percentage, ϕ_{HP}, of this HP mass flow is bled for turbine cooling purposes and the net mass flow exiting from the HP stage is w_{ch}. Thus

$$w_{HP} = \frac{w_{ch}}{1 - \phi_{HP}} = f(\frac{P_3}{P_{2.2}}, {N_{H_C}}^*)_{MAP} \tag{4.6}$$

Where the HPC mass flow, w_{HP}, itself is a function of pressure ratio, $P_3/P_{2.2}$, and the HP compressor corrected shaft speed, ${N_{H_C}}^* = N_H/\sqrt{T_{2.2}/T_{std}}$. The mass flow being accumulated inside the control volume is therefore

$$\dot{m}_{2.2} = w_{ci} - w_{HP} \tag{4.7}$$

4.1.2.3 Mass Flow Error at HPC Exit - ($\dot{m}_3$)

The inter-component volume, V_3, was placed at the HP compressor exit and combustor entry. The mass flows entering this volume are the main burner fuel flow, w_f, and the mass flow exiting from the HP compressor stage, w_{ch}. The mass flow, w_{th}, exiting from this volume is that extracted by the HP turbine. Thus the mass flow accumulated inside this volume is

$$\dot{m}_3 = w_{ch} + w_f - w_{th} \tag{4.8}$$

The HP turbine mass flow, w_{th} is a function of HP turbine pressure ratio, $P_4/P_{4.1}$, and HP turbine corrected shaft speed, ${N_{H_T}}^* = N_H/\sqrt{T_4}$ and is obtained from a turbine map. Thus

$$w_{th} = f(\frac{P_4}{P_{4.1}}, {N_{H_T}}^*)_{MAP} \tag{4.9}$$

Since a fixed percentage of total pressure loss is assumed inside the combustor, therefore the pressure derivative at HP turbine entry, $\dot{P}_4$, is proportional to combustor entry, $\dot{P}_3$, and no inter-component volume is required to calculate P_4.

4.1.2.4 Mass Flow Errors at HPT, IPT and LPT Exit - ($\dot{m}_{4.1},\ \dot{m}_{4.2},\ \dot{m}_5$)

In Figure 4.5, the inter-component volume, $V_{4.1}$, accepts mass flows from the HP turbine and also the cooling mass flow, $\phi_{HP}w_{HP}$, from the HP compressor stage. The mass flow, w_{ti}, exiting from volume $V_{4.1}$ is that ingested by the IP turbine stage and is a function of IP turbine pressure ratio $P_{4.1}/P_{4.2}$ and the IPT corrected shaft speed, ${N_{I_T}}^* = N_I/\sqrt{T_{4.1}}$.

$$w_{ti} = f(\frac{P_{4.1}}{P_{4.2}}, {N_{I_T}}^*)_{MAP} \tag{4.10}$$

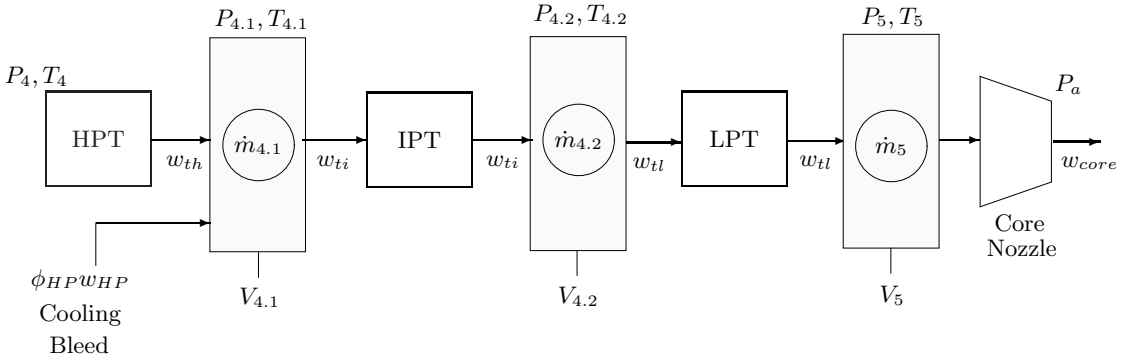

Figure 4.5: Inter-component turbine volumes $[V_{4.1}, V_{4.1}, V_5]$

From Figure 4.5, the accumulated mass at the HP, IP and LP turbine exits are

$$\dot{m}_{4.1} = w_{th} + \phi_{HP} w_{HP} - w_{ti} \tag{4.11}$$

$$\dot{m}_{4.2} = w_{ti} - w_{tl} \tag{4.12}$$

$$\dot{m}_5 = w_{tl} - w_{core} \tag{4.13}$$

The mass flow, w_{tl}, into the LP turbine is a function of LP turbine pressure ratio, $P_{4.1}/P_{4.2}$, and LP turbine corrected shaft speed, ${N_{L_T}}^* = N_L/\sqrt{T_{4.2}}$, and is obtained from the LP turbine map,

$$w_{tl} = f(\frac{P_{4.2}}{P_5}, {N_{L_T}}^*)_{MAP} \tag{4.14}$$

and the mass flow through the convergent core nozzle is

$$w_{core} = \frac{A_9 P_5}{R} \left(\frac{P_5}{P_a}\right)^{-1/\gamma} \sqrt{\frac{2 g_c c_p}{T_5} \left(1 - \left(\frac{P_5}{P_a}\right)^{-R/c_p}\right)} \tag{4.15}$$

where the pressure ratio (P_5/P_a) is limited to the choking pressure ratio. This completes the calculation of the mass flow errors inside the control volumes. The pressure derivatives can now conveniently be obtained using Equation 4.1. For the inter-component volumes associated with the compressors we have,

$$\dot{P_{2.1}} = \frac{RT_{2.1}}{V_{2.1}} \left(w_{cl} - w_{IP} - w_{bypass}\right) \tag{4.16}$$

$$\dot{P_{2.2}} = \frac{RT_{2.2}}{V_{2.2}} \left(w_{ci} - w_{HP}\right) \tag{4.17}$$

$$\dot{P_3} = \frac{RT_3}{V_3} \left(w_{ch} + w_f - w_{th}\right) \tag{4.18}$$

and similarly for the volumes associated with the turbines,

$$\dot{P_{4.1}} = \frac{RT_{4.1}}{V_{4.1}} \left(w_{th} + \phi_{HP} w_{HP} - w_{ti} \right) \tag{4.19}$$

$$\dot{P_{4.2}} = \frac{RT_{4.2}}{V_{4.2}} \left(w_{ti} - w_{tl} \right) \tag{4.20}$$

$$\dot{P_5} = \frac{RT_5}{V_5} \left(w_{tl} - w_{core} \right) \tag{4.21}$$

Now if the initial pressures are known, then from the knowledge of the initial state vector, X_0, the subsequent time history of P_i can be obtained by convenient numerical integration methods.

4.1.3 Calculation of Speed Derivatives - ($\dot{N}$)

The remaining derivatives of the state vector i.e. the rotational acceleration derivatives $\dot{N_L},\ \dot{N_I},\ \dot{N_H}$ can be calculated by estimating the difference in torque generated by the turbine and that required by the compressor,

$$\dot{N} = \frac{dN}{dt} = \frac{\left(\eta_m \tau_{turb} - \tau_{comp} \right)}{I_s} \tag{4.22}$$

The turbine torque, τ_{turb}, or the compressor torque, τ_{comp}, can be expressed in terms of turbine and compressor work and physical spool speeds. In addition, if there is a fraction of bleed ($\phi = w_b/w_c$) taken from a non-dimensional axial location (x/l) along the compressor, then the torque required by the compressor is

$$\tau_{comp} = \frac{60}{2\pi N} w_c c_p \Delta T_c \left((1 - \phi) + \phi \frac{x}{l} \right) \tag{4.23}$$

From reference [55], ΔT_c is,

$$\Delta T_c = \frac{1}{\eta_c} T_1 \left(\left(\frac{P_2}{P_1} \right)^{\frac{\gamma - 1}{\gamma}} - 1 \right) \tag{4.24}$$

Here subscripts 1 and 2, represent inlet and outlet conditions respectively, and do not relate to the three spool turbofan station designation. The problem with Equation (4.24) is that it is implicit, and the values of parameters like γ and c_p are in turn dependent upon exit conditions, $[T_2, P_2]$. Fixed values of these parameters had to be assumed. This was later found to introduce significant errors in high pressure stages. It was therefore decided to solve these equations iteratively using specific enthalpy, h, rather than total temperature. In terms of enthalpy change, the torques

for the compressor stages are,

$$\tau_{LPC} = \frac{60}{2\pi N_L} w_{LP}(h_{2.1} - h_2) \tag{4.25}$$

$$\tau_{IPC} = \frac{60}{2\pi N_I} w_{IP}(h_{2.2} - h_{2.1}) \left((1 - \phi_{IP}) + \phi_{IP}\frac{x}{l}\right) \tag{4.26}$$

$$\tau_{HPC} = \frac{60}{2\pi N_H} w_{HP}(h_3 - h_{2.2}) \left((1 - \phi_{HP}) + \phi_{HP}\frac{x}{l}\right) \tag{4.27}$$

and for the turbines,

$$\tau_{HPT} = \frac{60}{2\pi N_L} w_{th}(h_4 - h_{4.1}) \tag{4.28}$$

$$\tau_{IPT} = \frac{60}{2\pi N_I} w_{ti}(h_{4.1} - h_{4.2}) \tag{4.29}$$

$$\tau_{LPT} = \frac{60}{2\pi N_H} w_{tl}(h_{4.2} - h_5) \tag{4.30}$$

No bleed is taken from the LP compressor stage and it is assumed that the cooling mass flow into the HP or the IP turbine stages does not contribute toward turbine work. For the calculation of speed derivatives, it now remains to calculate the enthalpy change across each of the compressor or the turbine stages. This requires an iterative solution of algebraic thermodynamic equations and is discussed next.

4.1.4 Iterative Solution of Compressor Thermodynamics

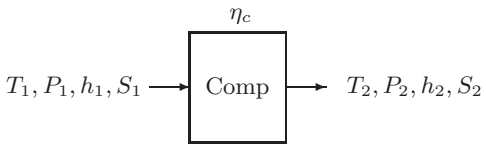

Figure 4.6: Thermodynamic conditions for the compressor

Figure 4.6, shows a compressor stage with input conditions $[T_1, P_1, h_1, S_1]$ and exit conditions $[T_2, P_2, h_2, S_2]$. The inter-component volume approach provides the pressure derivative and hence pressure at the compressor exit stage, therefore the exit pressure P_2 is known. From a knowledge of current spool speed, N, and the compressor pressure ratio, compressor efficiency, η_c, and mass flow, w_c, can be calculated from component maps. It is now desired to calculate exit temperature, T_2, specific enthalpy, h_2, and entropy, S_2, for the compressor stage. Figure 4.7 shows the iterative process that was used to solve the thermodynamic algebraic loop. The steps involved are detailed below and the computer code is listed in Appendix E.

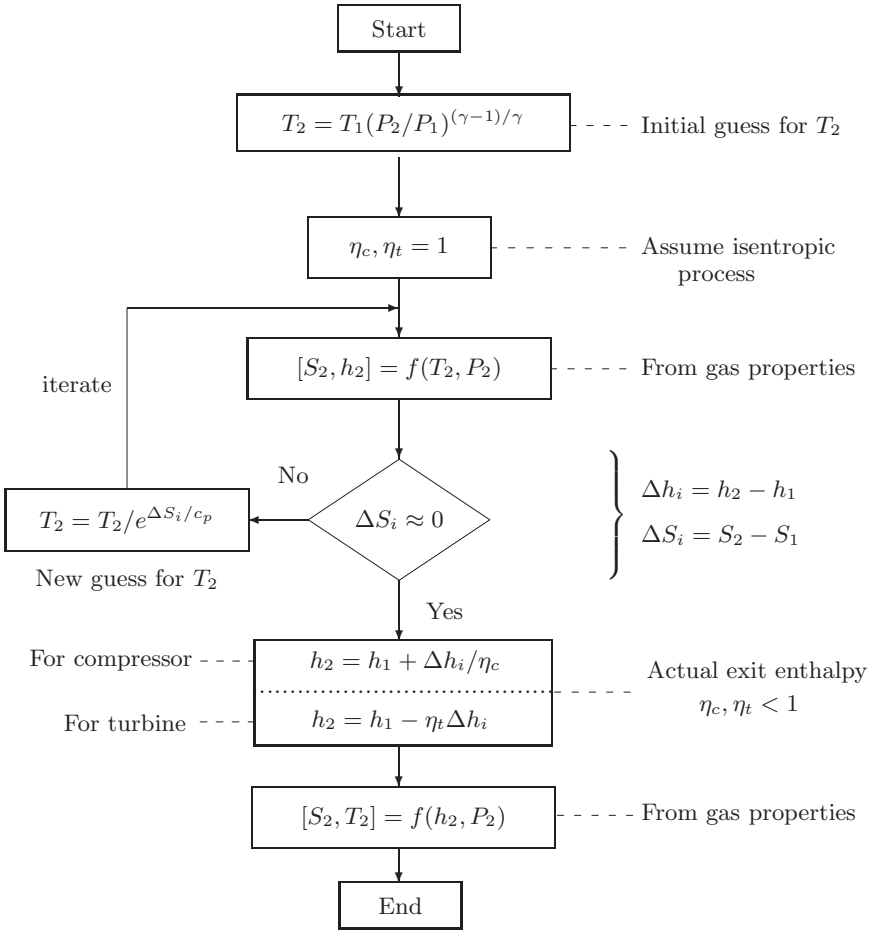

Figure 4.7: Iterative solution for compressor/turbine thermodynamics.

1. An initial guess for the exit temperature, T_2, is made using an estimate for compressor exit temperature as given by Saravanamutto [55].

2. Assuming the process to be isentropic ($\eta_c = 1$), the isentropic exit enthalpy, h_2, and entropy, S_2, are calculated using thermodynamic properties of air.

3. The difference in entropy, ΔS_i, is noted and a new guess for T_2 is made using the Gibbs Equation [56] for a calorically perfect gas.

4. The process is repeated until an exit temperature T_2, is found for which the process is nearly isentropic, i.e. $\Delta S_i \approx 0$.

5. The isentropic rise in enthalpy, Δh_i is divided by the compressor efficiency to get the actual change in enthalpy across the compressor stage.

6. Once the exit enthalpy is known, the corresponding exit temperature, T_2, is obtained iteratively by solving for exit enthalpy, h_2, and exit entropy, S_2, as function of temperature from gas tables.

4.1.5 Iterative Solution of Turbine Thermodynamics

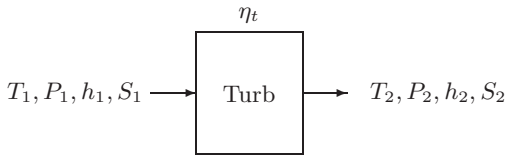

Figure 4.8: Thermodynamic conditions for the turbine

Figure 4.8 outlines a corresponding turbine stage. The turbine exit pressure, P_2, and therefore pressure ratio is known from the mass flow accumulation in the component volumes, hence the turbine efficiency, η_t, and mass flow, w_t, can be calculated from turbine maps. Since the turbine extracts energy from the flow there is a drop in pressure and temperature across the turbine stage.

The turbine exit parameters, T_2, h_2 and S_2 can be calculated using a similar approach as described for the compressor in Figure 4.7 except in this case the turbine pressure ratio, P_2/P_1, is less than 1.0 whereas for the compressor stage the converse was true. With the assumption that the turbine process is isentropic, the turbine exit enthalpy, h_2, is calculated iteratively. The isentropic process assumption implies that the drop in enthalpy would be higher, i.e. the turbine would be able to extract more work from the flow. This isentropic drop in enthalpy, Δh_i, is multiplied by the turbine efficiency to get the actual drop in enthalpy across the turbine stage. Once the exit enthalpy, h_2, is known, the corresponding exit temperature, T_2, is obtained by iteratively solving the equation $h = f(c_p(T), T)$ for the current value of the fuel to air ratio. The exit entropy, S_2, is then obtained as for the compressor.

4.1.6 Matlab Implementation

A MATLAB/Simulink model was developed based on the above formulation. The main structure is shown in Figure 4.9 and details are covered in Appendix E.

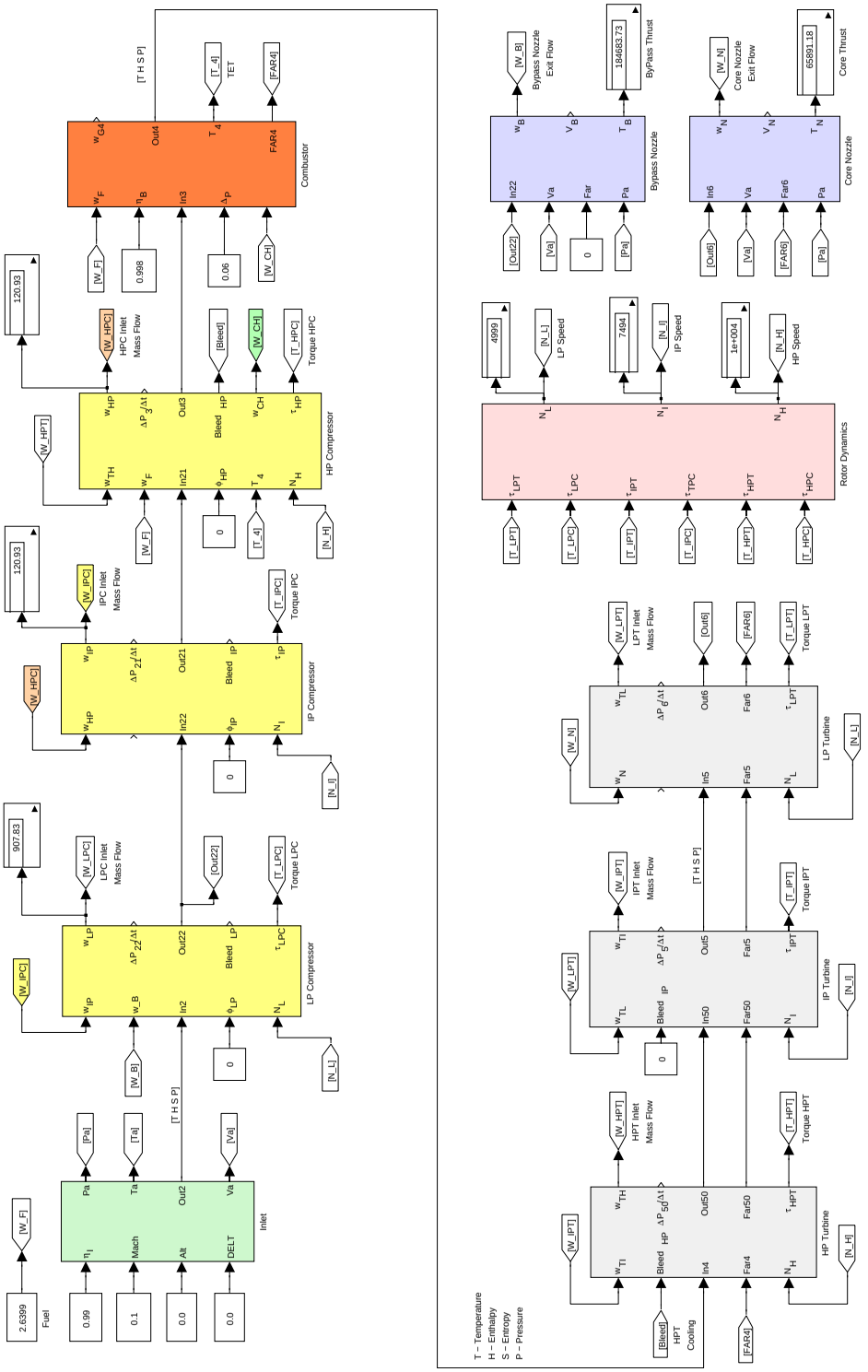

Figure 4.9: Three-spool turbofan hybrid engine model

4.2 Model Validation

The hybrid approach presented above was validated on the three spool Rolls Royce Trent 500 turbofan engine. Engine manufacturers usually keep the engine parameters proprietary and it is difficult to obtain real engine data. However, given the design point or nominal operating conditions, the DYNGEN program by Sellers [12] was used to automatically generate representative compressor and turbine maps for the Trent 500.

4.2.1 Design Point Validation

Stat.	**ID**	**M.Flow (kg/s)**	**Pressures (Atm)**			**Temperatures (K)**		
		DGen	**DGen**	**Hybrid**	**ICV**	**DGen**	**Hybrid**	**ICV**
1	Entry	902.55	1.000	1.000	1.000	288.15	288.15	288.15
2	Inlet	902.55	0.990	0.990	0.990	288.15	288.15	288.15
2.1	LPC	902.55	1.504	1.504	1.482	330.55	330.49	328.75
2.2	IPC	120.65	8.730	8.692	8.591	580.67	579.78	578.09
3	HPC	096.52	39.02	38.96	38.18	913.63	913.14	909.30
4A	Comb	099.16	36.68	36.62	35.89	1788.5	1788.2	1798.9
4	Comb	123.29	36.68	36.62	35.89	1632.5	1632.3	1642.9
4.1	HPT	123.29	14.23	14.15	13.74	1352.0	1351.5	1337.2
4.2	IPT	123.29	6.560	6.531	6.253	1148.3	1148.5	1114.4
5	LPT	123.29	2.005	1.992	1.895	885.75	885.96	838.94

Table 4.1: Rolls Trent 500 design point parameters validation

The engine model was initialized from a state X_0 and was then allowed to reach a steady state condition with the fuel set to the design point value of 2.6399 kg/s. Table 4.1 presents the resulting engine parameters at different engine stations. Three sets of data are presented for comparison purposes. These are,

1. The design point iterative solution from DYNGEN, which is considered most accurate and will be taken as reference.

2. The hybrid solution using the inter-component volume (ICV) method for pressures and the iterative method for subsystem thermodynamic parameters.

3. The third approach also uses the ICV method for pressures but the temperature rise across the compressor and the temperature drop across the turbine are calculated following standard relationships from Walsh [57],

$$\Delta T_c = \frac{1}{\eta_c} T_1 \left(\left(\frac{P_2}{P_1} \right)^{(\gamma-1)/\gamma} - 1 \right) \tag{4.31}$$

$$\Delta T_t = \eta_t T_1 \left(1 - \left(\frac{P_2}{P_1} \right)^{(\gamma-1)/\gamma} \right) \tag{4.32}$$

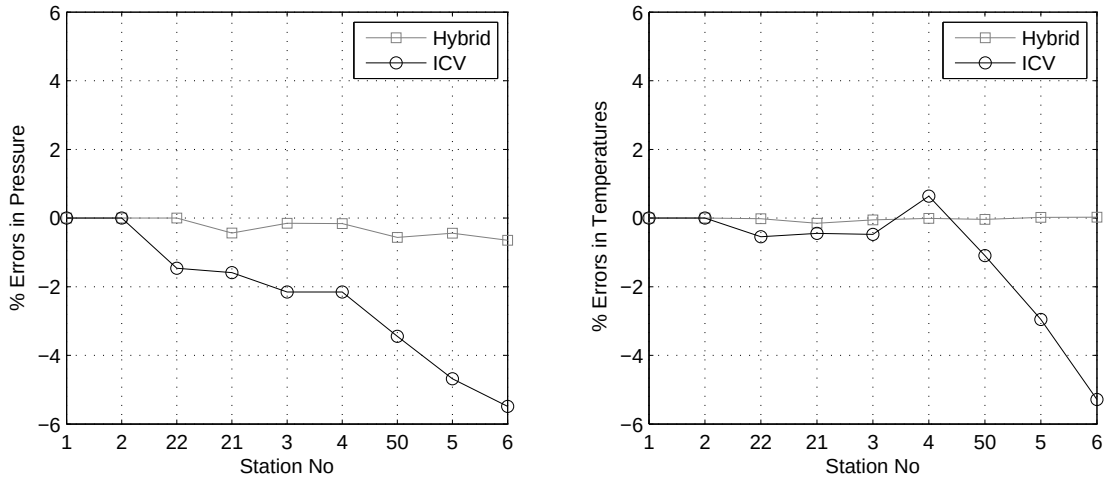

Figure 4.10: Percent errors in pressures and temperatures at design point

Table 4.1 shows that there is a good match between the iterative and hybrid approaches, whereas the pure ICV approach, which uses Equations 4.31 and 4.32 respectively, shows significant errors in the pressures and temperature calculation. Figure 4.10 illustrates these errors as a percentage of the reference iterative method values. Most of the errors in the hybrid approach are less than 0.5% and can be attributed to the fact that the component maps are represented by only 10 discrete points per line and linear interpolation is used for curves that are more adequately represented by 2nd or higher order polynomials. In addition, the net thrust generated by the hybrid method at the design point fuel setting is 278.2 kN in contrast to 264.6 kN from the ICV method. The thrust from iterative code (DYNGEN) was 278.6 kN.

4.2.2 Validation of Engine Transients

Transient response of the three spool turbofan was validated by a sudden reduction in fuel flow from 2.6399 kg/s (design point) to 2.0 kg/s. A fuel flow reduction rate of -5.0 kg/s^2 was assumed, so that it takes approximately 0.2 seconds to reach the new fuel setting. The response of the hybrid approach was compared with that of the iterative method. Figures 4.11 to 4.13 show the transient response on the compressor maps.

4.2.2.1 Transients on Compressor Maps

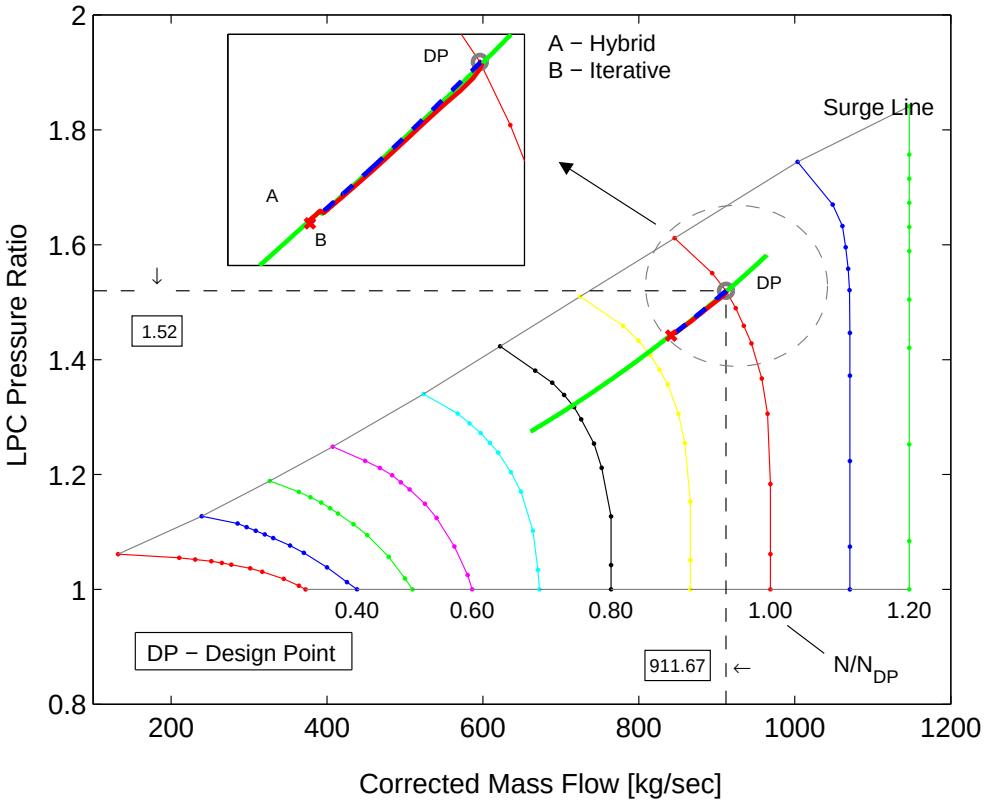

Figure 4.11: Transient on LPC map with step reduction in fuel

Figure 4.11 shows the LP compressor/Fan map with corrected mass flow on the x-axis and fan pressure ratio on the y-axis. The design point is indicated by DP. When the fuel flow is suddenly reduced to 2.0 kg/s from its initial design point value, the LP compressor slows down to its new steady state value on the running line. Two transient response plots are shown, Path DP to A is the response obtained with the hybrid approach and the Path DP to B with the iterative approach, DYNGEN. Both paths are almost identical indicating a good transient and steady-state match between the two approaches. It may be noted that although a substantial step in fuel flow was initiated, the transient response of the LP compressor remains almost entirely on the steady running line.

Figure 4.12 shows the locus of the transient on the IP compressor map. During the transient, the operating point moves up towards the surge line and then settles down on the running line corresponding to the new fuel setting. The hybrid and the iterative methods give consistent behavior during the transient and on the new steady state point.

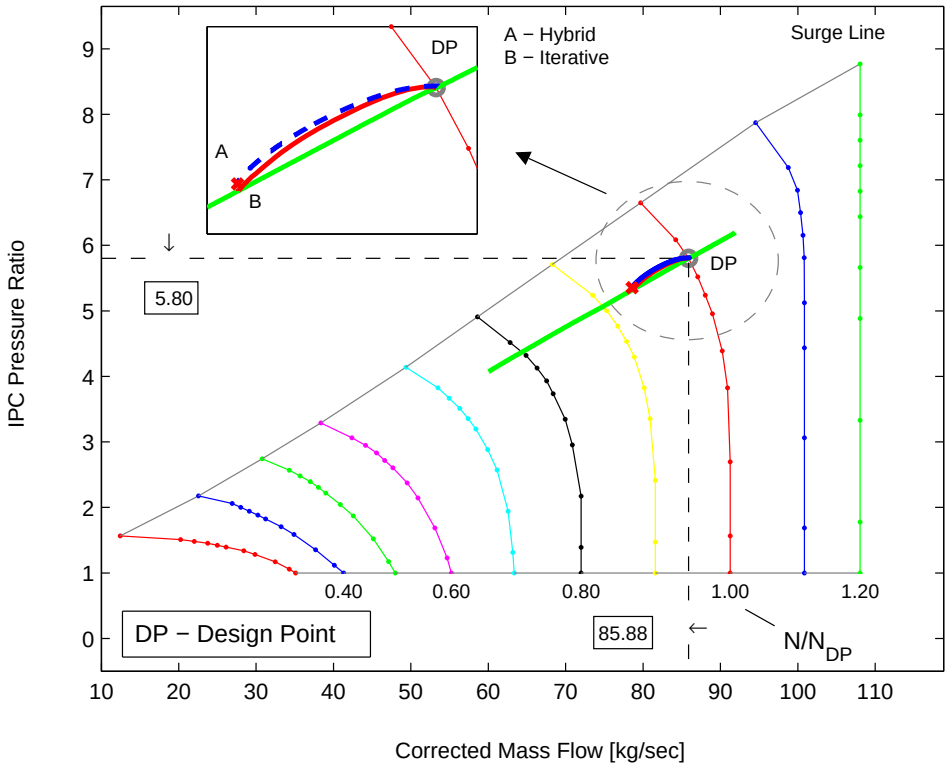

Figure 4.12: Transient on IPC map with step reduction in fuel

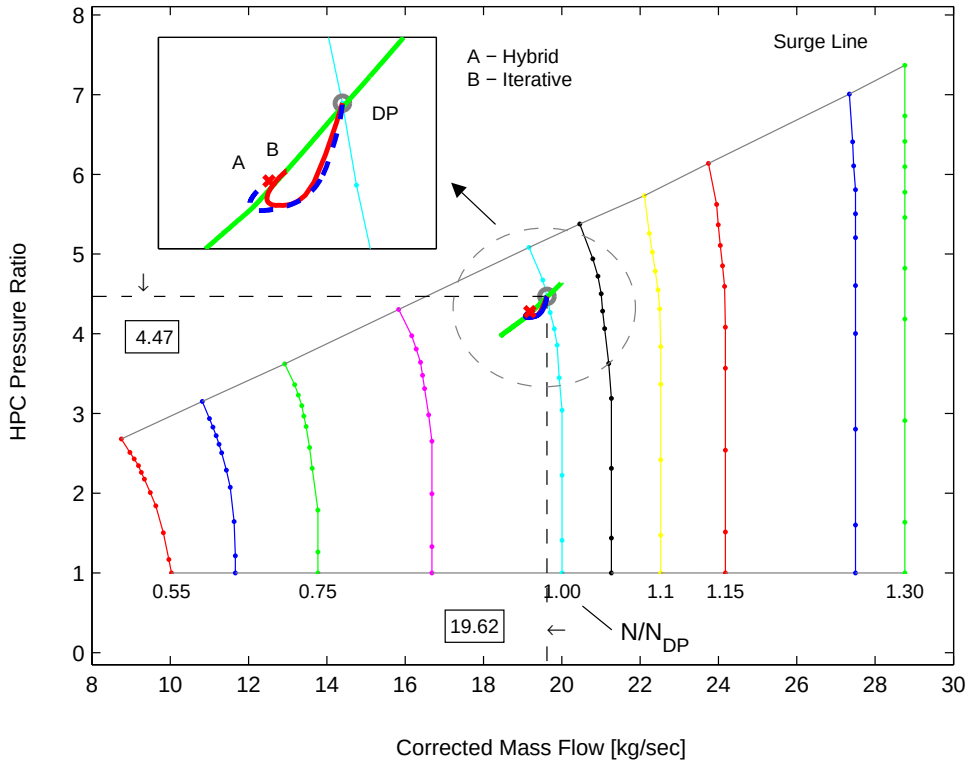

Figure 4.13: Transient on HPC map with step reduction in fuel

Figure 4.13 shows the HP compressor map. As the fuel flow is reduced, the operating point on the HP compressor moves away from the surge line and takes a curved path before settling down on the steady running line of the HP compressor. Here again, the transient response is quite consistent between the two methods, however the steady state operating point of the hybrid method (point A) is marginally offset from that of iterative method (point B). The reason for this offset is attributed to the fact that the turbine maps of the iterative method use enthalpy work function ($\Delta h/T$) as function of turbine corrected speed and turbine flow. The hybrid method however uses turbine pressure ratio as function corrected speed and turbine flow. The enthalpy work function turbine maps were converted to turbine pressure ratio form using the following relationship from Seldner [58],

$$\frac{P_2}{P_1} = \left(1 - \frac{1}{\eta_t c_p}(\frac{\Delta h}{T_1})\right)^{\frac{\gamma}{\gamma-1}} \tag{4.33}$$

For the map conversion process, the design point turbine entry temperatures were used. The matching of design point (DP) or the starting point of the transient is therefore very accurate, however for off-design conditions the operating point on the corresponding compressor maps settles down at a slightly offset location from that of the iterative method. This effect is pronounced for the high temperature stages and is almost negligible for the LP stages.

4.2.2.2 Validation of Pressure Derivatives

Figure 4.14 shows the transient response of the pressure derivatives evaluated in Section 4.1.1. The plot shows six pressure derivatives from the compressor to the turbine stages. Larger pressure changes are observed in the HP stages and vice versa. The transient response of the pressure derivatives from the hybrid and the iterative techniques show a good match.

It may be mentioned here that the simulation step size chosen for the hybrid approach was 5 msec whereas that of the iterative approach was set at 25 msec. The iterative method showed convergence problems below this time step and hence is limited in capturing very fast changes in pressure. All the pressure derivatives show consistent results with both approaches.

4.2.2.3 Validation of Thrust, Temperature and Pressures

Figure 4.15 shows the thrust plots. Both the bypass and the core thrust from the hybrid and iterative approaches are consistent at the design point, during the transient

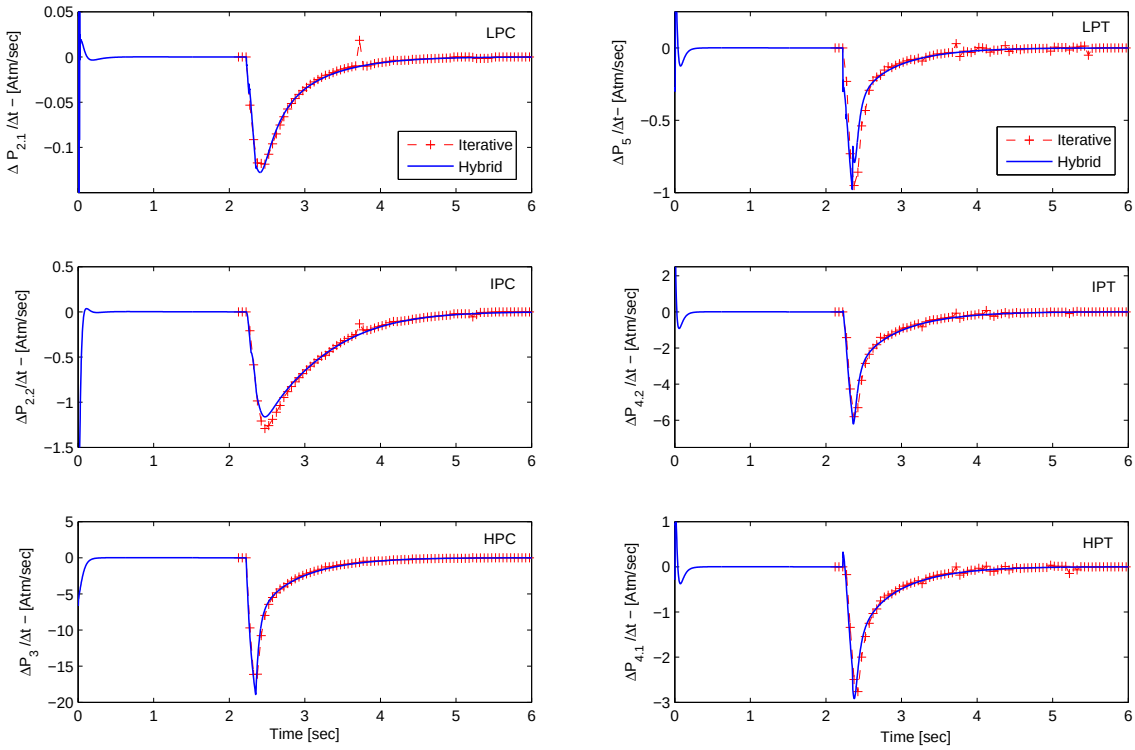

Figure 4.14: Pressure derivatives with step reduction in fuel

and at the off-design point. The integration of the pressure derivatives in Figure 4.14 yields the pressure at each engine station. An iterative technique was then applied to solve the thermodynamic algebraic equations and find out respectively the temperatures and enthalpies for each of the compressor and turbine exits. Figure 4.16 shows the temperature and pressure plots during the transients. Results from both the hybrid and iterative approaches are plotted and are in good agreement.

4.2.2.4 Limitations of the Method

- **Selection of Component Volumes and Simulation Step Time**

  One limitation of the component volume method is the selection of volumes for various stages along the engine length. Recalling the expression for pressure derivatives as given by Equation (4.1),

$$\dot{P} = \frac{R}{V}(T\dot{m} + m\dot{T}) \tag{4.34}$$

  Thus for a smaller component volume, V, the corresponding pressure derivative, $\dot{P}$, will be high and vice versa. If the value of component volume is small enough and the corresponding simulation step time is large, then the in-

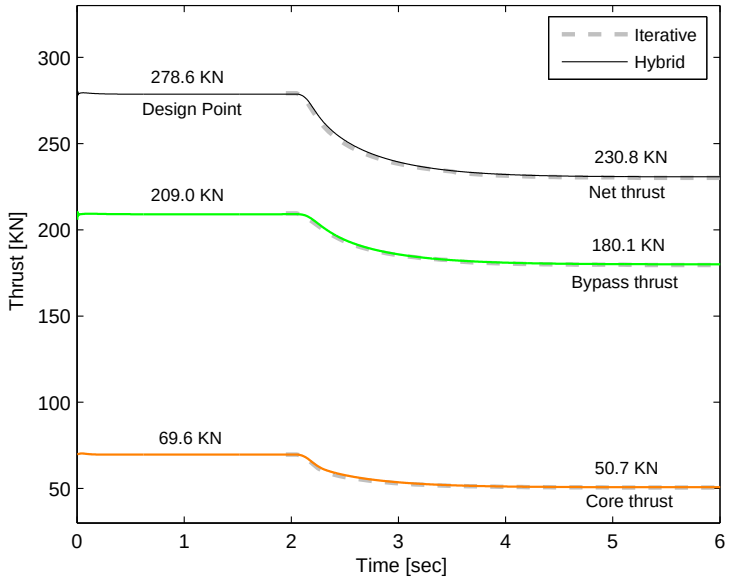

Figure 4.15: Thrust Transient with step reduction in fuel

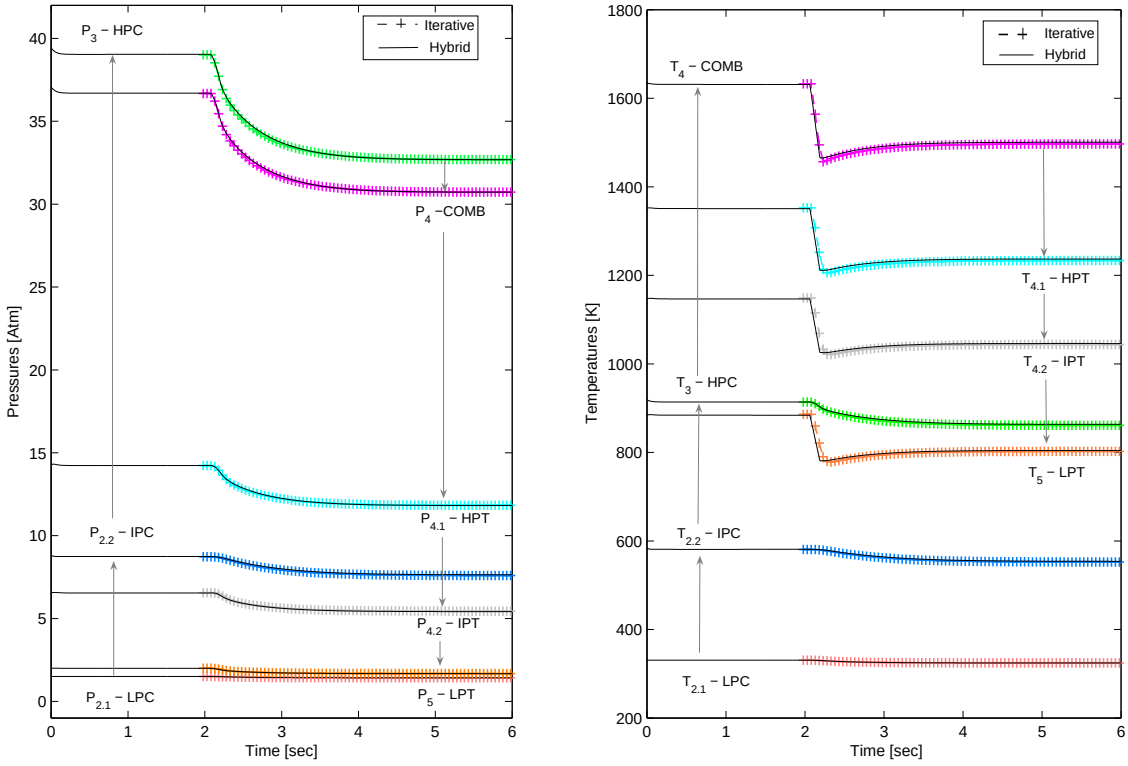

Figure 4.16: Pressure and temperature transient with step reduction in fuel

stantaneous pressure derivative may get very large and can lead to numerical instability. Thus an appropriate approach would be to select a small simulation step time and select a component volume that gives the best match with experimental results. Once the pressure derivatives are matched, the step time may be increased progressively to increase simulation speed. In this work, a

fixed step Euler numerical integration technique was used, with a step time of 5 msec. The selection of component volumes however affects the transient operation only, the equilibrium or the steady state condition remains un-affected.

- **Limitation of Component Maps**

  Engine components such as the compressor and the turbine may consist of more than one stages. For example a typical high pressure compressor (HPC) may have more than eight stages. In this simulation, component interstage dynamics were not simulated and single component maps were used to represent each engine subsystem.

4.3 Thrust Vectoring and Engine Performance

With the engine model in place, it is now desired to evaluate the performance of the Trent 500 engine in presence of thrust vectoring, IPC bleed extraction or both. Various performance parameters may be of interest, however for the present analysis, the following are considered; (i) the turbine entry temperature (T_4 or TET), (ii) the specific fuel consumption (SFC), (iii) the net engine thrust and (iv) the physical spool speeds.

4.3.1 Thrust Vectoring and Engine Transients

When the engine uses thrust vectoring or nozzle deflection, θ_n, for control purposes, the available axial thrust, which is the sum of bypass thrust, wing bleed thrust and core nozzle thrust, decreases. In an actual flight, the auto-throttling system or the pilot would adjust/increase the throttle to maintain desired thrust. However for the isolated engine case and purposes of the present analysis, a control system was designed to maintain constant axial thrust by controlling the LP shaft speed. The control architecture is presented in Figure 4.17.

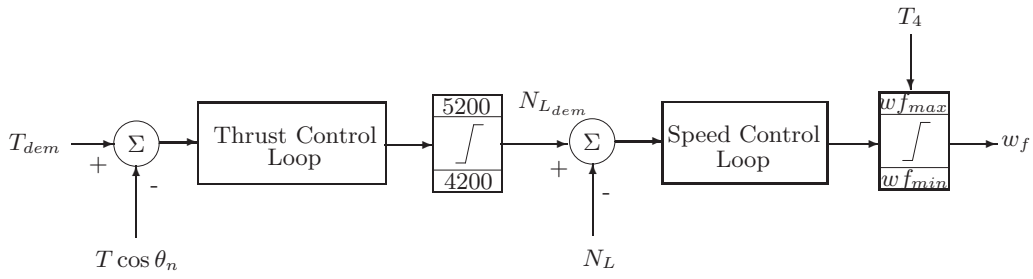

Figure 4.17: Control scheme for constant axial thrust in presence of TVC

Although a separate flow turbofan is simulated here, it would have been more pertinent to simulate a mixed flow turbofan for TVC analysis. However it is assumed that when the nozzle deflects, both the bypass and core streams are deflected. Upon nozzle deflection, the net axial thrust drops and the thrust control loop increases the shaft speed demand to maintain constant axial thrust.

At sea level static (SLS) conditions, for the Trent 500, almost 25% of design thrust is generated by the core and the rest is contribued by the bypass duct. This ratio however varies with flight speed and altitude. Results of the engine and its control system to a step nozzle deflection of $+20°$ are presented in Figure 4.18.

Initially the engine is allowed to reach a steady state with the fuel flow set so that the engine settles at the design point. At this stage, the nozzle is given a step deflection of +20°. The thrust drops immediately and the axial thrust controller increases the speed demand to regain the lost thrust. The system regains its nominal thrust in approximately 1.5 seconds. The corresponding values of specific fuel consumption and turbine entry temperature are shown. All figures are normalized to their design point values before the transient. The following observations can be made,

- The rise in RPM to compensate for loss in thrust is about +1.8%.
- The rise in SFC is almost +4.6%. This rise is quite significant considering four engines are used. However this will not effect the overall aircraft performance as thrust vectoring may only be required for terminal flight phases.
- The rise in turbine entry temperature (TET) is about +4.0%. For a design point TET of 1632K, this approximates to a rise of about +66K. This may not be a problem at landing when the thrust requirement is less, however at take-off, this rise in TET can be quite significant as the engine is already operating at a maximum throttle setting.

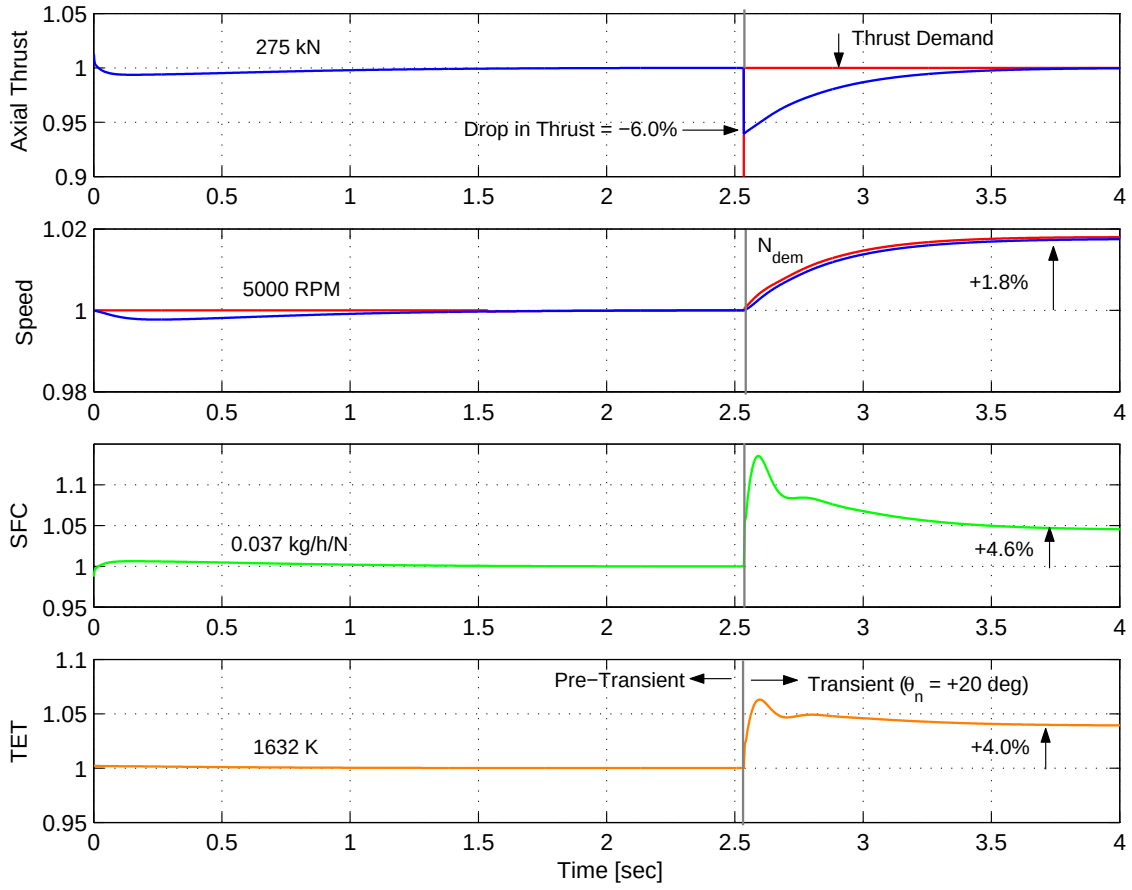

Figure 4.18: Nozzle deflection of +20° at constant axial thrust

4.3.2 Thrust Vectoring and Steady State Performance

The transient engine performance with a thrust vectoring nozzle was analyzed in the previous section. In this section a steady state analysis will be carried out. The same control scheme is used as in the previous section. The controller acts to maintain constant axial design point thrust. The nozzle deflection is varied from 0 to +30 degrees. At each step the engine is allowed to stabilize before the nozzle deflection angle is incremented. Normalized results are plotted in Figure 4.19.

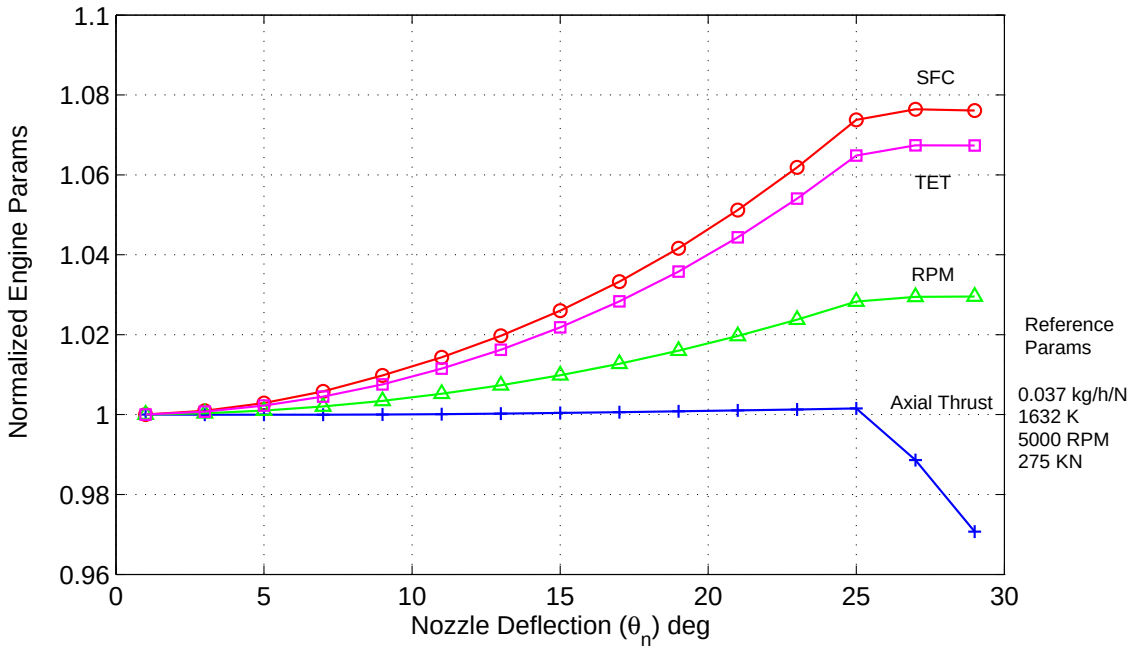

Figure 4.19: Engine performance with TVC at constant axial thrust

Following points may be highlighted,

- The controller maintains the axial thrust at its design value of 275 kN, up to a nozzle deflection of +25°, when the fuel flow limit is reached. Both SFC and turbine entry temperatures increase, with the normalized SFC being slightly higher than the TET. The Fan RPM also increases but at a lower rate.
- It can be inferred from above that the TET would be the parameter that will limit the nozzle deflection and hence the allowable pitching moment that can be generated using thrust vector control.
- Below a nozzle deflection of +15° the variation in all the engine performance parameters is less than 2.5%. Thus lower nozzle deflection ranges will be desirable from an engine performance point of view.

Finally it is pertinent to note that thrust vectoring does not affect the steady state running line of the engine, therefore stall and surge margins on the compressor section are not violated. Since thrust vectoring occurs downstream of the gas path, the engine operating point will always settle on the steady running line. The RPM however will be higher to compensate for loss in axial thrust.

4.4 Effect of Engine Bleed on its Performance

In this section, the effect of engine bleed on its performance is analyzed. For the Trent 500 about 20% bleed is extracted from the HPC stage for cooling of the high pressure turbine. The HP compressor is designed to handle this constant bleed at the design point. Keeping this in view, it was decided to bleed the intermediate pressure compressor or the IPC stage. However the final location would be dependent on wing duct pressure and temperature requirements.

When the engine is bled for lift/controls augmentation, the bleed air is actually made to discharge through very fine nozzles on or above the trailing edge of the wing. It has been argued by Englar [9], that most of thrust from the air bled in this way is actually recovered, hence the loss in net axial thrust is minimal. The bleed analysis can therefore be conducted with the following two options, (i) 100% thrust is recoverable from bleed nozzles. (ideal case) or (ii) 0% thrust is recoverable from bleed nozzles. (worst case). For the following analysis, a worst case is assumed and 0% thrust is available from bleed nozzles.

4.4.1 Transient Engine Performance with Step Bleed

This analysis is also broken down into two parts, transient and steady state. The same engine performance parameters will be used so that comparison could be made with the thrust vectoring case. However engine bleed has additional effects on the engine as the gas path is disturbed upstream at the IP compressor stage, this affects the mass flow and work balance for components downstream. The engine behavior under IPC bleed is first considered for the case of constant axial thrust and then that for a constant RPM.

Engine Transient with Bleed - At Constant Axial Design Thrust

Figure 4.20 shows the results of 10% bleed extraction from the IPC stage. The bleed is applied as a step with the assumption that zero thrust is contributed by the wing nozzle. From Figure 4.20, the following can be observed:

- Upon bleed extraction there is an initial drop in axial thrust. The axial thrust controller subsequently adjusts the RPM demand by +0.55% to maintain the same level of thrust.
- The SFC increases by +8.0% and the TET by +5.0%.

Since 0% thrust recovery is assumed, the above analysis is conservative. If this constraint is relaxed, the rise in fuel consumption and TET to maintain the same level of thrust will be less. This will be further investigated after establishing the exact bleed requirements for landing and take-off. Consequently, if the bleed requirements are high, the contribution of wing nozzle can be a significant portion of the net thrust generated.

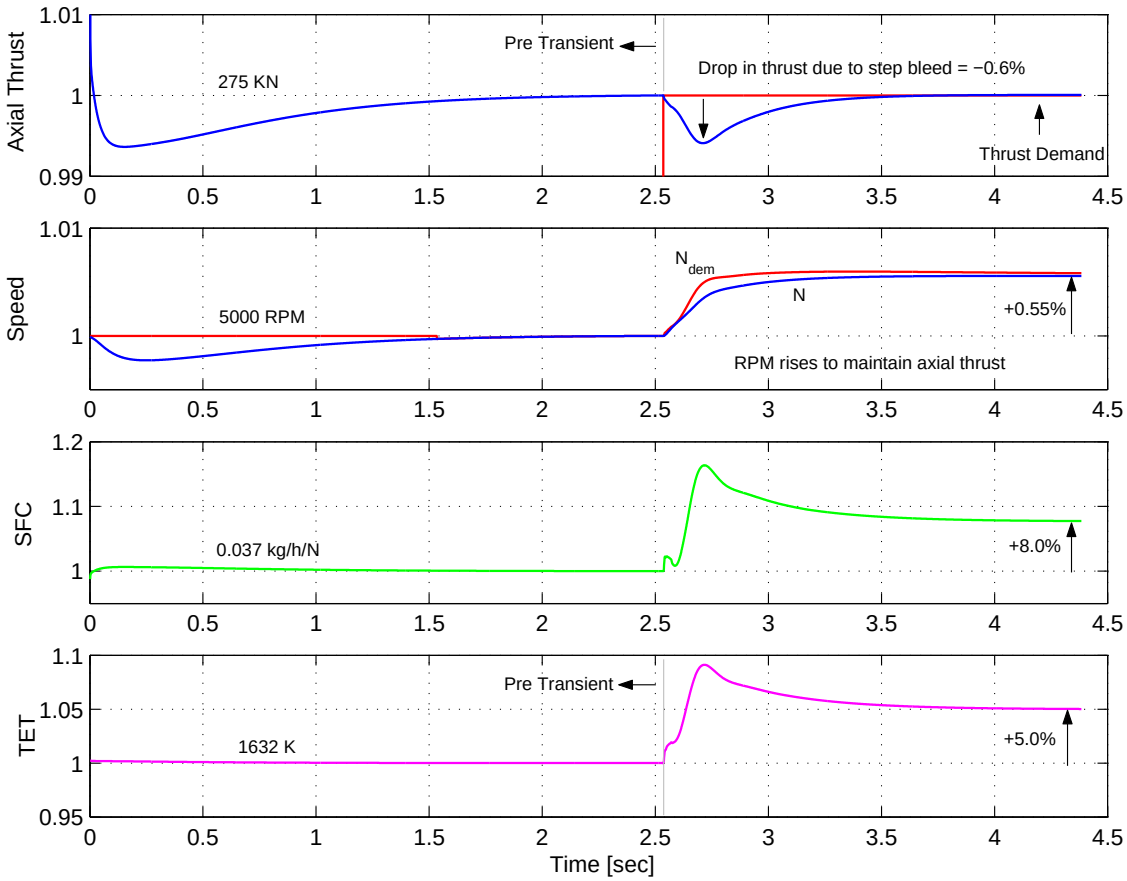

Figure 4.20: Engine performance with 10% IPC bleed at constant axial thrust

Engine Transient with Bleed - At Constant Fan (LPC) RPM

Figure 4.21 shows the results of the second case. The RPM is now held constant and the axial thrust is allowed to vary. Upon 10% bleed extraction from the intermediate compressor, the thrust drops by 2.0%. The SFC rises as the engine now has to maintain a higher turbine entry temperature as it is working with a reduced mass flow. The rise in TET of +3.8% is substantial and amounts to +62K at 1632K.

On the speed plot, a non-minimum phase behavior can be observed. Upon sudden bleed extraction, the LPC shaft initially shows a rise in RPM and then subsequently the RPM drops, which is then brought to its nominal value by the speed loop. From Figure 4.21 it can be observed that although the LPC/Fan speed is kept constant the IPC and HPC stages actually have to run on a higher RPM to generate the same amount of work for the LPC stage which is still operating with a full mass flow. The HPC shaft speed is of interest as it initially drops down and then rises under the action of increased fuel flow into the engine. These transients are due to the mass flow disruption and work imbalance upon sudden bleed extraction.

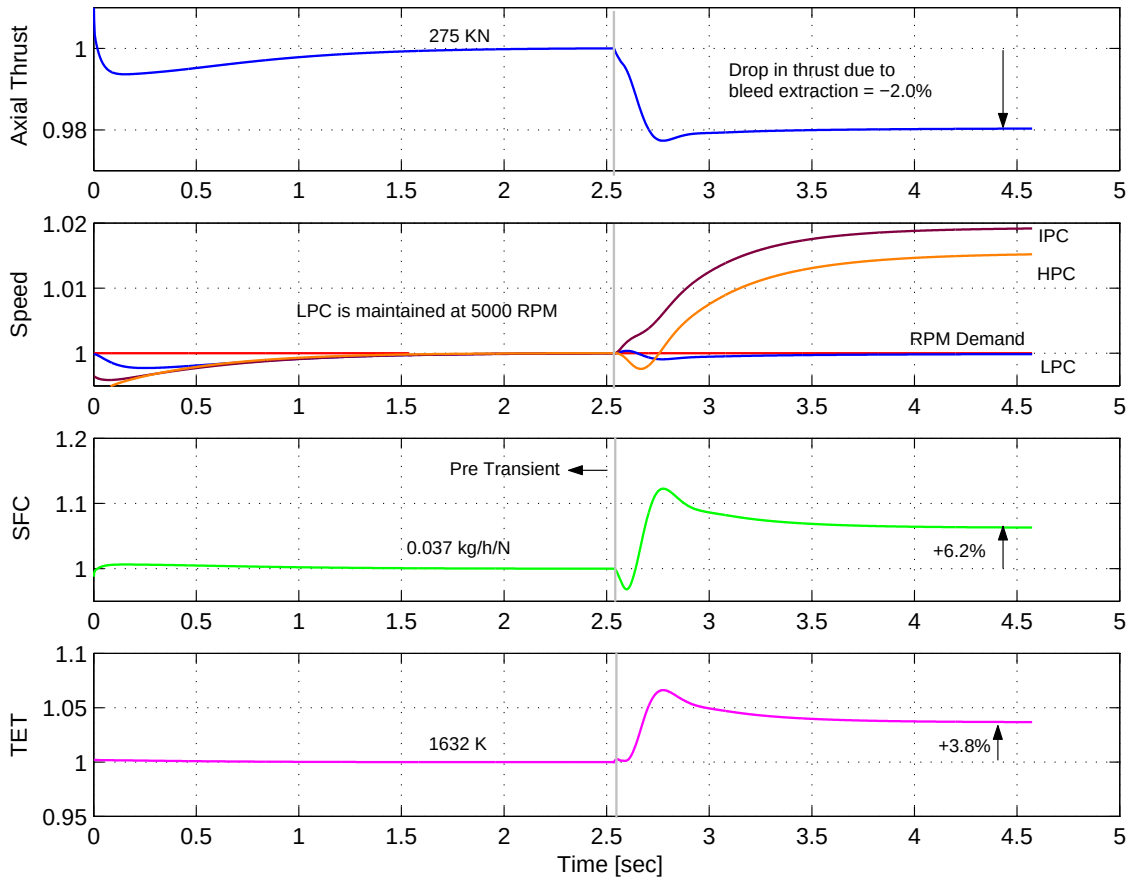

Figure 4.21: Engine performance with 10% IPC bleed at constant RPM

4.4.2 Engine Performance under Steady State Bleed

IPC Bleed and Engine Performance - From Figure 4.22, it is clear that the axial thrust control holds the thrust constant up to 20% IPC bleed, after which the fuel flow was limited. Both the thrust and RPM start to fall. This illustrates that if upon bleed extraction the control input is not adjusted, the engine will not be able to maintain the same level of RPM or thrust. The SFC and TET also rise almost linearly with bleed extraction, unlike the nozzle deflection case in which small nozzle deflections had minimal effect on engine performance. The rise in TET of about +15% amounts to almost +244K. Clearly this will be very damaging for the high pressure turbine stage. In contrast, the rise in TET at +25° nozzle deflection was about +8%. The rise in SFC is also significant, but since it is expected that bleed requirement will be limited to low flight speeds such as landing and take-off, the limiting parameter is therefore the rise in turbine entry temperature.

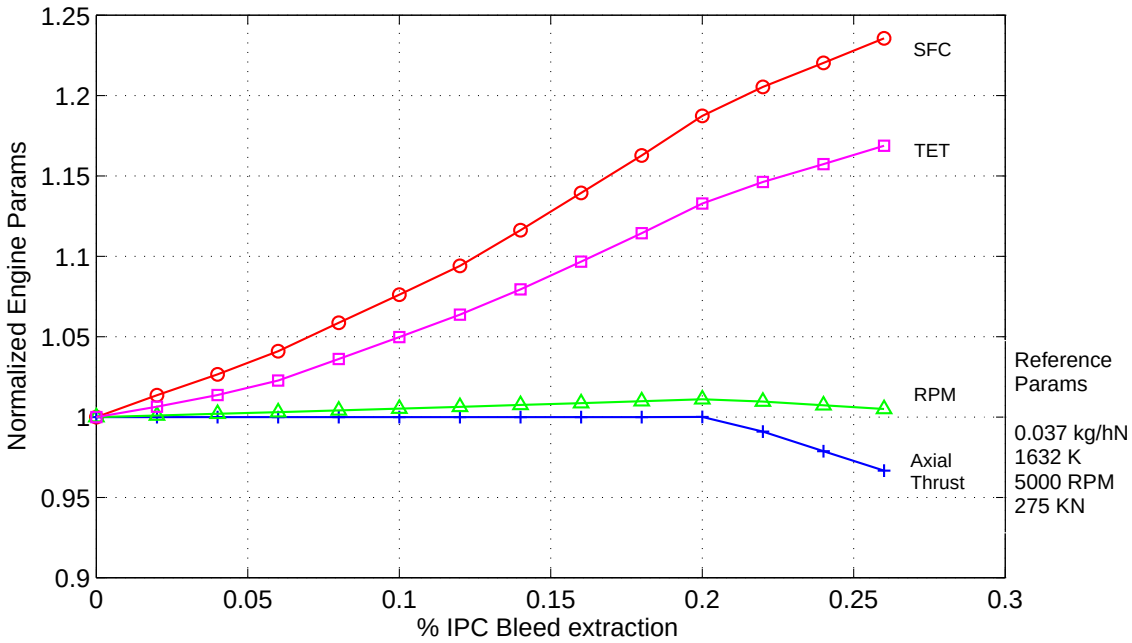

Figure 4.22: Engine performance with bleed at constant axial thrust

IPC Bleed and Engine Operating Point - Figure 4.23 shows the IP compressor map under steady state bleed extraction. The operating point starts for 0% bleed at the design point, DP, and ends at point, X, at 25% bleed. The operating point shifts away from the surge line and is at a higher corrected speed, higher corrected mass flow and a reduced pressure ratio, P_{21}/P_{22}. The surge margin is increased and the compressor efficiency is reduced. The IP compressor would now require greater energy input for the same temperature and pressure rise.

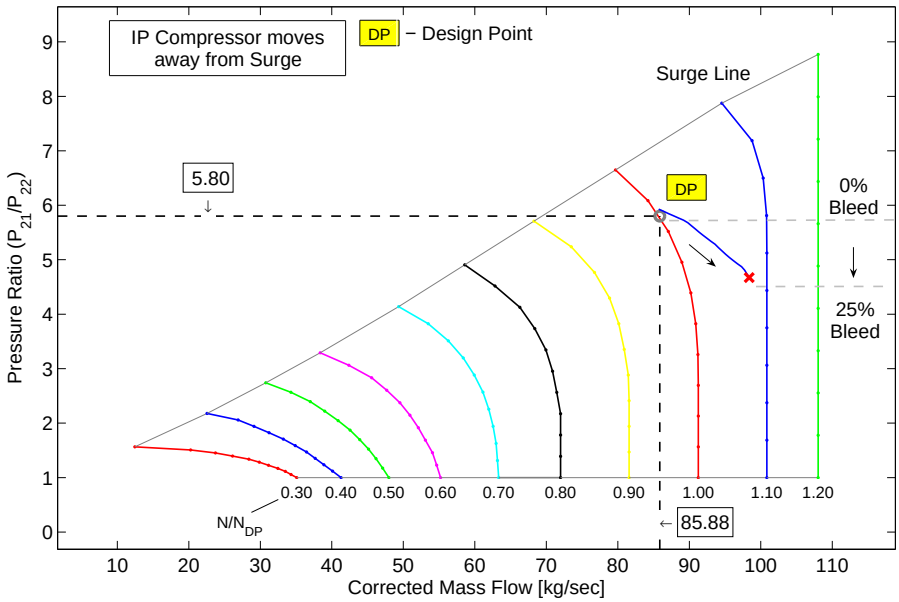

Figure 4.23: IP compressor map with IPC bleed at constant axial thrust

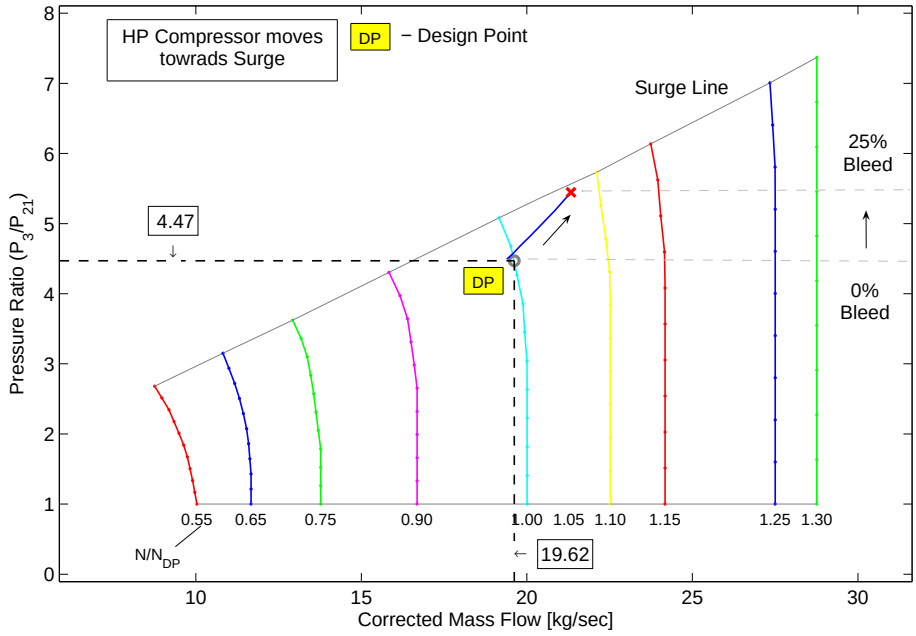

Figure 4.24: HP compressor map with IPC bleed at constant axial thrust

The results on HP compressor map, Figure 4.24, are quite the opposite. The operating point on the high pressure compressor map shifts towards the surge line. If some sort of surge protection measure is not taken, the HP compressor will almost surge upon 25% bleed extraction. Needless to say that this region is also of reduced efficiency, but more critical is the fact that if IPC bleed is not limited, the HPC surge margin limits can be violated quite easily.

4.5 Chapter - Summary

Development of a 3 Spool Turbofan Hybrid Engine Model - Two candidate methods have been identified for propulsion/control integration, namely, (i) thrust vectoring and (ii) lift/control enhancement using bleed air from the engine. Both of these approaches have potential implications on engine performance and require to be investigated. The Rolls Royce Trent 500 Engine model in the 275 kN thrust class was selected as a candidate engine. After the development of an initial theoretical framework for a hybrid engine model, design point and transient simulations were performed. The design point calculations reveal that the results of the hybrid approach are in good agreement to that of the iterative method. The non-iterative method showed increasing errors across the HP stages. The transient results of the hybrid method were also in good agreement with the iterative approach

Engine Performance under Thrust Vector Control (TVC) - When the core/bypass nozzle streams are deflected a loss in total axial thrust results. Under TVC, the engine consequently trims at a higher RPM and fuel flow to maintain constant axial thrust. Both transient and steady state engine performance were analyzed. The steady state analysis was performed for a nozzle deflection range of 0 to +30 degrees. For a nozzle deflection of +25° while maintaining constant axial thrust, the SFC increases by +8.0%, the TET by +6.9% and RPM by +2.5%. The rise in TET amounts to +112K, which is very significant if the engine is already operating its maximum RPM or near its TET limit. At +15° TVC, the rise in TET is less than +2.5% or +40.8K, thus lower TVC angles are desirable.

Engine Performance under IPC Bleed - The IP compressor was bled to provide mass flow for the wing nozzle. The wing nozzle discharges this mass flow through trailing edge flaps for lift/controls enhancement. Transient and steady state analysis were carried out up to a maximum bleed of 25% of the IPC mass flow. The steady state results at constant axial thrust were as follows, the SFC increases by +18.0%, the TET by +15.0% and the RPM by almost +1.5%. The rise in TET amounts to more than 200K, which is unacceptable. In addition, unlike the thrust vectoring case in which the engine does not shift away from its steady running line, upon 25.0% IPC bleed the HP compressor almost surges and the IP compressor almost chokes. It may be concluded that the bleed requirements must be minimized. If IPC bleed exceeds nominal limits then the engine components have to be matched for permanent IPC bleed, to ensure supply of additional mass to the wing nozzle. This would be further investigated in Chapter 6, on propulsion and controls integration.

Chapter 5

A BWB Model with Blown Flaps

5.1 Introduction

A significant part of this work went into the development and validation of a BWB aircraft model with blown flaps. This was a difficult task due to the complex nature of the aerodynamics problem and due to the absence of any previous aerodynamic data for such a configuration. Various approaches were possible to accomplish this task, these included, (i) building a three-dimensional wind tunnel model with blown flap capability and then performing a series of wind tunnel tests; limited time and resources did not allow such an approach, (ii) to build a CFD model and then try to estimate the blown flap effects computationally or (iii) to build an analytical aerodynamic model based on available databases such as the *Engineering Sciences Data Units* (ESDU) and then validate/fine tune this model with panel method codes and an earlier BWB aerodynamic model [7]. All three approaches were deliberated upon and the third approach was chosen owing to its flexibility in selection of airfoil/planform parameters and its implementation within the available resources. This aerodynamic model was subsequently used for trimming analysis and non-linear flight simulations. The method however is based on estimations, in order to improve upon its accuracy, CFD and wind tunnel experiments would be necessary.

This chapter explains the development of this aerodynamic model and covers aspects such as the general description of aircraft, the wing airfoil geometric characteristics/variation along the span, estimation of the wing forces and moments, aerodynamic contributions due to the vertical fins on wing tips and finally model validation. The development of this model was greatly facilitated by Cooke's work on the NFLC Jetstream [59] and by Amrane's work on the high performance sailplane [60].

5.2 General Description

At the start of this research, the best available aerodynamic data for the BWB aircraft was from a previous PhD work by Castro [7]. Castro actually compared several BWB configurations from different sources and in most of the cases the aerodynamic properties were estimated using computational techniques. This particular model however did not have any blown flaps, but proved to be valuable in model validation and the design of FCS. In continuation of the previous research efforts, it was decided that the planform geometry and the mass properties would be kept the same.

A general layout of the BWB aircraft is shown in Figure 5.1. The engines are located on top of the fuselage to enhance noise shielding [61] and also possibly to ingest the boundary layer on the upper surface [62]. The control surfaces are on the trailing edges of the wing and on the winglets.

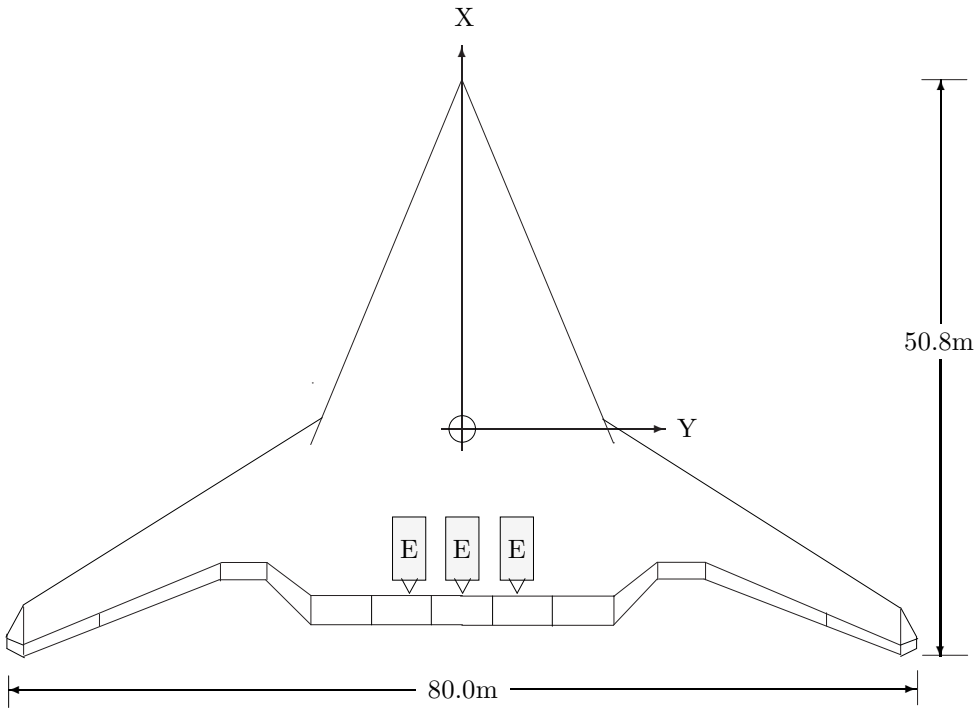

Figure 5.1: Blended wing body tailless aircraft with 15 control surfaces

A maximum take-off weight (MTOW) of 371,280 kg was assumed, whereas the maximum landing weight (MLW) was set at 322,599 kg. Design point cruise is at Mach 0.85 at an altitude of 10,059 m and the approach is at 150-160 kts at sea-level. The CG variation is from 29.4 to 33.4 m, with neutral point (NP) being at approximately 31.6 m. Further description of this model is given in Appendix A.

5.3 Building the BWB Aircraft Model

This section considers the development of a representative aerodynamic model for the BWB aircraft with blown flap effects, using ESDU data sheets and correlations. The conventional ESDU approach is to break down the whole aircraft into individual parts, such as the wing, the fuselage, the horizontal stabilizer, the vertical fin etc. Aerodynamic contributions from each of these components can then be estimated using specific ESDU data sheets and then summed up.

For the BWB aircraft however, there are only two significant airframe components, the blended-wing and the winglet rudders. In order to apply the ESDU estimation to the blended wing, an equivalent wing with no change in section sweep had to be considered. The lift/pitching moment estimates for flap deflections would now be for the equivalent wing and not the original. To cater for this limitation and in order to accommodate a variable section and twist profile along the span, it was decided that instead of considering the wing as a single unit, the wing may be divided into a number of sections/strips. The contributions of each strip to lift, drag and pitching moment could now be calculated using ESDU correlations and transformed to the centre of gravity. To cater for 3D effects, such as wing sweep, finite aspect ratio and wing taper, corrections were applied to the spanwise lift distribution using a panel method code, TORNADO [13].

5.3.1 The BWB Planform and Wing Sections

The blended wing was divided into a number of sections as shown in Figure 5.2. Each of the sections (1 to 6) corresponds to either a new section profile, a change in section sweep or a start of a new control flap. Data corresponding to each of these wing sections is presented in Table 5.1.

Parameters	Section 1	Section 2	Section 3	Section 4	Section 5	Section 6
Section Span	10.0	3.00	4.50	6.00	10.00	5.25
Sweep ($\Lambda_{1/4}$)	56.76	56.76	20.00	30.70	35.13	35.13
Dihedral (Γ)	0.00	2.00	1.500	1.500	3.00	3.00
Taper	0.576	0.7804	0.6464	0.663	0.6278	0.6888
Inner airfoil	REF	SYM	SYM	SC1	SC2	SC2
Outer airfoil	SYM	SYM	SC1	SC2	SC2	SC2

Table 5.1: Section characteristics for the BWB model

For the centre-body section a reflexed (REF) camber airfoil has been used, which provides positive pitching moment ($C_{m0} > 0$) at the cost of reduction in sectional lift coefficient. From $y = 0$ to 10 m, the reflexed profile is diminished linearly to a nearly symmetric (SYM) one, which is then maintained up till $y = 13$ m. Further out along the span, two different super-critical section profiles (SC1 and SC2) are used for high speed aerodynamic performance.

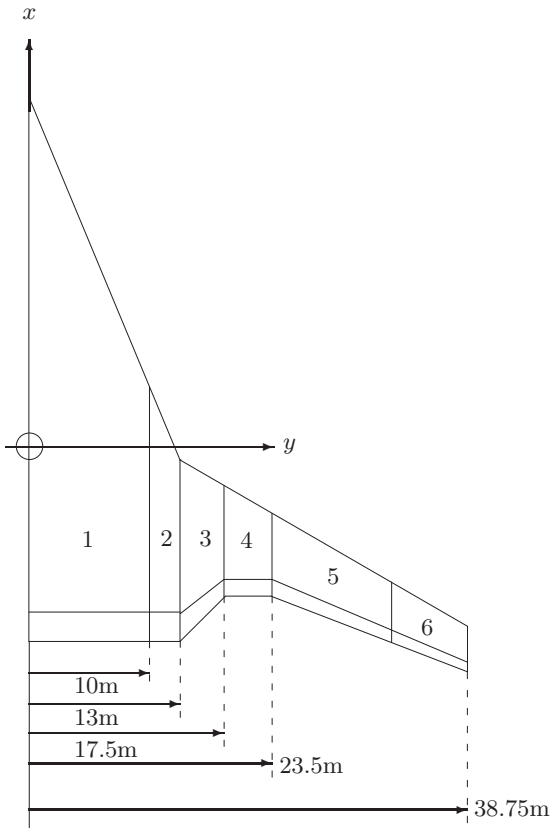

Figure 5.2: Wing partitions/sections for the BWB

With reference to Figure 5.2, it was possible to define arbitrary number of strips for each section, however in the final model a strip width of 1m was chosen. Reducing the strip width any further did not help in improving accuracy, thus for a wing span of approximately 78.5 m, 76 strips were used. As the section profile changes along the span, the sectional lift, drag and pitch moment characteristics also change. Thus for each pass through the aerodynamics calculations, 76 iterations were necessary. This slowed down the aerodynamics calculations when implemented in MATLAB, however when coded in C language this was not a limitation and real-time performance was easily achieved.

5.3.2 Validation of BWB Airfoil profiles

As a first step in the development of this model, it was considered important that 2D aerodynamic properties for different sections along the span be verified. It was noted in Table 5.1 that at least four different types of airfoil sections have been used on the BWB in an attempt to optimize the aerodynamic performance and trimming characteristics of the aircraft. These airfoil sections have been obtained from Qin et. al. [63] and are considered representative of a BWB configuration.

5.3.2.1 Sectional Geometry

The airfoil sections selected for validation were, (i) the reflexed camber airfoil at the root section or mid of centre-body, (ii) the symmetric airfoil at $y = 13$ m or tip of centre-body, (iii) a super-critical airfoil for the inner wing at $y = 17.5$ m and (iv) a thin super-critical airfoil section for the outer wing at $y = 23.5$ m. Figure 5.3 shows all of the four airfoil sections considered.

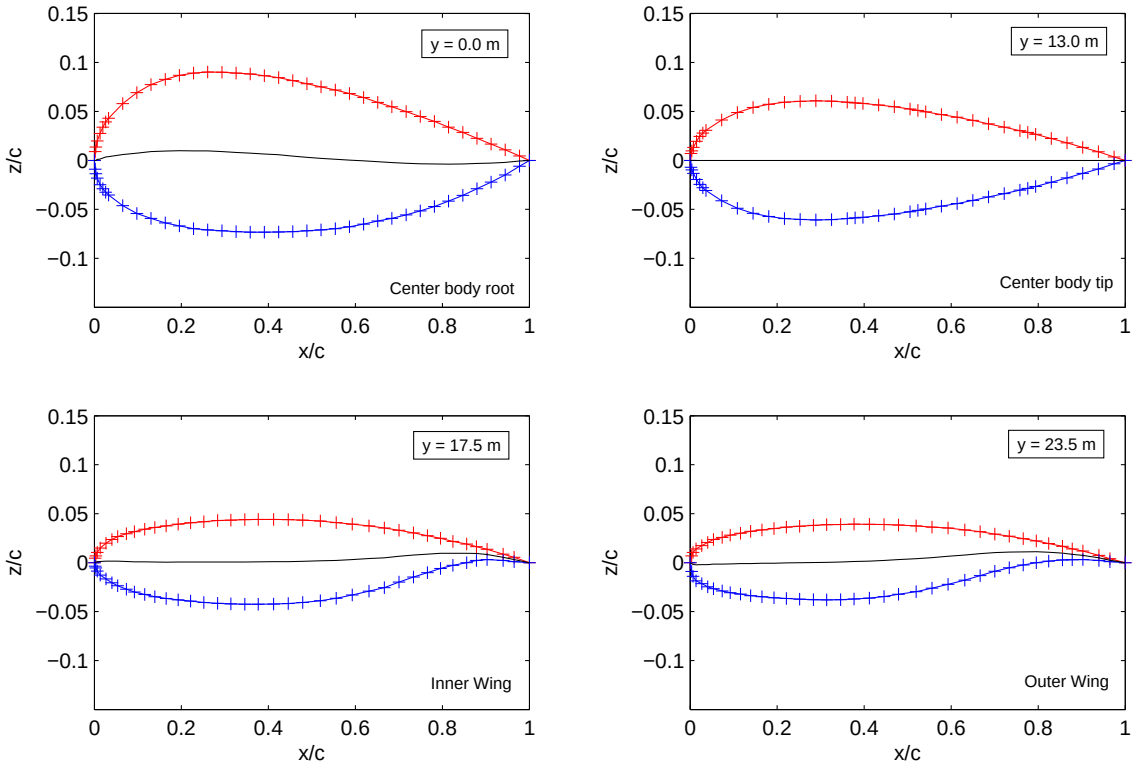

Figure 5.3: Centre-body : inner and outer wing section profiles [63]

Coefficients of lift, drag and pitching moment about the quarter chord position were calculated w.r.t variation in angle of attack. Results for Mach = 0.2, Reynolds number = 3×10^8 and transition at 20% of chord length are presented in the next section.

5.3.2.2 Sectional Aerodynamic Characteristics

The sectional aerodynamic parameters such as the inviscid lift curve slope (C_{L_α}), position of aerodynamic center (x_{ac}) along the chord length and zero lift angle of attack (α_0) were calculated using ESDU 72024 [64] and corrected for the effects of viscosity by ESDU 97020 [65]. Compressibility or effect of Mach number was also taken into account. The VGK CFD program [66], which performs a 2D computational solution, was then used to validate the ESDU calculations.

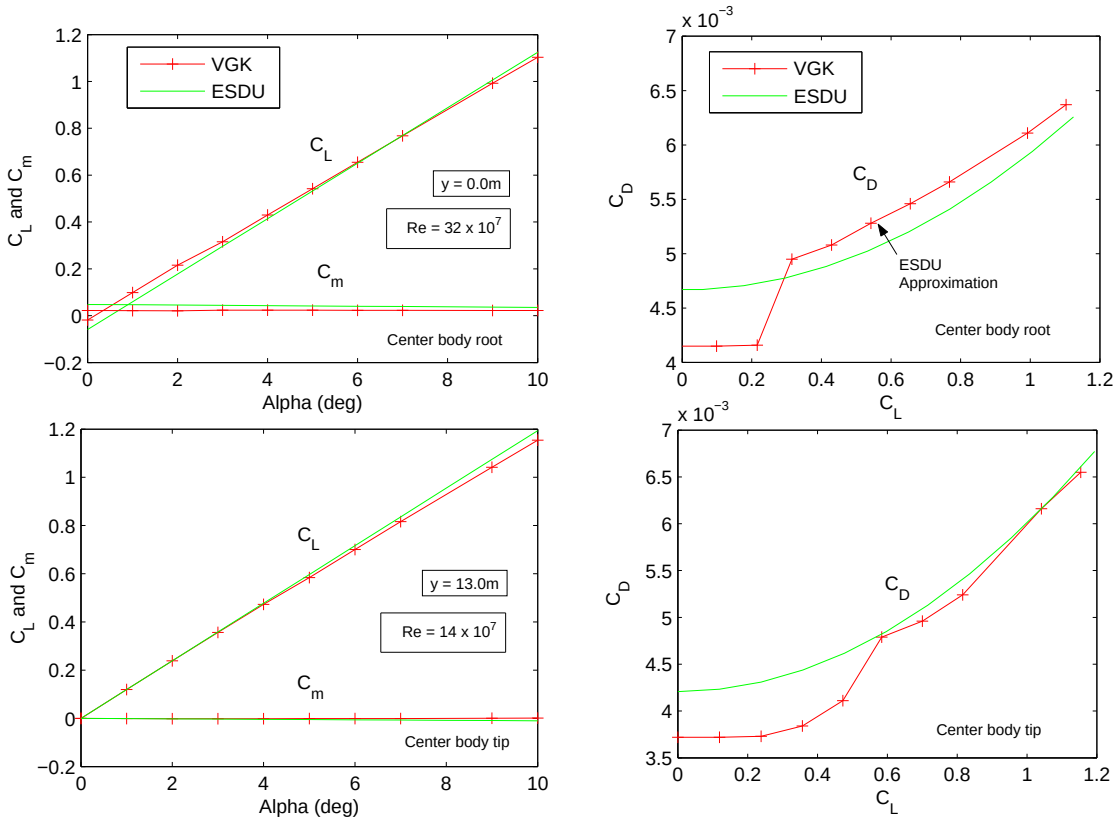

Figure 5.4: Centre-body : sectional lift, drag and pitching moment, Mach = 0.3

Figure 5.4 shows the lift, drag and pitching moment characteristics for the reflexed and symmetric (REF and SYM) airfoil sections of the centre-body. Due to the reflexed camber design at the wing root, the lift coefficient at $\alpha = 0$ is negative and the pitch moment at quarter chord is positive. Thus at zero angle of attack, this part of the wing generates almost no lift but positive pitching moment, which will later be shown of great value in trimming the BWB aircraft in the longitudinal axis. At the tip of the centre-body ($y = 13$ m), the profile is symmetric hence zero lift and pitch moment at zero angle of attack. Also shown are the drag polars for the airfoil sections, the VGK results show a drag bucket at low C_L values. The same is not visible in ESDU drag coefficient approximation which is essentially a sum of

profile drag and lift dependent drag. Nevertheless, the results of both VGK and ESDU show good consistency.

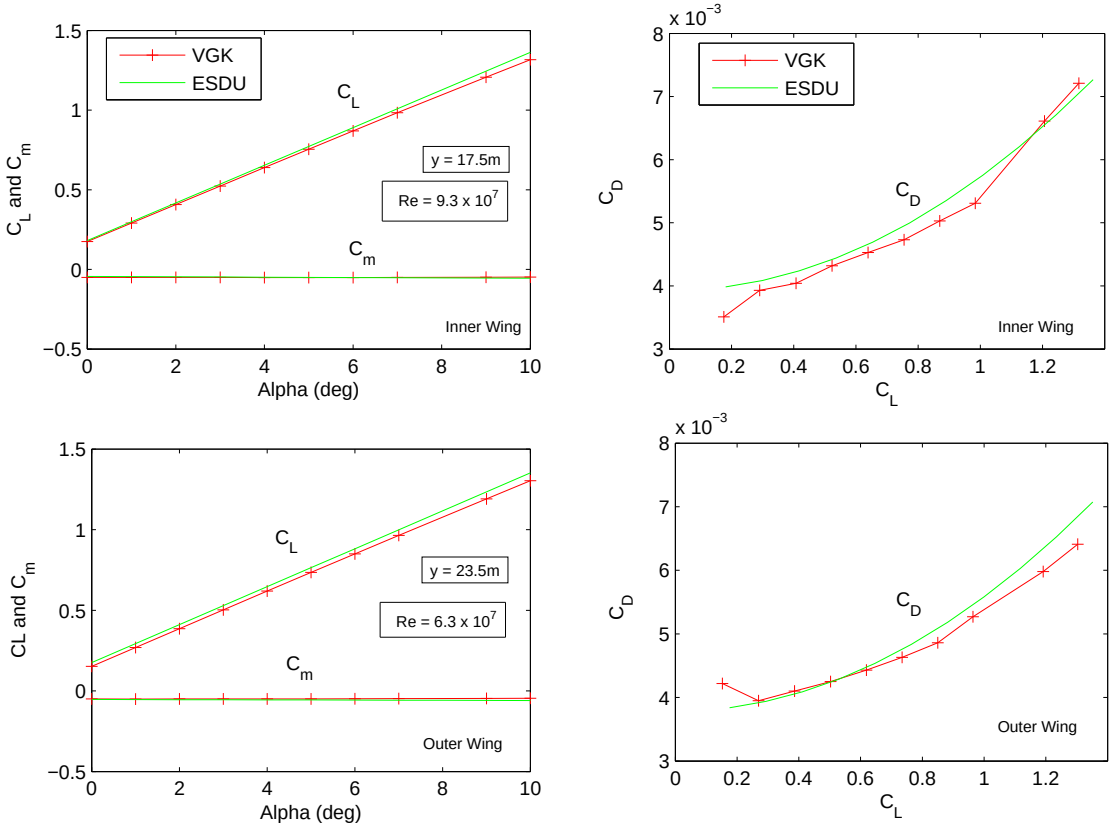

Figure 5.5: Inner and outer wing : sectional lift, drag and pitch moment, Mach = 0.3

Figure 5.5 shows similar results for the inner and outer wing super-critical airfoil sections (SC1 and SC2). The sectional pitching moment at quarter chord is negative and the lift is positive at zero alpha. Results for the both the inner and outer wing cases are consistent with the VGK and the ESDU methods.

5.3.3 Wing Forces and Moments

In this section, the methodology adopted for calculating the body axis forces (X, Y, Z) and the moments (L, M, N) about the center of gravity is presented. This has been broken down into the following steps, (i) setting up the wing geometry, (ii) estimation of sectional lift, drag and pitch moment, (iii) transformation and summation of forces from wind to body axis and (iv) calculation of body axis moments due to forces on individual strips about the center of gravity.

5.3.3.1 Setting Up the Geometry

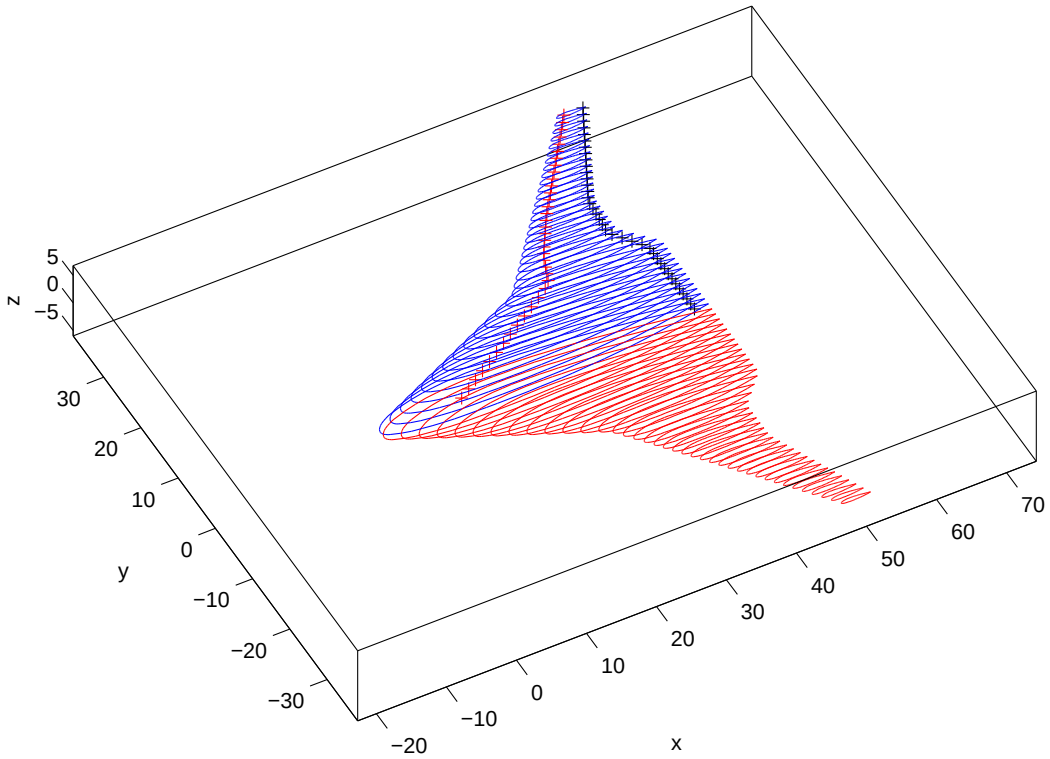

Figure 5.6: BWB strip elements : geometry setup

A geometry setting up module was implemented to set up the various geometrical parameters that are required to calculate sectional aerodynamic characteristics. These included parameters such as sectional chord lengths, lateral position of the center of each strip from the wing root, y_{strip}, area of each strip, S_{strip}, quarter chord position from the datum, flap chord size and deflection etc. Some of these parameters like the flap deflections are variable and could be changed in real time, the rest of the airfoil parameters relating to its geometry were kept fixed. Although not done as part of this research, the sectional profile of airfoil could also be changed in real time to simulate structural changes and aerodynamic interaction. Figure 5.6 shows a sample output from the geometry setting up module showing 76 airfoil sections.

5.3.3.2 Effective Angles of Attack and Sideslip

The net wing lift shall be a summation of contributions from each of the individual strips, however the dynamic pressure and the local angle of attack for each of these strips can be different. The dynamic pressure varies as the effective velocity seen by each strip depends upon its position and its linear velocity along the span.

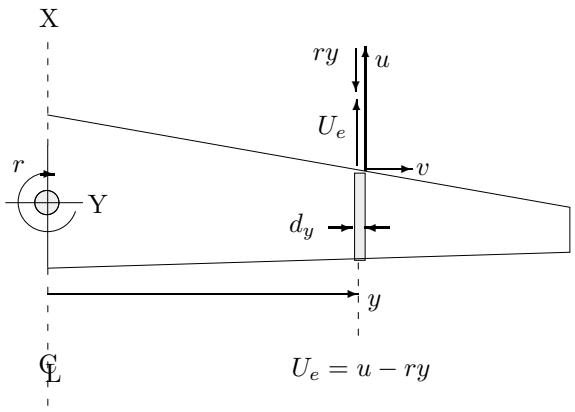

Figure 5.7: Effective forward velocity : U_e

Consider an element, d_y, at a distance, y, along the span, as shown in Figure 5.7. As the aircraft goes through a positive rotation rate, r, along the z-body axis, the element, d_y, sitting on the starboard wing, sees a net reduction in relative velocity. A similar element on the port wing will see a net increment in x-body velocity. Thus the effective forward velocity, $[U_e]_y$, along the span will vary on account of yaw rate.

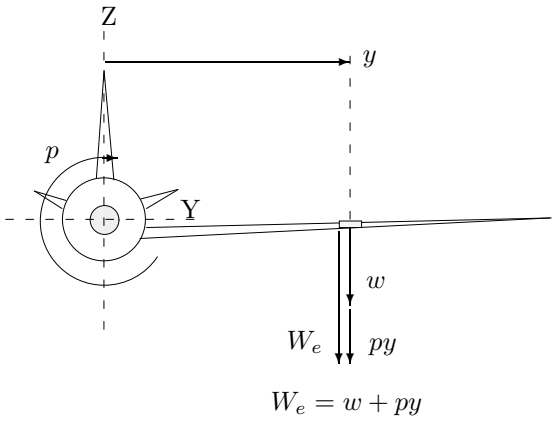

Figure 5.8: Effective vertical velocity: W_e

Similarly in Figure 5.8, as the aircraft goes through a positive rotation rate, p, along the x-body axis, the starboard wing sees a relative increase in vertical velocity by

an amount, py. The port wing however sees a relative decrease in vertical velocity. Thus the effective vertical velocity, $[W_e]_y$, along the span will vary on account of roll rate. With positive roll rates, the starboard wing generates greater lift and thus causes resistance to rolling. For each of the strip elements the net relative velocity, angle of attack and side slip is given as,

$$[Vt]_y = \sqrt{U_e^2 + v^2 + W_e^2} \tag{5.1}$$

$$[\alpha]_y = \tan^{-1}(\frac{W_e}{U_e}) \tag{5.2}$$

$$[\beta]_y = \sin^{-1}(\frac{v}{Vt}) \tag{5.3}$$

5.3.3.3 Lift Estimates with Blowing

The lift coefficient on each of the wing strips was calculated using Equation 5.4, the effect of flap blowing has also been incorporated.

$$[C_L]_y = [C_{L0_B}]_y + K_1 C_{L_\alpha}(\alpha_y + \Delta\alpha_\Gamma + \Delta\alpha_{twist}) + \Delta C_{L0_{flap}} + \Delta C_{L0_{C_u}} \tag{5.4}$$

The terms are explained below.

- C_{L0_B}

  This is the basic lift coefficient at zero alpha for the clean airfoil with no flap deflection. For a viscid lift curve slope, C_{L_α}, and inviscid zero lift angle of attack, α_{0i}, the lift coefficient at zero alpha is given as,

  $$C_{L0_B} = -C_{L_\alpha}\alpha_{0i} \tag{5.5}$$

  where C_{L_α} and α_{0i} are obtained using ESDU 72024 [64] and 97020 [65].

- $\Delta C_{L0_{flap}}$

  The increment in lift coefficient due to flap deflection is obtained using ESDU 94028 [67]. In case of elevators, the flap deflections are symmetric and generate a net change in lift and pitching moment. If the flap deflects asymmetrically, as in the case of an aileron, there is a difference in lift on starboard and port wings and a rolling moment is produced.

- $\Delta C_{L0_{C_u}}$

  If the flap is blown and is also deflected, then depending upon the sectional blowing momentum coefficient, C_u, the flaps generate an additional lift force.

This increment is based on 2D experimental results by Williams [15] and also verified theoretically by Spence [14]. For a 2D section,

$$\Delta C_{L0_{C_u}} = C_{L\delta}\delta \tag{5.6}$$

$$C_{L\delta} = [4\pi C_u(1 + 0.151C_u^{1/2} + 0.139C_u)]^{1/2} \tag{5.7}$$

where δ here is the flap deflection. Figure 5.9 shows the result graphically.

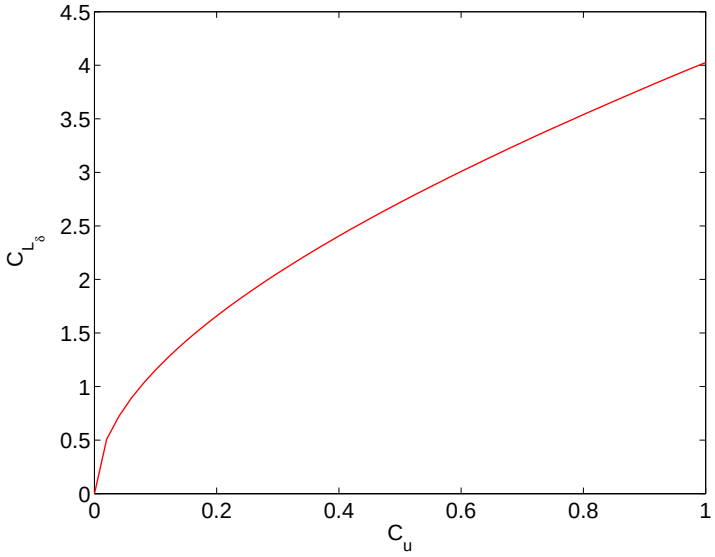

Figure 5.9: $\partial C_L/\partial\delta$ for a 2D airfoil with flap blowing [15]

- K_1

  The factor, K_1, was incorporated to simulate effect of increase in lift curve slope with blowing. Williams [15] suggests that the lift curve slope of a thin 2D flat plate with trailing edge blowing is given by,

$$\left(\frac{\partial C_L}{\partial \alpha}\right) = 2\pi(1.0 + 0.151C_u^{1/2} + 0.219C_u) \tag{5.8}$$

  Thus under the influence of blowing the lift curve slope increases by a certain factor, above its nominal value of 2π for a thin flat plate. Williams [15] then applies a correction factor for the finite thickness to chord ratio (t/c) of the airfoil. These have already been accommodated in the calculation of lift inviscid/viscid lift curve slopes for the airfoil by use of methods ESDU 72024 and 97020. The increase in lift curve slope with trailing edge flap blowing was incorporated as,

$$K_1 = (1.0 + 0.151C_u^{1/2} + 0.219C_u) \tag{5.9}$$

  Graphically this is illustrated in Figure 5.10.

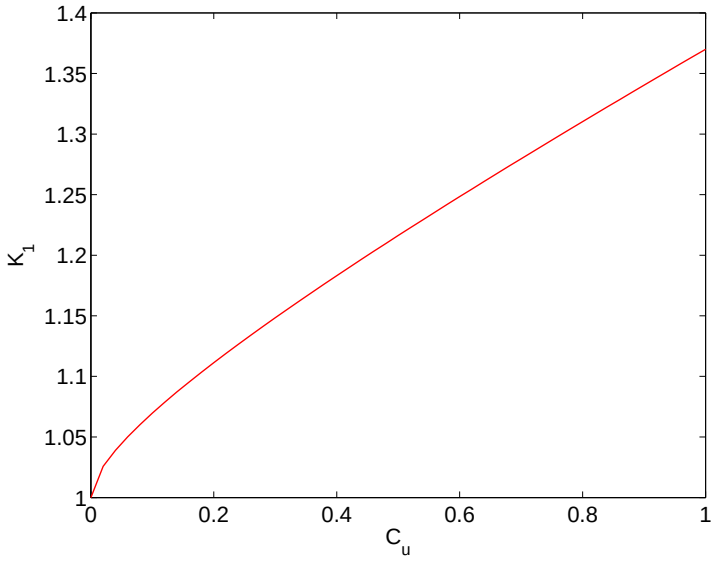

Figure 5.10: Increase in lift curve slope for a 2D airfoil with flap blowing

- $\Delta\alpha_\Gamma$

  The effective angle of attack for each strip along the span is modified by local dihedral (Γ_y) on account of side slip. The change in local angle of attack due to side slip and wing dihedral is given by Mclean [29] as,

$$[\Delta\alpha]_\Gamma = \beta\Gamma \tag{5.10}$$

- $\Delta\alpha_{twist}$

  Lastly, the twist distribution is shown in Figure 5.11 and has been obtained from reference [63]. Positive twist means that the leading edge is rotated upwards. However for the BWB aircraft considered here, the centre-body and the outer wing are rotated downwards with respect to the inner or central part of the wing. The reason for the wash out (reduction in angle of attack) on the outer wing is to reduce the lift coefficient on that section and so prevent a tip stall. For the centre-body the wash out may help in reducing the lift coefficient and achieve an overall elliptical lift distribution profile.

5.3.3.4 Correction for 3D Effects

The strip theory formulation as presented above is essentially a two-dimensional approach. However wing planform parameters such as the wing finite aspect ratio (A), the taper ratio (λ) and the wing sweep (Λ) introduce three dimensional effects that modify the spanwise lift distribution. Effectively, depending upon the planform shape, a particular wing section may be more loaded (operating at higher lift coeffi-

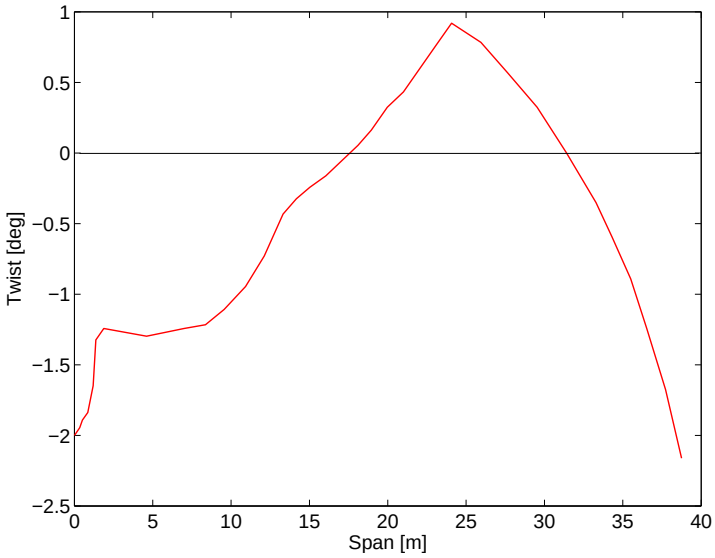

Figure 5.11: Twist distribution for BWB planform [63]

cient) than other parts of the wing, although the geometric angle of attack may be the same for all wing sections. This phenomenon or the variation in spanwise lift distribution occurs because the the trailing edge vortices may either induce a downwash or an upwash along the lifting line of the wing as given by Prandtl theory [35]. A downwash (ϵ) reduces the effective angle of attack of a given wing section whereas an upwash increases it. Thus some parts of the wing may actually stall earlier than rest of the wing. The effective angle of attack (α_e) as seen by the local airfoil section on a wing of finite span, is simply given by

$$\alpha_e = \alpha - \epsilon \tag{5.11}$$

where the downwash (ϵ) may vary along the span. Figure 5.12 shows this effect graphically.

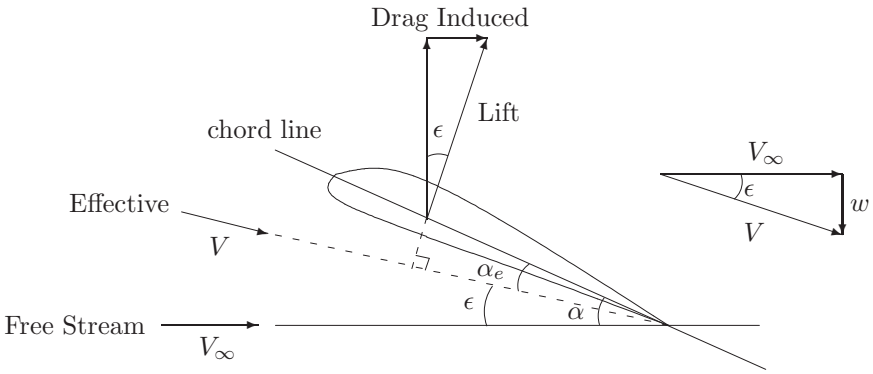

Figure 5.12: Downwash effect on the local flow over an airfoil section of a finite wing

For the considered blended wing body planform, the effective downwash was estimated using the spanwise lift distribution obtained from a vortex lattice code solution [13]. A symmetrical airfoil section was used for the whole span and it was assumed that there is no twist and no flap deflection, so that the lift distribution is only affected by the planform shape. The spanwise lift distribution thus obtained was normalized w.r.t to the geometric angle of attack results from strip theory. Figure 5.13 shows the results. From Figure 5.13, it may be seen that the downwash effect is very significant on the inboard section and this section therefore operates relatively unloaded, however for the outboard wing sections there is an upwash effect and the effective angle of attack exceeds the geometric angle of attack.

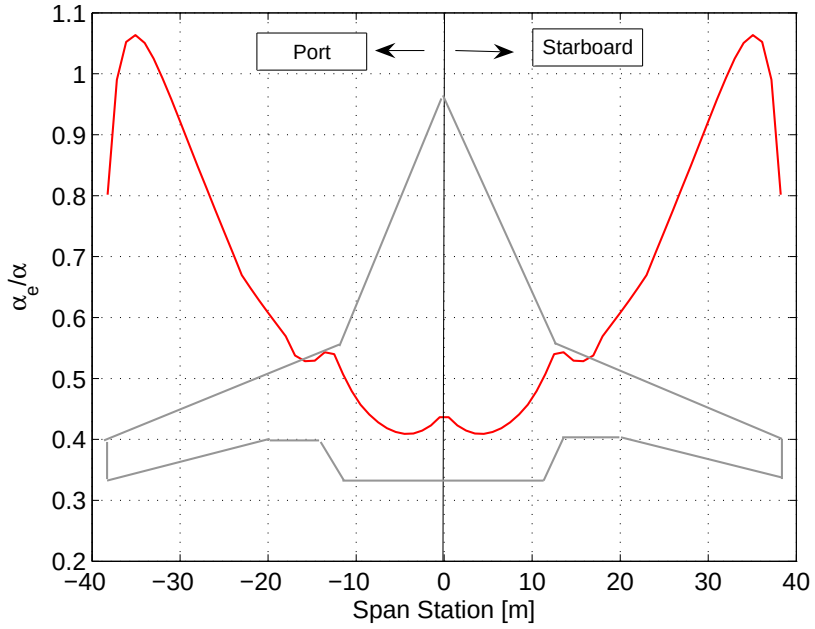

Figure 5.13: Variation in effective to geometric angle of attack across span

Thus in the 2D strip element model the local geometric angle of attack is modified by the downwash effect as shown in Figure 5.13. Once this correction is applied the spanwise lift distribution from the vortex lattice code matches with the strip theory approach. The strip theory approach however allows for a calculation of sectional blown flap effects using Spence's Jet Flap theory [14], which is otherwise not possible with the available panel method code. It may be noted that the downwash effect computed here is a function of planform shape. If the planform shape is modified, this downwash correlation will also change and hence have to be recomputed.

5.3.3.5 Drag Estimates

The sectional drag coefficient is calculated as a sum of two parts, (i) the profile drag coefficient (C_{D_0}) and (ii) the drag due to lift or vortex drag (C_{D_v}). Thus

$$[C_D]_y = C_{D_0} + C_{D_v} = C_{D_{0B}} + \Delta C_{D_{0flap}} + KC_L^2 \tag{5.12}$$

The profile drag coefficient of a clean airfoil $C_{D_{0B}}$ is obtained using ESDU 00027 [68]. Profile drag comprises of pressure drag + skin friction drag. The ESDU method however does not attempt to separate the two. The profile drag was approximated by the following expression.

$$C_{D_0} = K_c K_m C_{D_{thick}} \tag{5.13}$$

where K_c accounts for the effect of camber, K_m accounts for the effect of compressibility and $C_{D_{thick}}$ is the profile drag due to thickness distribution. The increment in profile drag due to flap deflection, $\Delta C_{D_{0flap}}$ was estimated using ESDU 87005 [69] and is a function of flap chord length and flap deflection. The lift dependent drag term, K, was approximated using the drag polar obtained from VGK CFD runs.

5.3.3.6 Pitching Moment Estimates

The pitch moment characteristics are important as they contribute to trim and control characteristics of the aircraft. For the BWB aircraft they become even more important as trailing edge flap deflections not only affect the pitch control but also the trimmed lift coefficient. Large negative flap deflections result in a loss of lift and the aircraft has to trim at a higher angle of attack to sustain the aircraft weight. The sectional pitch moment coefficient about the quarter chord position is given as,

$$[C_{m_{c/4}}]_y = [C_{m0i}]_{c/4} + [\Delta C_{m0}]_{flap} - (C_L - C_{L0_B} - \Delta C_{L0_{flap}})h_1 \tag{5.14}$$

This is illustrated in Figure 5.14 and explained briefly as follows,

- $[C_{m0i}]_{c/4}$

  This is the pitching moment about the quarter chord position for a clean airfoil at zero alpha. It is calculated using ESDU 72024 [64] and is given as,

$$[C_{m0i}]_{c/4} = [C_{m0i}]_{AC} - C_{L0_B} h_0 \tag{5.15}$$

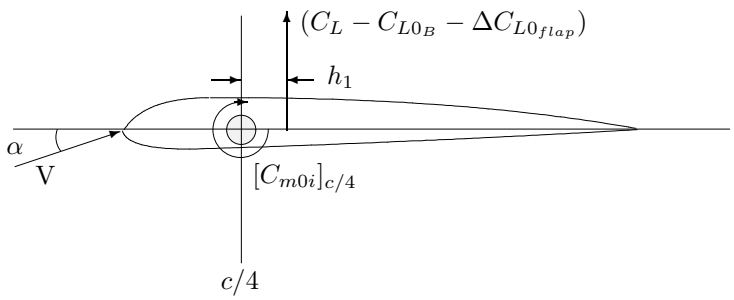

Figure 5.14: Sectional pitch moment at positive alpha

where $[C_{m0i}]_{AC}$ is the pitching moment about aerodynamic center, C_{L0_B} is the lift coefficient at zero alpha and h_0 is the distance between aerodynamic center and quarter chord position, taken through $\alpha = 0$.

- $[\Delta C_{m0}]_{flap}$

  This is the increment in pitching moment at zero alpha due to the deflection of a plain trailing edge flap and is calculated using ESDU 98017 [70].

- Δh_1

  The variation in the location of center of lift, Δh_1, due to angle of attack and flap deployment, aft of c/4 position is calculated using ESDU 03017 [71]. Note $h_1 = h_0 + \Delta h_1$.

Using the above, it was possible to obtain the sectional pitching moment coefficient about the quarter chord position for each strip. In addition, the lift acting on each element generates a pitching amount about the center of gravity (CG) position. For positive lift and for wing sections where the quarter chord position is ahead of the CG position, the pitching moment due to lift will be positive and vice versa.

5.3.3.7 Forces and Moments in Body Axis

The forces and moments acting on each element of the wing were defined in the wind axis. Since body axis equations of motion were used these were required to transformed to body axis using a wind to body axis transformation. The elemental lift and drag forces when converted to body axis generate elemental $[X_y, Y_y, Z_y]$ forces in body axis distributed along the span.

$$\begin{bmatrix} X_y \\ Y_y \\ Z_y \end{bmatrix}_{body} = \begin{bmatrix} \cos\alpha\cos\beta & -\cos\alpha\sin\beta & -\sin\alpha \\ \sin\beta & \cos\beta & 0 \\ \sin\alpha\cos\beta & -\sin\alpha\sin\beta & \cos\alpha \end{bmatrix} \begin{bmatrix} -D_y \\ 0 \\ -L_y \end{bmatrix}_{wind} \tag{5.16}$$

Each of these forces can now be summed up to generate the net X, Y, Z force in body axis due to wing alone. The net force can be considered acting at the CG if the moments generated by these forces are computed about that point. Thus,

$$\begin{bmatrix} X \\ Y \\ Z \end{bmatrix}_{body} = \sum_{1}^{n} \begin{bmatrix} X_y \\ Y_y \\ Z_y \end{bmatrix}_{body} \tag{5.17}$$

Similarly the elemental pitching moment about $c/4$ position was transformed from wind to body axis $[L_y, M_y, N_y]$,

$$\begin{bmatrix} l_y \\ M_y \\ N_y \end{bmatrix}_{body} = \begin{bmatrix} \cos\alpha\cos\beta & -\cos\alpha\sin\beta & -\sin\alpha \\ \sin\beta & \cos\beta & 0 \\ \sin\alpha\cos\beta & -\sin\alpha\sin\beta & \cos\alpha \end{bmatrix} \begin{bmatrix} 0 \\ M_y \\ 0 \end{bmatrix}_{wind} \tag{5.18}$$

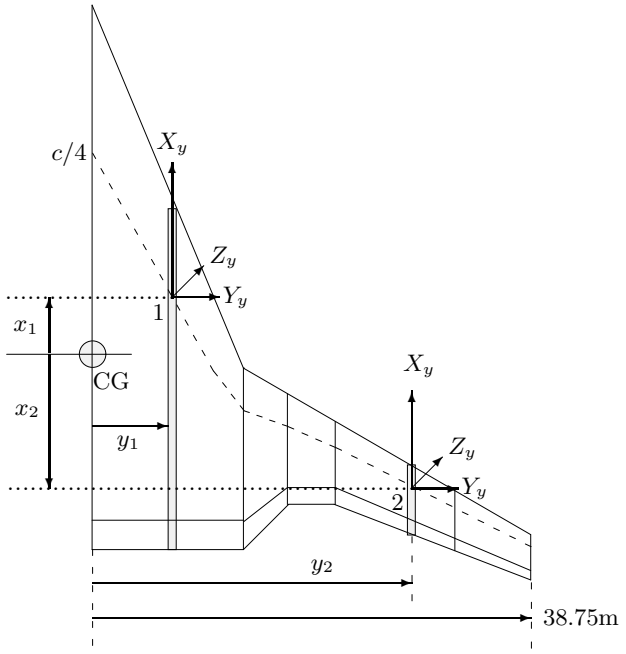

Figure 5.15: Forces and moments on the BWB wing

Figure 5.15 shows two elements 1 and 2, with the body axis forces acting ahead and behind the center of gravity respectively. For point 1, an upward Z force generates a positive pitching moment and a negative rolling moment. Similarly for point 2,

an upward Z force shall generate a negative pitching moment and a negative rolling moment. The net moments about the CG were calculated as the sum of moments for each of these strip elements.

Net Roll Moment - For positive span (starboard wing), positive Z force (down), generates a positive rolling moment about the CG.

$$l_{cg} = \sum_{1}^{n} (l_y + Z_y y) \tag{5.19}$$

where L_y is the rolling moment acting on a given strip, Z_y is the normal force on that strip and y is the lateral distance of that strip from centerline, positive starboard.

Net Pitch Moment - If x_{mrp} is the distance of the moment reference point or the CG from the nose datum, being positive aft and $x_{pos_{c/4}}$ the position of quarter chord position for each given strip, then positive Z force shall generate a nose down or negative pitch moment if $(x_{mrp} - x_{pos_{c/4}})$ is positive. Thus

$$M_{cg} = \sum_{1}^{n} (M_y - Z_y(x_{mrp} - x_{pos_{c/4}})) \tag{5.20}$$

where M_y is the pitching moment about the quarter chord position for each strip. Note that in Figure 5.15, the distance $(x_{mrp} - x_{pos_{c/4}})$ is simply referred as x_1 or x_2, with $x_1 > 0$ and $x_2 < 0$.

Net Yaw Moment - For a positive span, y, towards right or starboard wing, a positive X force on the starboard wing will generate a negative yaw moment and vice versa. Similarly a positive Y force will generate positive yaw moment about CG if $(x_{mrp} - x_{pos_{c/4}})$ is positive.

$$N_{cg} = \sum_{1}^{n} (N_y - X_y y + Y_y(x_{mrp} - x_{pos_{c/4}})) \tag{5.21}$$

This completes the calculation of wing forces and moments.

5.3.4 Vertical Fin Forces and Moments

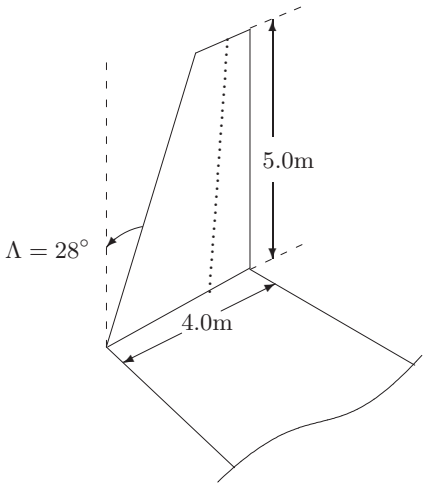

Figure 5.16: Vertical fin on BWB wing tips

Figure 5.16 shows one of the two winglets or vertical fins for the BWB aircraft. Unlike the blended wing the winglets are not treated as strip elements, but are considered as a single lifting surface. These fins also contribute significantly toward the forces and moments on the BWB aircraft and this section discusses it briefly.

Parameter	Value	Parameter	Value
Fin Airfoil	NACA 0012	t/c ratio	0.12
Root chord	4.0 m	Tip chord	1.35 m
Fin height	5.0 m	Sweep(Λ_0)	28.0°
Fin area (S_{fin})	10.0 m^2	Fin aspect ratio (A_{fin})	3.73
Rudder chord ratio	0.25	Fin taper ratio	0.6

Table 5.2: Geometrical parameters for the BWB winglet

The fin side force, Y_{fin}, the rolling moment, L_{fin} and the yawing moment due to fin, N_{fin}, are computed as follows,

$$Y_{fin} = \bar{q}S\left(Y_v(\frac{v}{V_t}) + Y_r(\frac{rb}{V_t}) + Y_p(\frac{pb}{V_t}) + Y_{\delta r}\delta r\right) \tag{5.22}$$

$$L_{fin} = \bar{q}bS\left(L_v(\frac{v}{V_t}) + L_r(\frac{rb}{V_t}) + L_p(\frac{pb}{V_t}) + L_{\delta r}\delta r\right) \tag{5.23}$$

$$N_{fin} = \bar{q}bS\left(N_v(\frac{v}{V_t}) + N_r(\frac{rb}{V_t}) + N_p(\frac{pb}{V_t}) + N_{\delta r}\delta r\right) \tag{5.24}$$

The side velocity derivatives (Y_v, L_v, N_v) were computed using ESDU 82010 [72].

These are in turn a function of the fin lift curve slope, $a_{1_{fin}}$, which was estimated using ESDU 70011 [73]. Fin contributions due to yaw rate, (Y_r, L_r, N_r), and contributions due to roll rate, (Y_p, L_p, N_p) were computed using ESDU 82017 [74] and 83006 [75] respectively. The control derivatives $(Y_{\delta r}, L_{\delta r}, N_{\delta r})$ were estimated through ESDU 87008 [76]. The above derivatives are in the wind axis and were transformed into body axis before addition to the main wing forces and moments.

5.3.4.1 Effect of Flap Blowing on Vertical Fin

As suggested by reference [15], for a wing with a finite aspect ratio, A, and full or partial span jet flaps, the two-dimensional values $(\partial C_L/\partial\delta)_{2D}$ and $(\partial C_L/\partial\alpha)_{2D}$ can be corrected for 3D effects as,

$$C_L = F\left[(1+\frac{t}{c})\left\{\lambda\delta\left(\frac{\partial C_L}{\partial\delta}\right)_{2D} + \nu\alpha\left(\frac{\partial C_L}{\partial\alpha}\right)_{2D}\right\}\right] - \frac{t}{c}C_u(\delta+\alpha) \tag{5.25}$$

where λ and ν are part span correction factors to incorporate the effects of lift increments due to jet deflection, δ and wing incidence, α. For a full span blown flap rudder as in our case both λ and ν can be taken as unity. Factor, F, is a function of the wing aspect ratio and the blowing momentum coefficient and is given as

$$F = f(C_u, A) = \frac{A + (2C_u/\pi)}{A + 2 + 0.604(C_u)^{1/2} + 0.876C_u} \approx \frac{A}{A+2} \text{ for small } C_u \tag{5.26}$$

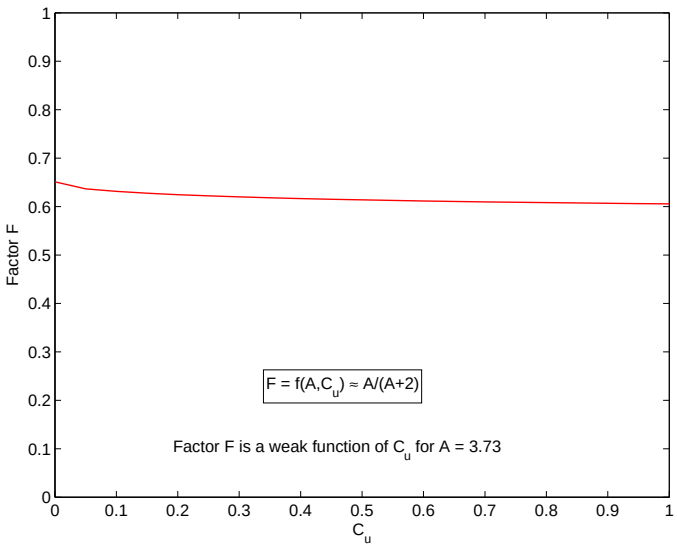

Figure 5.17: Factor F as function of C_u for A = 3.73

Figure 5.17 shows a plot of factor, F, as a function of C_u and aspect ratio $A = 3.73$. It is evident that this lift slope reduction factor is a weak function of C_u and almost

entirely depends upon A, hence F was approximated by $A/(A+2)$. The thickness to chord ratio factor $(1+t/c)$ accounts for increment in lift slope due to thickness for a baseline value of 2π for a 2D flat plate. Lastly for a small thickness to chord ratio, t/c, and low values of C_u, the last part of Equation (5.25) can be neglected in comparison to the first. Thus Equation (5.25) reduces to

$$C_L = F\left[\left(1+\frac{t}{c}\right)\left\{\delta\left(\frac{\partial C_L}{\partial \delta}\right)_{2D} + \alpha\left(\frac{\partial C_L}{\partial \alpha}\right)_{2D}\right\}\right] \tag{5.27}$$

where for a 2D thin flat plate,

$$\left(\frac{\partial C_L}{\partial \alpha}\right)_{2D} = 2\pi(1.0 + 0.151C_u^{1/2} + 0.219C_u) = 2\pi K_1 \tag{5.28}$$

we have,

$$C_L = F\left(1+\frac{t}{c}\right)\delta\left(\frac{\partial C_L}{\partial \delta}\right)_{2D} + F\left(1+\frac{t}{c}\right)2\pi K_1\alpha \tag{5.29}$$

In the calculation of $a_{1_{fin}}$ by ESDU 70011, the wing aspect ratio and thickness to chord ratio are already taken into account, thus replacing $(F(1+\frac{t}{c})2\pi)$ by $a_{1_{fin}}$ we have,

$$C_L = F\left(1+\frac{t}{c}\right)\delta\left(\frac{\partial C_L}{\partial \delta}\right)_{2D} + a_{1_{fin}}K_1\alpha \tag{5.30}$$

Thus for a blown winglet fin, the fin lift curve slope $a_{1_{fin}}$ was multiplied by a factor, K_1 where $K_1 = f(C_u)$ and is greater than 1.0. The first part of the equation which represents the component of lift due to a blown flap deflection was implemented as such and added to the baseline component Y_{δ_r}, where $(\delta = \delta_r)$ or rudder deflection for the case of a winglet fin and $(\partial C_L/\partial\delta)$ is given by Equation (5.7).

5.4 Model Validation

The ESDU model was validated against a baseline aerodynamic model [7] and wherever possible with the panel code [13], for a BWB aircraft with similar planform. This section therefore covers, (i) some results of the panel method code, (ii) the spanwise lift and pitch moment distributions, (iii) the effect of flap deflections and body rates (p, q, r) on aerodynamic forces/moments and (iv) the the increments in lift and pitching moment at different blowing momentum coefficients, C_u.

5.4.1 Tornado Results

Figure 5.18 shows the pressure distribution results of the panel method at a flight speed of 200 m/s and an angle of attack of 4°. Prandtl Gaurret's compressibility correction [35] was not applied and the flap settings/body rates were initialized at zero. The planform was kept similar to that used for the ESDU model.

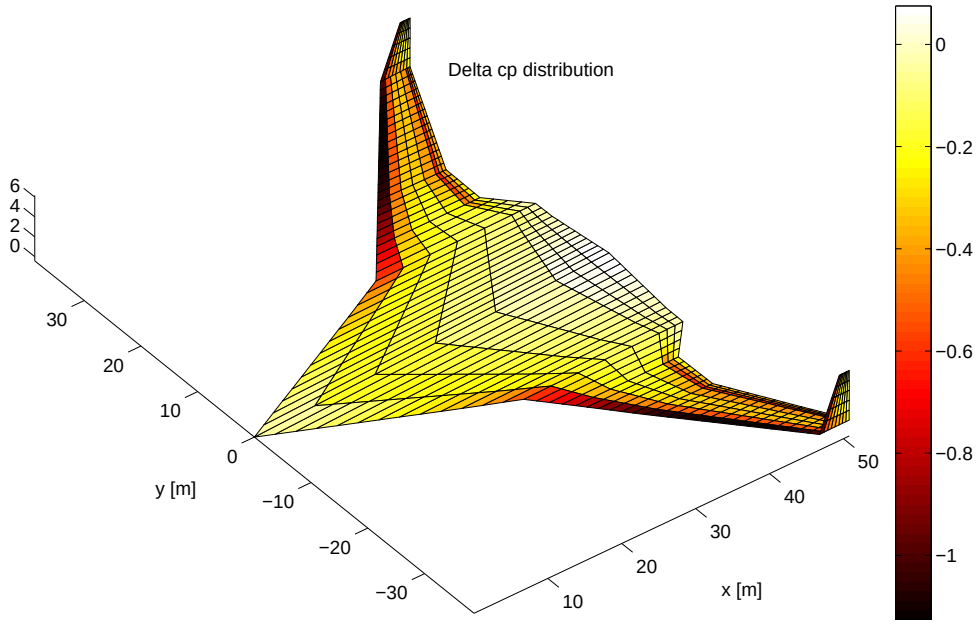

Figure 5.18: Tornado results : pressure distribution at V =200 m/s, $\alpha = 4°$

Figure 5.19 shows the corresponding forces and moments computed by the panel code. Since the body rates are zero and there is no side slip ($\beta = 0$), the lateral directional forces and moments are zero. It may be noted that the lift to drag ratio, $(C_L/C_D = 0.2246/0.0034 = 66)$ is very high, suggesting that the drag prediction of this method is not accurate. This was further verified when the drag data was compared with the strip element aerodynamic prediction in the next section.

Tornado Computation Results

Reference area:	1431.9049				
Reference chord:	27.2088	Reference point pos:	29.3	0	0
Reference span:	87.5	Center of gravity :	29.3	0	0

Net Wind Forces: (N)		Net Body Forces: (N)		Net Body Moments: (Nm)	
Drag:	121388.863	X:	−428549.0741	Roll:	−5.7637e−009
Side:	6.0936e−011	Y:	6.0936e−011	Pitch:	−33271802.8248
Lift:	7879444.1648	Z:	7868717.8938	Yaw:	−1.6553e−010
CL	0.2246	CZ	0.2243	Cm	−0.034857
CD	0.0034602	CX	−0.012216	Cn	−5.3924e−020
CY	1.737e−018	CC	1.737e−018	Cl	−1.8776e−018

STATE:

alpha:	4	P:	0		
beta:	0	Q:	0	Flap setting [deg]:	0 0 0 0 0 0 0
Airspeed:	200	R:	0		
Altitude:	0	PG Correction:	0		

Figure 5.19: Tornado results : forces and moments at V =200 m/s, $\alpha = 4°$

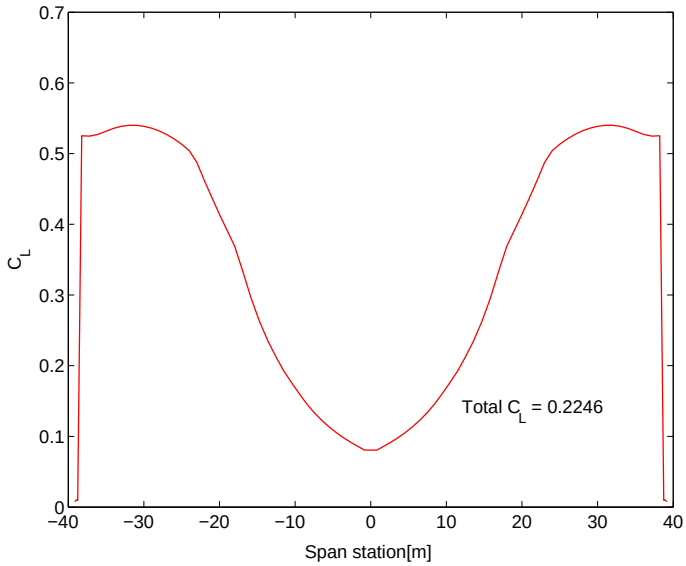

Figure 5.20: Tornado results : spanwise lift coefficient at V =200 m/s, $\alpha = 4°$

Figure 5.20 shows the variation in spanwise lift coefficient for the BWB planform. Due to the very high sweep back angle of the centre-body and the large variation in root to tip chord, the lift coefficient values in the middle of the wing span are quite low, however the outer wing is much more highly loaded, which is typical of sweep back wing designs with low taper ratios.

5.4.2 Validation of Spanwise Lift and Pitching Moment

Various cases were considered with angle of attack varying from 2 to 8 degrees. Figure 5.21 shows the results of spanwise lift coefficient distribution, indicating a good match between the panel code and the ESDU model.

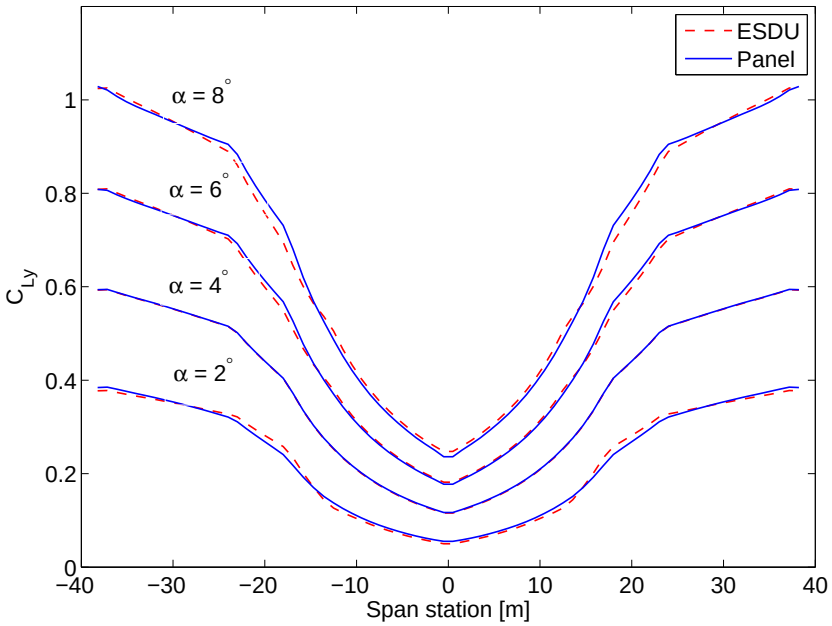

Figure 5.21: Validation : Spanwise lift coefficient

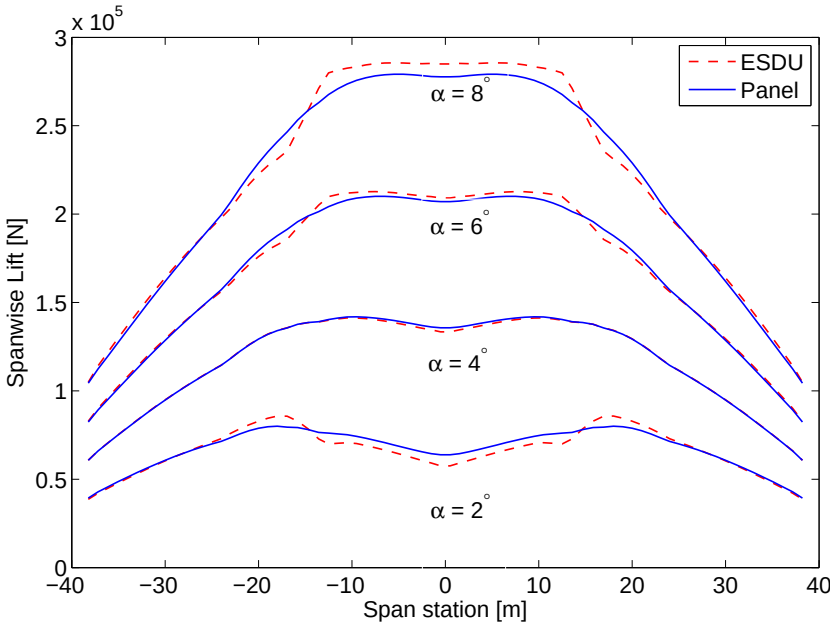

Figure 5.22: Validation : Spanwise lift

Figure 5.22 shows the corresponding spanwise lift distribution. Although the center section is operating at a lower lift coefficient, but due to its larger surface area, the

overall lift distribution profile is more or less elliptical. At higher angles of attack the lift distribution profile shows marginal errors as compared to the panel method code, however these were considered to be within acceptable limits.

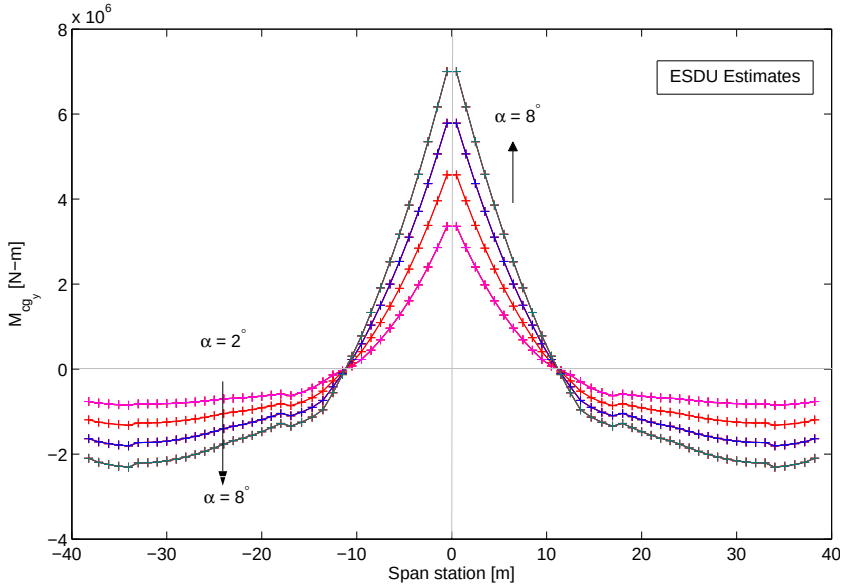

Figure 5.23: Spanwise pitching moment about CG

Figure 5.23 shows the results of spanwise pitching moment distribution about the center of gravity for the ESDU model. Spanwise pitching moment distribution data was not available for the panel code. For the centre-body section, up to a span of about 12 m the pitching moment contribution about the CG is positive. Thus an increase in lift for the centre-body causes a positive pitching moment as the center of lift is ahead of the center of gravity. Further out along the span, ($y > 12$ m), the lift force causes a negative pitching moment about the center of gravity. Thus the centre-body destabilizes and the outer wing stabilizes. For the aircraft to be in trim, the sum of all these moments (the area under the curve) must be zero.

Figure 5.23 also shows the reason why a reflexed camber profile is so important for the BWB. It causes the aircraft to generate a positive pitching moment thus reducing trim elevator deflections. In addition, the sweep back or the position of the outer wing with respect to the center of gravity brings an inherent pitch stability to the aircraft.

5.4.3 Validation of Aero Derivatives w.r.t Air Angles

In this section, the variation in aerodynamic forces and moments with respect to angle of attack (α) and angle of side slip (β) will be considered. Wherever possible comparison is made between the baseline, the panel method and the strip element ESDU models. The baseline aerodynamic model which relies on previous research work and collection of aerodynamic databases [7] uses the same planform as the panel method and the strip element models, however the exact airfoil profile and twist distribution for the baseline model was not available. In the absence of any other data this was considered to be the best available reference.

5.4.3.1 Variation with Angle of Attack (α)

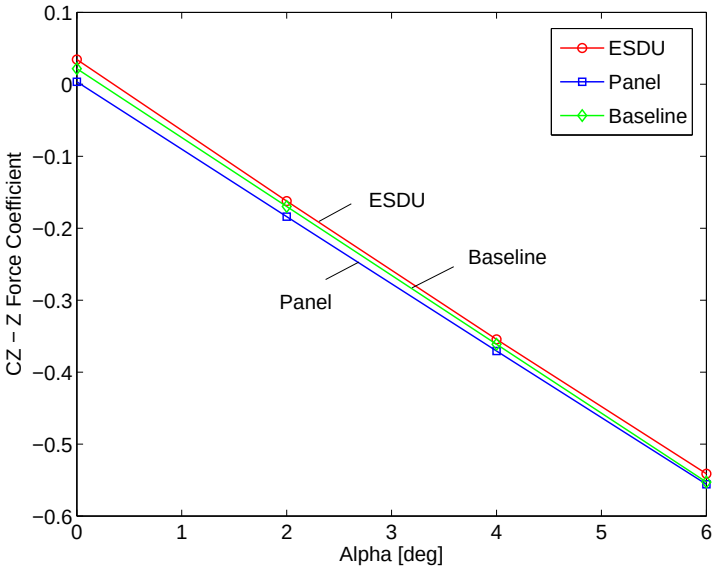

Figure 5.24: Z force coefficient (C_Z)

Z Force w.r.t alpha - ($C_{Z\alpha}$) - Figure 5.24 shows the variation in the Z force coefficient with respect to angle of attack. A body axis notation has been adopted in which the z-axis points downwards, y-axis towards the starboard wing and x-axis towards the nose. Two points may be noted in the figure. Firstly, at zero angle of attack the coefficient, C_Z, is almost zero or positive, indicating almost zero or negative lift at zero angle of attack. The reason for this is the reflexed camber/symmetric airfoils for the centre-body and inner wing respectively. Secondly, the slopes of the curve $C_{Z\alpha}$ match well. It may be pointed out further that in the baseline model the compressibility effect was not included, the same has been done for the strip element and panel codes. When the compressibility effect is added the normal force coefficient slope increases with Mach number.

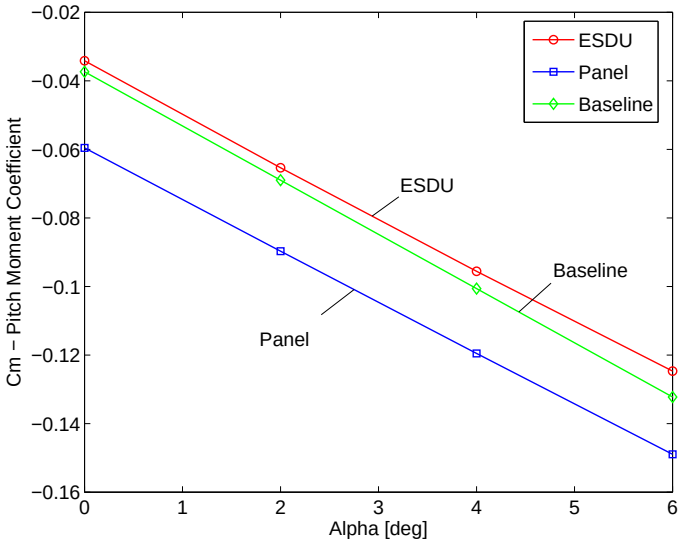

Figure 5.25: Pitching moment coefficient (C_m) with $x_{cg} = 29.4$ m

Pitch Moment w.r.t alpha - ($C_{m\alpha}$) **-** Pitching moment variation with angle of attack is a strong function of CG position. For positive pitch stiffness it must be negative ($C_{m\alpha} < 0$). Figure 5.25 shows the pitching moment variation for a forward CG location, ($x_{cg} = 29.4$ m). All three models give the correct slopes, with the panel method at a slightly greater negative offset, than the other two methods.

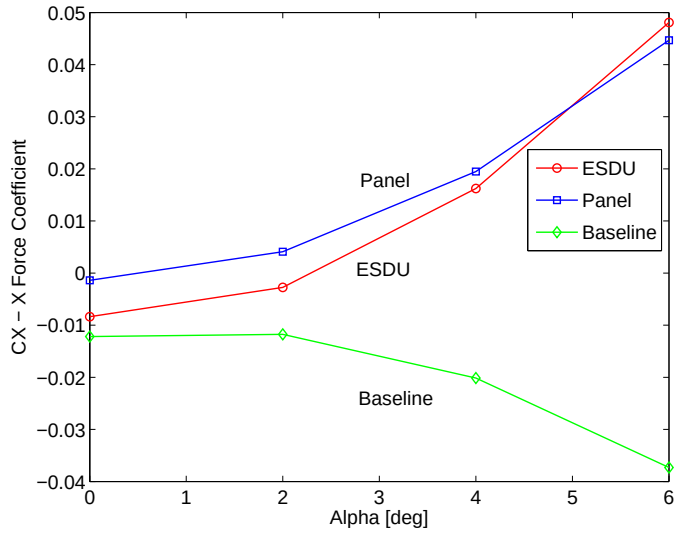

Figure 5.26: X force coefficient (C_X)

X **Force w.r.t alpha -** ($C_{X\alpha}$) **-** The X force depends primarily on the drag of the aircraft and a component of the lift in the positive X direction. Both the panel method and the strip element ESDU method predicted far lower values of drag as compared to the baseline model. The baseline model considers the X force

coefficient, C_X, as a 2$^{\text{nd}}$ order polynomial of the normal force coefficient, C_Z,

$$C_X = -\left(C_{x_0} - C_{x_1}C_Z + C_{x_2}C_Z^2\right) \tag{5.31}$$

where C_{x_0}, C_{x_1} and C_{x_2} are constants. An alternate option was to simply use a higher value of K in the expression ($C_D = C_{D0} + KC_L^2$) to match the baseline drag coefficient, however it was decided that the simple expression for X force in Equation (5.31) would be used for the ESDU model as well.

5.4.3.2 Variation with angle of sideslip (β)

The presence of sideslip not only generates a yawing moment, $C_{n\beta}$, but also a rolling moment, $C_{l\beta}$, on account of the wing dihedral, Γ, and an asymmetrical flow distribution on starboard and port wings. If vertical fins are present, a significant amount of side force is also generated. For the BWB aircraft in particular these forces are difficult to determine as the size of winglet fins is small and the relative size of side force and consequently the yawing moment is less.

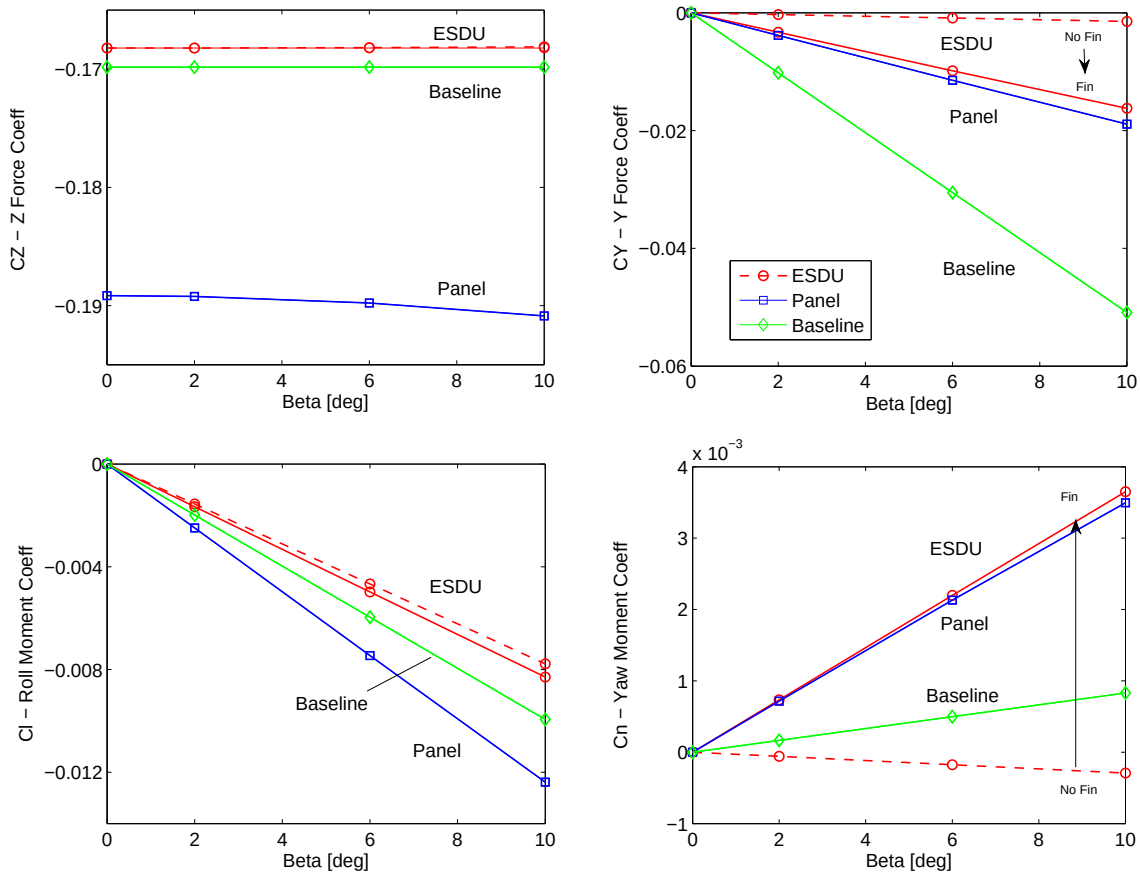

Figure 5.27: Variation in aerodynamic coefficients with sideslip (β)

Side force with sideslip - ($C_{Y\beta}$) Figure 5.27 shows that the main contribution to side force comes from the winglet fins. Unlike the wing, the ESDU method considers the winglet as a single unit rather than strip elements and matches very well with panel method prediction.

Yawing moment with sideslip - ($C_{n\beta}$) The yawing moment from the baseline model is much less than what is indicated by ESDU and the panel methods, which match very well. This is counter intuitive, as in the presence of a bigger side force for the baseline model, the yawing moment must also be relatively large. One possible explanation of this effect is the de-stabilizing contribution from the fuselage section in front of the center of gravity. Due to the unconventional planform shape, this de-stabilizing fuselage contribution is difficult to predict analytically and requires a CFD solution or an experimental setup for accurate prediction. Figure 5.27 shows that the vertical fin is the main stabilizing contributor towards yawing moment.

Rolling moment with sideslip - ($C_{l\beta}$) The rolling moment prediction with side slip was much better. With the baseline prediction falling in the middle of ESDU and the panel method. Presence of vertical fin has little effect on rolling moment, as the main contribution comes from the wing dihedral and wing sweep.

5.4.4 Validation of Aero Derivatives w.r.t Body Rates (p, q, r)

A well designed aircraft should have positive damping in all three axes. The main contribution in damping for the roll axis comes from the wing itself, with the wing resisting any rate of roll ($C_{lp} < 0$). In Figure 5.28, the ESDU prediction matches quite well with the baseline, the panel method however predicts slightly lower values of roll rate damping. The damping in the yaw axis due to yaw rate, C_{n_r}, also shows a good match, with the ESDU method now being on the lower side.

For a conventional aircraft the pitch damping derivative, C_{m_q} is mainly determined by the distance of the horizontal tail from the center of gravity (CG) and the size of the tail itself, while contributions from the wing are usually neglected. For the BWB aircraft however there is no tail and pitch damping comes the wing alone. In the presence of pitch rate, the wing sees an asymmetrical flow distribution, with the leading edge and trailing edge seeing opposite components of vertical velocity, w, due to rate of rotation about the CG. Figure 5.28 shows a good match between ESDU and panel methods however the baseline prediction is much lower. Since the baseline prediction is based on CFD methods it is considered to be more accurate.

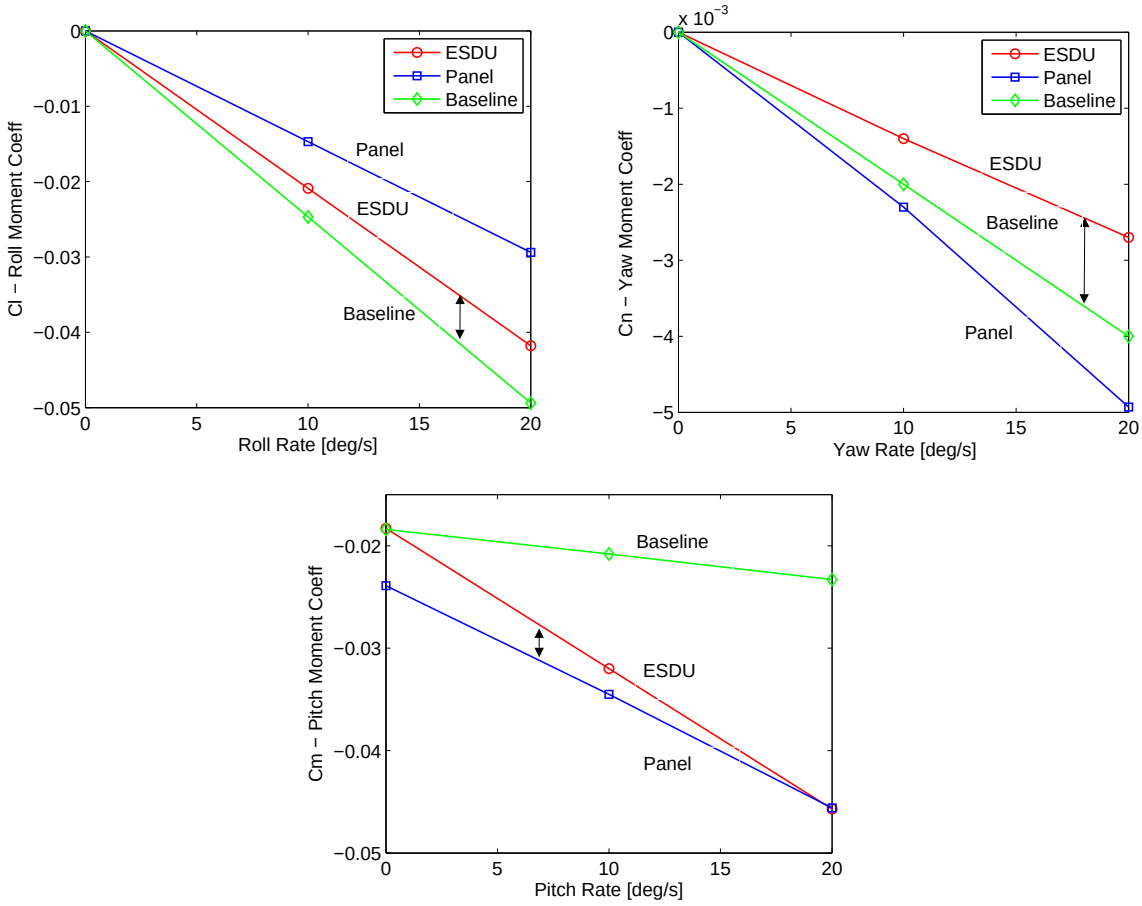

Figure 5.28: Variation in aerodynamic coefficients with body rates (p, q, r)

5.4.5 Validation of Control Derivatives

This section reviews the effect of flap deflection on normal force coefficient, $C_{Z_{\delta_f}}$ and pitching moment, $C_{m_{\delta_f}}$, in case the flap is being used for pitch control and on rolling moment, $C_{l_{\delta_f}}$, in case it is being used as aileron.

Flap 1 - Mid Body Section - (δ_{f1})

Figure 5.29 shows the location and extent of Flap 1. It is being used for pitch control and strongly affects the normal force and pitching moment of the aircraft. The spanwise lift coefficient distribution from the ESDU model is also shown for 0 and $\pm 5°$ of flap deflection. The change in normal force and pitching moment match very well for the baseline and the ESDU model. The panel method results are not shown as it was not possible to define a flap of fixed chord length in the TORNADO [13] program for the centre-body. The flap effectiveness starts to reduce with increasing flap deflections in the ESDU model, therefore a slight curvature can be seen in ESDU results. No such effect was present in the baseline model.

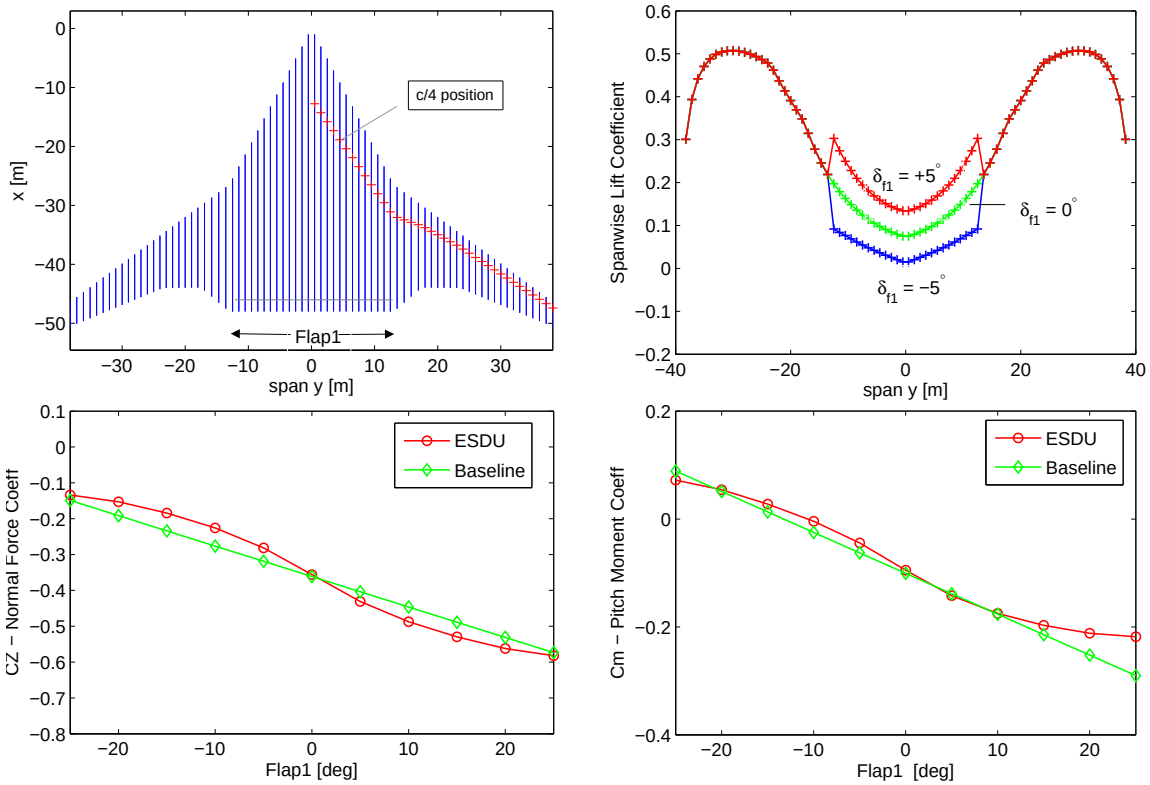

Figure 5.29: Normal force (C_Z) and pitch moment (C_m) variation with δ_{f1}

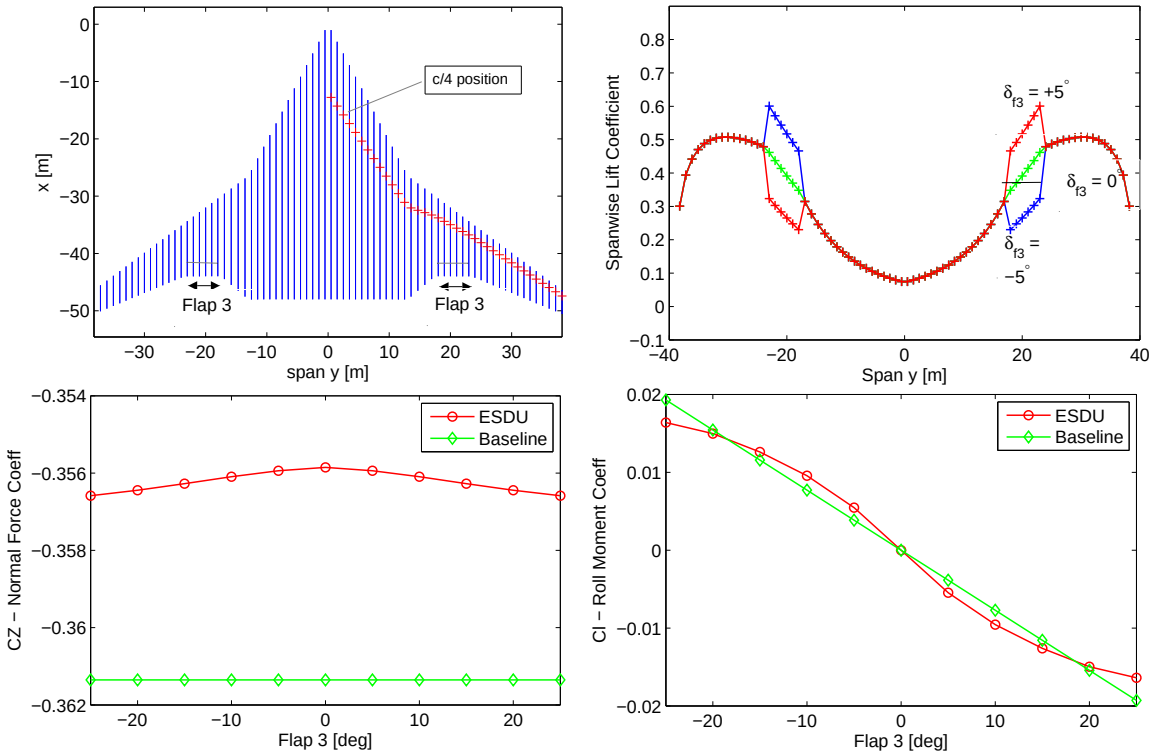

Figure 5.30: Normal force (C_Z) and roll moment (C_l) variation with δ_{f3}

Flap 3 - Inner Wing Section - (δ_{f3})

Figure 5.30 shows the location of Flap 3 which was used as an inboard aileron. It spans from 13.5 to 17.5 m on the starboard and and port wings and consists of a super critical airfoil section. The lift distribution profile, the normal force coefficient and the rolling moment produced by these inboard flaps is shown. The normal force coefficient or lift shows little or no effect of differential deflection of this flap. The rolling moment correlation between the ESDU and baseline models was found to be very good.

Besides the derivatives discussed above, there were other control derivative terms for the remaining flaps and some cross derivatives. Limited space restricts the discussion of all of these. The purpose of this section was to establish the validity of the ESDU model with reference to the baseline. It now remains to discuss the effects of trailing edge blowing in the ESDU model using the jet flap theory [14].

5.5 Effect of Blown Flaps on Aero Derivatives

This section considers the effect of flap blowing on the BWB aircraft aerodynamics. As discussed earlier, the extent of blowing is determined by a non-dimensional parameter, C_u, called the blowing momentum coefficient. It is defined as,

$$C_u = \frac{\dot{m} V_{jet}}{\bar{q} S} \tag{5.32}$$

where $\dot{m}$ is the jet mass flow rate, V_{jet} the jet velocity, $\bar{q}$ the free stream dynamic pressure and S is the reference area. Thus at a lower dynamic pressures or low airspeeds, higher C_u values are possible for the same values of mass flow rate and jet velocity. This section reviews the effect of C_u on, (i) the spanwise lift distribution and pitching moment, (ii) the change in net lift and pitching moment coefficients with flap blowing and flap deflection and (iii) the relative effectiveness of individual flaps in terms of lift generation and pitching moment per unit span.

5.5.1 Effect on Spanwise Lift and Pitch moment

Figure 5.31 shows the spanwise variation in lift distribution and pitching moment at an angle of attack of 4° and a nominal CG position corresponding to a static margin of $K_n = 15\%$. The effect of blowing on trailing edge flaps is to increase the lift curve

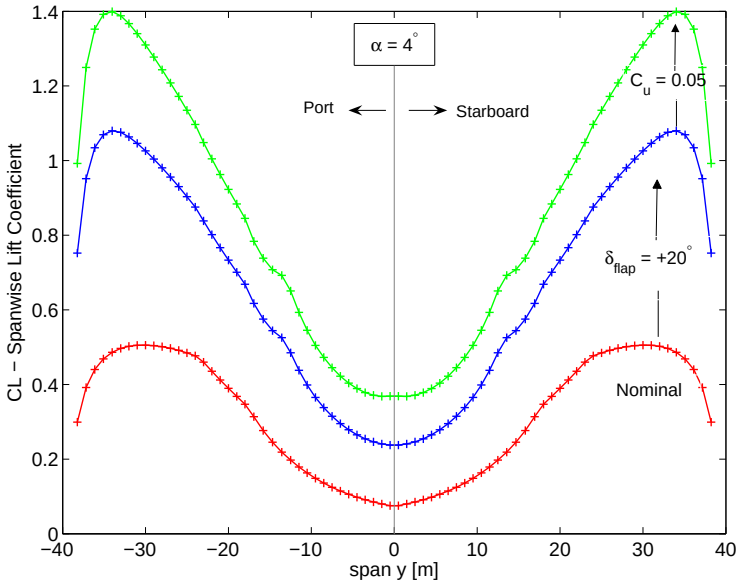

Figure 5.31: Spanwise C_L with blown flaps ($C_u = 0.05$, $\delta_f = +20°$)

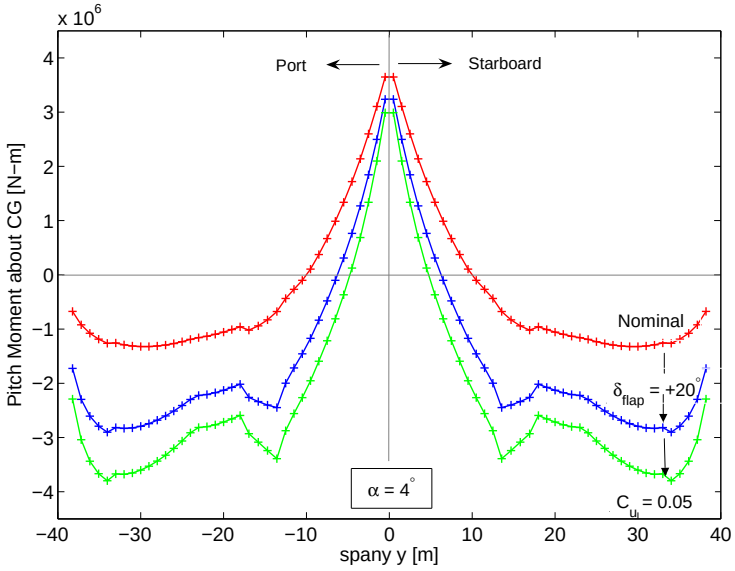

Figure 5.32: Spanwise C_M with blown flaps ($C_u = 0.05$, $\delta_f = +20°$)

slope and flap effectiveness in lift generation when deflected. In Figure 5.31, the lift generated is increased significantly with all flaps blown at $C_u = 0.05$, however the downside is the corresponding large increase in negative pitch moment with flap blowing. This is indicated by shifting of the pitch moment curve on the negative side in Figure 5.32.

On a conventional aircraft the tail plane is usually much more powerful and can provide the necessary positive pitching moment to trim the aircraft. On the BWB aircraft however, if blown flaps are to be used for high lift, this negative pitching

moment has to be overcome by some alternate arrangement. For example on the Hunting 126 aircraft [33], this negative pitching moment associated with blown flaps was overcome by directing some of the thrust in the vertical direction, ahead of the center of gravity.

5.5.2 Lift and Pitch moment (C_L, C_m) with Flap Blowing

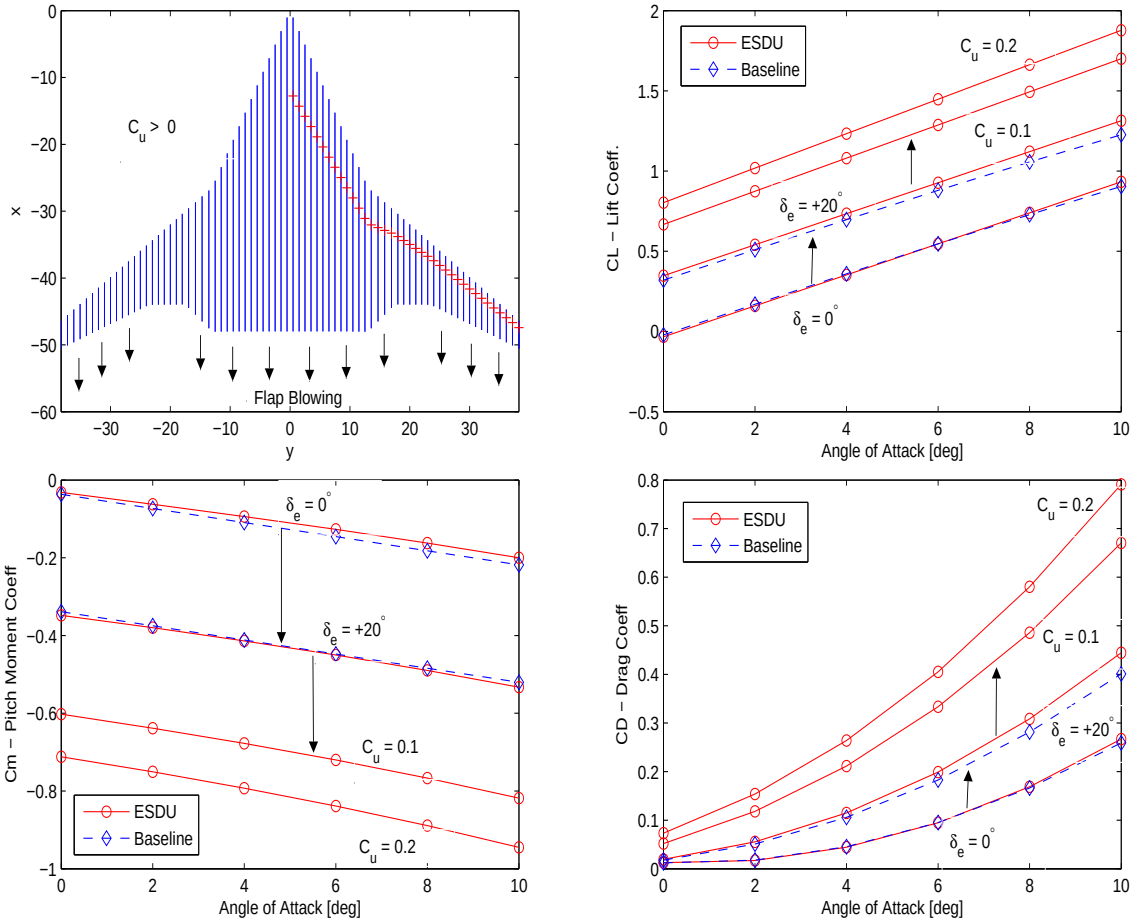

Figure 5.33: Effect of flap blowing (Flaps 1,2,4 and 5) on pitch axis

For the BWB aircraft, the controls have been allocated so that Flap 3 which is at a spanwise location from 17.5 to 23.5 m is used as an inboard or high speed aileron. The remaining flaps on the mid-body section and outer wing are used as elevators.

Figure 5.33 shows the net lift coefficient, C_L, and pitching moment coefficient, C_m, at C_u values of 0.1 and 0.2 respectively. A constant flap deflection of $+20°$ is assumed on all flaps except Flap 3 which is being used as an aileron. Two points can be noted from Figure 5.33, (i) the change in lift with increasing C_u values is not constant and (ii) the negative increment in pitching moment is significant. Also

shown for the unblown flap case, the results of the baseline model [7], to reflect upon the accuracy of the strip element ESDU model.

Shown in Figure 5.34 is a map of change in net lift coefficient and pitch moment with flap blowing and deflection. ΔC_L of greater than 1.0 can be easily achieved at a flap deflection of $+20°$ and C_u values of close to unity. The corresponding increase in negative pitch moment is also shown.

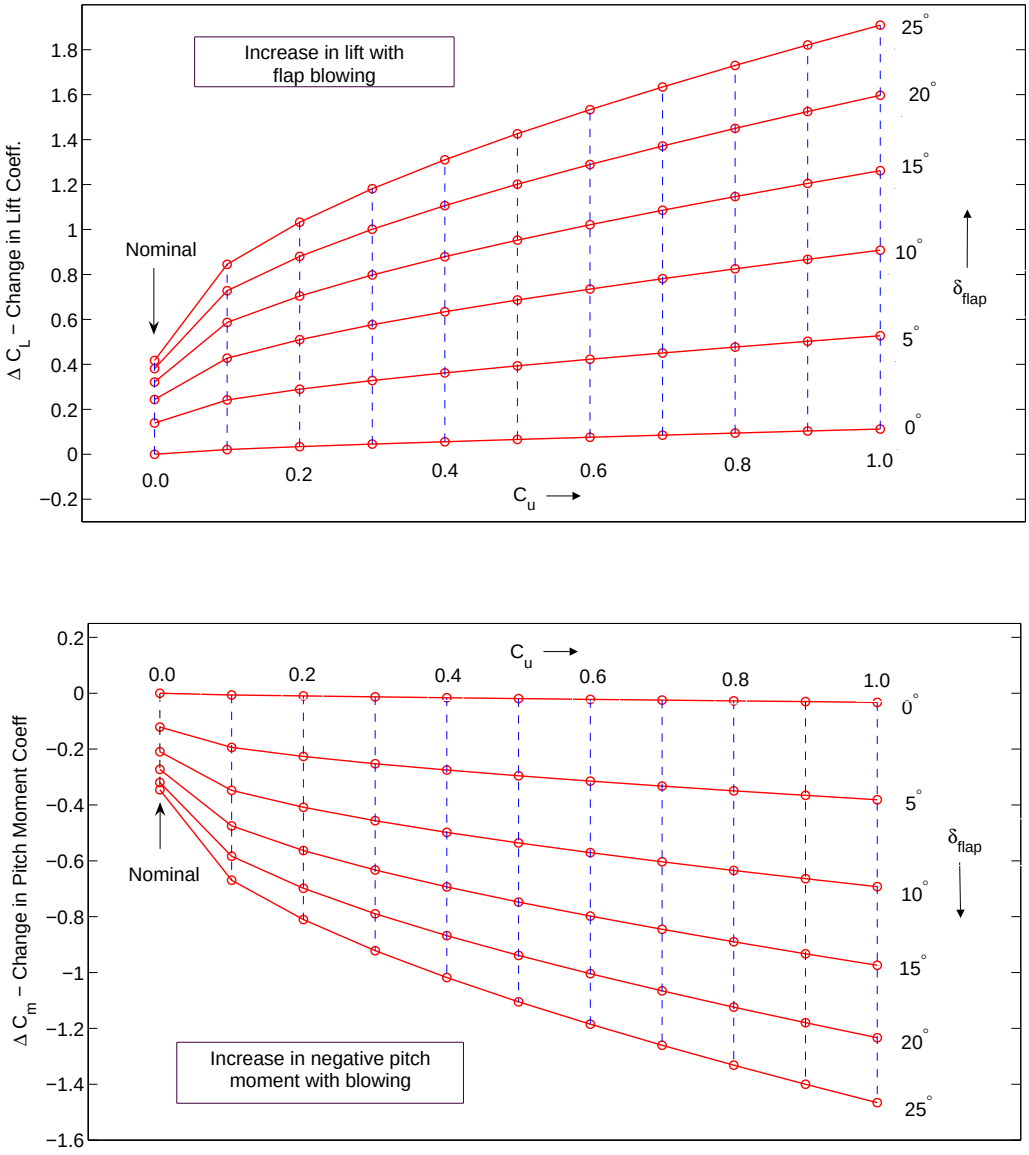

Figure 5.34: Change in lift and pitching moment with blown flaps

5.5.3 Increase in Roll moment (C_l) with Flap Blowing

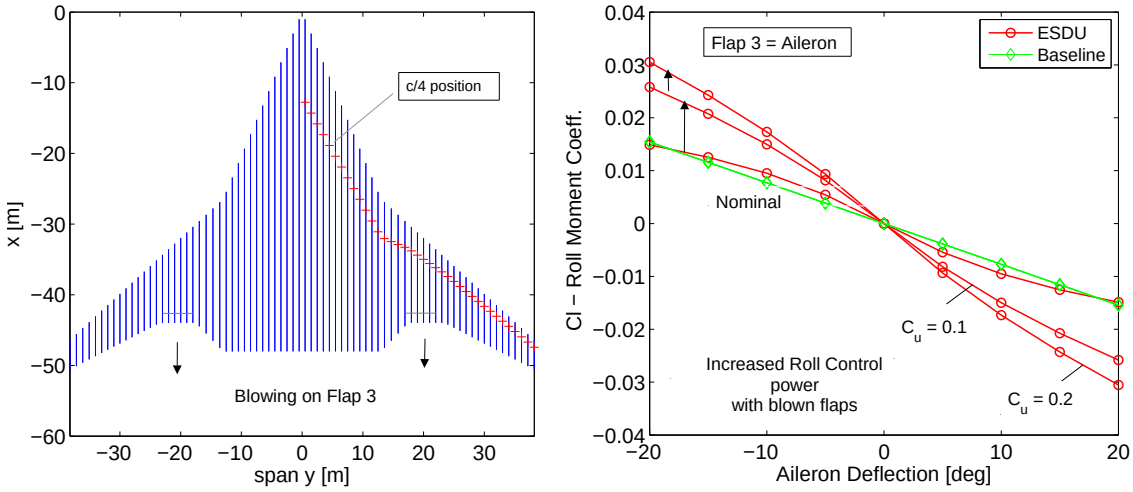

Figure 5.35: Effect of blowing on Flap 3 (roll axis)

Figure 5.35 shows the increase in roll control power with blown flaps. The roll power almost doubles for a blowing momentum coefficient of $C_u = 0.2$. This will later be shown to be of great advantage as the handling qualities analysis in Chapter 3, showed that the inboard aileron alone is inadequate to achieve the required roll rates at landing and take-off speeds. If the outboard wing flaps are allocated for roll control to increase the roll power during such conditions, the pitch axis control power gets reduced significantly. Blown flaps at lower airspeeds may be the answer to this roll control power/allocation problem.

5.5.4 Increase in Yawing moment (C_n) with Flap Blowing

Figure 5.36 shows how the rudder effectiveness is almost doubled at a blowing coefficient of $C_u = 0.2$. Correlation with the nominal or the baseline is shown. As mentioned earlier in Chapter 3, that under cross winds or asymmetric thrust conditions, the nominal rudder control power proves to be insufficient. Rudder control power has to be increased by some means to trim the aircraft in the directional axis. Other options to enhance rudder power are to, (i) increase the vertical fin area by incorporating conventional vertical fins on the centre-body, which in turn means increased profile drag and weight or, (ii) to use Flap 4 or 5 on the outboard wings as split flap drag rudders but this again results in a loss of control power for the pitch axis. Blown flaps seems to be an attractive option to solve this problem.

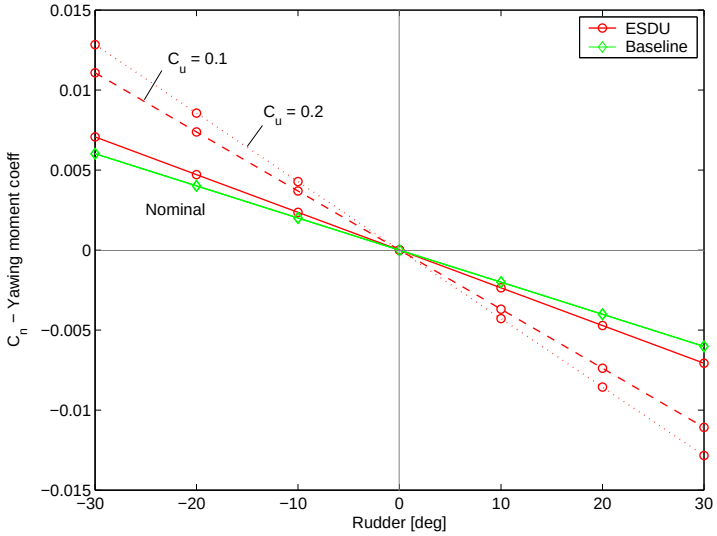

Figure 5.36: Effect of blowing on rudder (yaw axis)

5.5.5 Relative Flap Effectiveness

Lastly, a brief analysis was carried out to investigate which flap is the best candidate for blowing, so that it contributes the maximum change in lift with a minimum change in pitching moment coefficient. The parameter of interest was $(\Delta C_L/\Delta C_m)$. Figure 5.37 shows the results. It turns out that Flap 1 which has the maximum extent of ± 13 m and is located on the centre-body produces the maximum change in lift coefficient, however the corresponding change in pitching moment is also higher. The graph on the right gives the same results per unit span and reveals that Flap No. 2 and 3 are the best candidates for achieving maximum $(\Delta C_L/\Delta C_m)$ per unit span in a blown flap arrangement. These two sections generate the minimum pitching moment as they are close to the center of gravity of the aircraft.

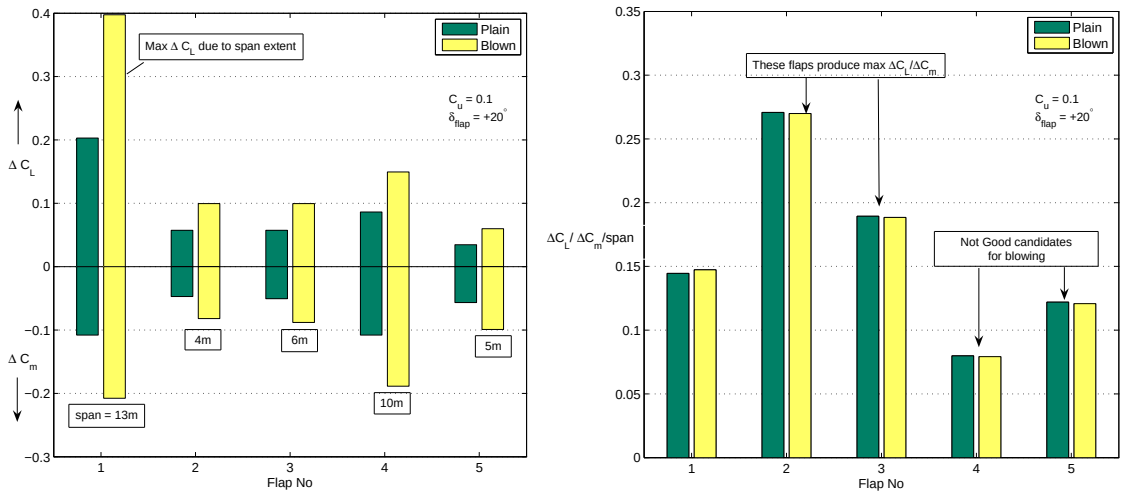

Figure 5.37: Evaluation of flap effectiveness $(\Delta C_L/\Delta C_m)$

5.6 Chapter - Summary

A BWB aerodynamic model using strip element techniques and Engineering Sciences Data Units (ESDUs) was developed. The effect of trailing edge blowing and the corresponding increase in lift coefficient was incorporated in the model. The following points may be observed,

- For the longitudinal axis, flap blowing causes a significant increase in lift coefficient along with a corresponding increase in negative pitching moment. For a high lift configuration, usually required at take-off or landing, this negative pitching moment has to be overcome before the full potential of flap blowing can be realized.
- Although for the BWB, a high lift configuration may be difficult to achieve due to the negative pitching moment, the flap effectiveness with blowing shows a major improvement. More effective flaps i-e a high $\Delta C_L/\delta_f$ value, means reduced trim elevator deflections or greater control authority. Having short moment arms both for the pitch and yaw axes, flap blowing seems to be an attractive option to achieve greater control effectiveness without increasing the physical flap size or reducing the static margin.
- For the lateral-directional axis, the control power was doubled at a blowing momentum coefficient of $C_u = 0.2$ for the both the inboard aileron and the winglet rudder. This proved to be of significant value as revealed later by the lateral (roll) axis handling qualities analysis and trimming in directional (yaw) axis with small winglet rudders under asymmetric thrust/cross wind conditions.

Chapter 6

Propulsion and Controls Integration

In the preceding chapters, a BWB model with blown flaps and a three spool turbofan engine model were developed. In this chapter some results of the integration of these two models are presented. The following aspects will be covered,

- **Allowable bleed and achievable lift/pitch moment**

  The questions to be answered here are, (i) what is the most appropriate location for bleed off-take, LPC, IPC, HPC or directly from the main exhaust, (ii) what are the optimum bleed slot heights, (iii) how much bleed can be taken from a particular arrangement and how much blowing coefficient (C_u) can be achieved and (iv) what are the increments in lift and pitching moment.

- **Controls performance with blowing**

  A particular value of blowing momentum coefficient would be assumed and dynamic responses in roll, pitch and yaw axis would be presented. Results would indicate handling qualities improvements if any.

- **Controls performance with thrust vectoring**

  A comparison of longitudinal control responses for pure aerodynamic flight control (AFC), thrust vector control (TVC), and AFC + TVC would be made.

- **Trim results with flap blowing and thrust vectoring**

  Trim results with flap blowing and TVC would be presented at different airspeeds.

6.1 Engine Bleed and Lift/Pitching Moment

As pointed out earlier, for a blown flap arrangement, the lift and pitching moment characteristics can be modified by adjusting the blowing momentum coefficient (C_u). This section explores that how much C_u can be achieved for the BWB by either bleeding the engine or using the main exhaust directly, as for an embedded wing/distributed propulsion concept [42]. It is possible to get this bleed from the low pressure (LP), the intermediate pressure (IP) or the high pressure (HP) compressor stages depending upon the wing duct pressure requirements. However for the three spool turbofan considered, 20% of the HP compressor mass flow is already used for HP turbine cooling and the wing nozzle pressure requirements for flap blowing purposes are usually less, it was therefore decided not to bleed the HP stage further. This discussion will therefore consider only the intermediate (IPC) and the low pressure compressor (LPC) stages for flap blowing.

6.1.1 Internally Blown Flaps (IBF) - Using IPC Bleed

Figure 6.1 shows bleed off-take from the intermediate pressure compressor (IPC). Since internal wing ducts are used, this is a case of internally blown flaps. In such an arrangement, a number of parameters would effect the achievable blowing coefficient (C_u), these include, (i) the slot height that sets the actual wing nozzle exit area, (ii) the bleed off-take location, which sets the total pressure and temperature [P,T] of the source reservoir in combination with the throttle setting and (iii) airspeed. IPC bleed will therefore be considered in context of these parameter variations.

6.1.1.1 Internally Blown Flaps - Effect of IPC Bleed Slot Height

Variation in flap slot height directly controls the wing nozzle exit area and hence the mass flow or bleed from a given compressor stage. To see the effect of slot height on strip-wise blowing momentum coefficient, $[C_u]_y$, consider

$$[C_u]_y = \frac{\dot{m}_{jet} V_{jet}}{\bar{q} S_y} \tag{6.1}$$

where $\dot{m}_{jet}$ is the exiting mass flow for each strip, V_{jet} is the jet velocity, $\bar{q}$ is the free stream dynamic pressure and S_y is the local strip area. Substituting for ($\dot{m}_{jet} = \rho_{jet} A_{jet} V_{jet}$), ($A_{jet} = wh$) and ($S_y = wc_y$), where w is the strip or slot width and h is the slot height we have,

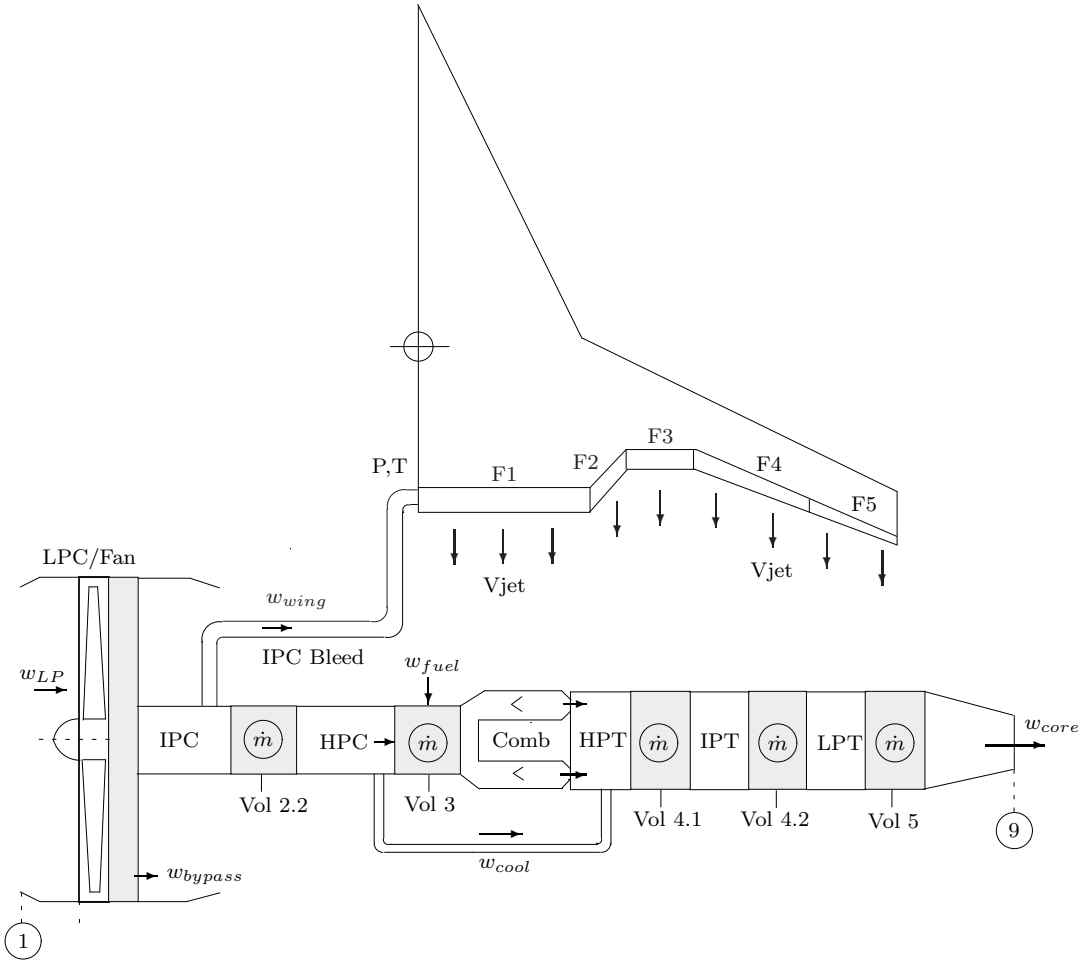

Figure 6.1: BWB aircraft with IPC bleed for internally blown flaps

$$[C_u]_y = \frac{\rho_{jet} A_{jet} {V_{jet}}^2}{\bar{q} S_y} = \frac{\rho_{jet} w h {V_{jet}}^2}{\bar{q} w c_y} = \frac{\rho_{jet} h {V_{jet}}^2}{\bar{q} c_y} \tag{6.2}$$

Thus for a constant slot height, h, the spanwise blowing momentum coefficient will vary with local chord, c_y. In order to achieve the same blowing momentum coefficient along the span the slot height has to be made variable so that (h/c_y) is a constant or the local jet velocity has to be adjusted. However for the current work, a constant slot height is assumed and the blowing momentum coefficient is allowed to vary along the span.

The following analysis presents results for IPC bleed slot height variation at a flight speed of 200 kts and an altitude of 1000 ft. The purpose being to quantize the effect of bleed slot height variation on various engine parameters such as rotor speeds, station temperatures, compressor delivery pressures etc. and the resulting increments in lift and pitching moment coefficients. The angle of attack and flap deflections were fixed at +8.0 and -10.0 degrees respectively, typical of a low speed approach

flight condition. Flap number 3 which spans from 13.0 to 17.5 m is used as the inboard aileron and operates at zero flap deflection ($\delta_a = 0°$). It is assumed that bleed is extracted from the end of the intermediate pressure compressor (IPC), thus wing nozzle entry pressure and temperature [P,T] are relatively high. Full span flap blowing is considered and 4 × 275 kN Trent 500 engine configuration is used.

Figure 6.2 shows the actual value of bleed flow (kg/s) and the corresponding jet velocity. At 3 mm slot height, IPC bleed corresponds to approximately 45 kg/s which equals 40% of the net IPC mass flow.

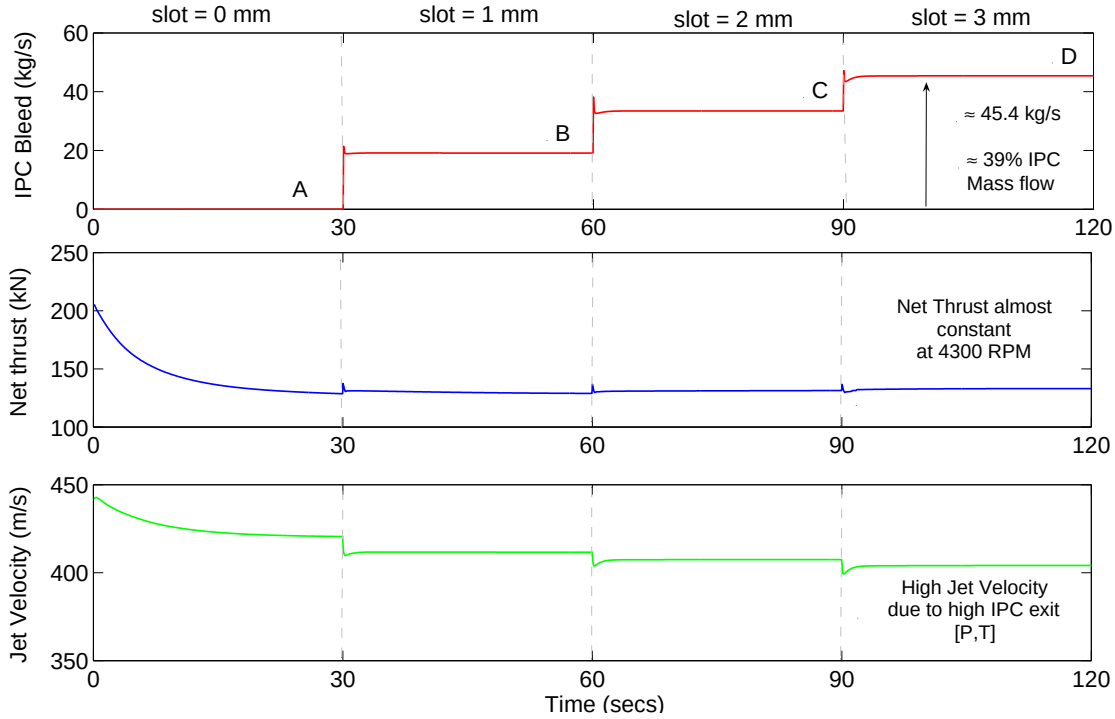

Figure 6.2: Effect of bleed slot height on jet velocity, thrust and mass flow

Rotor Speeds and IPC Bleed Slot Height - Figure 6.3 shows the speeds of the three rotors as the bleed slot height is increased from 0 to 3 mm. Initially, the three spool engine was allowed to reach a steady state at 4300 RPM under the control of the Fan/LPC RPM control loop. This corresponded to a normalized speed of 0.86, against a design speed of 1.0 at 5000 RPM. As the bleed is extracted from the engine by adjusting the slot height (h), the fan speed was kept constant at 4300 RPM, to simulate a fixed throttle setting. The engine was allowed to reach a steady state before adjusting the slot height at 30 second intervals. The RPM control loop holds the low speed rotor speed constant whereas the intermediate and the high speed rotors settle at higher speeds as more and more bleed is extracted from the engine.

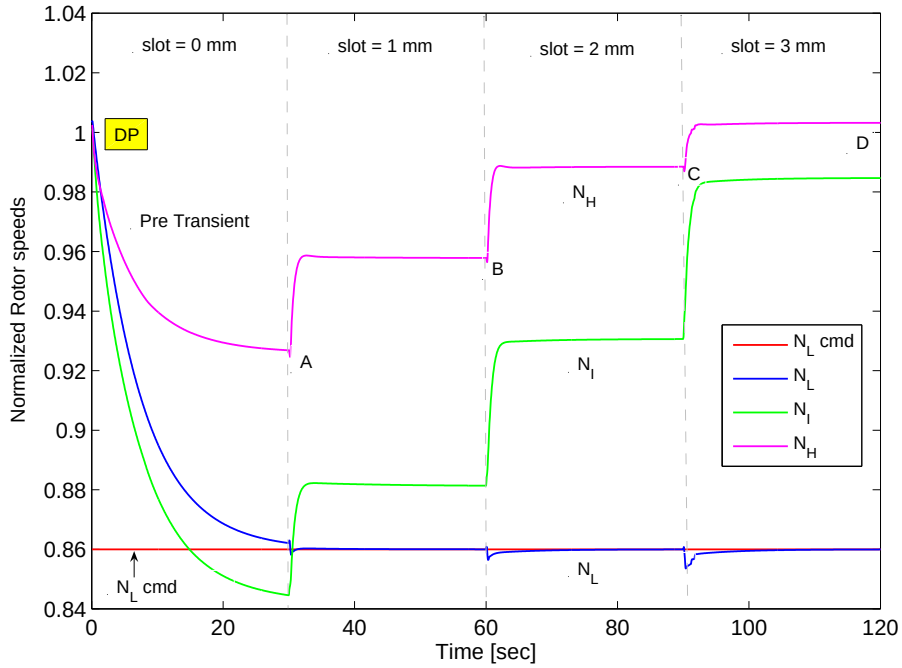

Figure 6.3: Effect of bleed slot height on rotor speeds

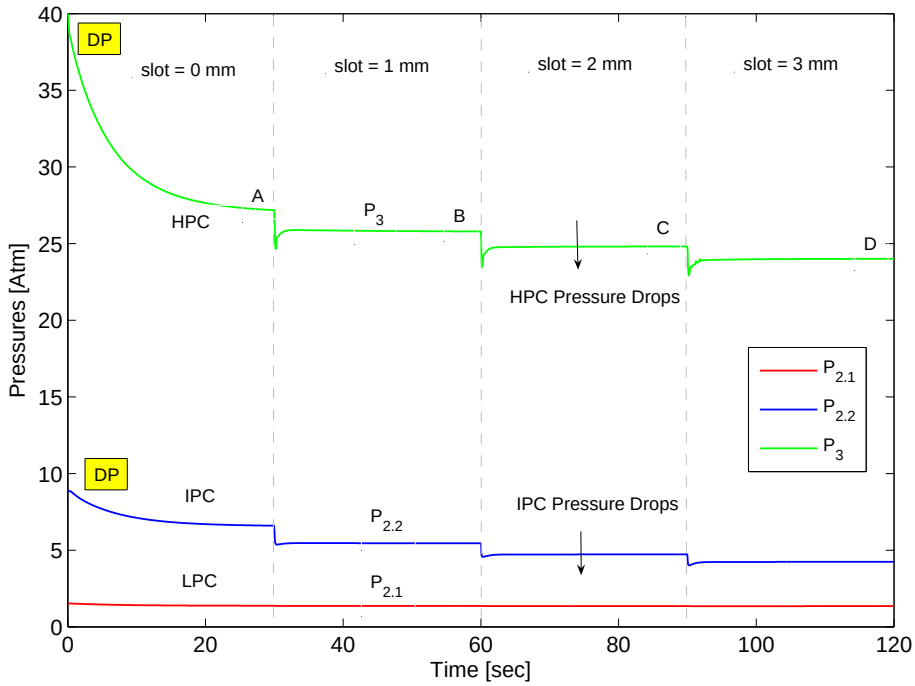

Figure 6.4: Effect of bleed slot height on compressor delivery pressures

Compressor Delivery Pressures and IPC Bleed Slot Height - In Figure 6.4 as the Fan/LPC speed is kept constant, therefore the Fan exit pressure, $P_{2.1}$, is almost constant. However the IPC and HPC delivery pressures start to fall as the engine settles to its new equilibrium state with increasing IPC bleed. Thus both the IP/HP stages deliver less pressure whereas their corresponding rotor speeds are

increasing. This is counter intuitive as the compressor delivery pressure normally rises with RPM, however the unaccounted bleed off-take from IPC exit disrupts the thermodynamic balance/matching across engine components and causes the compressors to shift away from their nominal steady state running lines.

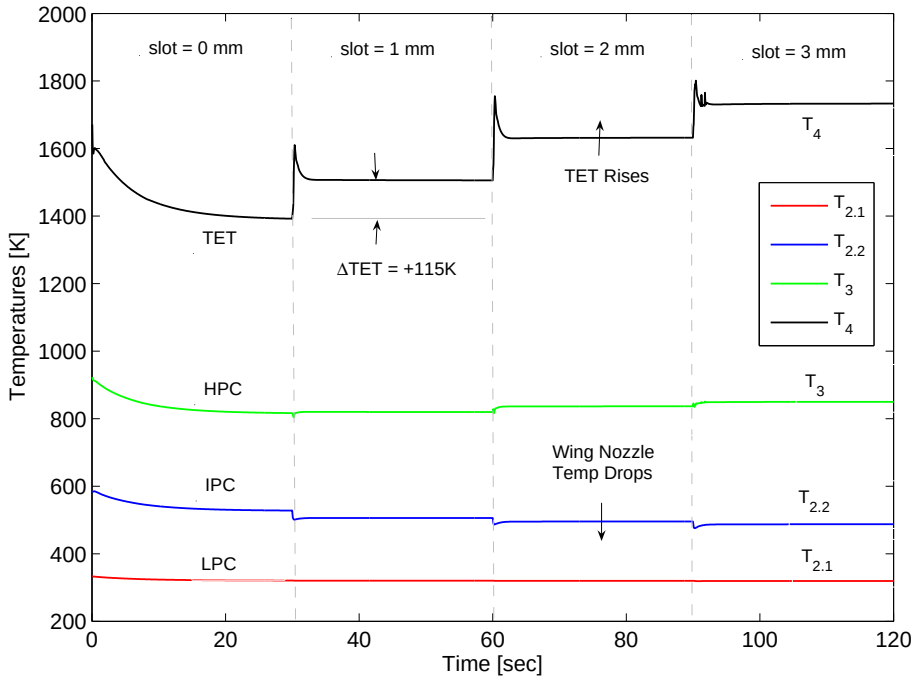

Figure 6.5: Effect of bleed slot height on station temperatures

Station Temperatures and IPC Bleed Slot Height - Figure 6.5 shows the significant rise in turbine entry temperature (TET) as the slot height is increased from 0 to 3 mm. As more and more bleed is extracted, the TET(T_4) almost hits an upper limit of 1800K at a reasonably lower throttle setting of 4300 RPM. Pilidis [77] explains that upon bleed extraction the downstream turbines have to operate with a lower mass flow and if the speed is kept constant, the turbine has to produce the same work required by the compressor. This results in a higher turbine entry temperature (T_4) and therefore higher exhaust gas temperature. The turbine is designed to operate choked even at relatively reduced mass flows, therefore the non-dimensional mass flow ($w_t\sqrt{T}_4/P_4$) through the turbine is constant. To keep the non-dimensional mass flow constant, the turbine entry pressure (P_4) will drop. This implies that compressor pressure ratio will fall. The steady state running line will shift toward choke with a corresponding reduction in compressor efficiency. Pilidis [77] further suggests that when the non-dimensional bleed (ϕ) is small, the

decrease in compressor pressure ratio due to bleed extraction is approximated as

$$\left(\frac{P_2}{P_1}\right)_{bleed} \approx \left(\frac{P_2}{P_1}\right)_{nobleed} \sqrt{1-\phi} \tag{6.3}$$

where subscripts 1,2 represent compressor entry and exit conditions. The corresponding increase in turbine entry temperature (T_4) is

$$(T_4)_{bleed} \approx (T_4)_{nobleed} \frac{1}{(1-\phi)} \tag{6.4}$$

Compressor Transients and IPC Bleed Slot Height - Figures 6.6 through 6.8 show the transients on the LP, IP and HP compressors. Since the bleed is extracted from the IP stage and the Fan or the LPC stage is still made to run at the constant RPM of 4300 under RPM control, the operating point on the fan map does not change. On the IPC stage however (Figure 6.7) the operating point moves progressively away from the steady state/equilibrium running line away from surge and in an area of reduced compressor efficiency. Points marked A,B,C,D indicate the steady state points on the map as the slot height is adjusted from 0 to 3 mm.

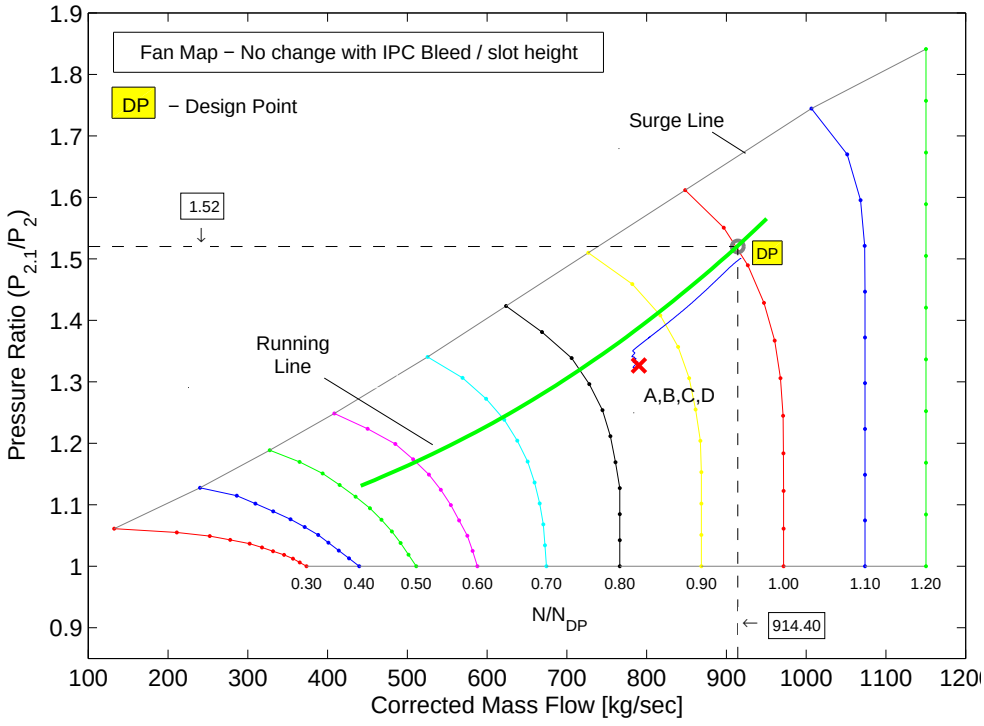

Figure 6.6: Transients on LPC map with variation in bleed slot height

Figure 6.8 shows the high pressure compressor map, which is now receiving less and less mass flow at its inlet and tends toward surge. This shift in operating line both

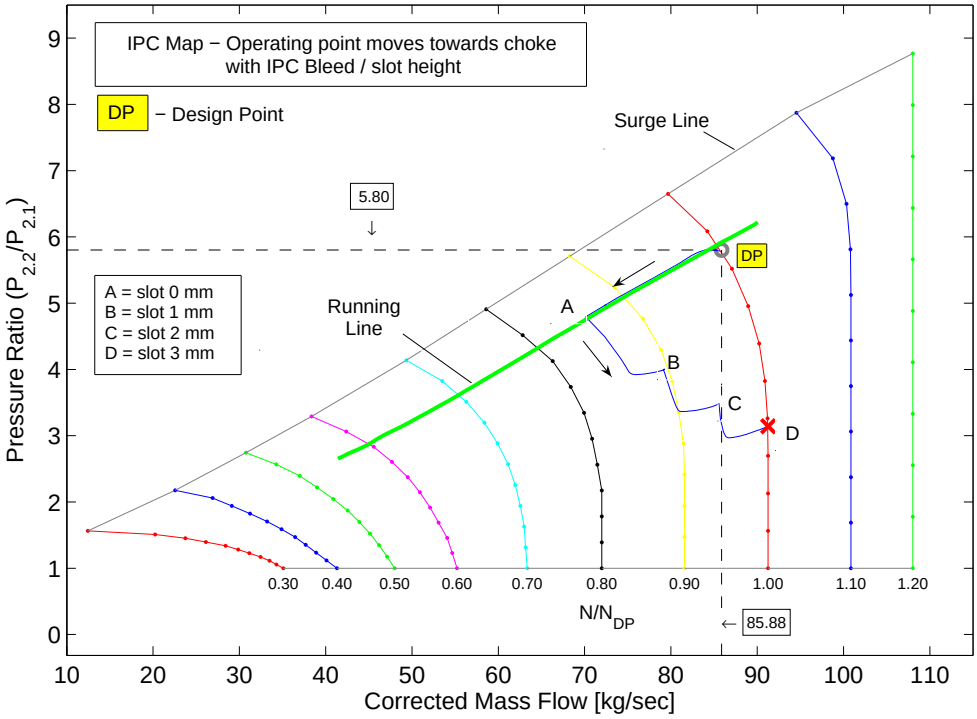

Figure 6.7: Transients on IPC map with variation in bleed slot height

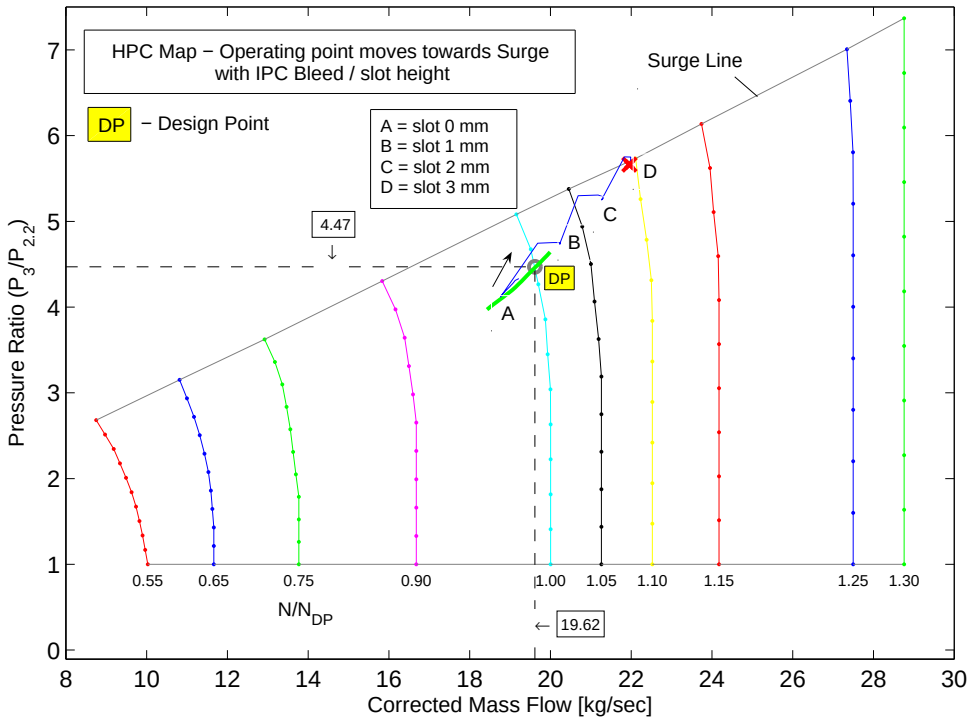

Figure 6.8: Transients on HPC map with variation in bleed slot height

for the intermediate pressure (IP) and the high pressure (HP) compressor stages is absolutely critical in determining in engine performance and its reliable operation. Optimally the running line should be as close as possible to the surge line, while

maintaining reasonable surge margin during steady state and transient operation. Any such variations in the running line or equilibrium conditions due to bleed extraction therefore has to be minimized, either through incorporation in the initial engine design or minimizing the bleed requirements.

Blowing Momentum Coefficient and IPC Bleed Slot Height - Figure 6.9 shows the achievable blowing momentum coefficients as given by Equation (6.2). When the slot height is zero ($h = 0$ mm), there is no bleed and hence zero blowing momentum coefficient (Case A). As the slot height is increased the spanwise blowing coefficient increases. On the centre-body section, by virtue of the high value of local chord the blowing coefficient is low, however as the local chord decreases along the span, the blowing coefficient increases to a certain maximum value. As per Figure 2.14 from Section 2.2, the likely values of blowing coefficient for high lift are above 0.1 and the critical value of blowing coefficient ($C_{u_{crit}}$) for potential flow lift is of the order 0.02 to 0.03. From Figure 6.9 we see that these critical values of C_u are achieved on the outboard wing sections for a slot height of 2 to 3 mm.

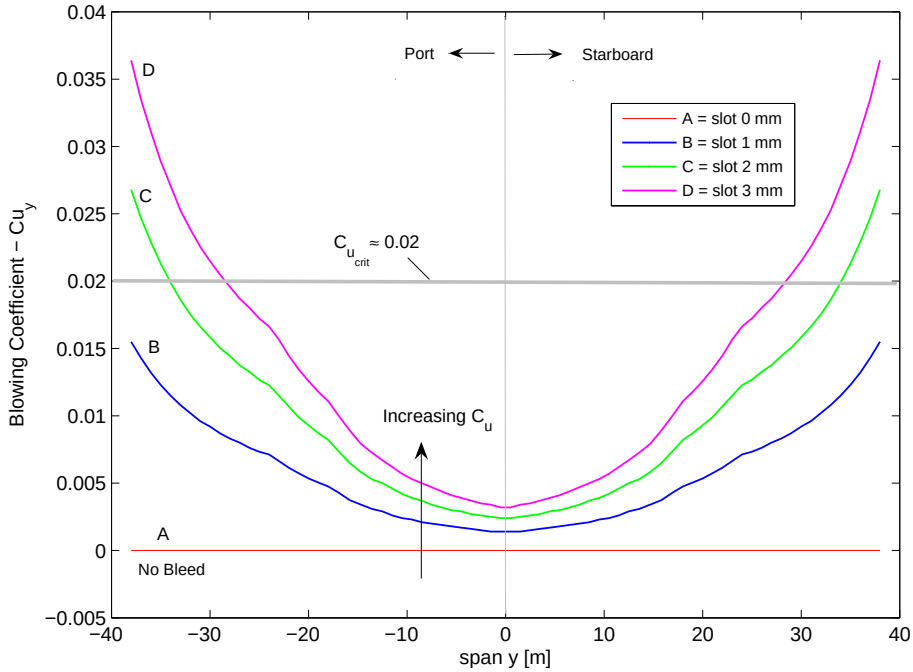

Figure 6.9: Effect of bleed slot height on spanwise blowing coefficient

For this analysis full span ($\approx$ 80m) flap blowing is assumed. If only selected flaps are blown, like the aileron or the rudder, much higher blowing coefficients can be achieved with relatively better engine performance. In addition, the Trent 500 engines were not designed for permanent IPC bleed extraction. In order to improve engine performance it is possible to re-design the engine with a built in high IPC

bleed-off capability. This aspect will be covered in detail later in this chapter.

Lift and Pitching Moment Coefficients and Slot Height - Figure 6.10 shows the spanwise lift coefficient with variation in slot height. Flap 3 which is used as an inboard aileron is undeflected ($\delta_a = 0°$) and the remaining flaps which are used elevators are deflected at a negative value ($\delta_{flap} = -10°$) to provide pitch trim. Figure 6.10 shows that the undeflected aileron section generates significantly higher lift as compared to rest of the wing section. This is indicative of a strong loss in wing lift due to negative flap deflections.

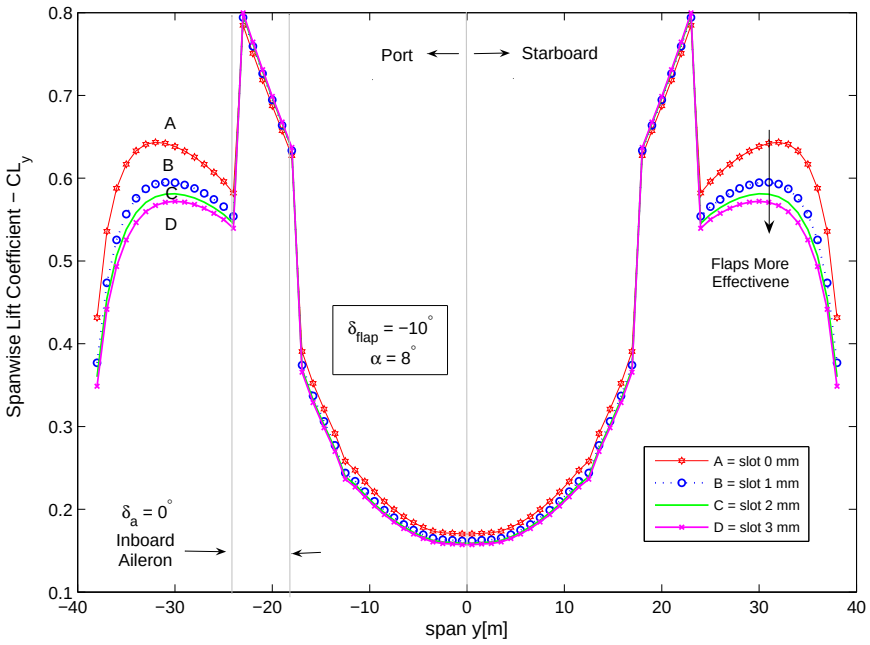

Figure 6.10: Effect of bleed slot height on spanwise lift coefficient

The effect of blowing appears as increased flap effectiveness ($\Delta C_L/\Delta_{flap}$), since the flaps are deflected negative to provide pitch trim and not high lift, the decrement in lift coefficient is higher for the blown flap case. Four cases A,B,C and D are considered for variation in slot heights from 0 to 3 mm. Due to the non-linear relationship between C_L and C_u as discussed earlier, the increase in flap effectiveness is greater from A to B (at small values of C_u) and is then almost constant from B to C and C to D (for higher values of C_u).

Figure 6.11 shows the corresponding increase in pitching moment coefficient about the local quarter chord point for each strip. As the slot height/blowing momentum increase, the pitching moment about the quarter chord point also increases. The final effect would be a net reduction in trim flap deflection with almost little or no

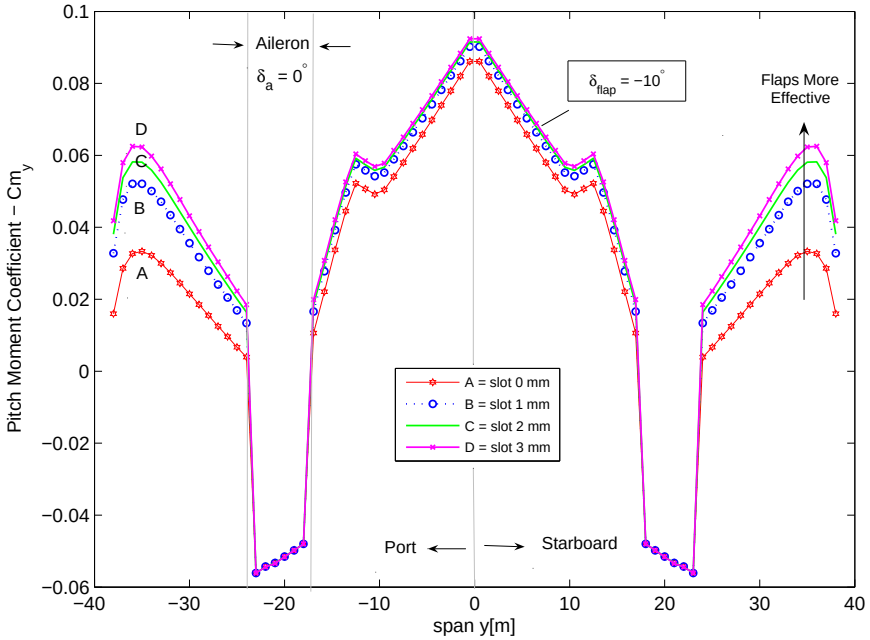

Figure 6.11: Effect of bleed slot height on spanwise pitch moment coefficient

change in angle of attack. This will be discussed in further detail later in the trim analysis section. Finally the very high negative pitching moment contribution due to undeflected aileron section may be noted. This negative pitching moment has to be catered for by the rest of the wing section at the expense of loss in net lift.

No	Slot ht	ΔTET	$P_{2.2}$	$T_{2.2}$	$\dot{m}_{jet}$	V_{jet}	C_u	$\Delta C_L/\Delta_{flap}$	$\Delta C_m/\Delta_{flap}$
	mm	K	Atm	K	kg/s	m/s	Average	Relative	Relative
1	No bleed	0	6.57	528	0	0	0.000	1.000	1.000
2	1.0	114	5.44	506	19.1	411	0.006	1.095	1.122
3	2.0	241	4.72	495	33.4	407	0.010	1.119	1.159
4	3.0	341	4.24	487	45.4	404	0.014	1.143	1.183

Table 6.1: Engine/airframe parameters and slot height variation

Table 6.1 summarizes the results obtained for bleed off-take from the end of the intermediate compressor. Increments in the lift and pitching moments are presented relative to the unblown case. With a slot height of 3 mm and full span flap blowing, the IPC bleed is 45.4 kg/s per engine. The relative flap effectiveness for pitching moment is 1.183 or an increase of 18.3%. The jet velocities are almost constant as the wing nozzle is choked due to high IPC exit pressure and temperature $[P_{2.2}, T_{2.2}]$. The rise in TET is +341K is very high, however it may be tolerated at lower throttle settings such as during approach or landing.

6.1.1.2 Internally Blown Flaps - Effect of Bleed off-take Location

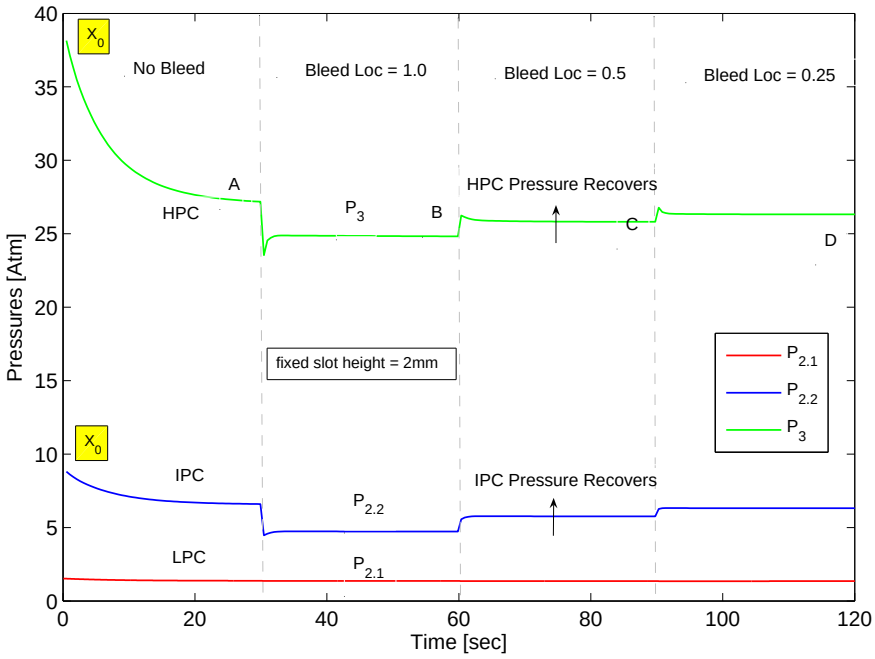

Figure 6.12: Effect of IPC bleed location on station pressures

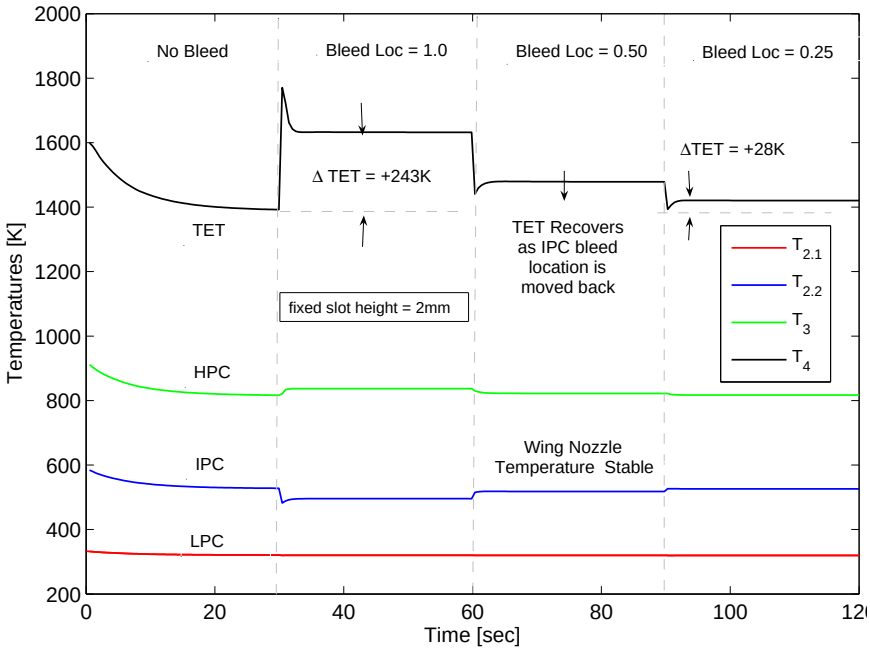

Figure 6.13: Effect of IPC bleed location on station temperatures

In this section, the effect of IPC bleed location is investigated. The bleed slot height is kept fixed at $h = 2$ mm and the bleed location, x, is varied along the compressor length, l. Specifically, the non-dimensional bleed locations of $(x/l = 0.5)$ or IPC(0.5) and IPC(0.25) are compared with IPC(1.0).

IPC Bleed Location and Pressures/Temperatures - As the bleed location is moved at an earlier location along compressor length, both the wing nozzle delivery pressure pressure and temperature [P,T] drop, correspondingly reducing the jet mass flow, $\dot{m}_{jet}$ and velocity, V_{jet}. The blowing momentum coefficient, C_u, being a function of these two parameters also decreases. Figures 6.12 and 6.13 shows the results for pressures and temperatures for shifting the IPC bleed location aft, while keeping the slot height fixed. Both the HPC and IPC pressures recover, whereas the turbine entry temperature (TET) in Figure 6.13 shows a major improvement. For an IPC bleed location variation of 1.0 to 0.25, the rise in TET reduces from +241K to just +39K, which is significant.

IPC Bleed Location and Compressor Transients - Figures 6.14 and 6.15 show the corresponding transient paths on the intermediate and high pressure compressors. Point A marks the steady state operating point for zero IPC bleed, point B corresponds to IPC($x/l = 1.0$) with 2mm slot height, C for IPC(0.5) and D for IPC(0.25). The intermediate paths between these points indicates engine transients.

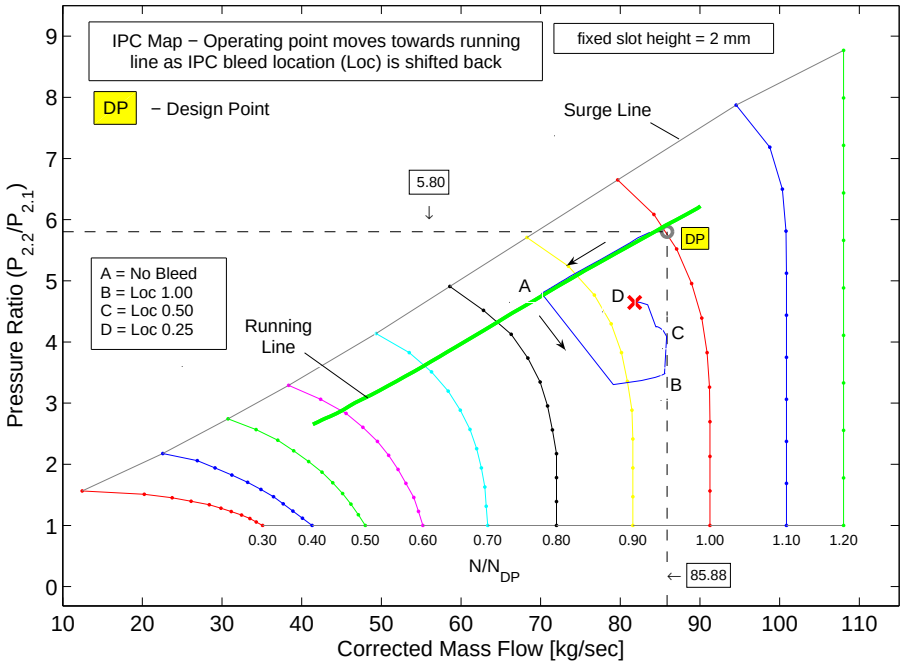

Figure 6.14: Effect of IPC bleed location on IP compressor

On the IPC map (Figure 6.14), as the bleed location is moved aft, the the engine starts to recover from point B and back towards the equilibrium running line at point D, although still away from it. The major improvement, however, appears on the HPC map (Figure 6.15) where the HP compressor shifts from an almost surged position at point B back to the steady state running line at point D.

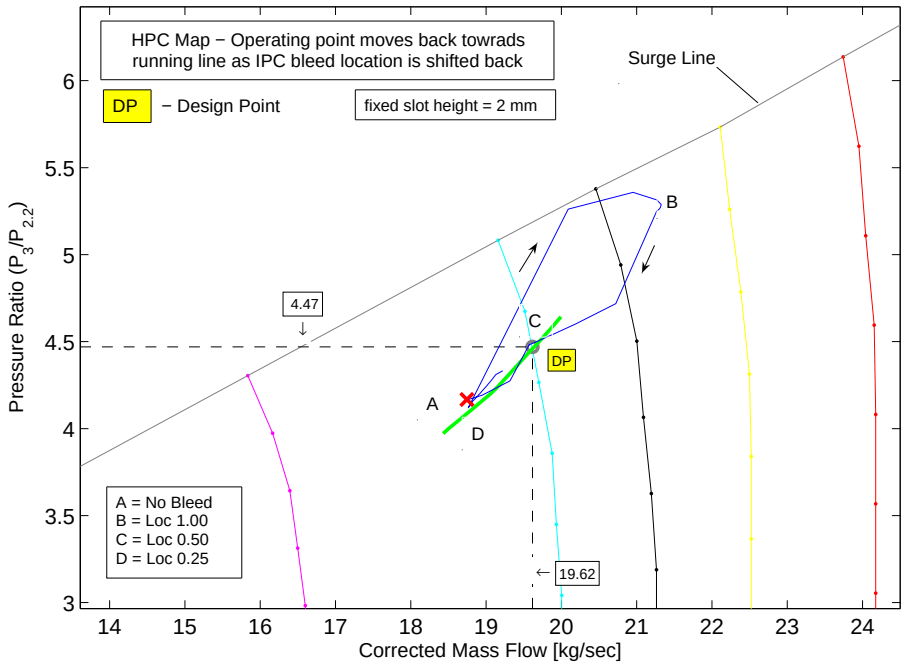

Figure 6.15: Effect of IPC bleed location on HP compressor

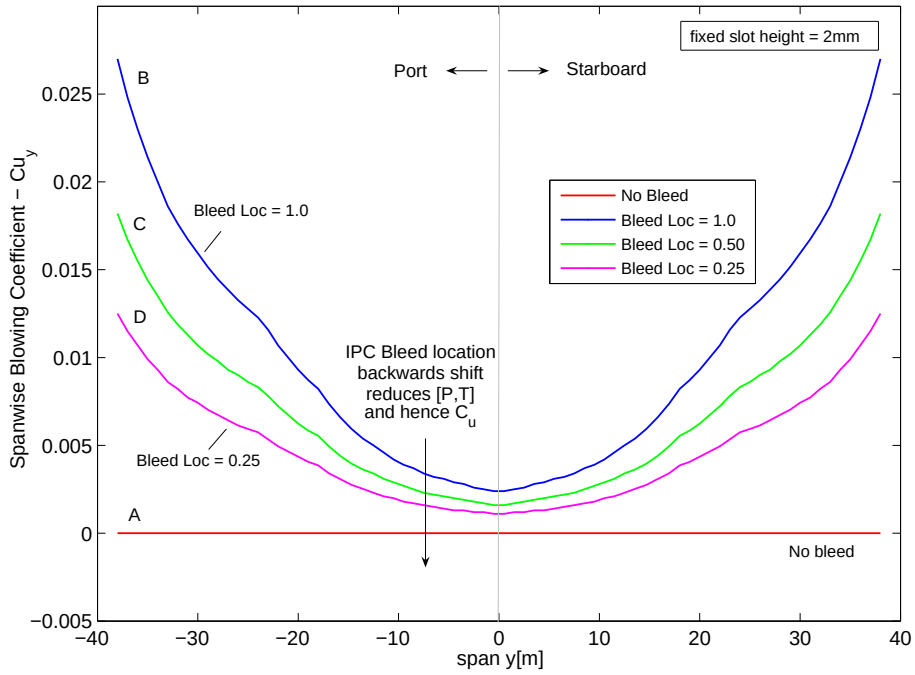

Figure 6.16: Effect of IPC bleed location on blowing momentum coefficient

IPC Bleed Location and Effect on Blowing Coefficient - Figure 6.16 shows the effect of IPC bleed location on spanwise blowing momentum coefficient. The curve marked as B represents the IPC(1.0) bleed case. Cases C and D represent IPC(0.5) and IPC(0.25) respectively. As the bleed location is moved aft and the jet mass flow reduced, the blowing momentum coefficient also decreases. For IPC(0.25)

or curve D, the bleed mass flow and jet velocity both decrease as compared to IPC(1.0) or curve B, correspondingly the blowing momentum coefficient is also reduced.

IPC Bleed Location and Lift/Pitching Moment Coefficients - Figures 6.17 and 6.18 show the spanwise lift and pitching moment coefficients. On Figure 6.17 the lift curves for a 2 mm slot height and bleed locations IPC(1.0), IPC(0.5) and IPC(0.25) are grouped quite close together and the change in lift coefficient, ΔC_L, is not in proportion to relatively larger change in blowing coefficients. This indicates that even relatively small blowing coefficients for IPC(0.25) or IPC(0.5) may also produce a significant change in flap effectiveness with lower penalties on engine performance. A similar picture can be seen for the pitching moment curve on Figure 6.18. Table 6.2 summarizes these results.

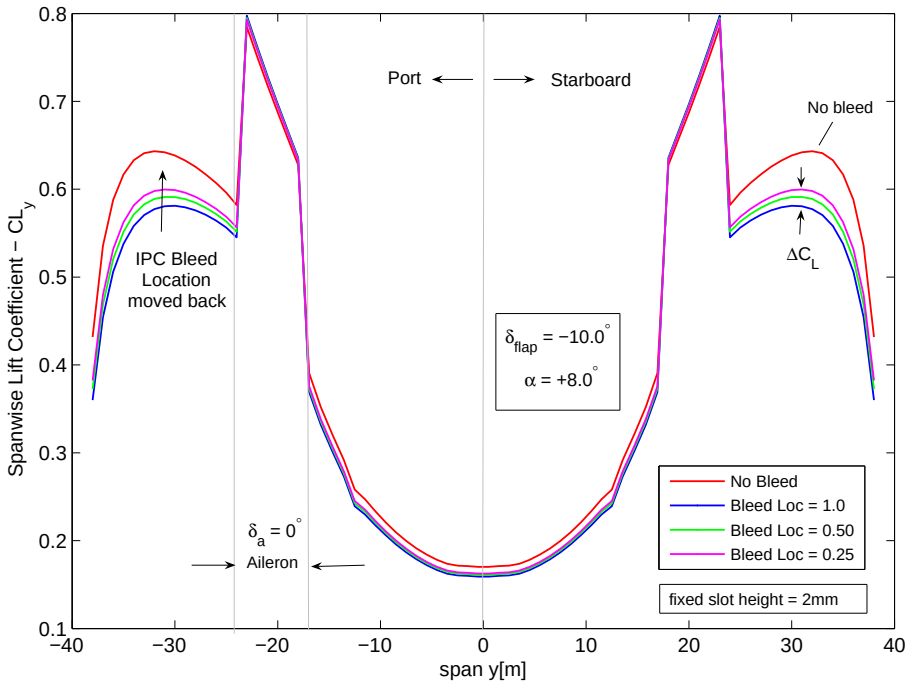

Figure 6.17: Reduction in blowing coefficient as IPC bleed location moved aft

From Table 6.2, it may be seen that with an IPC bleed location of $x/l = 0.25$, the jet mass flow reduces to 21.1 kg/s per engine and the rise in TET is just +39K. The wing nozzle pressure and temperature [P,T] are also much lower than the IPC(1.0) case. The conclusion that can be drawn here is that if the wing nozzle pressure and temperature requirements are lowered or the IPC bleed location is moved aft, the adverse effects on engine performance can be drastically reduced. For the three spool turbofan considered, IPC bleed locations from 0.25 to 0.50 are enough to sustain

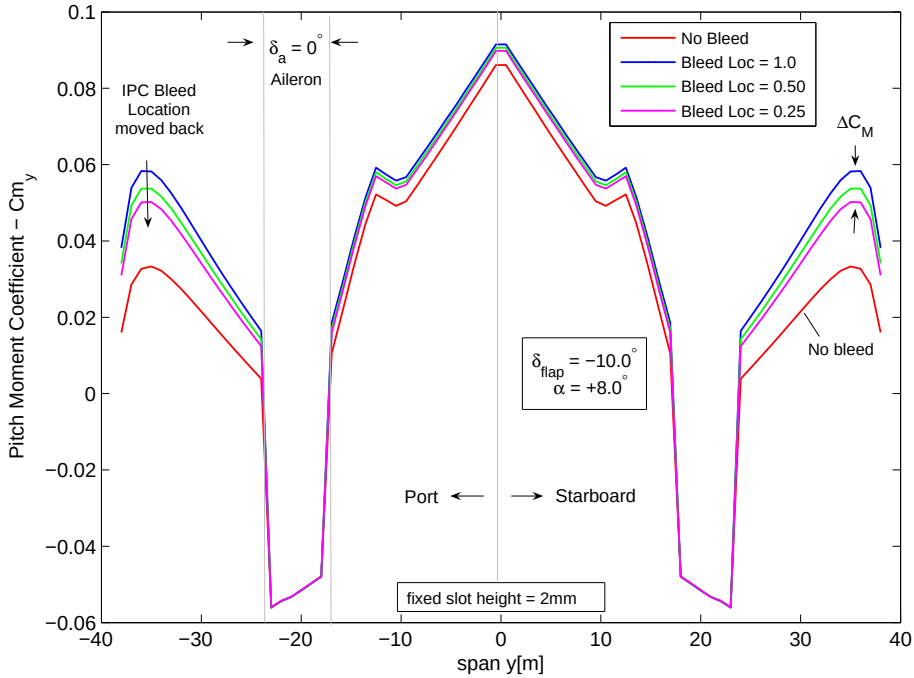

Figure 6.18: Spanwise pitching moment coefficient and IPC bleed location

No	Bleed Loc	ΔTET	$P_{2.2}$	$T_{2.2}$	$\dot{m}_{jet}$	V_{jet}	C_u	$\Delta C_L/\Delta_{flap}$	$\Delta C_m/\Delta_{flap}$
	(x/l)	K	Atm	K	kg/s	m/s	Average	Relative	Relative
1	No bleed	0	6.57	528	0	0	0.0000	1.000	1.000
2	1.00	241	4.71	495	33.4	407	0.0103	1.119	1.159
3	0.50	100	3.52	418	27.1	374	0.0078	1.107	1.135
4	0.25	39	2.58	371	21.1	352	0.0057	1.092	1.116

Table 6.2: Engine/airframe parameters and IPC bleed location at 4300 RPM

high jet velocities (374 to 352 m/s) and mass flows (27.1 to 21.1 kg/s) at 4300 Fan RPM. The average blowing coefficient is reduced from 0.0103 to 0.0057, however the relative flap effectiveness is still 11.6% higher than the unblown case.

6.1.1.3 Internally Blown Flaps - Effect of Airspeed

The reduction in dynamic pressure while keeping the jet velocity and mass flow constant, causes an increase in the spanwise blowing momentum coefficient, C_u. Table 6.3 shows the results of corresponding increase in flap effectiveness at fixed design RPM of 5000, IPC($x/l = 0.25$) and a fixed slot height of 2 mm. From Table 6.3 it can be seen that the blowing coefficient almost doubles from 200 kts to 140 kts and the flap effectiveness increases by 18.5% relative to the unblown value of 200 kts. The rise in TET of +72K is constant as the bleed conditions are unchanged. The

values of the wing duct pressure and temperature ($P_{2.2}, T_{2.2}$) are kept constant so as to simulate a fixed throttle setting and only the airspeed or the dynamic pressure is allowed to vary. For the case of a level flight at low airspeeds, the throttle setting will however be higher due to an increase in the amount of induced drag and $P_{2.2}, T_{2.2}$ will consequently rise and therefore also the blowing momentum coefficient.

No	Airspeed	ΔTET	$P_{2.2}$	$T_{2.2}$	$\dot{m}_{jet}$	V_{jet}	C_u	$\Delta C_L/\Delta_{flap}$	$\Delta C_m/\Delta_{flap}$
	(kts)	K	Atm	K	kg/s	m/s	Average	Relative	Relative
1	No Bleed	0	8.77	581	0	0	0	1.000	1.000
2	200	+72	3.14	394	25.0	363	0.0070	1.014	1.129
3	180	+72	3.14	394	25.0	363	0.0088	1.111	1.144
4	160	+72	3.14	394	25.0	363	0.0112	1.124	1.162
5	140	+72	3.14	394	25.0	363	0.0146	1.141	1.185

Table 6.3: Engine/airframe parameters and airspeed variation with IPC(0.25)

6.1.1.4 Internally Blown Flaps - Effect of Throttle Setting

Table 6.4 shows IPC bleed results for a higher throttle setting. For higher throttle settings the flap effectiveness and the IPC bleed mass flow were slightly higher due to higher wing nozzle source pressure and temperature. However, it was not possible to bleed the end of IPC compressor IPC($x/l = 1.0$) for a slot height of 2 mm as the turbine entry temperature limit was hit and the RPM control was not able to hold the demanded speed. Table 6.4 therefore presents results only for the IPC(0.50) and IPC(0.25) case at a higher Fan speed of 5000 RPM.

No	Bleed Loc	ΔTET	$P_{2.2}$	$T_{2.2}$	$\dot{m}_{jet}$	V_{jet}	C_u	$\Delta C_L/\Delta_{flap}$	$\Delta C_m/\Delta_{flap}$
	(x/l)	K	Atm	K	kg/s	m/s	Average	Relative	Relative
1	No bleed	0	8.75	581	0	0	0.0000	1.000	1.000
2	0.50	+147	4.43	452	32.9	389	0.0097	1.118	1.151
3	0.25	+72	3.14	394	25.0	363	0.0069	1.100	1.128

Table 6.4: Engine/airframe parameters at 5000 Fan RPM

6.1.2 Externally Blown Flaps (EBF) - Using LPC/Fan Bleed

The bleed mass flow from the LP compressor stage can either be blown over the full span as in the case of a distributed propulsion concept, or the full exhaust including the bypass and the core mass flow can be blown over selected flaps directly, without the need for internal wing ducting. For the blended wing body, some researchers are already proposing to embed the engines within the fuselage to enhance noise shielding [78]. This means that the engine's vertical offset from the Fuselage Reference Line (FRL) would be small and it is theoretically possible to place a rectangular engine exhaust just before the trailing edge flap, specifically Flap 1 which has a span of 26m. This will result in an externally blown flap arrangement for the centre-body section. Such a configuration is shown in Figure 6.19.

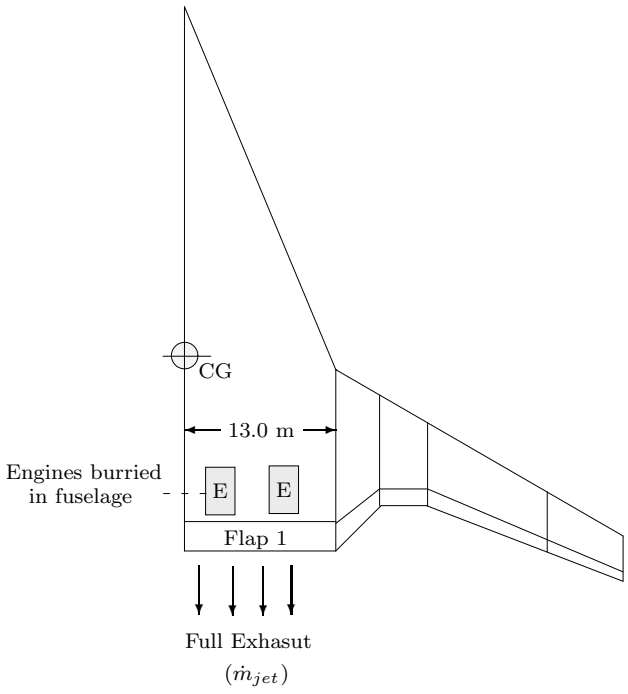

Figure 6.19: Flap 1 in a fully blown external flap arrangement

Consider the design point calculations for the Trent 500 in Table 6.5. At the design point, the bypass flow is 781.9 kg/s, a jet velocity of 267.3 m/s and a bypass nozzle design area of $A_{29} = 2.44$ m^2. If the bypass flow from an N $\times$ 275 kN engine configuration is made to flow above Flap 1 on the centre-body section, then for $N = 4$, the required slot height (h) would be,

$$h = \frac{NA_{29}}{L_1} = \frac{4 \times 2.44}{26.0} = 0.375\text{m} \tag{6.5}$$

Station	F.A.R.	Mass Flow	PTotal	Ttotal	Vel.	Area.	Designation
		kg/s	Atm	K	m/s	m^2	Exit
2	0.0	902.55	0.990	288.15	***	***	INLET
21	0.0	902.55	1.504	330.55	***	***	LPC
22	0.0	120.65	8.730	580.67	***	***	IPC
3	0.0	096.52	39.026	913.63	***	***	HPC
4	0.0218	123.29	36.685	1632.96	***	***	CMB
4.1	0.0218	123.29	14.238	1352.48	***	***	HPT
4.2	0.0218	123.29	6.564	1148.79	***	***	IPT
5	0.0218	123.29	2.007	886.25	***	***	LPT
9	0.0218	123.29	2.007	886.25	540.82	0.4497	CORE NOZ
29	0.0	781.89	1.489	330.55	267.29	2.4437	BYPS NOZ
Net Thrust = 278.75 kN, SFC = 0.034 kg/h/N							

Table 6.5: Design point calculations for the Trent 500

where N are the number of engines and L_1 is the flap length. If a mixed flow exhaust is used then this slot height would increase sightly to accommodate the additional mass flow from the main nozzle. It is also interesting to note that when using LP compressor mass flow for flap blowing, the engine operating point does not change and the engine performance is not compromised. With the flight speed fixed at 200 kts and the altitude at 1000 ft, the centre-body flap was externally blown using the LP mass flow at different throttle settings, the results follow.

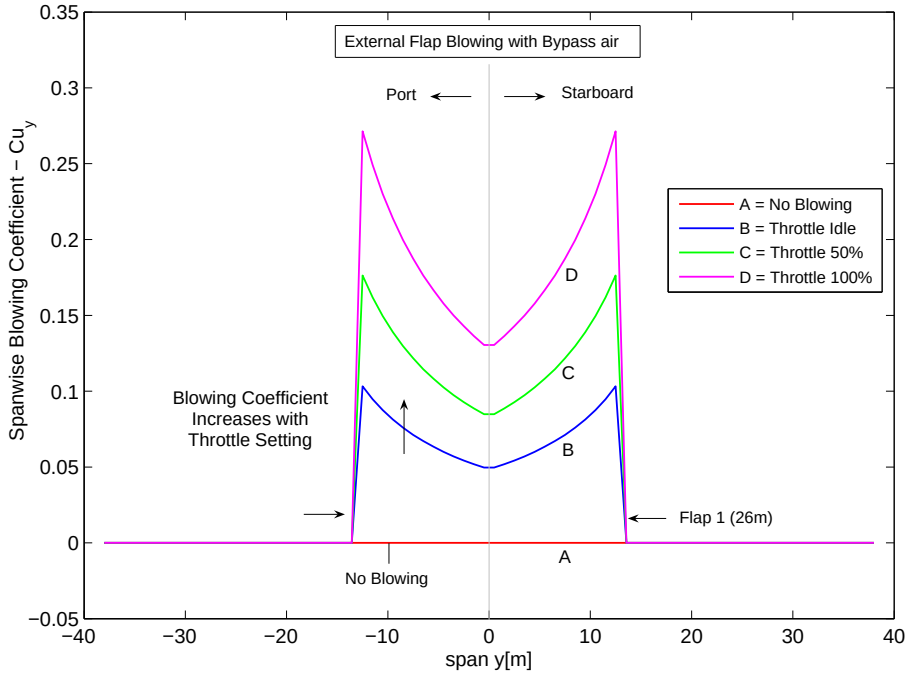

Figure 6.20: Spanwise blowing coefficient - Externally blown centre-body flap

Figure 6.20 shows the increase in blowing coefficient, C_u, for Flap 1 due to external flap blowing using bypass air. At 100% throttle setting and with a 4 × 275 kN

engine configuration, the average value of C_u for Flap 1 is approximately 0.2. This may seem to be a little low keeping in view that the full bypass air is blown over the flaps. However, the local chords for the centre-body section area are large (48 m for the root section) which makes it difficult to achieve high blowing coefficients. In addition, Flap 1 has a length of 26 m which reduces the mass flow per unit span.

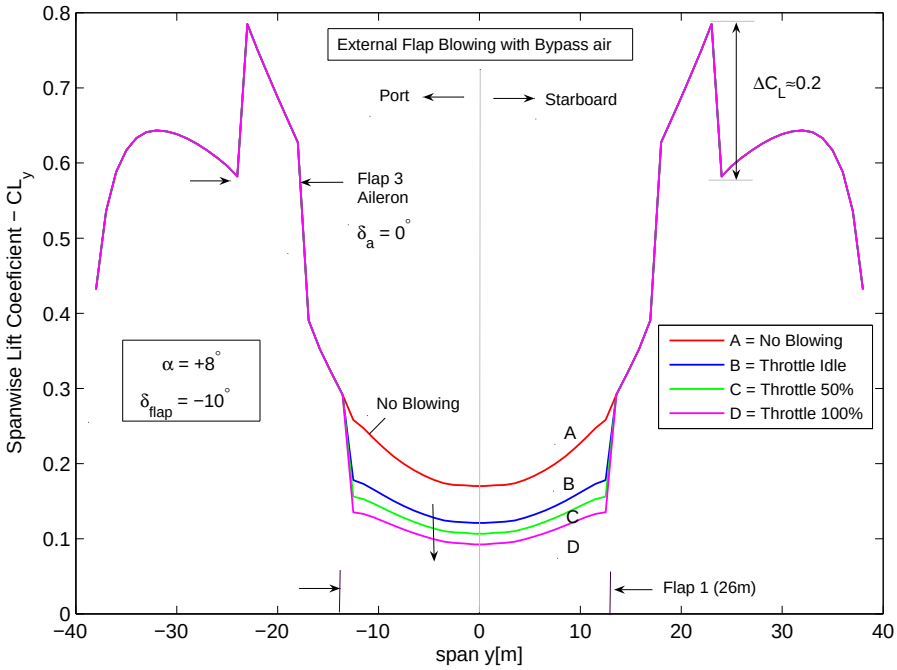

Figure 6.21: Spanwise lift coefficient - Externally blown centre-body flap

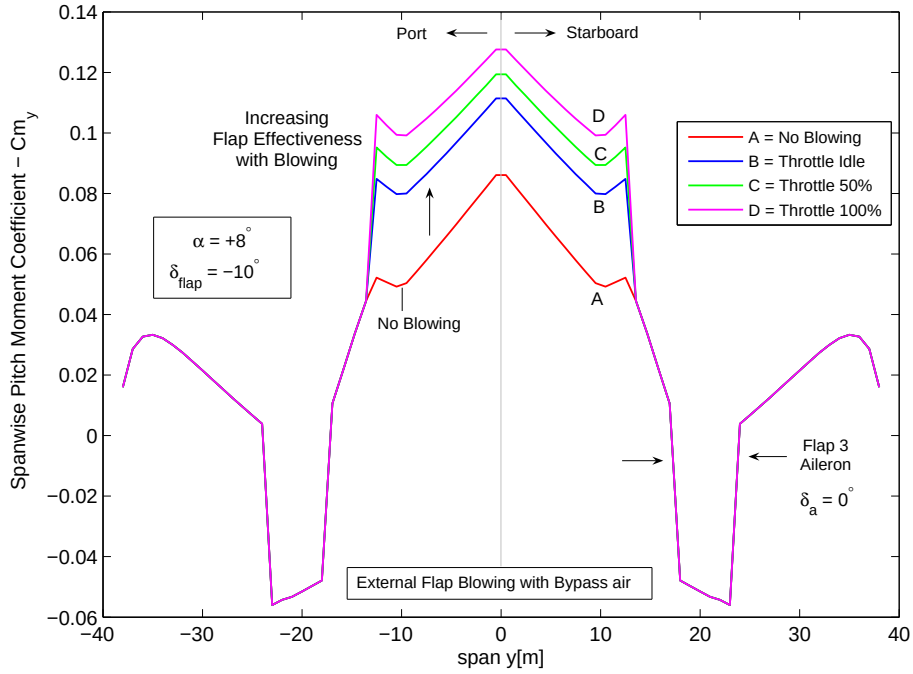

Figure 6.22: Spanwise pitch moment coeff. - Externally blown centre-body flap

Figure 6.21 shows the corresponding spanwise lift coefficient for an angle of attack of $+8.0°$ and spanwise flap deflection of $-10°$. The aileron section was kept at zero deflection. The increase in flap effectiveness due to blowing for the centre-body are obvious. Similar results can be seen for spanwise pitching moment coefficient on Figure 6.22. Flap 1 is now able to make a significant contribution to the nose up pitching moment as compared to the unblown case.

No	RPM	Thrust	BFlow	CFlow	BVel.	CVel.	$[C_u]_{F1}$	$\Delta C_L/\Delta_{flap}$	$\Delta C_m/\Delta_{flap}$
		kN	kg/s	kg/s	m/s	m/s	Average	Relative	Relative
1	Idle	-	-	-	-	-	0	1.000	1.000
2	Idle	47.5	523.4	54.8	182.0	220.0	0.0734	1.248	1.264
3	50%	116.0	683.4	88.6	238.7	386.2	0.1262	1.317	1.352
4	100%	238.5	840.5	135.1	297.2	567.8	0.1930	1.385	1.442
B = Bypass, C = Core									

Table 6.6: External blown centre-body flap using bypass flow

The results have been summarized in Table 6.6. Even at idle throttle settings the increase in flap effectiveness is +26.4% relative to the unblown case. At full throttle, this increases to +44.2%. In this analysis only the centrebody flaps are blown, the flap effectiveness is however considered for the full span or the overall moment generated about the centre of gravity and not for individual flaps, which is considerably higher and is illustrated in Figure 6.22. The addition of core flow increases the flap effectiveness figure from +44.2% to +51.0%. Lastly, these results are for an airspeed of 200 kts, at reduced airspeeds such as those required during take-off or landing, better results are expected due to relativey higher values of achievable blowing momentum coefficient.

Another possible advantage of the externally blown flap arrangement is that the deflection of Flap 1 can automatically generate a deflection of thrust in the pitch axis. As will be shown in the next chapter, that deflected thrust or TVC gives a clear advantage in achieving early pitch rotation during take-off and therefore a net reduction in take-off distances. Further work using CFD or experimental methods will however be necessary to ascertain the amount of thrust deflection that can be achieved with such an arrangement.

6.1.3 Engine Matched for Additional Bleed at Design Point

It was mentioned in Section 6.1.1 that IPC bleed is very expensive in terms of rise in turbine entry temperature and loss of thrust. Up to 45 kg/s of IPC bleed was extracted from the Trent 500 engine for flap blowing purposes in an effort to enhance flap effectiveness. This amounts to more than 30% of the net IPC mass flow of 120.2 kg/s at design point. Upon such values of bleed extraction the HP and IP compressors shift from their nominal running lines either towards choke or surge.

This section briefly presents results of a redesigned Trent 500 Engine matched for additional bleed at design point. The turbine entry temperature was kept fixed at 1788K, and the net mass flow into the engine was increased. The bypass duct flow was kept constant at 781.92 kg/s but the IPC compressor now ingests a flow greater than 120.2 kg/s (design point flow with no bleed). Bleed is then extracted from an appropriate station along the length of IP compressor and was varied from 0 to 50 kg/s from stations IPC(1.0) and IPC(0.5) respectively. Three cases of thrust recovery from the wing duct nozzle were assumed, 0%, 50% and 100%. Thrust specific fuel consumpiton (SFC) and turbine entry temperatures were recorded. A modified DYNGEN [12] program was used for these design point caluclations.

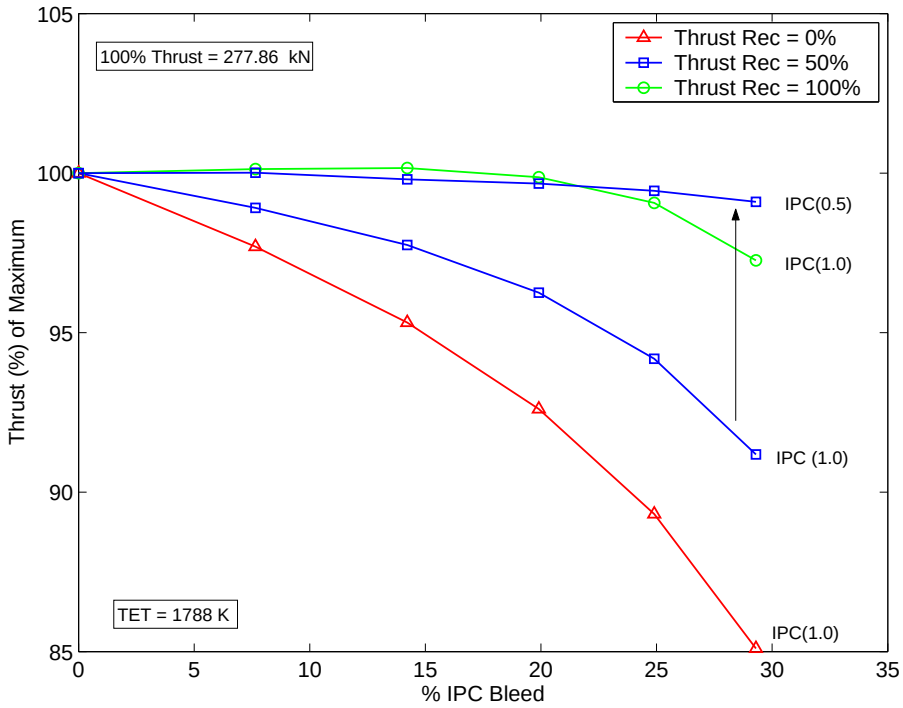

Figure 6.23: Thrust at design point for engine matched for IPC bleed

Figure 6.23 shows the achievable design point thrust while holding the turbine entry temperature constant in all design cases. As the bleed extraction is increased the

design point thrust decreases. In addition, IPC bleed location has a significant effect in improving the design point thrust, for example for the IPC(0.5) case i-e IPC bleed location at $x/l = 0.5$, the loss in design point thrust is much lower. Although the engine diameter may have to be increased slightly to accommodate the additional mass flow (approximately 50 kg/s in this case) into the system.

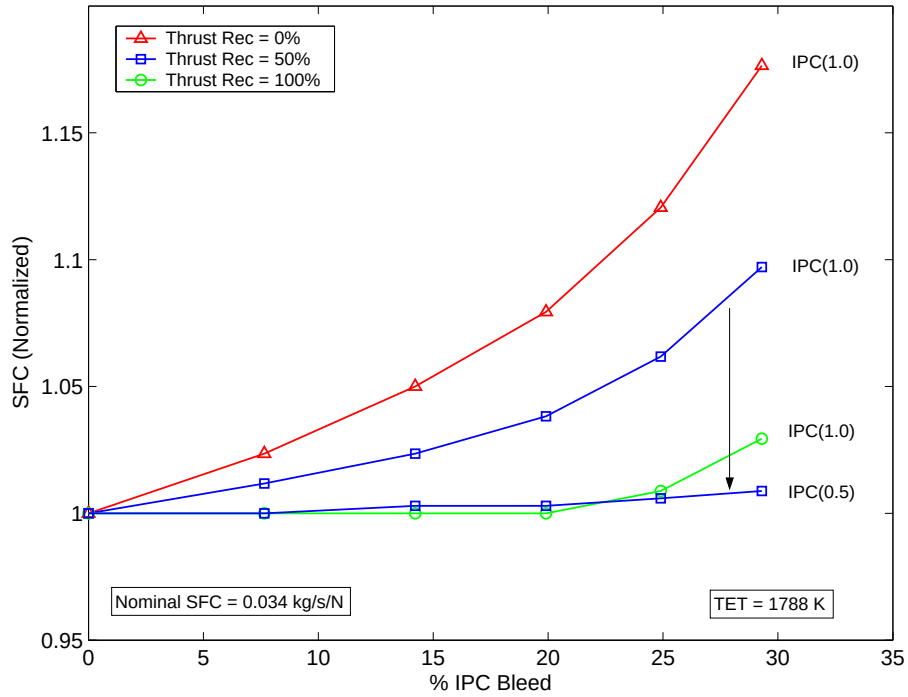

Figure 6.24: SFC at design point for engine matched for IPC bleed

Figure 6.24 shows the corresponding specific fuel consumption results. As the design point thrust drops and the the TET kept constant at 1788K, the thrust specific fuel consumption increases. Again the effect of aft bleed location is to bring the SFC back to its nominal value of 0.034 kg/h/N. Table 6.7 summarizes these results.

No	IPC Bleed		LPC Flow	Thrust (kN)			SFC (kg/h/N)		
	kg/s	% Net	kg/s	100%R	50%R	0%R	100%R	50%R	0%R
1	0	0	902.5	277.8	277.8	277.8	0.0340	0.0340	0.0340
2	10	7.65	912.5	278.2	274.8	271.4	0.0340	0.0344	0.0348
3	20	14.22	922.5	278.3	271.6	264.8	0.0340	0.0348	0.0357
4	30	19.91	932.5	277.5	267.4	257.3	0.0340	0.0353	0.0367
5	40	24.90	942.5	275.2	261.6	248.1	0.0343	0.0361	0.0381
6	50	29.30	952.5	270.2	253.5	236.4	0.0350	0.0373	0.0400
R = Thrust Recovery of Wing Nozzle									

Table 6.7: Trent 500 matched for permanent IPC bleed at constant TET

6.2 Controls Performance with Flap Blowing

This section analyzes the effect of flap blowing on controls performance. Traditionally, blown flaps have been used for generation of high lift at low speeds, however for the BWB aircraft, blown flaps are implemented in an attempt to improve controls effectiveness and compensate for the absence of a horizontal stabilizer and a conventional rudder. All three, pitch, roll and yaw axes are considered separately.

6.2.1 Control of Pitch Axis with Blown Flaps

It was shown in the previous section that using full span blowing the achievable blowing coefficient using IPC bleed was limited in case the engine is not designed or matched for large bleed off-takes. Alternatively the main + bypass exhaust from the engines buried in the fuselage can be made to flow over the centre-body flap (±13m) in an externally blown flap arrangement. Blowing coefficients of ($C_u > 0.2$) were shown to be achieved easily in this case. In the following results, the externally blown centre-body flaps were used to enhance pitch control, whereas the IPC bleed was used selectively on inboard aileron and winglet rudder to improve roll and yaw control effectiveness respectively.

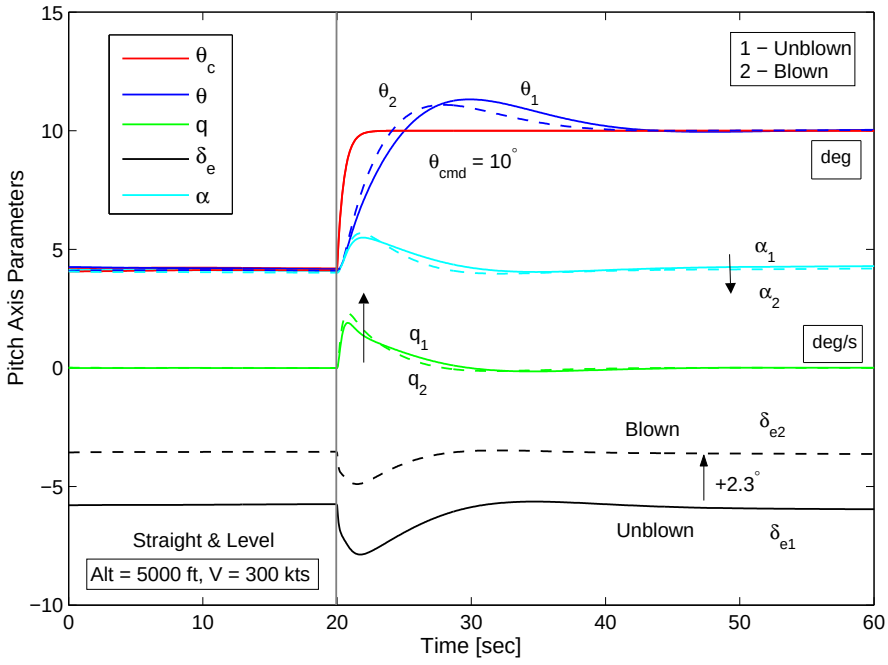

Figure 6.25: Pitch control with externally blown centre-body flaps at 300 kts

Figure 6.25 illustrates the improvement in pitch response for a bandwidth limited pitch angle demand. The pitch angle response (θ_2) for the blown flap case is slightly faster than the unblown case (θ_1), along with a reduction in trim elevator deflection

(δ_{e2}). The gains of the pitch control loop were kept constant in both cases. The angle of attack reduces only slightly, as the flaps although more effective than before are still deflected in the negative direction to maintain pitch trim. Before initiating the pitch angle step demand, the BWB aircraft was trimmed for a straight and level flight at an altitude of 5000 ft, airspeed of 300 kts and a CG location of 29.4 m.

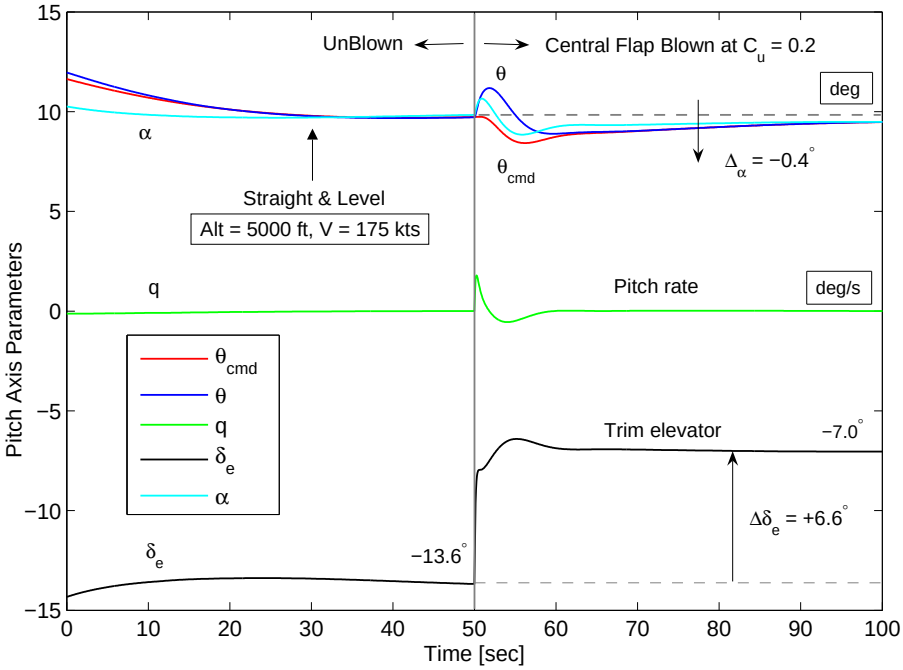

Figure 6.26: Pitch control with externally blown centre-body flaps at 175kts

Figure 6.26 shows similar results but for a much reduced airspeed of 175 kts. The reduction in trim elevator deflection is evident. In this case however, the straight and level trim condition is maintained, with flap blowing initiated at 50 seconds. The angle of attack shows only a marginal improvement of about 4%. It was illustrated in Section 3.1.1 that at reduced airspeeds the trim elevator deflection reaches close to saturation. Reduction of these elevator deflections to almost half using flap blowing, without increasing the control surface area seems to be an obvious advantage.

6.2.2 Roll Control and Blown Flaps

In Section 3.3.2, the open loop lateral-directional dynamics of the baseline BWB configuration were found to be very poor at low airspeeds. The dutch roll dominates the roll angle response and a lateral-directional stability augmentation system (SAS) was found to be necessary to achieve satisfactory performance. Even with the SAS in place, the system falls short of meeting the handling qualities requirements at low airspeeds. In particular, at speeds below 300 kts, the time to reach 30° bank angle

was too high. The limited control power of the inboard aileron, coupled with large roll damping and high roll axis inertia were the underlying reasons.

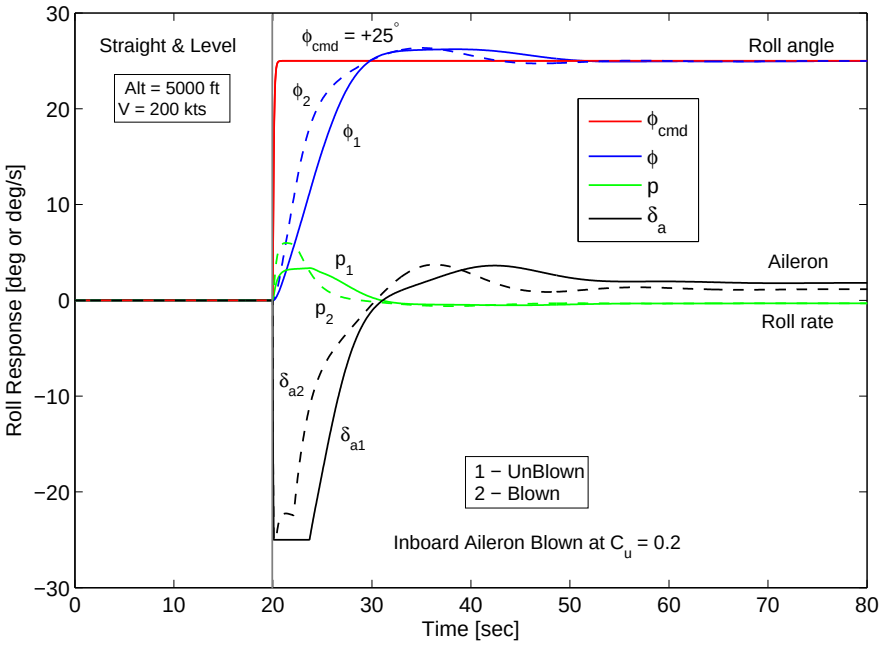

Figure 6.27: Roll response at 200 kts with inboard aileron blown at $C_u = 0.2$

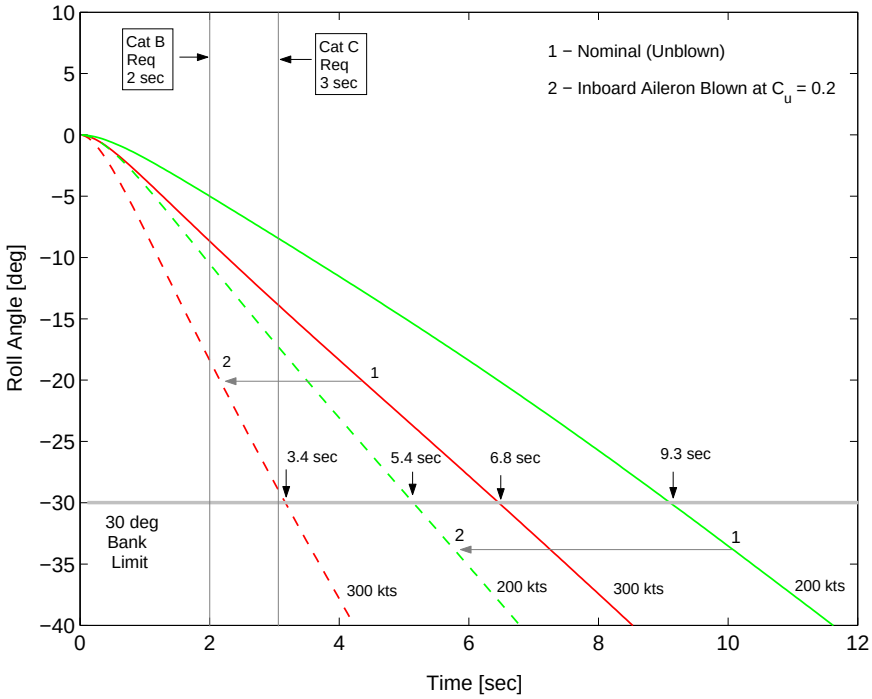

Figure 6.28: Time to reach 30° bank angle with and without flap blowing

Figures 6.27 and 6.28 shows the improvement in roll response obtained with an internally blown inboard aileron at a blowing coefficient of $C_u = 0.2$. In particular the roll angle response (ϕ_2) is faster and the aileron (δ_{a2}) does not saturate. The roll

rate (p_2) with flap blowing is also higher. The time to reach $-30°$ bank angle at a speed of 200 and 300 kts with full aileron deflection of $+25°$ is also greatly improved, but still falling short of Category B and Category C flight phase requirements for a large transport aircraft.

6.2.3 Directional Control and Blown Flap Rudder

Handling of high crosswinds, asymmetric thrust and suppression of adverse yaw through an aileron to rudder interconnect puts severe demands on the small winglet rudders of the BWB. If conventional rudders are to be avoided, it is desirable to make the winglet rudders as effective as possible. By virtue of their location, increasing the fin surface area is not an option. Alternatively blown flaps may be used to enhance control effectiveness. To evaluate the effects of a blown flap rudder the flight control system shown in Figure 6.29 was used.

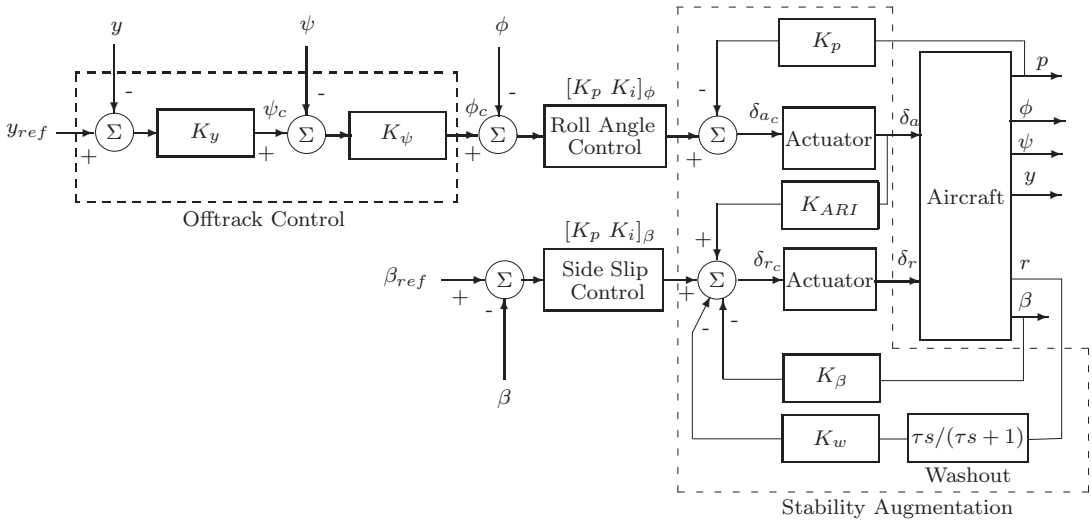

Figure 6.29: Lateral FCS loop structure used for non-linear simulation

Table 6.8 shows the schedule of FCS gains as a function of dynamic pressure. Very high values of gains for aileron to rudder interconnect may be noted, with K_{ARI} exceeding 1.0 at low dynamic pressures. At low speeds the BWB aircraft requires almost the same amount of rudder as aileron to ensure a coordinated turn.

To evaluate the effects of flap blowing on rudder control, the BWB aircraft was trimmed at a height of 5,000 ft and an airspeed of 200 kts. The initial off track distance (y) was set at -1000 m. Negative off track distance means that the aircraft

$\bar{q}$	K_w	K_β	K_p	$[K_p]_\phi$	K_{ARI}
5,000	-3.771	0.561	-1.512	-2.804	1.558
10,000	-2.841	0.961	-0.680	-2.080	0.876
15,000	-2.230	0.934	-0.224	-1.651	0.575
20,000	-1.829	0.680	-0.039	-1.391	0.493
25,000	-1.530	0.404	-0.022	-1.175	0.464

Table 6.8: Lateral FCS - Gain schedule

is to the left of the navigation track and vice versa. The off-track control system causes the aircraft to bank to the right and brings the aircraft on a zero off-track within 100 secs. Figure 6.30 shows the time history.

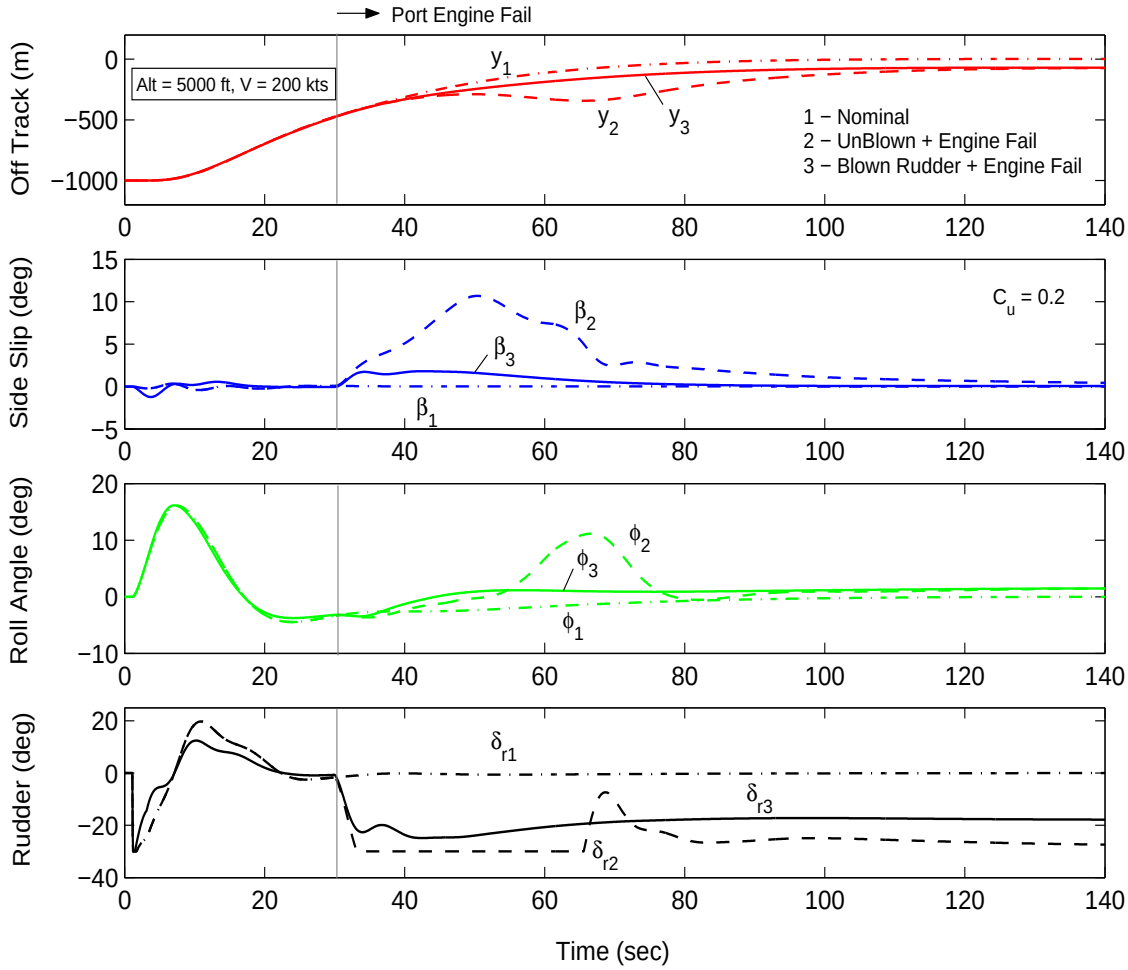

Figure 6.30: Yaw axis response with flap blowing on rudder at $C_u = 0.2$

With the sideslip suppression system operative, a port engine failure was simulated at 30 seconds. The asymmetric thrust generated by the starboard engine causes a negative yawing moment. The aircraft starts to generate a positive sideslip. In order to suppress this sideslip a negative rudder deflection is generated by the FCS.

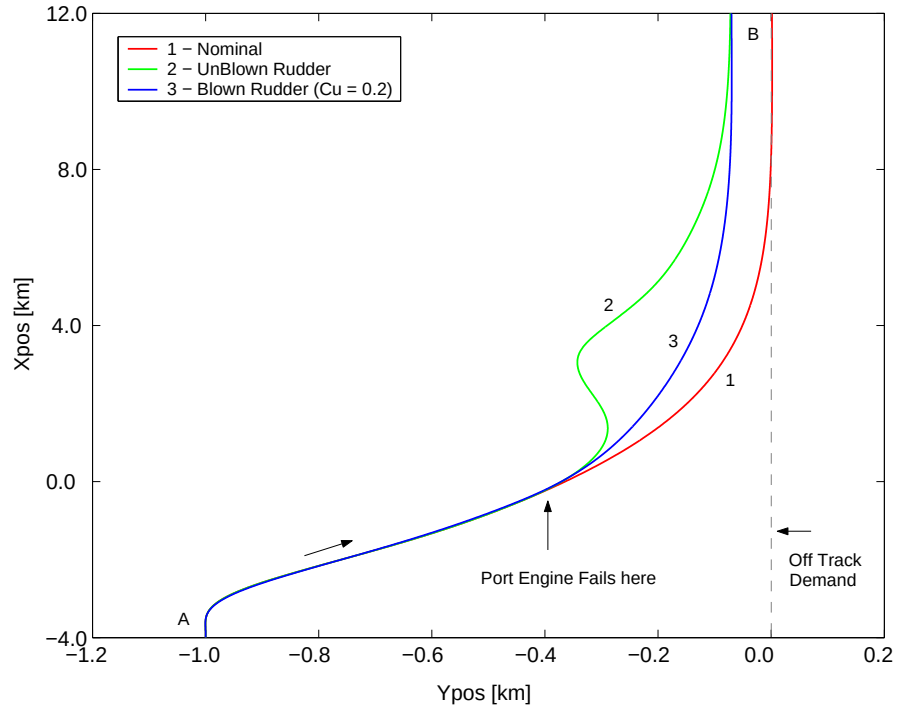

Figure 6.31: XY trajectory with and without flap blowing on rudder

On Figure 6.31 three time histories are plotted. Case 1 is the nominal case with no engine failure or flap blowing. Very little sideslip is noted and the only rudder deflections necessary are in the first 30 seconds for turn coordination.

Case 2 shows the results for the unblown case with port engine failure. The rudder quickly saturates at $-30°$ and the sideslip is not suppressed. Although not shown this large of amount of sideslip (β_2) also generates a significant roll moment causing a non zero trim aileron deflection. Under a high enough sideslip, the aircraft may diverge in both the roll and yaw axis simultaneously. However in this case the aircraft eventually recovers from saturation and back onto the reference trajectory. Figure 6.31 shows the XY path taken by the aircraft.

Case 3 is similar but now with the rudders blown at $C_u = 0.2$. The sideslip is effectively suppressed to less than $2°$ even at the onset of port engine failure. Unlike the previous case, the trim rudder deflection (δ_{r3}) never hits the saturation limit and the flight path on Figure 6.31 shows a nominal behavior, except for a constant offtrack error at the end of flight path at point B, due to the presence of a constant negative yawing moment from the starboard engine about the centre of gravity.

For this analysis, the starboard engine was assumed to be located at an offset of 5 m from the centreline. In practice higher offsets are likely, hence the sideslip and the resulting drift from nominal trajectory are expected to increase. To sustain level flight, a trim thrust value of 320 kN was required from each of the centreline and the starboard engines. A 3×440 kN engine configuration was assumed, so the thrust from the 275 kN Trent 500 engine was upscaled to simulate this flight condition.

6.3 Controls Performance with Thrust Vectoring

Thrust vectoring is an alternate method to enhance controls performance. However its implementation for a commercial civil transport has never been implemented. For the blended wing body case however, absence of a horizontal stabilizer has renewed interest in this option. Researchers at the Silent Aircraft Initiative [4] are already suggesting some level of thrust vectoring in their designs [5]. Trim results with pure TVC follow.

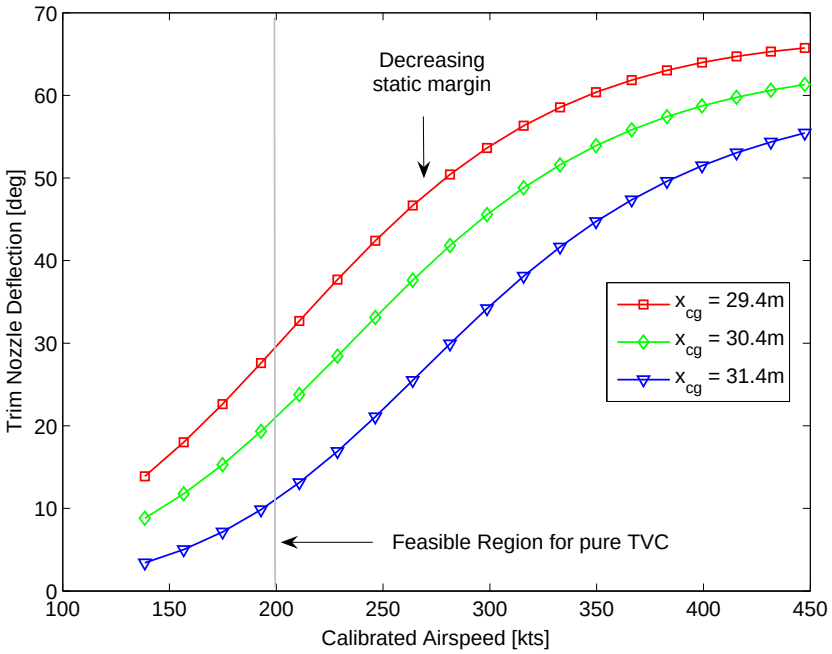

Figure 6.32: Trim Nozzle deflections for pure TVC

Figures 6.32 and 6.33 show the required nozzle deflection and trim throttle as function of calibrated airspeed in the pure TVC mode . Various CG positions were considered. It is observed that with a TVC moment arm of 25 m and $x_{cg} = 29.4$ m, the required nozzle deflections exceed 30° above 200 knots. Thus implementation of a pure TVC scheme is improbable, rather it would be much more feasible to use TVC in combination with Aerodynamic Flight Control (AFC), especially in those

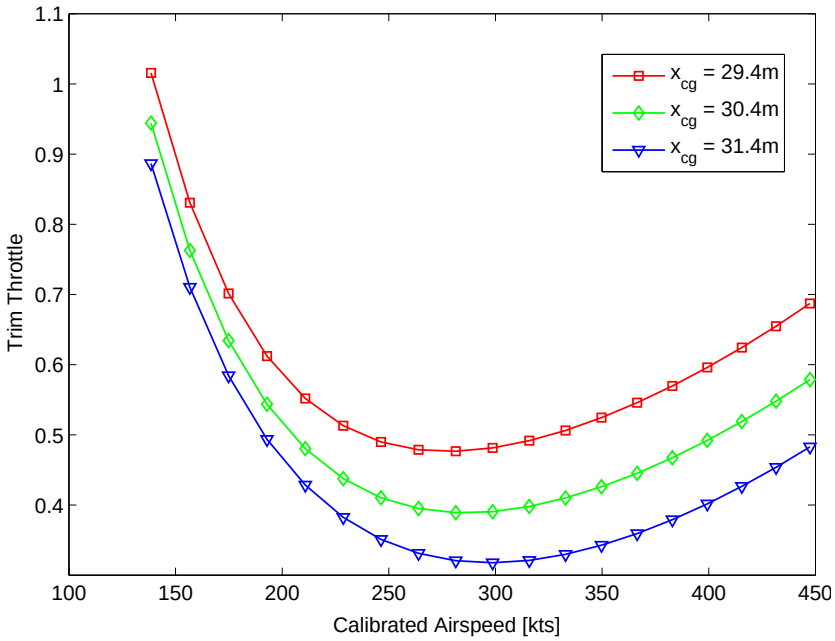

Figure 6.33: Trim Throttle for pure TVC

parts of the flight envelope where the AFC is weak, such as at take-off or landing.

Results for pure TVC control and TVC+AFC are now presented. Figure 6.34 shows switching from pure AFC to pure TVC at an altitude of 5000 ft and an airspeed of 200 kts. The inner stability augmentation loops are still under AFC control, primarily due to the higher bandwidth of the elevator servos, only the pitch angle control or trim is maintained by the vectored thrust. In the pure TVC mode, the trim angle of attack is reduced by almost 20% and the trim elevator to almost zero. The system is able to hold both speed and altitude by use of vectored thrust.

Figure 6.35 illustrates the corresponding engine parameters. The trim nozzle deflection settles at almost +30° as predicted. The loss in axial thrust is compensated automatically by the FCS through an 8% increase in throttle setting. The rise in TET is +75K. From Figure 6.35 it is noted that at all times the throtte setting was above 80% and therefore there was always an adequate amount of thrust available for the pure TVC mode. However as soon as the net axial thrust drops either due to an increase in altitude or a decrease in throttle setting, the pure TVC mode is not able to maintain pitch trim and aerodynamic control is necessary. Thrust vectoring would be thus be most effective at take-off, when throttle is at a maximum.

Another possible option is to augment the aerodynamic controls by limited TVC. Figures 6.36 and 6.37 show some interesting results for AFC+TVC mode, with

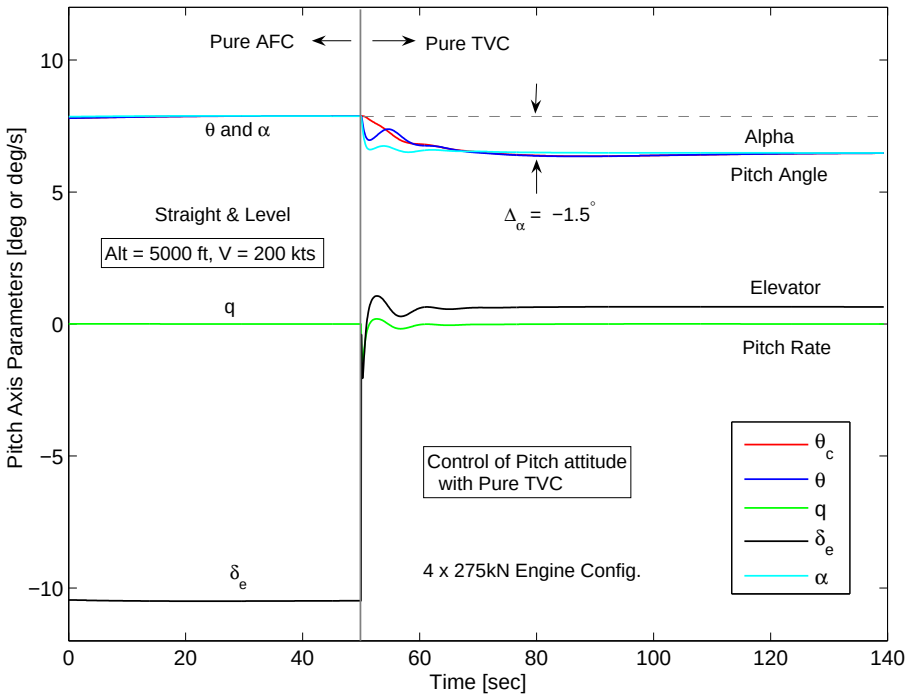

Figure 6.34: Pure TVC Mode : Control of pitch attitude at 200 kts, $x_{cg} = 29.4$ m

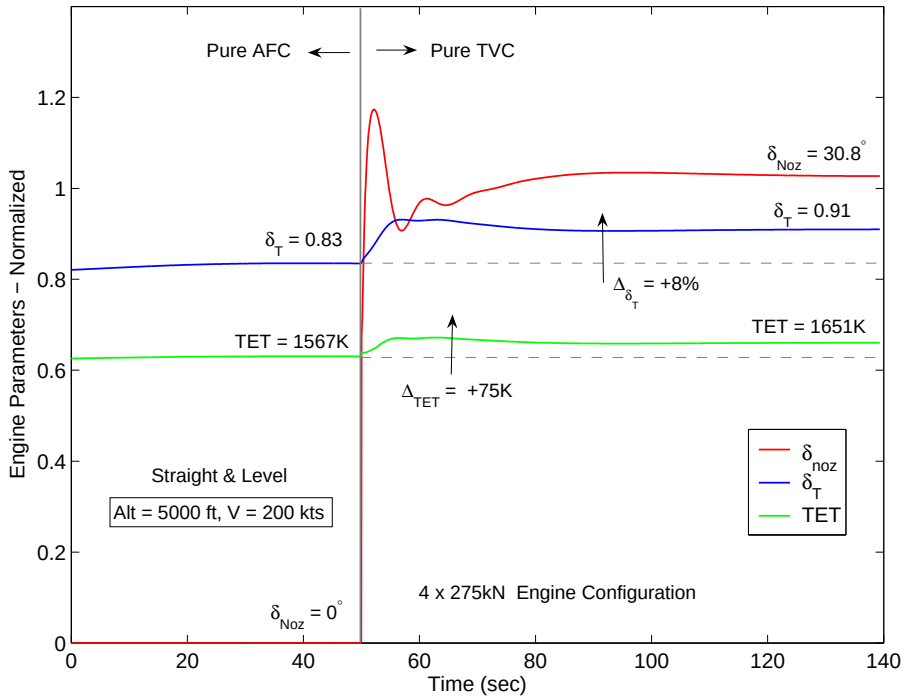

Figure 6.35: Pure TVC Mode : Trim throttle and nozzle deflection, $x_{cg} = 29.4$ m

$\delta_{noz} = \delta_e$. Trim elevator deflections reduce by almost 30% and angle of attack by 4.6%. Interestingly, the effect on throttle position and TET was negligible, primarily due to the reduction in angle of attack and corresponding trim drag. Similar results were achieved if fixed and limited TVC ($< 10°$) is used. The AFC+TVC mode in

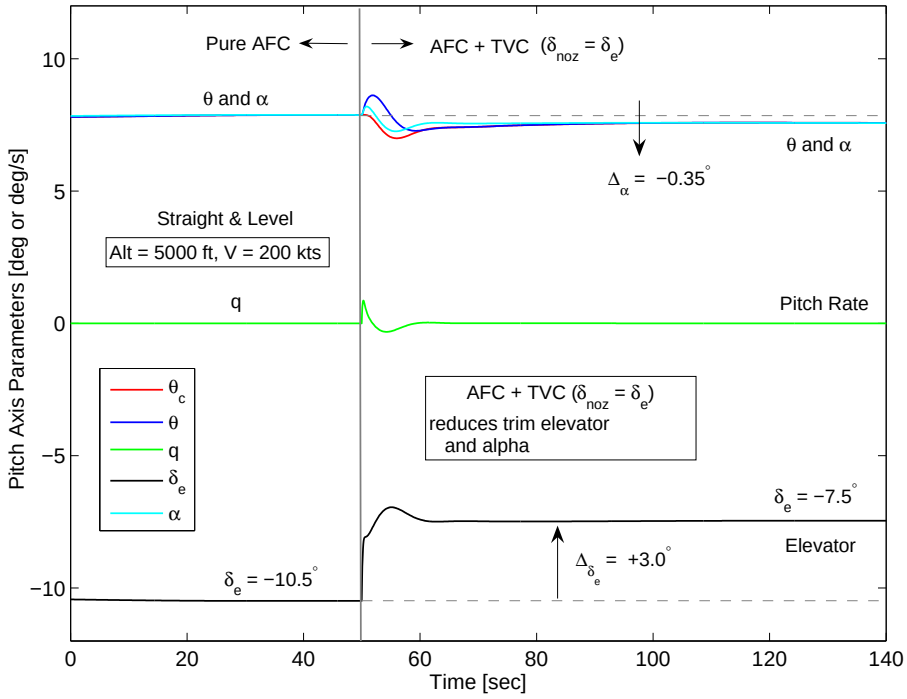

Figure 6.36: AFC + TVC Mode ($\delta_{noz} = \delta_e$) : Pitch control at 200 kts, $x_{cg} = 29.4$ m

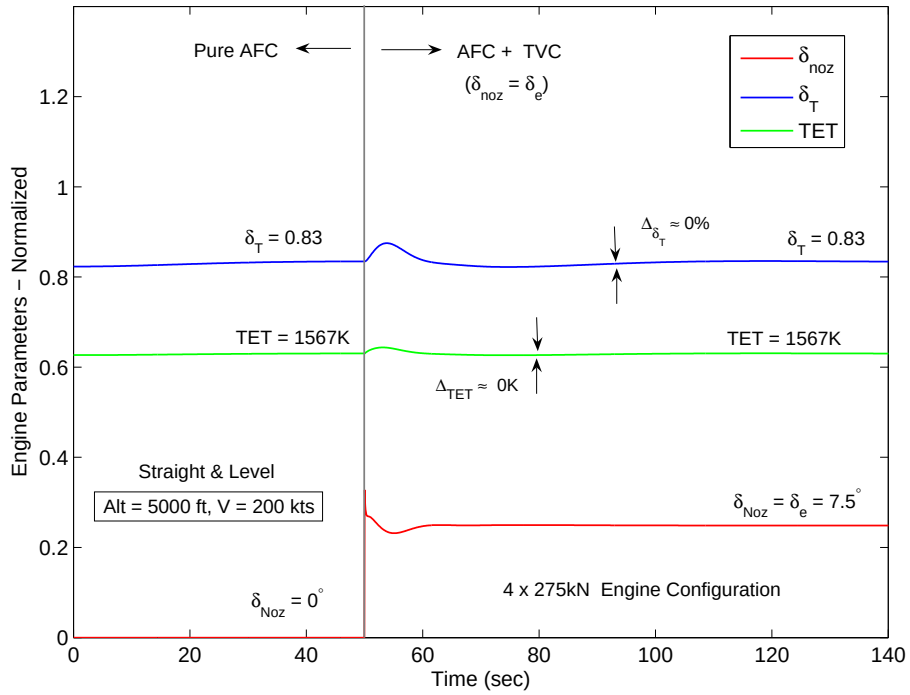

Figure 6.37: AFC + TVC Mode ($\delta_{noz} = \delta_e$) : Trim throttle and nozzle deflection, $V = 200$ kts, $x_{cg} = 29.4$ m

combination with flap blowing has the potential to provide a solution to the controls saturation problem. The following trim analysis shall look into this in more detail.

6.4 Trim Results with Flap Blowing and TVC

This chapter is concluded by presentation of trim results in presence of flap blowing and TVC. Fixed values of TVC and blowing momentum coefficients will be assumed. The aim is to reduce the trim elevator deflection, angle of attack and throttle setting. Augmentation of aerodynamic controls with TVC is considered first.

6.4.1 Trimming with AFC + Fixed TVC

Consider the trim angle of attack results with a range of fixed thrust vectoring angles in Figure 6.32. A straight and level flight condition was assumed. For the nominal case with (TVC = 0°), the trim angle of attack at an airspeed of 150 kts reaches +16.8°, which may lead to flow separation. Vectored thrust at 10, 20 and 30 degrees provides the necessary pitching up moment and recovers some of the lost trim lift coefficient. Although 30° of thrust deflection may be difficult to implement, even with a TVC of 20°, the trim angle of attack is reduced to a more acceptable level of +14.6°, though still on the high side. At higher speeds of more than 200 kts, the angle of attack is only weakly influenced by thrust vector control.

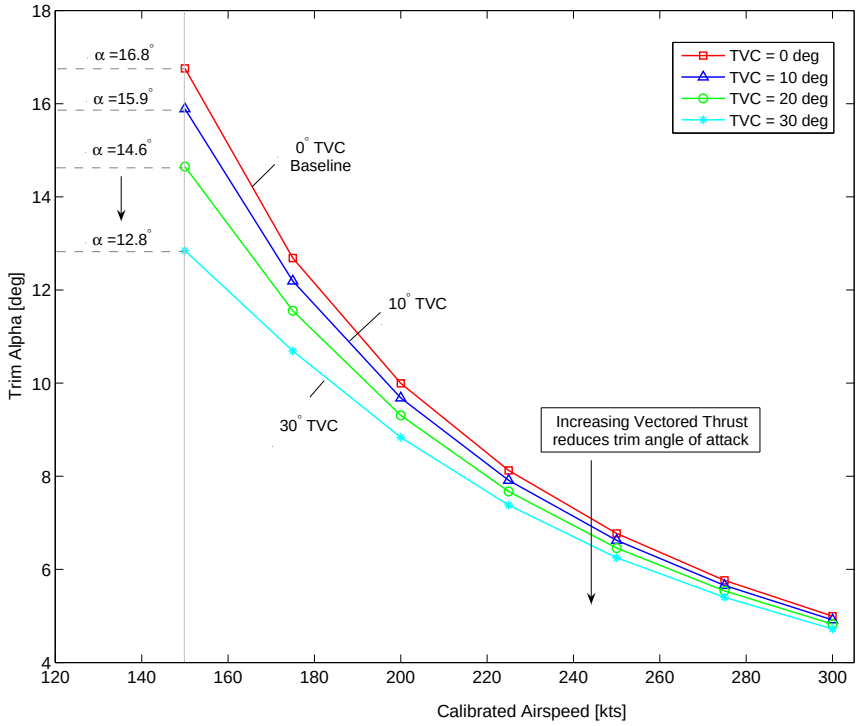

Figure 6.38: AFC + Fixed TVC ($\delta_{noz} = 10°$) : Trim angle of attack, $x_{cg} = 29.4$ m

The corresponding trim elevator deflections for the AFC + TVC configuration are presented in Figure 6.39. For 10° of TVC, the trim elevator deflection is −6.2°,

recovering from $-20.8°$ with no TVC. Thus vectored thrust strongly influences the trim elevator deflections. From the above results it seems that a good and practical TVC range for the BWB is between 10 and 20 degrees.

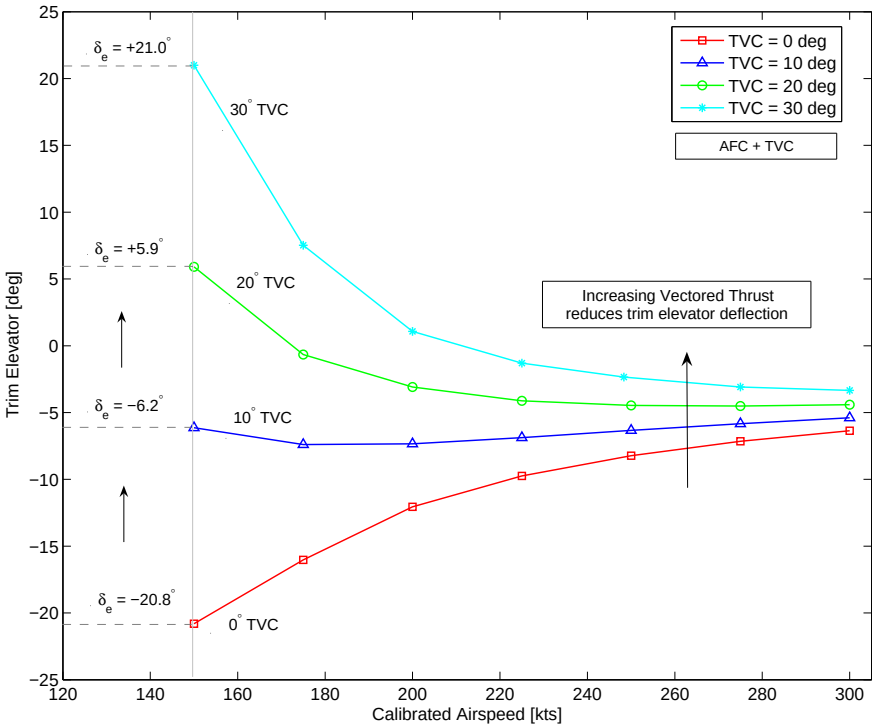

Figure 6.39: AFC + Fixed TVC ($\delta_{noz} = 10°$) : Trim elevator, $x_{cg} = 29.4$ m

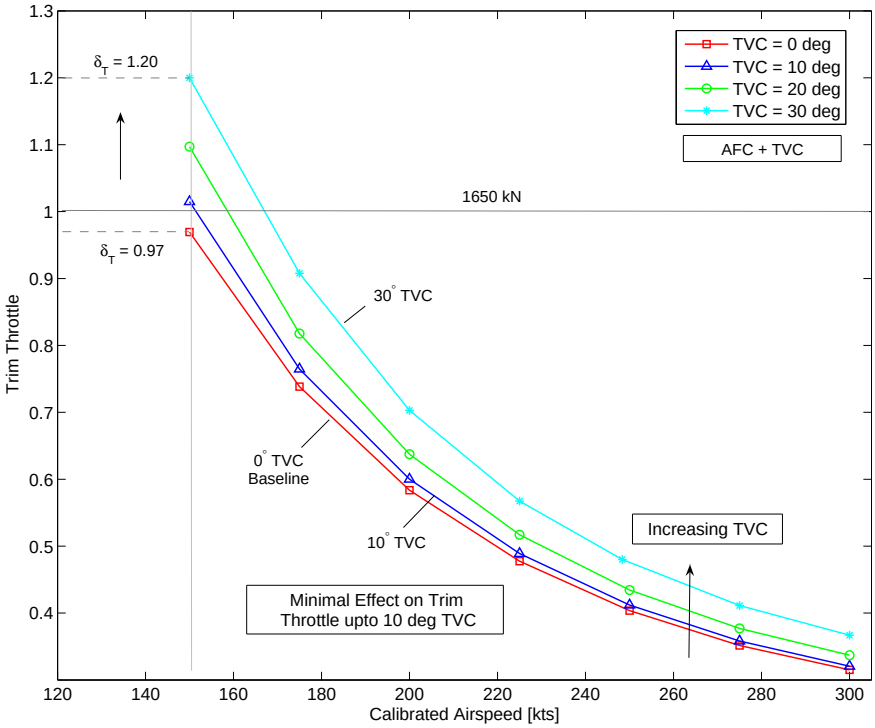

Figure 6.40: AFC + Fixed TVC ($\delta_{noz} = 10°$) : Trim throttle, $x_{cg} = 29.4$ m

The benefits of reduction in trim angle of attack and elevator deflections by thrust vectoring comes at a cost. The loss in net available axial thrust by vectored thrust is compensated for by an increase in throttle setting. Figure 6.40 shows the results. What however is encouraging is that up to 10° of TVC the increase in trim throttle is minimal ($< 4\%$). Beyond this range the thrust loss becomes significant.

6.4.2 Trimming with Blown Flaps

It was shown in Section 6.1 that either full span flap blowing using IPC bleed air or blowing just the central flaps with exhaust (main + bypass) air in an externally blown flap arrangement can improve flap effectiveness and reduce trim deflections. Trim results for the central flap blowing case are now presented.

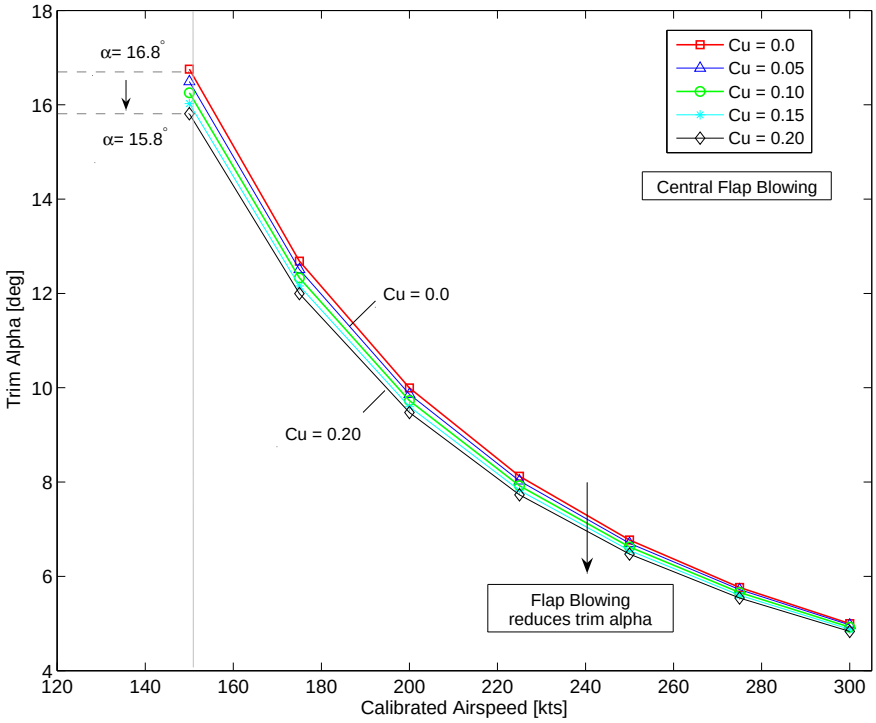

Figure 6.41: AFC + Central flap blowing ($C_u = 0.2$) : Trim angle of attack, $x_{cg} = 29.4$ m

The gains achieved in terms of reduction in angle of attack by flap blowing (Figure 6.41) are relatively less than the vectored thrust case. However, the trim elevator deflections are strongly influenced by flap blowing as shown in Figure 6.42. For a blowing coefficient of $C_u = 0.2$ on the central body flaps (spanning an extent of 26 m) the elevator deflections reduce from $-20.8°$ to $-9.6°$. This means better control saturation margin, lesser gains on the controllers and faster response. The trim angle of attack however is only marginally improved. The reason for this is that although the flap deflections are reduced, the loss in lift coefficient is still almost

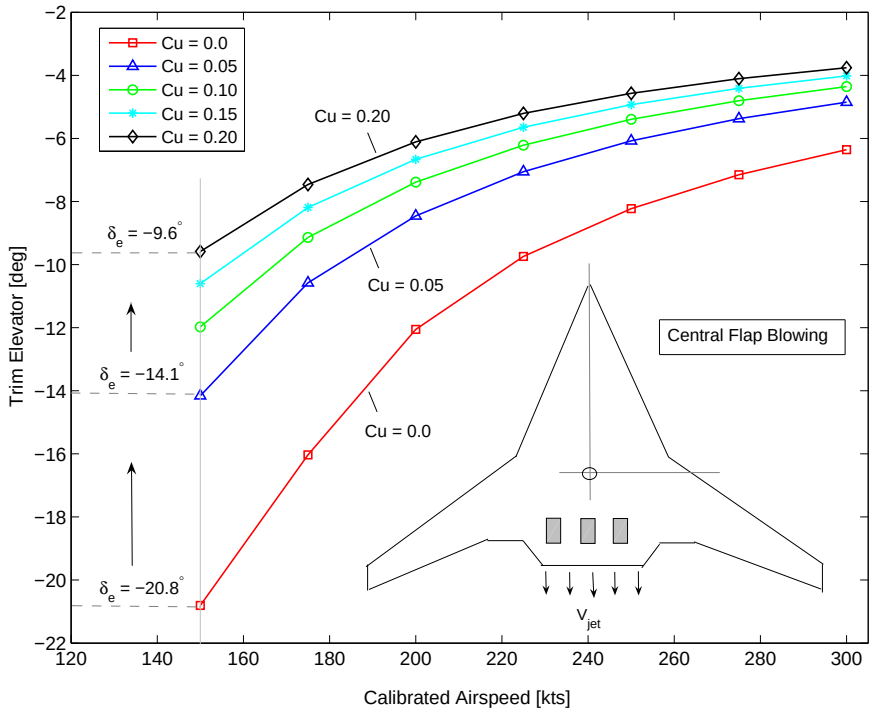

Figure 6.42: AFC + Central flap blowing ($C_u = 0.2$) : Trim elevator, $x_{cg} = 29.4$ m

the same and requires an almost similar angle of attack to sustain the weight of the aircraft.

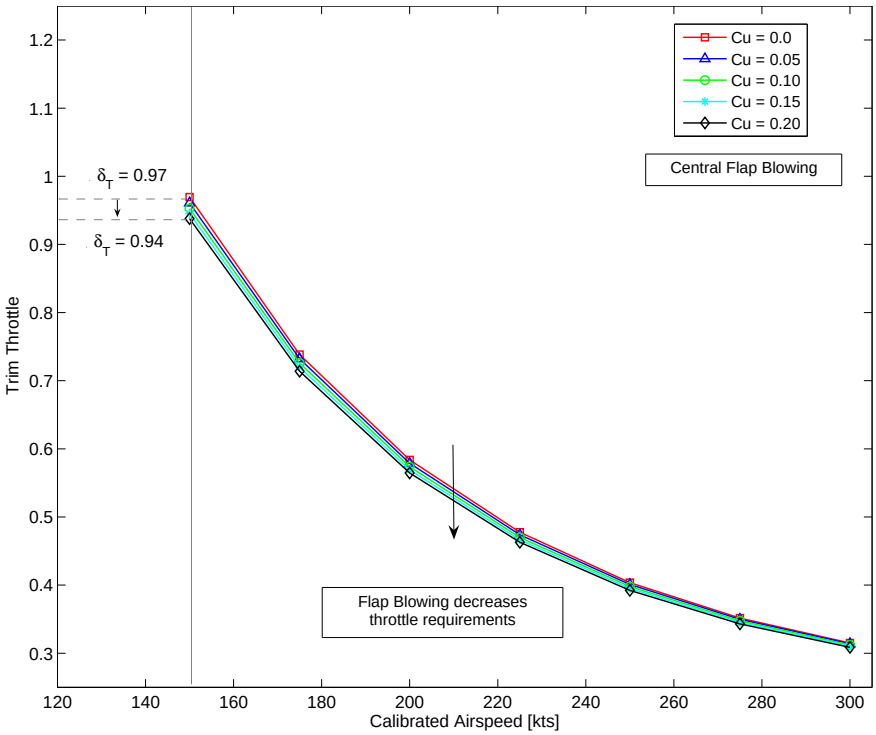

Figure 6.43: AFC + Central flap blowing ($C_u = 0.2$) : Trim throttle, $x_{cg} = 29.4$ m

The trim throttle also reduces in proportion with reduction the trim angle of attack and is illustrated in Figure 6.43. Trim results for flap blowing and thrust vectoring, at an airspeed of 150 kts are put together in Table 6.9 for comparison purposes.

No	AFC with Central Flap Blowing				AFC + TVC			
	C_u	$[\alpha]_{trim}$	$[\delta_e]_{trim}$	$[\delta_T]_{trim}$	δ_{Noz}	$[\alpha]_{trim}$	$[\delta_e]_{trim}$	$[\delta_T]_{trim}$
1	0.0	16.80	-20.8	0.97	0.0	16.8	-20.8	0.97
2	0.05	16.49	-14.1	0.96	10.0	15.9	-6.2	1.01
3	0.10	16.25	-12.0	0.95	20.0	14.6	+5.9	1.10
4	0.20	15.80	-9.6	0.94	30.0	12.8	+21.0	1.20

Table 6.9: Trim results with central flap blowing and TVC at 150 kts CAS

6.5 Chapter Summary

Various aspects of propulsion and controls integration for the BWB were covered in this chapter. The results may be summarized as follows.

- Adjustment of slot height and the wing nozzle pressure and temperature [P,T] establishes the mass flow and jet velocity through the slots on the wing trailing edge. Slot heights of up to 3 mm were tested. Bleeding from the end of intermediate compressor IPC(1.0) at 4300 Fan RPM causes almost 40% of IPC net mass flow to be bled and significant deterioation in engine performance. If the engine is not matched for permanent IPC bleed and full span blowing is to be incorporated, slot height has to be limited to keep bleed mass flow within acceptable limits. The rise in TET, IPC choking and HPC surge can be avoided by bleeding the IPC at an earlier station along its axial length. Even with IPC(0.25) the gains in flap effectiveness were not highly compromised.

- Higher throttle settings provide higher blowing coefficients and greater flap effectiveness. Similarly lower airspeeds or reduced dynamic pressures increase the blowing momentum coefficient.

- At design engine speed, with 2 mm bleed slot height and an IPC bleed location of $x/l = 0.25$, approximately 20% increase in flap effectiveness can be achieved with a +72K rise in TET.

- The rise in TET due to IPC bleed can be avoided by bleeding the LPC stage or matching the engine for permanent IPC bleed. Both these options can provide much higher blowing coefficients without affecting engine performance.
- Both thrust vectoring and flap blowing have the potential to increase flap effectiveness. Elevator deflections were shown to be reduced to half with a central flap blowing coefficient of 0.2. Similar results were achieved for the aileron and the rudder.
- To keep the blowing duct diameter small, it is suggested that minimal bleed be taken from the intermediate compressor. To achieve this, only selective flaps such as aileron and the winglet rudders may be blown at lower airspeeds. For the longitudinal axis, it is suggested to use external flap blowing directly, thus not only providing larger blowing coefficients, but also a mechanism to deflect thrust, thus eliminating the need for special thrust vectoring nozzles. The amount of thrust deflection that can be actually achieved with such an arrangement shall however requires further CFD/experimental work, and can be made part of future research.

Chapter 7

Landing and Take-off Performance

7.1 General Description

This chapter may be considered as a continuation of the previous chapter on propulsion and controls integration, however it considers the longitudinal axis only and takes a closer look at the landing and take-off phases. The aim is to expand upon the results obtained earlier and investigate the benefits of thrust vectoring or flap blowing for these particular low speed flight conditions.

To achieve the above objective, a non-linear six degree of freedom flight simulation was programmed in the C Language in which both the strip element airframe and the engine models were simulated in real time. Body axis equations of motion were used for the aircraft and the engine model was implemented using the hybrid approach developed earlier. The atmospheric properties were simulated using the international standard atmospheric (ISA) model. The simulation runs in real time with 76 strip elements and provides a visual environment to study both aircraft dynamics and engine responses simultaneously. Blowing coefficients can be user specified or set by means of adjusting the slot height and specifying a bleed location.

A flight control system (FCS) was also designed that provided control with both AFC and TVC modes. The design of this FCS is covered in Appendix C. Figure 7.1 shows a snapshot of the simulation showing a graphical representations of the engine and the aircraft.

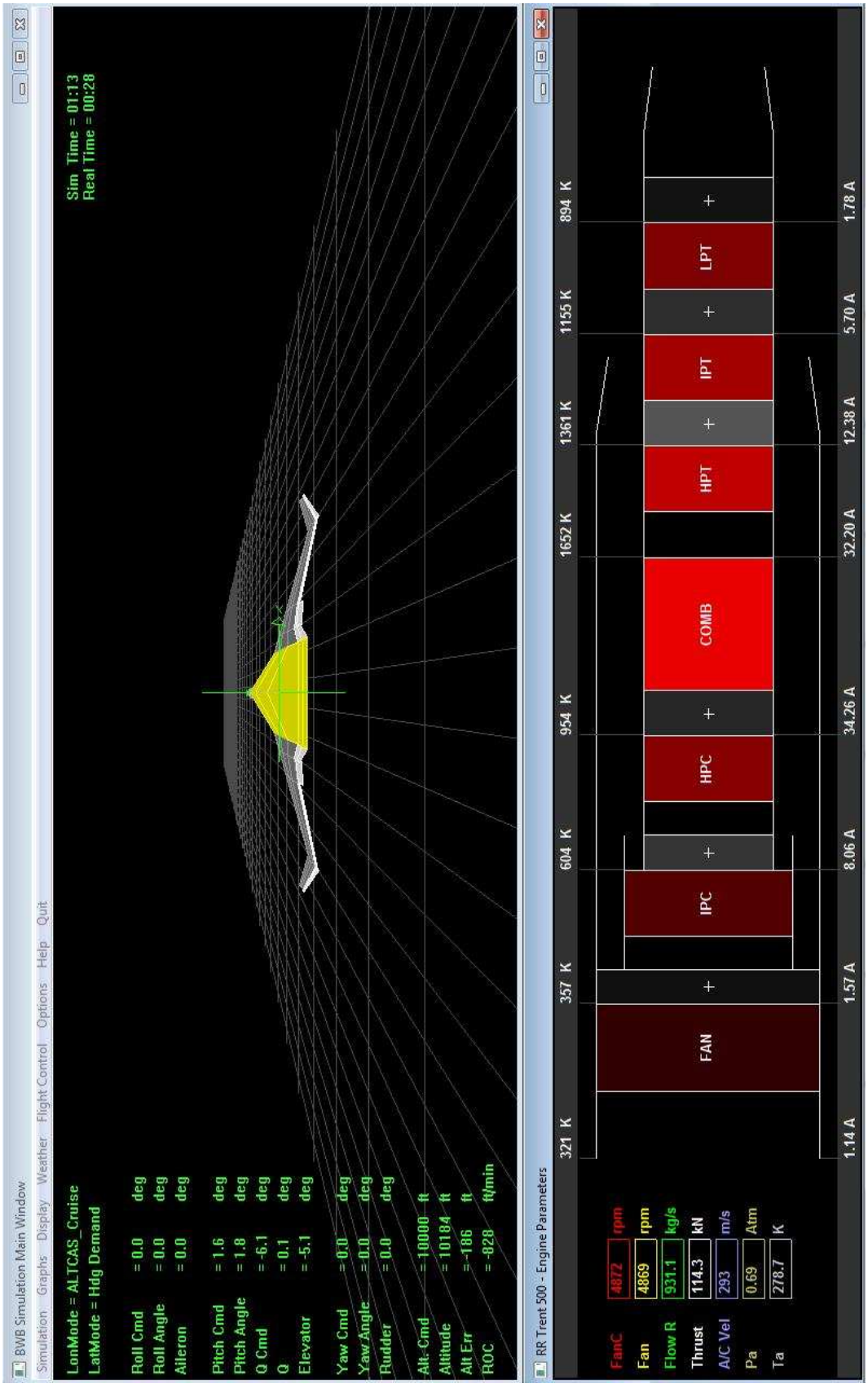

Figure 7.1: BWB and engine simulation output window

7.2 Landing with TVC and Flap Blowing

Various parameters are important in the approach and landing task, these include the approach speed, the maximum landing weight, the approach attitude or pitch angle and control deflections. For a conventional aircraft, both take-off and landing are performed with a high lift configuration, so that the take-off and landing speeds are low and the pitch attitude is usually not more than 5-7 degrees. For the BWB aircraft however, a high lift configuration is difficult to use as there is no horizontal stabilizer to trim the resulting negative pitching moment from the wing, consequently for nominal static margins, the approach attitude and trim elevator deflections are unusually high.

The landing task considers a BWB aircraft making a runway approach from an initial lateral offset of 1 km and a down-range of 10 km. An approach airspeed of 160 kts was to be maintained at a glide slope of $-2.5°$. Results for AFC + TVC = $10°$ and with addition of central flap blowing at $C_u = 0.2$ are presented. The aim of TVC and flap blowing is to reduce the landing performance parameters (approach attitude and trim elevator) stated above. For simplicity, the under-carriage model and the ground effects were not simulated, however ground friction and braking were included. Figure 7.2 shows the approach trajectory from point A to B under FCS control.

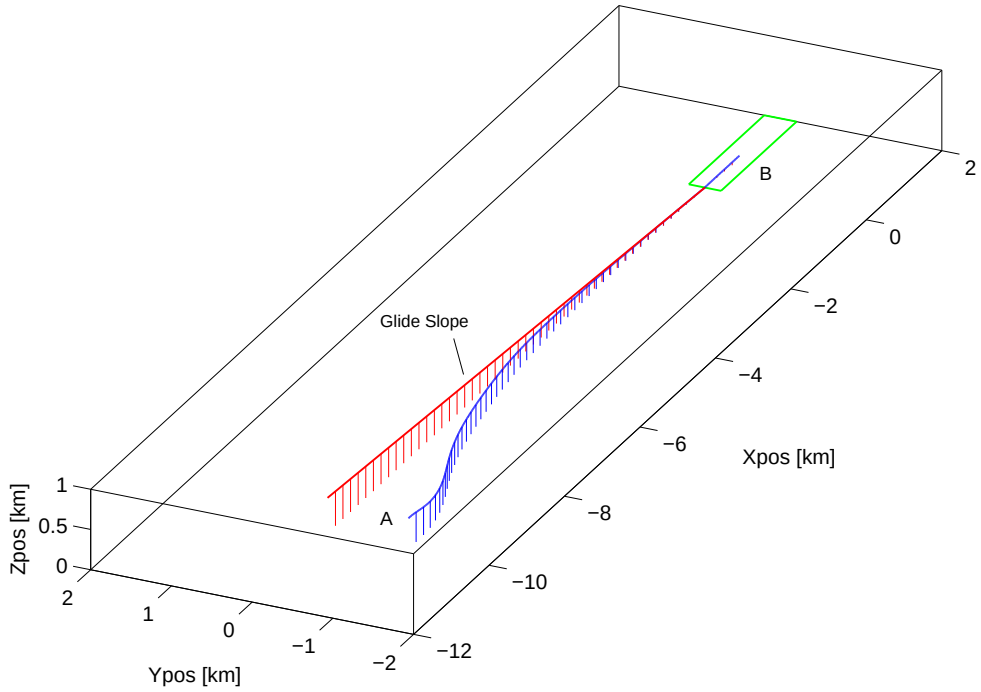

Figure 7.2: Glide slope coupler with an initial lateral offset of -1000m

7.2.1 Landing with Fixed TVC

Figure 7.3 shows the time histories for approach/landing task with and without TVC. Case A is the nominal configuration under pure aerodynamic flight control (AFC) whereas case B is with addition of fixed thrust vector control of 10°. The CG position was set at a nominal value of 29.4 m corresponding to a static margin of 18%. A forward CG location was selected so as to ascertain the benefits of TVC or flap blowing for flight cases when aerodynamic controls on the BWB are near saturation.

For the pure AFC (case A), the trim elevator deflections are high (−17.2°) along with an angle of attack of +11.3°. When TVC is activated at 75 seconds, the trim elevator deflections reduce to −9.8° and the angle of attack reduces by 4.5%. The throttle however increases by 1.0% due to loss of net axial thrust, which is not a significant price to pay. The reduction in angle of attack is marginal as compared to reduction in trim elevator deflection as the vertical component of thrust acts downwards and takes away a significant portion of lift. Thus to sustain the weight of the aircraft, the angle of attack remains high.

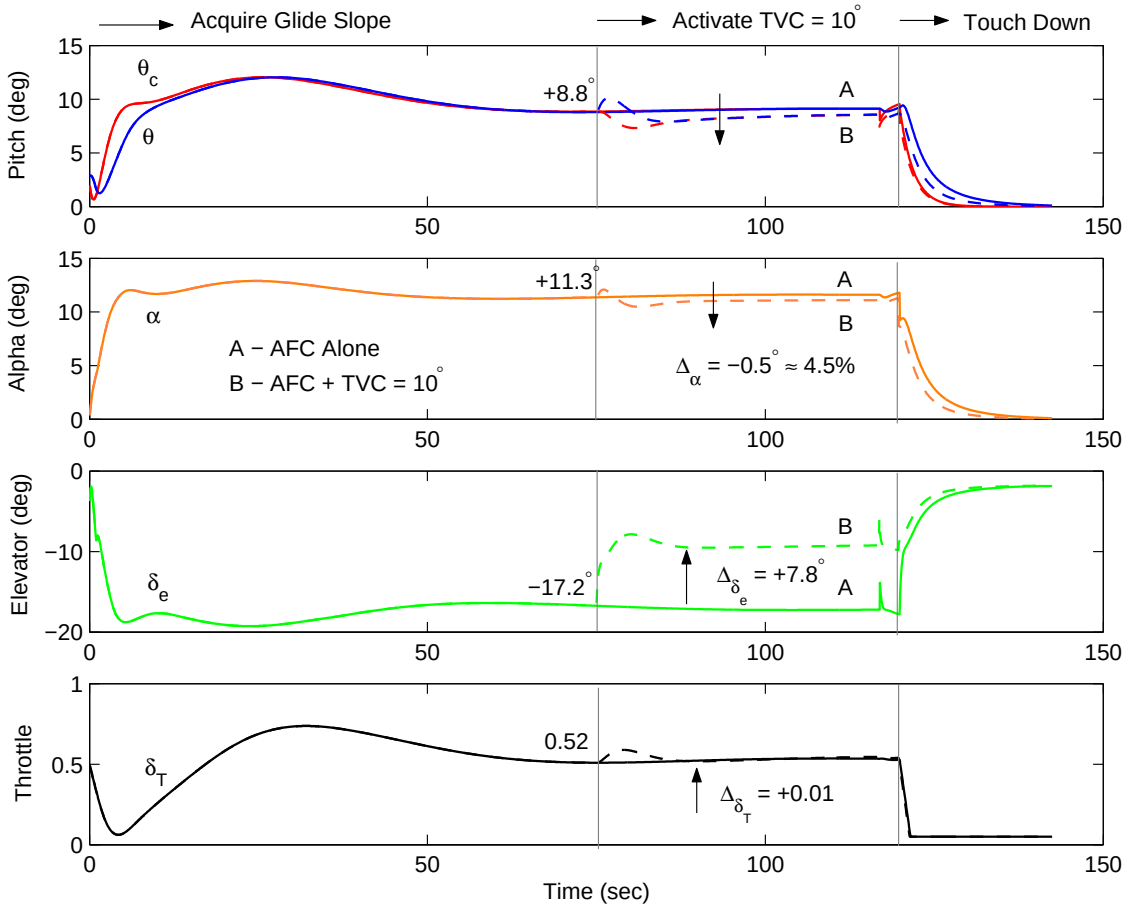

Figure 7.3: Landing at 160kts with fixed TVC = 10°

7.2.2 Landing with Fixed TVC + Flap Blowing

In Figure 7.4, the addition of flap blowing to TVC has similar effects, except the trim throttle reduces by 5.0% for a blowing momentum coefficient of 0.2 on the central flaps. The angle of attack, the trim elevator and the pitch attitude reduce further. The reduction in trim throttle could be explained by the fact that with flap blowing the reduction in angle of attack causes a net reduction in trim drag and hence the thrust required to maintain flight. The net reduction in angle of attack is now 10% which is significant. Table 7.1 summarizes these results.

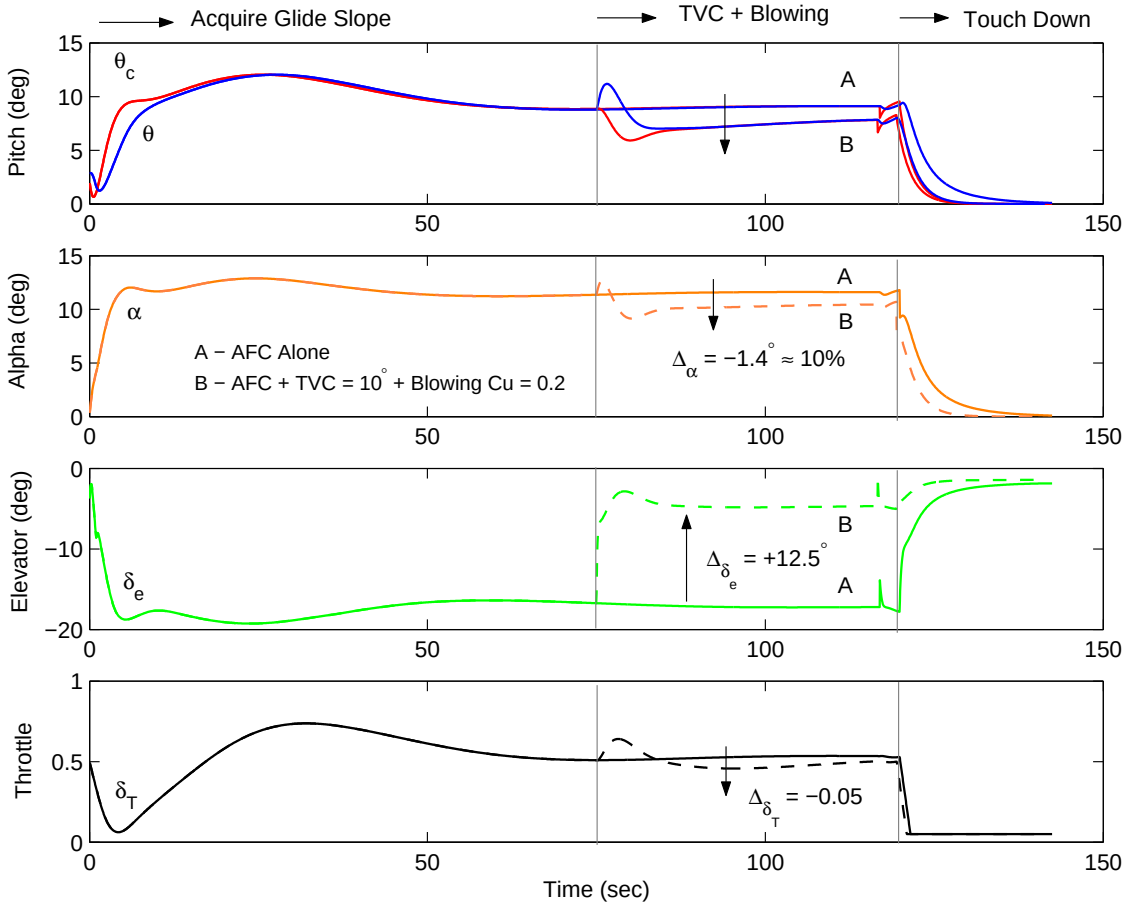

Figure 7.4: Landing with TVC = 10° + Central flap blowing at $C_u = 0.2$

No	TVC	C_u	$\Delta\alpha$ (%)	$\Delta\delta_e$ (%)	$\Delta\delta_T$ (%)
1	0	0	0	0	0
2	10.0	0	-4.50	-46.0	+0.62
3	10.0	0.05	-6.26	-61.3	-1.12
4	10.0	0.10	-7.75	-66.3	-2.45
5	10.0	0.15	-9.07	-69.8	-3.67
6	10.0	0.20	-10.4	-72.4	-4.82

Table 7.1: Approach/Landing performance with TVC and central flap blowing

7.3 Take-off Performance

7.3.1 Description of Take-off Phases

Before considering the take-off performance for the BWB, it is pertinent to review some of the basic definitions and requirements for the take-off phase. These are illustrated in Figure 7.5 and explained below.

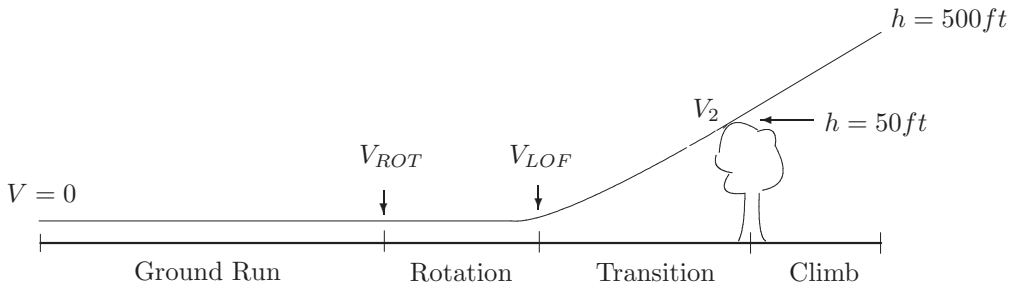

Figure 7.5: Take-off phases

- **Ground Run -** During the ground-run phase the aircraft accelerates from $V = 0$ to V_{LOF} in T_g seconds. The distance covered during this phase is R_g. The angle of attack remains constant as determined by the landing gear geometry and the velocity vector remains parallel to the runway.

- **Rotation -** After the aircraft has built up sufficient speed for aerodynamic controls to become effective, the aircraft is rotated to a higher angle of attack. At this moment the aircraft speed is

$$V = V_{LOF} = k_1 V_{stall} \tag{7.1}$$

where

$$V_{stall} = \sqrt{\frac{W}{1/2\rho S C_{L_{max}}}} \tag{7.2}$$

and $k_1 = 1.1$ or 1.15 depending upon the type of aircraft. The trouble with the BWB is that the lift coefficient is a strong function of elevator deflection. As soon as the flaps are deflected negative (upwards) the lift coefficient drops. The result is that a higher lift-off speed is needed so that the flaps are more powerful and need to be deflected less to achieve the desired nose rotation.

- **Transition -** From the time the aircraft breaks ground until it reaches an altitude of 50 ft and a speed of $V_2 = 1.2V_{stall}$ or greater, it is considered to be in transition phase. The total horizontal distance traveled by the aircraft from start of ground-run to the end of transition phase (clearance of 50 ft obstacle) is the take-off field length.

7.3.2 Forces and Moments on BWB During Take-off

Consider a BWB aircraft in take-off run in Figure 7.6. During the take-off phase additional forces and moments come into play, such as ground friction and reaction. In addition, the pitch rotation takes place about the main landing gear and not the centre of gravity. This means that the weight of the aircraft along Z-body axis, Z_g and the Z-axis aerodynamic force, Z_a, also exert a moment about the landing gear. The distance of the CG from the main landing gear, l_1, thus becomes an important consideration. In addition the axial thrust, X_E also exerts a negative pitching moment about the main landing gear. Since the engines are assumed to be embedded within the fuselage, the perpendicular distance of thrust line from the ground, h, has to be kept to a minimum. This all is bad news for the BWB as the elevators have already been shown to be less effective at low airspeeds, overcoming these additional pitching moments during take-off therefore becomes an issue.

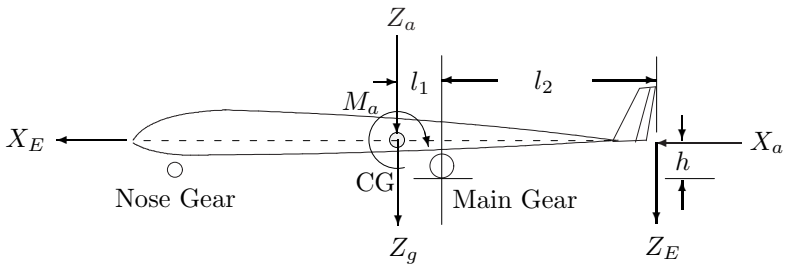

Figure 7.6: Forces and moments on the BWB during take-off

The pitching moment equation used for take-off analysis is given below. The reaction force from the nose landing gear has been neglected.

$$M_{LG} = M_a - (Z_a + Z_g)l_1 - (X_a + X_E)h + Z_E l_2 \tag{7.3}$$

Here M_a represents the aerodynamic moments about the CG including the blown flap effects and the term $Z_E l_2$ represents the positive pitching moment due to vectored thrust. For the current analysis, l_1 was set at 4.0 m, l_2 at 16.0 m and the perpendicular distance of thrust line from main landing gear, h, was set at 3.0 m.

7.3.3 Nominal Un-Assisted Take-off

For take-off simulations, following assumptions were made, (i) ground friction coefficient was taken as 0.016 as per reference [7] and is typical of rolling friction coefficients for hard rubber on concrete, (ii) a maximum take-off weight (MTOW) of 371,280 kg and (iii) a nose gear pitch setting angle, $\theta_{LG} = 0°$.

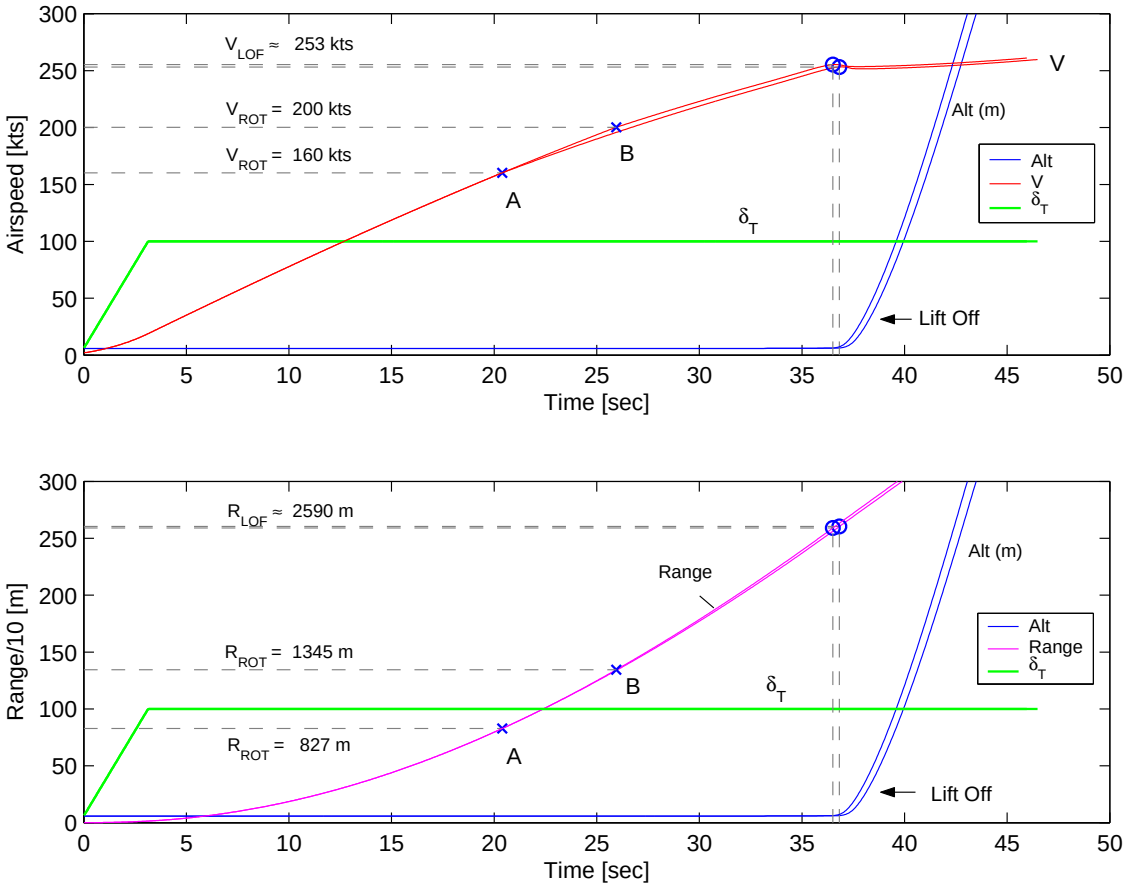

Figure 7.7: Take-off simulations for BWB aircraft, (No TVC or flap blowing)

Figure 7.7 shows the range, speed and altitude profiles during the take-off phase. No TVC or flap blowing was applied. The nose rotation speed, V_{ROT}, was adjusted from 160 kts for case A to 200 kts for case B. With minor variations, the lift-off speed, V_{LOF}, was approximately 253 kts and the lift-off range, R_{LOF}, was 2.59 km.

With reference to Figure 7.8, at about 20 seconds or an airspeed of 160 kts, the elevator deflection is set at $-25°$ (max) by the FCS in an attempt to bring the aircraft nose up to a pitch demand of $+12.5°$. The nose however does not start to rotate until about 30 seconds and the lift-off occurs above 250 kts when sufficient angle of attack has built up. These take-off characteristics for the BWB can be explained by the breakdown of pitching moment about the main landing gear (Figure 7.8).

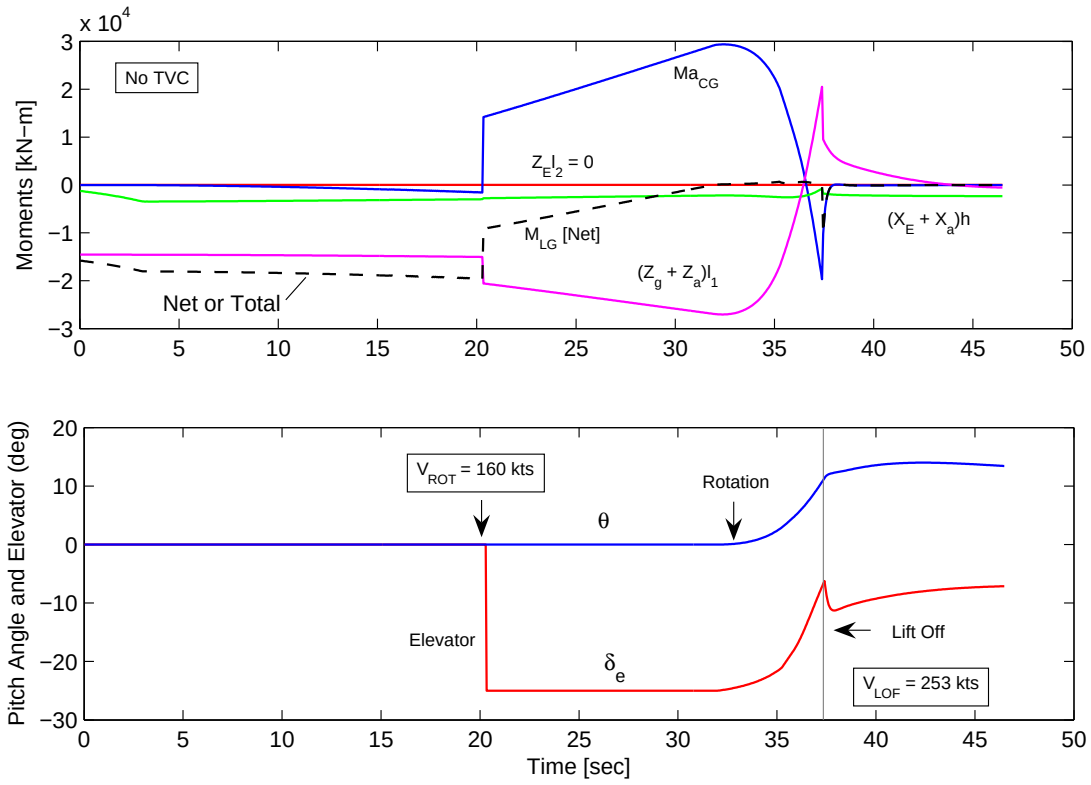

Figure 7.8: Pitch moment break down about the main landing gear

- $Z_E l_2$ - Since no thrust vectoring is assumed this component is zero.
- $(X_E + X_a)h$ - When $X_E > X_a$ i-e thrust greater than aerodynamic drag, the pitching moment about main landing gear due to these forces is negative.
- $(Z_a + Z_g)l_1$ - At low airspeeds and small angle of attack $Z_g > Z_a$, i-e the weight of the aircraft is much higher than lift and since the CG is ahead of the main landing gear by distance l_1, the pitch moment due to these Z-axis forces is again negative or nose down. Only at a higher airspeed and angle of attack during the pitch rotation phase does this component reverse and act upwards.
- $M_{a_{CG}}$ - The only nose up pitching moment comes from the elevator, which gets stronger as the airspeed is built up. At a certain airspeed, the net moment about the landing gear (M_{LG}) becomes positive and the nose begins to rotate.

Various parameters strongly affect these take-off simulation results, such as the distance of main landing gear from the CG ($l_1 = 4$ m), the height of the thrust line from the ground ($h = 3$ m), and the nose landing gear pitching offset angle ($\theta_{LG} = 0°$). However the purpose of this exercise is to establish a worst case baseline and then evaluate the increments above it due to propulsion/controls integration.

7.3.4 Take-off Performance with TVC and Flap Blowing

It was observed in the previous section that when the trailing edge flaps on the BWB are deflected for pitch rotation there is a significant drop in lift or the Z-axis aerodynamic force, Z_a. This is a problem specific to tailless designs, due to the dual role of wing in producing lift and provision of longitudinal controls. The aircraft thus has to attain a higher dynamic pressure and angle of attack for lift-off. Use of thrust vectoring is therefore an attractive option to achieve early pitch rotation.

Take-off Performance with TVC - Figure 7.9 shows take-off simulation results for vectored thrust up to 20°. For a fixed TVC of 20°, the lift-off speed reduces from 253 to 193 kts and the lift-off range reduces to 1413 m. This is a significant improvement. The TVC however should be applied only when the pitch rotation is required, after the aircraft enters the climb phase, use of TVC will restrict the maximum achievable rate of climb. Similar results were achieved by use of the blown flap arrangement.

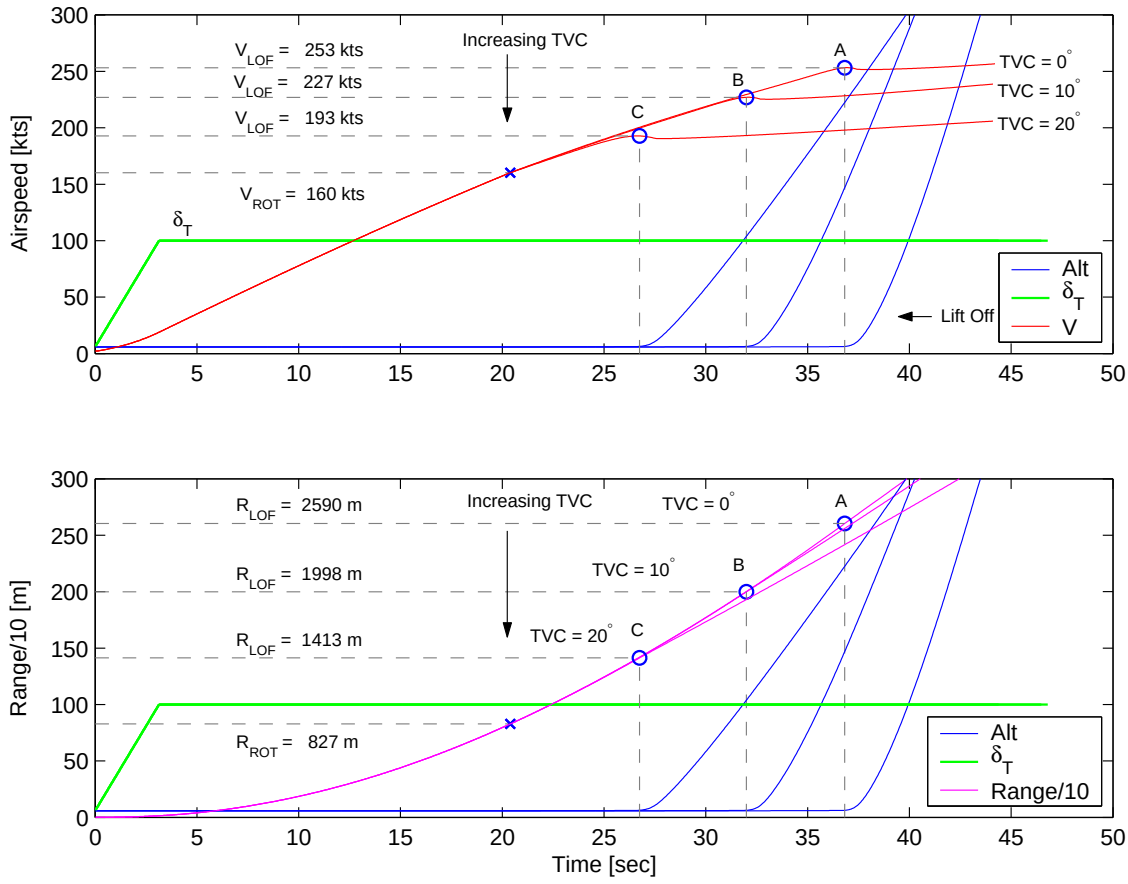

Figure 7.9: Take-off performance with thrust vectoring

Take-off Performance with TVC and Externally Blown Flaps - Figure 7.10 shows results of TVC of 10° and flap blowing on the centre-body at C_u of 0.2. The results are quite similar to the TVC with 20°, the lift-off speed is now reduced to 187 kts at lift-off range of 1330 m.

As in Figure 7.11, as soon as the elevator is applied at the rotation speed of 160 kts, the nose of the aircraft begins to rotate. The pitching moment due to vectored thrust ($Z_E l_2$) is now positive and corresponds to a TVC angle of 10°. The elevator also does not saturate as in the un-assisted take-off case, and the pitch angle error is reduced very quickly. The effect of blown flaps appears in the form of increased aerodynamic pitch moment about the CG. This in combination with the pitching moment from TVC are enough to rotate the nose even at an airspeed of 160 kts.

It may be mentioned here that these results are representative, in actuality there are many parameters aerodynamic, geometric or environmental that will affect the take-off performance. A summary of these results is presented in Table 7.2.

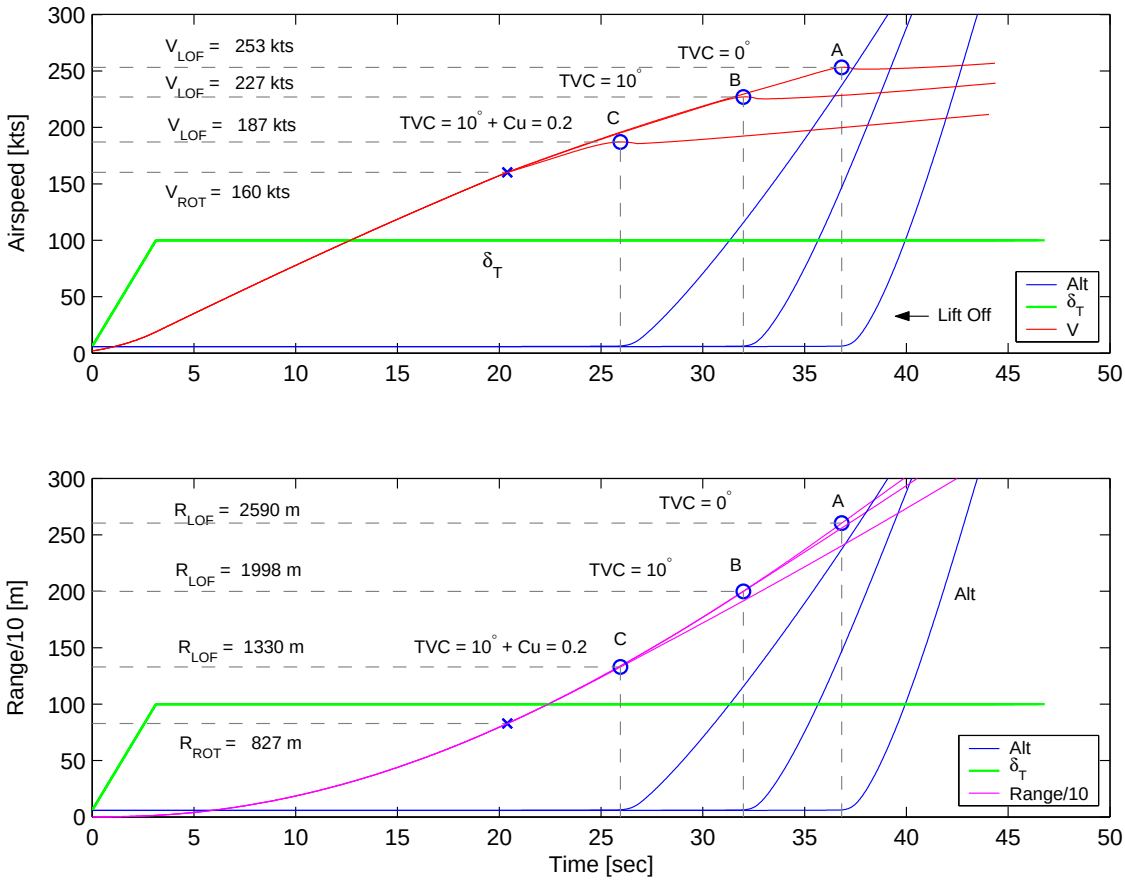

Figure 7.10: Take-off performance with limited TVC and central flap blowing

No	TVC	C_u	V_{ROT}	R_{LOF}	ΔR_{LOF}	V_{LOF}	ΔV_{LOF}
	deg		kts	m	(%)	kts	(%)
1	0	0	160	2590	0	253	0
2	10.0	0	160	1998	-22.86	227	-10.28
3	20.0	0	160	1413	-45.44	193	-23.72
4	10.0	0.20	160	1330	-48.65	187	-26.10

Table 7.2: Take-off performance with TVC and central flap blowing

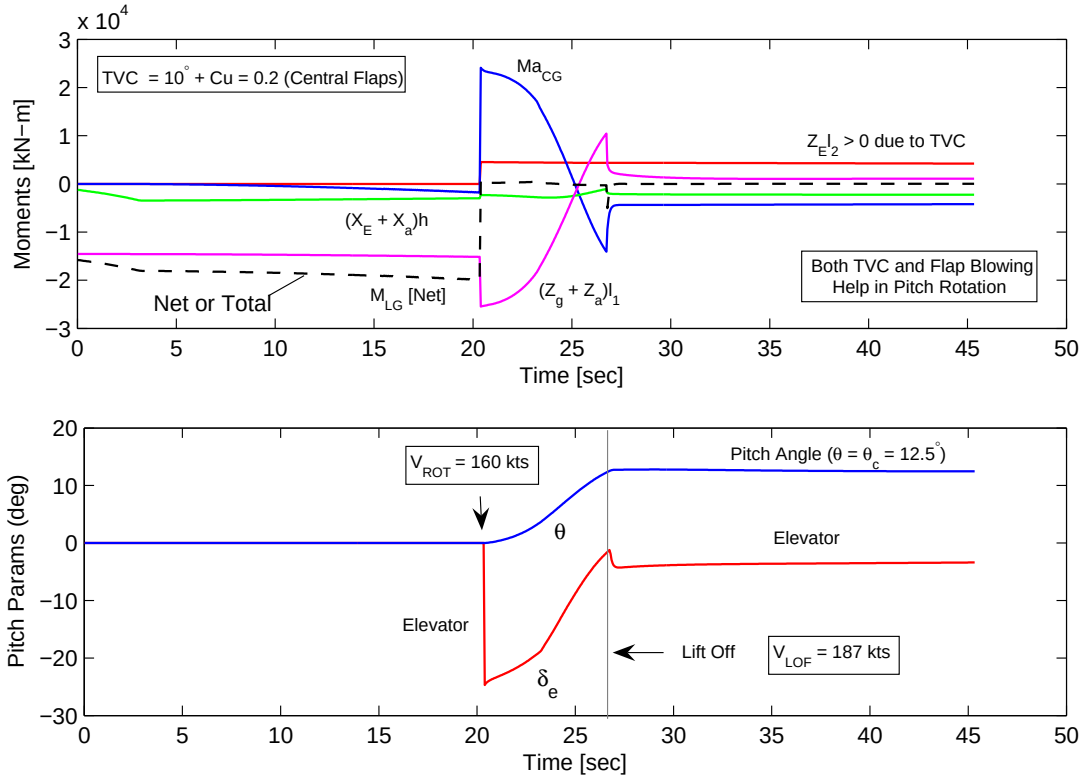

Figure 7.11: Pitch moments about main landing gear with TVC and flap blowing

7.4 Chapter Summary

This chapter presented the results of TVC and flap blowing for the landing and take-off flight phases of the BWB. For the landing task use of TVC/flap blowing reduces the trim elevator deflections significantly and the angle of attack and trim throttle settings marginally. Use of limited TVC and central flap blowing for the take-off phase have very significant benefits in terms of reduction of take-off field length and lift-off speeds. A careful airframe/propulsion integration and controls augmentation can result in large pay-offs for these low speed flight conditions.

Chapter 8

Conclusions and Further Research

This chapter concludes this research work and presents a summary of the main findings. In addition, it suggests some guidelines for further research on the subject.

8.1 Conclusions

The integration of propulsion and flight control systems for the BWB aircraft is a multidisciplinary design problem. Excluding structural aspects, it involved at least three major areas, namely, (i) the propulsion system, (ii) the airframe and the last but not the least (iii) the flight control system. Thus the basic research question needed expertise in all these well defined and intricate disciplines. It was therefore difficult for a single researcher to be able to address all these areas with equal efficacy, however a humble effort has been made in a limited time frame and certain conclusions were drawn. These are summarized as follows.

- **Control Authority of the Baseline Configuration -** Longitudinal trim analysis reveals that for nominal static margins ($K_n > 15\%$) and low airspeeds ($V < 200$ kts), large negative elevator deflections are required to maintain trim and as a consequence the BWB aircraft looses much of its lift generation capability. This is contrary to what is desired at take-off and landing speeds when the required lift coefficient must be high to sustain the weight of the aircraft. If conventional aerodynamic controls are to be retained it becomes apparent from longiudinal trim analysis alone that the only efficient way to fly the BWB aircraft is to fly it either neutrally stable or at a much reduced static margin ($5\% < K_n < 10\%$). A similar analysis for the lateral directional axis shows that at low dynamic pressures, the small winglet rudders are not sufficient to maintain direction under an asymmetric thrust flight condition.

These results however do not come as a surprise since the BWB design neither has a conventional horizontal stabilizer or a vertical fin. A price has to be payed in order to achieve the promised high speed aerodynamic efficiency. To conclude, both rudder and elevator control authority augmentation are considered necessary at landing and take-off speeds.

- **Linear Dynamics and Stability Augmentation -** Longitudinal linear analysis suggests that as soon as the static margin gets below 10%, the short period mode detoriates rapidly. This is contrary to the longitudinal trim requirements where a lower static margin is desirable. In either case, a stability augmenation system (SAS) using angle of attack and pitch rate feedback was designed and implemented, ensuring Level 1 flying qualities throughout the flight enevelope. This flight control system was found to work adequately well even with the blown flap and thrust vectored arrangements.

  The open loop lateral-directional dynamics were very poor, with strong roll/yaw cross coupling and high values of adverse yaw. The dutch roll mode is very slow and poorly damped however it was improved using sideslip and yaw rate feedback but higher gains had to be used due to limited rudder control power. The adverse yaw problem was also severe, and large values of aileron to rudder interconnect were required to maintain coordinated turns. In fact at low airspeeds, the aileron to rudder interconnect gain (K_{ARI}) exceeds 1.0, that is the same amount of rudder deflection as the aileron. Considering its small size, both the static and dynamic requirements on the winglet rudder are severe.

  The roll axis was also found to be sluggish due to the large roll axis inertia. The inboard ailerons were not able to meet the handling qualities requirements at low airspeeds, necessitating the use of control allocation or use of additional outboard flaps for the roll control below 200 kts. This means a further reduction in pitch control authority and strengthening of the earlier argument for using alternate means of control augmentation for the pitch axis.

- **Propulsion and Airframe Models with Blown Flap Effects -** A hybrid three spool turbofan model using a combination of iterative and inter-component volume techniques was developed. The model provided valuable insight into the effects on engine performance due to IPC/LPC bleed, required for flap blowing or due to thrust vectoring, required for pitch controls

augmentation. Subsequently a BWB aerodynamic model using strip element techniques and Engineering Sciences Data Units (ESDUs) was developed and validated against the baseline [7]. The effect of trailing edge flap blowing and the corresponding increase in lift coefficient was incorporated in the model using the Spence's jet flap theory [14].

Flap blowing causes a significant increase in flap effectiveness ($C_{L_{\delta_e}}$) and therefore the pitching moment ($C_{m_{\delta_e}}$) produced by it. For positive flap deflections, usually required for high lift, the change in lift coefficient ($\Delta C_{L_{\delta_e}}$) is positive and the pitching moment negative. For negative flap deflections, required for pitch trim, the converse is true. Flap blowing has traditionally been used to generate high lift, however the accompanying negative pitching moment is a problem for the BWB. This negative pitch moment has to be overcome either by a provision of an additional control surface such a canard, or through propulsive means, before the full potential of flap blowing for high lift can be realized. For the BWB aircraft however, the flaps are deflected negative to maintain pitch trim, the effect of blown flaps appears as reduction in trim elevator deflections or greater pitch control power.

The increments in lift and pitching moments were evaluated at various blowing coefficients, C_u, for full span flap blowing. Even for a conservative C_u of 0.2 at +25 deg flap deflection, the increment in lift coefficient ($\Delta C_{L_{\delta_e}}$) exceeds 1.0, but at the same time is also accompanied by a strong nose down pitch moment. For the lateral-directional axis the control power was doubled at $C_u = 0.2$ for both the inboard aileron and the winglet rudder.

- **Allowable Engine Bleed and Achievable Blowing Coefficients -** With the engine and airframe models in place, it was now possible to integrate these models in a non-linear simulation environment. Allowable engine bleeds, suitable bleed locations and the achievable blowing coefficients were the first few questions to be answered.

  1. **IPC Bleed - Internal Flap Blowing -** Bleeding from the end of intermediate compressor IPC(1.0) with a 3 mm slot height at 4300 Fan RPM causes almost 40% of IPC net mass flow to be bled and a significant degradation in engine performance. The resulting blowing coefficients were just below $C_{u_{crit}} = 0.02 - 0.03$, the minimum momentum to prevent

flow separation. If the engine is not matched for permanent IPC bleed and full span blowing is to be incorporated, slot height has to be limited to keep bleed mass flow within acceptable limits. The rise in TET due to IPC bleed, IP compressor choking and HP compressor surge can be avoided by bleeding the IPC at an earlier station along its axial length. Even with an IPC bleed location of $x/l = 0.25$, the gains in flap effectiveness were not highly compromised. An alternate and more feasible option is to match the engine for permanent IPC bleed, this however requires freezing the airframe design first to establish bleed requirements. The airframe and engine designs thus become inter-dependant. Both of these options can provide much higher blowing coefficients with relatively lower penalties on engine performance. However to keep the blowing duct diameters small it is suggested that minimal bleed be taken from the intermediate compressor. To achieve this, only selected flaps such as the aileron or the winglet rudder may be blown at lower airspeeds.

2. **LPC Bleed - External Flap Blowing -** If the LPC/Fan stage is used for flap blowing, the Fan exit pressure is generally less and therefore the jet velocities are low. However there is theoretically no limit on the amount of mass flow that could be used for flap blowing. A feasible option is therefore to consider all of the LPC/core mass flow for external flap blowing for the center body section which has a span of 26 m. Thus all the mass flow from the engine exhaust impinges upon the center body flaps. Blowing coefficients in excess of 0.25 were shown to be easily achieved in this way. For the longitudinal axis or pitch control, it is suggested to use external flap blowing directly, thus not only providing larger blowing coefficients, but also a possible mechanism to deflect thrust. The amount of thrust deflection that can be achieved with such an arrangement shall however require further CFD/experimental work, and can be made part of future research.

- **Controls Performance with Flap Blowing and TVC** Two aspects of controls augmentation from the propulsion system were considered, namely thrust vectoring and flap blowing.

  1. **Thrust Vector Control (TVC) -** For nominal static margins, pure thrust vectoring is able to maintain pitch trim but only under high thrust conditions. At lower throttle settings, the nozzle deflection exceeds nominal limits. However, thrust vectoring is effective when used in combina-

tion with aerodynamic flight controls (AFC). For the low speed approach flight condition at 160 kts and with AFC assisted by just 10° of fixed TVC, the trim elevator reduces by 46%, angle of attack by 4.5% and accompanied by only a marginal increase in trim throttle setting. The main benefit occurs in the take-off flight condition, where thrust vectoring helps in achieving early pitch rotation, thus significantly reducing the take-off field lengths and the lift-off speeds. For example with 10° of TVC, lift-off range reduces by 22% and lift-off velocity by almost 10%.

2. **Flap Blowing -** Utilization of blown flaps had similar effects. Blown flaps were helpful in reducing trim flap deflections during approach and landing and reducing lift-off distances during take-off runs. For example addition of central flap blowing at $C_u = 0.2$, in addition to 10° TVC, reduces the lift-off distance by another 25% and lift-off velocities by a further 15%. Similarly, at approach speeds, flap blowing makes the flaps more efffective, resulting in a reduction of trim flap deflections. This is accompanied by a marginal reduction in angle of attack, which reduces induced drag and hence in turn the required thrust to sustain flight. For an approach case at 160 kts, addition of central flap blowing at $C_u = 0.2$ in addition to 10° of TVC, reduces trim elevator deflections by a further 26% and the throttle setting by almost 5%.

To conclude, both flap blowing and thrust vector control have comparable advantages in provision of additional of pitch, roll and yaw control powers. For the BWB aircraft in particular when operating with forward CG locations at low airspeeds, controls begin to saturate and the angle of attack begins to increase. Provision of propulsion augmentation to the aerodynamic controls at these low speed flight conditions has potential benefits if implemented properly. However a multi-disciplinary design approach has to be adopted to make the overall integration of airframe, flight control system and the propulsion system successful.

8.2 Further Research

With regards to future work on the subject, following suggestions are made,

- **Experimental/CFD Aerodynamic Data -** The aerodynamic models developed in this work used both empirical (ESDUs) and vortex lattice methods (VLM) to predict lift, drag, pitching moment and other aerodynamic characteristics for the BWB. Effect of blown flaps was added using the well established jet-flap theory [14]. This aerodynamic model however must be further improved using either CFD techniques or experimental methods for aerodynamic prediction. These methods will provide better aerodynamic estimates for the blown flap configuration and a more accurate control systems analysis can be carried out.

  Trailing edge flap blowing or distributed propulsion concepts have the potential of reducing the overall drag by re-energizing the low energy wake from the trailing edge [42]. In the current work, only lift and pitching moment were of specific interest and no effort was made to evaluate the reduction in aerodynamic drag due to trailing edge blowing. Any future work must also address this important aspect of aircraft design.

  It has been reported in this work that externally blown trailing edge flaps on the center section can provide a possible mechanism of thrust deflection. How much thrust deflection can practically be achieved with such an arrangement was however not investigated. If feasible, this may provide a simple and efficient way of vectored thrust for the BWB, which was considered to be valuable during the take-off and landing phases.

- **A Higher Thrust Engine Model -** At the start of this research work, the Trent 500 series engine with a sea-level static thrust of 275 kN was selected. This was done primarily due to availability of the design point information for this engine and also due to the fact that the Boeing-747, which is of a similar weight class uses this engine. However later on, as further analysis was carried out it was found that at reduced airspeeds, specifically at approach, the induced drag is very high and a $4\times275 = 1100$ kN engine configuration is not enough to maintain the desired flight path. The total thrust was scaled up to 1650 kN both for take-off and landing analysis. Any future research effort can expand upon the current propulsion model by updating the compressor

and turbine maps and other associated engine parameters to simulate a higher thrust engine.

- **Structural and Aerodynamic Interaction -** The BWB aircraft considered in this research had a span of approximately 80 m, structures of such large size are generally not rigid. The aerodynamic model that has been developed as part of this work considers the aircraft as a rigid structure, however the strip element approach allows easy integration of any structural changes under variable aerodynamic loading. This may include wing bending, torsion or even flutter. Structural/aerodynamic interaction aspects may therefore be also considered for further research.

- **Modifications to the Basic Airframe -** Both thrust vectoring and flap blowing were able to solve the control authority problem, however at lower airspeeds and high static margins ($K_n > 15\%$) the problem of high angle of attack remains. A simple an efficient means to solve this problem is to relax the static margin, which causes significant reduction in both trim angle of attack and elevator deflections. If however, the static margin is to be maintained as may be desirable for a commercial airliner, an alternate option is to use a canard arrangement. This has the potential of providing the requisite nose up pitching moment and reducing the trim angle of attack at low speed flight conditions. The pros and cons of such a configuration, specifically its effects on cruise conditions however need to be carefully examined.

  The rudder control authority problem for asymmetric thrust conditions was shown to be improved using a jet flapped rudder. However the size of the rudder is still too small and directional stability augmentation gains, specifically the washout and the aileron to rudder interconnect are too high. If the cruise drag penalties are not great, it is suggested that conventional twin vertical fins be incorporated to the basic planform. This will also speed up the dutch roll by providing natural directional stiffness into the aerodynamic design.

  Further research specifically by an aerodynamicist will be required to validate if the above suggestions are appropriate.

8.3 Dissemination of Results

The findings have been published/presented at the following forums.

Journal Publications

- Rahman, N.U and Whidborne, J.F (2008). A Numerical Investigation into the Effect of Engine Bleed on Performance of a Single-Spool Turbojet Engine, *Journal of Aerospace Engineering, IMECHE*, Vol 222, Part G, pp 939-949.
- Rahman, N.U and Whidborne, J.F (2009). Real-Time Transient Three Spool Turbofan Engine Simulation: A Hybrid Approach, *Journal of Gas Turbines and Power, ASME*, Published Online, 051602-2 / Vol. 131, Sept 2009 .
- Rahman, N.U and Whidborne, J.F (2009). Propulsion and Flight Controls Integration for the Blended Wing Body Transport Aircraft, Submitted to the *Journal of Aircraft*.

Conference Proceedings

- Rahman, N.U and Whidborne, J.F (2008). A Lateral Directional Flight Control System for the Blended Wing Body Aircraft, *Proc, UKACC International Control Conference, 2008*, Manchester, UK.
- Rahman, N.U and Whidborne, J.F (2008). A Longitudinal Flight control System for the Blended Wing Body Aircraft, *Proc, IBCAST International Bhurban Control Conference, 2009*, Islamabad, Pakistan.
- Rahman, N.U and Whidborne, J.F (2008). A Numerical Investigation of Engine Bleed on the performance of a Single Spool Turbojet Engine, *Proc, IEEE Controls Conference Imperial College, 2007*, London, UK.

Appendix A

BWB Data - Baseline

A.1 General Description

This section discusses the geometric, mass and aerodynamic properties for the reference BWB aircraft, used for model validation and FCS design. The data has been obtained from a previous work done at Cranfield University by H.D. Castro [7]. Castro actually compared several BWB configurations and in most of the cases the aerodynamic properties were estimated using computational techniques. Figure A.1 shows the general layout of the aircraft.

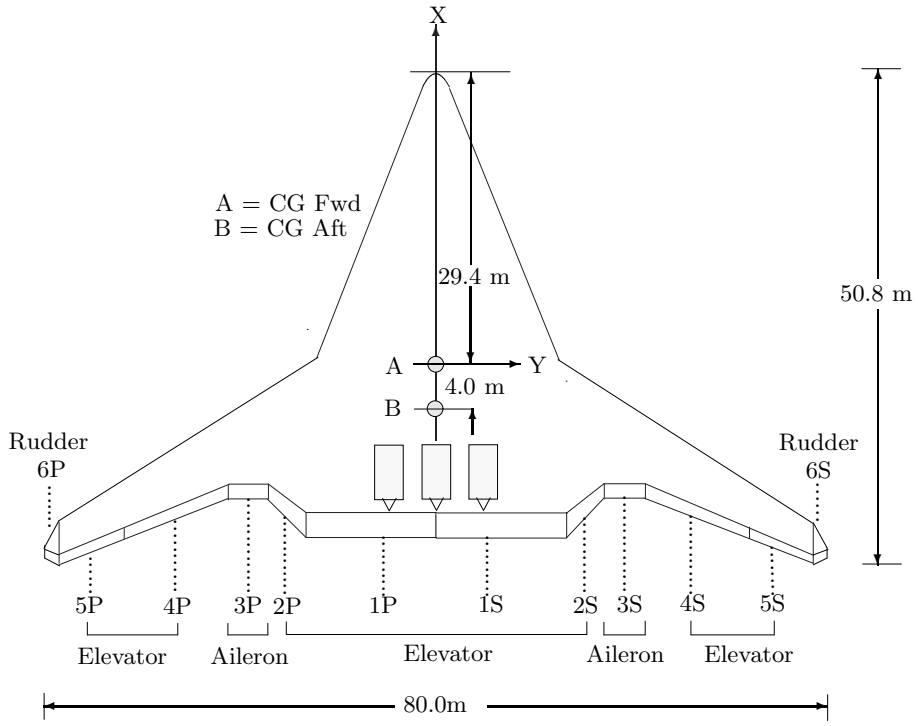

Figure A.1: General layout of the BWB aircraft

The aircraft has 12 control surfaces numbered from left to right. Two of these surfaces 6S (starboard) and 6P (port), are on the vertical fins and provide the rudder function. The remaining 10 control surfaces are located on the trailing edge of the lifting body and provide for lateral (roll) and longitudinal (pitch) control functions. It may be noted that nearly all the control surfaces except control surfaces 3S and 3P, are used as elevators. The reason for this unusual control allocation is that a larger elevator surface is required to compensate for the loss in moment arm caused by omission of the horizontal tail. Figure A.2 shows the controls convention used. From reference [7] a maximum flap deflection range of $\pm 30^{\circ}$ is assumed on all flaps including the winglet rudder.

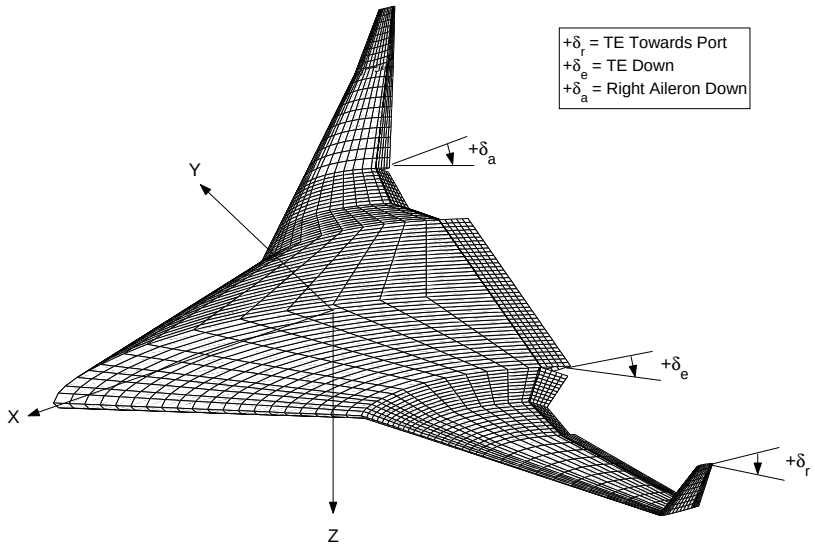

Figure A.2: Control convention on the BWB aircraft

A.2 Mass and Inertia Properties

The mass and inertia properties at maximum take-off weight (MTOW) from Appendix D of reference [7] are listed in Table A.1. The values at maximum landing weight (MLW) were extrapolated by assuming a reduction in mass from 371,280 to 322,600 kg. From Table A.1, it may be noted that the value of I_{zz} is particularly high, specifically I_{zz} must be less than $(I_{xx} + I_{yy})$, which is not true in this case. Higher I_{zz} values will cause the lateral directional dynamics to be slower and therefore difficult to augment, especially in the absence of a conventional rudder. However noting that I_{zz} values will be on the high side owing to the un-conventional planform shape and in the absence of any further information on the mass properties

for this configuration, these inertia values were considered adequate for the initial control system design and analysis.

Parameter	BWB (MTOW)	BWB (MLW)	Units
Aircraft mass , m	371,280	322,600	kg
Inertia about X axis, I_{xx}	47.03e+06	40.72e+06	kg-m^2
Inertia about Y axis, I_{yy}	25.06e+06	21.70e+06	kg-m^2
Inertia about Z axis, I_{zz}	99.73e+06	86.36e+06	kg-m^2

Table A.1: BWB mass and inertia properties [7]

A.3 Geometric properties

The key geometric properties of the baseline BWB aircraft are listed in Table A.2.

Wing Parameter	Notation	Value	Units
Gross area	S_{gross}	1390.6	m^2
Wing reference area	S_{ref}	841.70	m^2
Wing span	b	80.00	m
Mean aerodynamic chord	$\bar{c}$	12.31	m
Trapezoidal aspect ratio	AR	7.14	-
Root chord	c_{root}	48.0	m
Tip chord	c_{tip}	4.0	m
Leading edge sweep	Λ_{LE}		
Center		63.8	deg
Trapezoidal wing		38.0	deg
Thickness to chord ratio	t/c		
Centre		16.5%	
Maximum		18.0%	
Outboard		8.0%	
Dihedral	Γ		
Centre		0.0	deg
Crank		1.5	deg
Outer Wing		3.0	deg

Table A.2: BWB geometric properties [7]

The geometric characteristics of the winglets were not available from Castro's work, therefore they were obtained from an alternative source, Qin et. al [63]. These are given in Table A.3.

Winglet Parameter	Notation	Value	Units
Fin area	S_{fin}	13.37	m^2
Fin aspect ratio	A_{fin}	3.73	m
Fin height	h_{fin}	5.0	m
Root chord	c_{root}	4.0	m
Tip chord	c_{tip}	1.35	m
Leading edge sweep	Λ_{LE}	28.0	deg
Thickness to chord Ratio	t/c	12%	

Table A.3: BWB winglet parameters [63]

A.4 Aerodynamic Properties

The aerodynamic coefficients for this model are expressed in the body axis system. These coefficients are in general a function of body rates (p, q, r), air incidence angles (α, β), geometry changes or controls/flap deflections $(\delta_e, \delta_a, \delta_r)$ and center of gravity position. The data does not include the effect of Mach and Reynolds number. The predicted aerodynamic forces and the corresponding longitudinal/lateral stability characteristics may therefore vary under high-speed flight conditions. The coefficients C_X, C_Y, C_Z represent the force coefficients along the X, Y and Z body axis whereas roll, pitch and yaw moment coefficients are given by C_l, C_m, C_n.

A.4.1 Normal Force Coefficient, C_Z

The normal force coefficient is,

$$C_Z = C_{Z_0} + C_{Z_\alpha}\alpha + \frac{c}{V_t}\left(C_{Z_q}q + C_{Z_{\dot\alpha}}\dot\alpha\right) + C_{Z_{\delta_e}}\delta_e \tag{A.1}$$

C_{Z_0}	C_{Z_α}	$C_{Z\delta_{F1}}$	$C_{Z\delta_{F2}}$	$C_{Z\delta_{F3}}$	$C_{Z\delta_{F4}}$	$C_{Z\delta_{F5}}$
0.0217	-5.4868	-0.4866	-0.1602	-0.2222	-0.2274	-0.1042

Table A.4: Normal force coefficient (C_Z)

X_{CG} (m)	29.4	30.4	31.4	32.4	33.4	34.4
C_{Z_q}	-1.0787	-0.9678	-0.8568	-0.7459	-0.6351	- 0.5243

Table A.5: Aerodynamic derivative (C_{Z_q})

The Z force derivative due to pitch rate, C_{Z_q}, was a function of CG position, whereas the derivative due to rate of change of angle of attack, $C_{Z_{\dot\alpha}}$, was assumed zero [7].

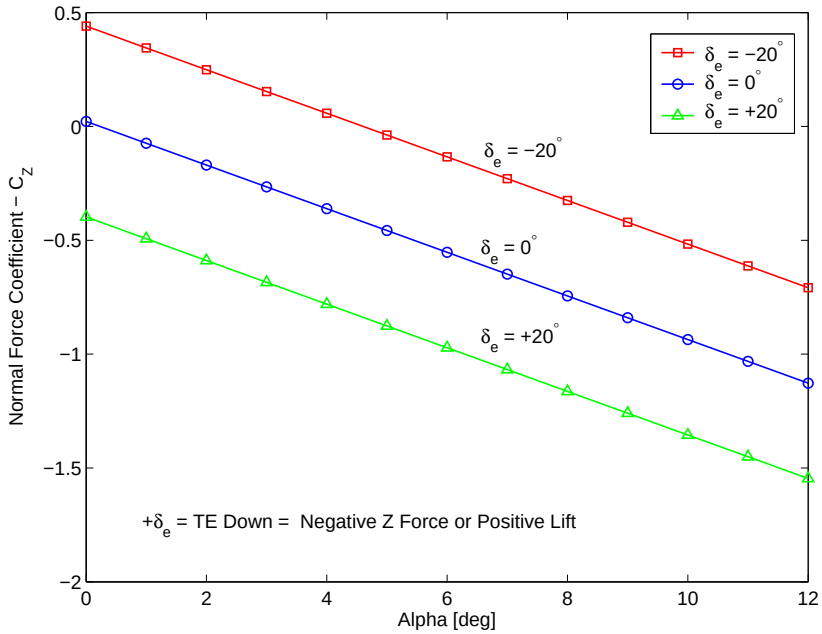

Figure A.3: Normal force coefficient (C_Z), [all flaps as elevators]

A.4.2 Axial Force Coefficient, C_X

The X body force coefficient, C_X, is expressed as a 2nd order polynomial of the Z force co-efficient, C_Z, and is analogous to an aircraft's drag polar.

$$C_X = -\left(C_{x_0} - C_{x_1}C_Z + C_{x_2}{C_Z}^2\right) \tag{A.2}$$

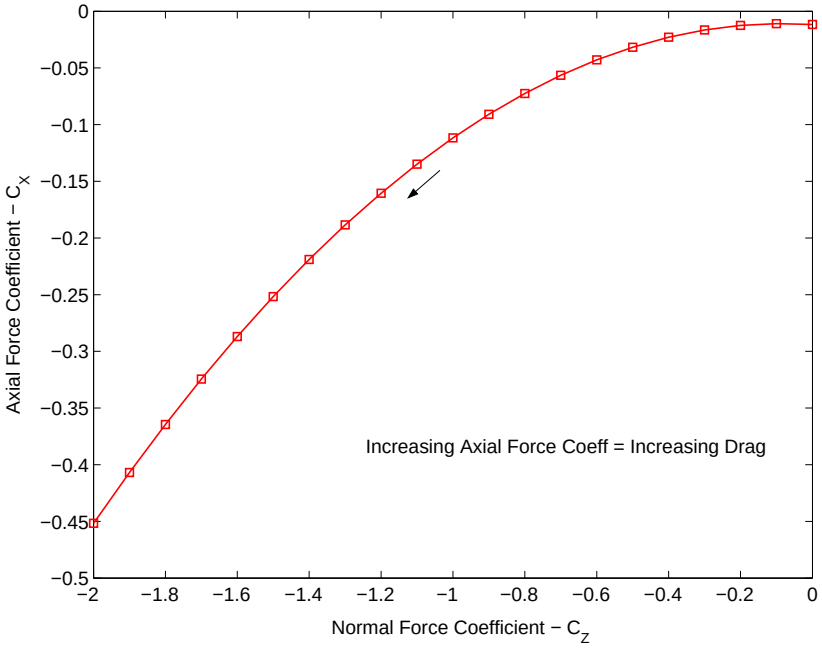

Figure A.4: Axial force coefficient (C_X)

C_{x_0}	C_{x_1}	C_{x_2}
0.0117	-0.0200	0.1200

Table A.6: Axial force coefficient polynomial parameters

A.4.3 Side Force Coefficient, C_Y

For the side force, some of the aerodynamic derivatives C_{Y_β} and C_{Y_p} were expressed as a function of angle of attack.

$$C_Y = C_{Y_\beta}\beta + \frac{b}{V_t}\left(C_{Y_r}r + C_{Y_p}p\right) + C_{Y_{\delta_r}}\delta_r \tag{A.3}$$

where

$$C_{Y_\beta} = C_{Y_{\beta_0}} + C_{Y_{\beta_\alpha}}\alpha \tag{A.4}$$

$$C_{Y_p} = C_{Y_{p_0}} + C_{Y_{p_\alpha}}\alpha \tag{A.5}$$

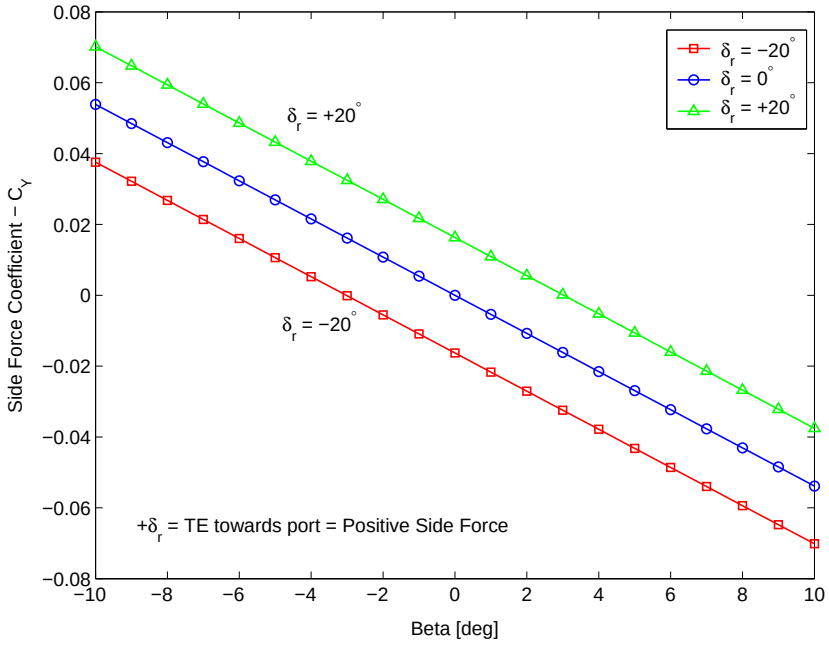

Figure A.5: Side force coefficient (C_Y), $[p = r = 0]$

$C_{Y_{\beta 0}}$	$C_{Y_{\beta_\alpha}}$	$C_{Y_{p_0}}$	$C_{Y_{p_\alpha}}$	$C_{Y_{\delta_{F1}}}$	$C_{Y_{\delta_{F2}}}$	$C_{Y_{\delta_{F3}}}$	$C_{Y_{\delta_{F4}}}$	$C_{Y_{\delta_{F5}}}$	$C_{Y_{\delta_r}}$
-0.3086	0.4879	-0.0814	2.0666	-0.0092	-0.0060	-0.0088	-0.0154	-0.0184	0.0467

Table A.7: Aero derivatives - side force coefficient (C_Y)

The Y force derivative due to yaw rate, C_{Y_r}, was given as a function of CG position.

X_{CG} (m)	29.4	30.4	31.4	32.4	33.4	34.4
C_{Y_r}	-0.1555	-0.1655	-0.1675	-0.1750	-0.1800	-0.1940

Table A.8: Aero derivative (C_{Y_r})

A.4.4 Roll Moment Coefficient, C_l

$$C_l = C_{l_\beta}\beta + \frac{b}{V_t}\left(C_{l_r}r + C_{l_p}p\right) + C_{l_{\delta_r}}\delta_r + C_{l_{\delta_a}}\delta_a \tag{A.6}$$

where

$$C_{l_\beta} = C_{l_{\beta_0}} + C_{l_{\beta_\alpha}}\alpha \tag{A.7}$$

$$C_{l_p} = C_{l_{p_0}} + C_{l_{p_\alpha}}\alpha \tag{A.8}$$

$$C_{l_r} = C_{l_{r_0}} + C_{l_{r_\alpha}}\alpha \tag{A.9}$$

The roll derivative due to yaw rate, C_{l_r}, is given as a function of CG position.

$C_{l_\beta 0}$	$C_{l\beta_\alpha}$	C_{lp_0}	C_{lp_α}	$C_{l\delta_{F1}}$	$C_{l\delta_{F2}}$	$C_{l\delta_{F3}}$	$C_{l\delta_{F4}}$	$C_{l\delta_{F5}}$	$C_{l_{\delta_r}}$
-0.0465	-0.3007	-0.3562	0.0735	-0.0274	-0.0230	-0.0442	-0.0644	-0.0396	0.0156

Table A.9: Aero derivatives - roll moment coefficient (C_l)

X_{CG} (m)	29.4	30.4	31.4	32.4	33.4	34.4
$C_{l_{r_0}}$	0.0272	0.0261	0.0250	0.0239	0.0229	0.0218
$C_{l_{r_\alpha}}$	0.5867	0.5797	0.5727	0.5658	0.5588	0.5518

Table A.10: Roll derivative (C_{l_r})

A.4.5 Pitch Moment Coefficient, C_m

The pitching moment coefficient was expressed as,

$$C_m = C_{m_0} + C_{m_\alpha}\alpha + \frac{c}{V_t}\left(C_{m_q}q + C_{m_{\dot\alpha}}\dot\alpha\right) + C_{m_{\delta_e}}\delta_e \tag{A.10}$$

The pitching moment derivative ($C_{m_{\dot\alpha}}$), that exists due to the transient disturbance in downwash on the tail-plane due to a perturbation in vertical velocity ($\dot w$) on the main wing, was assumed zero as there is no tail-plane.

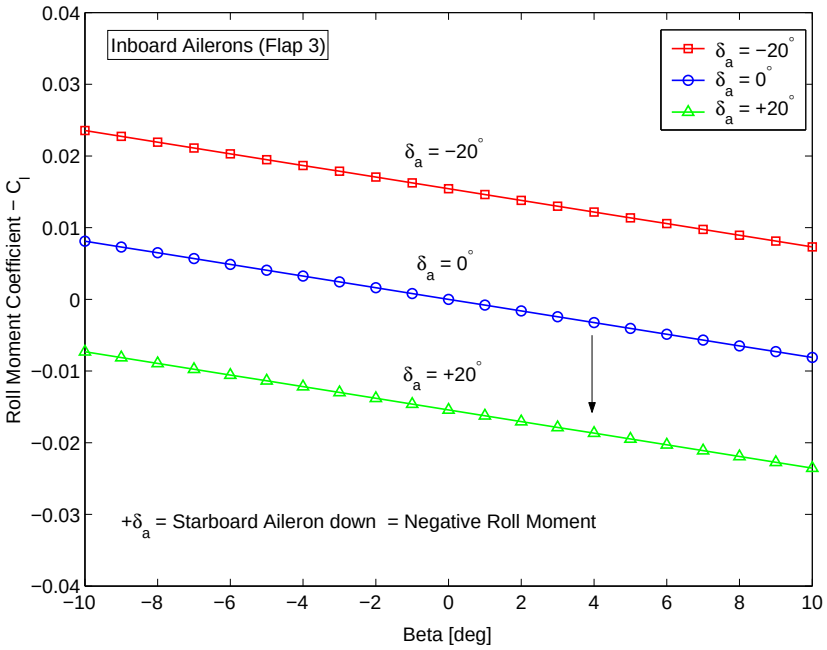

Figure A.6: Roll moment coefficient (C_l), [$p = r = 0$, $\alpha = 0$, $\delta_r = 0$]

X_{CG} (m)	29.4	30.4	31.4	32.4	33.4	34.4
C_{m_0}	-0.0370	-0.0388	-0.0405	-0.0423	-0.0441	-0.0458
C_{m_α}	-0.9950	-0.5493	-0.1036	0.3422	0.7879	1.2336
C_{m_q}	-0.8799	-0.7809	-0.7001	-0.6374	-0.5929	-0.5665
$C_{m_{\delta_{F_1}}}$	-0.3562	-0.3168	-0.2771	-0.2375	-0.1981	-0.1585
$C_{m_{\delta_{F_2}}}$	-0.1046	-0.0916	-0.0786	-0.0656	-0.0526	-0.0396
$C_{m_{\delta_{F_3}}}$	-0.1432	-0.1252	-0.1070	-0.0890	-0.0710	-0.0530
$C_{m_{\delta_{F_4}}}$	-0.1944	-0.1760	-0.1574	-0.1390	-0.1206	-0.1020
$C_{m_{\delta_{F_5}}}$	-0.1238	-0.1154	-0.1068	-0.0984	-0.0900	-0.0814

Table A.11: Aero derivatives - pitch moment coefficient (C_m)

A.4.6 Yaw Moment Coefficient, C_n

The yawing moment coefficient is expressed as,

$$C_n = C_{n_\beta}\beta + \frac{b}{V_t}\left(C_{n_r}r + C_{n_p}p\right) + C_{n_{\delta_r}}\delta_r + C_{n_{\delta_a}}\delta_a \tag{A.11}$$

$$C_{n_\beta} = C_{n_{\beta_0}} + C_{n_{\beta_\alpha}}\alpha \tag{A.12}$$

$$C_{n_p} = C_{n_{p_0}} + C_{n_{p_\alpha}}\alpha \tag{A.13}$$

$$C_{n_r} = C_{n_{r_0}} + C_{n_{r_\alpha}}\alpha \tag{A.14}$$

This completes the description of aerodynamic coefficients for the baseline BWB.

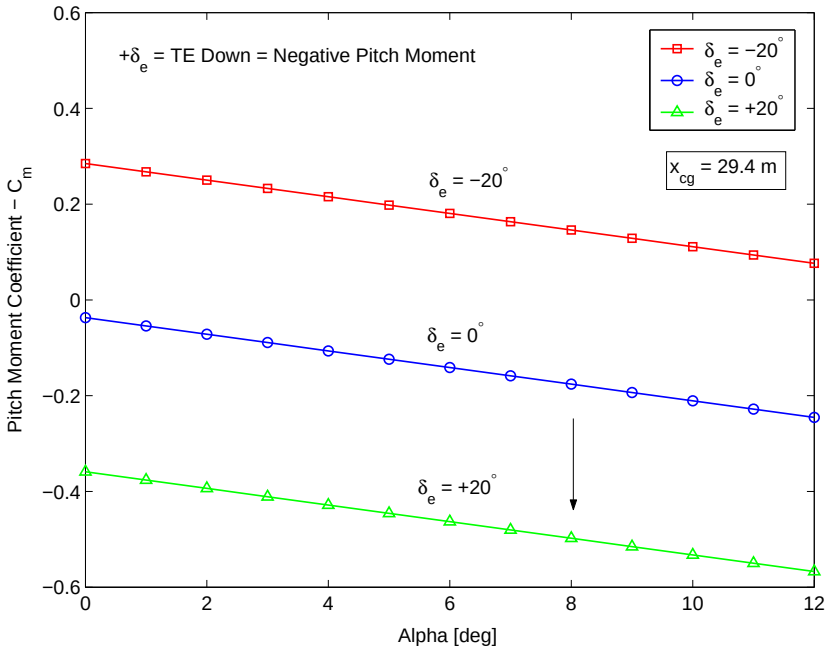

Figure A.7: Pitch moment coefficient (C_m), [$q = 0$, all flaps as elevators]

X_{CG} (m)	29.4	30.4	31.4	32.4	33.4	34.4
$C_{n_{\beta_0}}$	0.0152	0.0114	0.0075	0.0037	-0.0002	-0.0041
$C_{n_{\beta_\alpha}}$	-0.2787	-0.2726	-0.2665	-0.2604	-0.2543	-0.2482
$C_{n_{p_0}}$	0.0134	0.0124	0.0114	0.0103	0.0093	0.0083
$C_{n_{p_\alpha}}$	-0.8733	-0.8475	-0.8217	-0.7958	-0.7700	-0.7442
$C_{n_{r_0}}$	-0.0315	-0.0332	-0.0351	-0.0372	-0.0394	-0.0419
$C_{n_{r_\alpha}}$	0.0867	0.0805	0.0746	0.0690	0.0637	0.0587
$C_{n_{\delta_{F_1}}}$	0.0016	0.0014	0.0014	0.0012	0.0010	0.0010
$C_{n_{\delta_{F_2}}}$	0.0012	0.0010	0.0010	0.0010	0.0008	0.0008
$C_{n_{\delta_{F_3}}}$	0.0014	0.0012	0.0012	0.0010	0.0010	0.0008
$C_{n_{\delta_{F_4}}}$	0.0028	0.0026	0.0024	0.0022	0.0020	0.0018
$C_{n_{\delta_{F_5}}}$	0.0042	0.0040	0.0038	0.0036	0.0032	0.0030
$C_{n_{\delta_r}}$	-0.0115	-0.0115	-0.0115	-0.0115	-0.0115	-0.0115

Table A.12: Aero derivatives - yawing moment coefficient (C_n)

Appendix B

BWB Linear Model

This section develops the linear model for the BWB aircraft. Specifically it covers, (i) the derivation of dimensional derivatives specific to the BWB, (ii) some linearization results, (iii) validation of the linear airframe model and (iv) variation in longitudinal and lateral -directional dynamic modes with CG position and airspeed.

B.1 Dimensional Derivatives

This section discusses the derivation of X and Z force derivatives specific for the BWB, and is then followed by the derivation of the linear model (A,B,C,D matrices). This linear model is subsequently validated using a non-linear simulation and the output of MATLAB <`linmod.m`> linearization utility.

The small perturbation equations of motion from Cooke [43] are reproduced below. For control system analysis, it is desirable that the longitudinal motion of the aircraft be uncoupled from the lateral motion. To achieve this decoupling, it is assumed that the trim angular velocities are zero, ($P_1 = Q_1 = R_1 = 0$). In addition, zero side slip velocity ($V_1 = 0$) and steady wings level flight ($\phi_1 = 0$) are assumed. The linearized uncoupled longitudinal equations of motion are,

$$m\dot{u} = (\overset{\circ}{X}_u + \overset{\circ}{X}_{T_u})u + \overset{\circ}{X}_w w + \overset{\circ}{X}_{\dot{w}}\dot{w} + \overset{\circ}{X}_q q + \overset{\circ}{X}_{\delta_e}\delta_e - mg\theta\cos\theta_1 - mqW_1 \quad \text{(B.1)}$$

$$m\dot{w} = (\overset{\circ}{Z}_u + \overset{\circ}{Z}_{T_u})u + \overset{\circ}{Z}_w w + \overset{\circ}{Z}_{\dot{w}}\dot{w} + \overset{\circ}{Z}_q q + \overset{\circ}{Z}_{\delta_e}\delta_e - mg\theta\sin\theta_1 + mqU_1 \quad \text{(B.2)}$$

$$I_{yy}\dot{q} = (\overset{\circ}{M}_u + \overset{\circ}{M}_{T_u})u + (\overset{\circ}{M}_w + \overset{\circ}{M}_{T_w})w + \overset{\circ}{M}_{\dot{w}}\dot{w} + \overset{\circ}{M}_q q + \overset{\circ}{M}_{\delta_e}\delta_e \quad \text{(B.3)}$$

$$\dot{\theta} = q \quad \text{(B.4)}$$

$$\dot{h} = \sin\theta_1 u - \cos\theta_1 w + (U_1\cos\theta_1 + W_1\sin\theta_1)\theta \quad \text{(B.5)}$$

and for the lateral-directional axis,

$$m\dot{v} = \overset{\circ}{Y}_v v + \overset{\circ}{Y}_p p + \overset{\circ}{Y}_r r + \overset{\circ}{Y}_{\delta_a}\delta_a + g\phi\cos\theta_1 - mrU_1 + mpW_1 \tag{B.6}$$

$$I_{xx}\dot{p} = I_{xz}\dot{r} + \overset{\circ}{L}_v v + \overset{\circ}{L}_{\dot{v}}\dot{v} + \overset{\circ}{L}_p p + \overset{\circ}{L}_r r + \overset{\circ}{L}_{\delta_a}\delta_a \tag{B.7}$$

$$I_{zz}\dot{r} = I_{xz}\dot{p} + \overset{\circ}{N}_v v + \overset{\circ}{N}_{\dot{v}}\dot{v} + \overset{\circ}{N}_p p + \overset{\circ}{N}_r r + \overset{\circ}{N}_{\delta_r}\delta_r \tag{B.8}$$

$$\dot{\phi} = p + r\tan\theta_1 \tag{B.9}$$

$$\dot{\psi} = r\sec\theta_1 \tag{B.10}$$

Each of the force $(\overset{\circ}{X}, \overset{\circ}{Y}, \overset{\circ}{Z})$ and moment $(\overset{\circ}{L}, \overset{\circ}{M}, \overset{\circ}{N})$ derivatives used in the above expressions can be obtained by the partial derivation with respective state or control variables and can be readily found in the literature. However for the BWB aircraft, the X force coefficient, C_X, is expressed in an unconventional form as a function of normal force coefficient, C_Z, and some additional derivations were necessary.

B.1.1 Axial Force (X) Derivatives

X force derivative w.r.t forward velocity, $(\overset{\circ}{X}_u)$

$$\overset{\circ}{X}_u = \frac{\partial X}{\partial U} = \frac{\partial}{\partial U}(\bar{q}SC_X) \tag{B.11}$$

Taking partial derivatives, with reference area (S) as constant,

$$\overset{\circ}{X}_u = C_X S\frac{\partial}{\partial U}(\bar{q}) + \bar{q}S\frac{\partial}{\partial U}(C_X) \tag{B.12}$$

For the BWB, the axial force coefficient (C_X) is given as a function of normal force coefficient (C_Z), and with zero side slip $(V = 0)$, we have

$$C_X = -(C_{x0} + C_{x1}(-C_Z) + C_{x2}{C_Z}^2)$$
$$\bar{q} = \frac{1}{2}\rho(U^2 + W^2)$$

Substituting for C_X and dynamic pressure $\bar{q}$ in Equation B.12 we get,

$$\overset{\circ}{X}_u = C_X S\frac{\partial}{\partial U}\left[\frac{1}{2}\rho(U^2 + W^2)\right] - \bar{q}S\frac{\partial}{\partial U}\left[C_{x0} + C_{x1}(-C_Z) + C_{x2}{C_Z}^2\right] \tag{B.13}$$

or

$$\overset{\circ}{X}_u = \rho USC_X - \bar{q}S\frac{\partial}{\partial U}\left[C_{x0} + C_{x1}(-C_Z) + C_{x2}{C_Z}^2\right] \tag{B.14}$$

Since (C_{x0}, C_{x1}, C_{x2}) are constants, the above expression simplifies to,

$$\overset{\circ}{X}_u = \rho U S C_X - \bar{q} S \left[2 C_{x2} C_Z - C_{x1}\right] \frac{\partial}{\partial U} \left(C_Z\right) \tag{B.15}$$

Now substituting for C_Z,

$$\overset{\circ}{X}_u = \rho U S C_X - \bar{q} S \left[2 C_{x2} C_Z - C_{x1}\right] \frac{\partial}{\partial U} \left[C_{Z_0} + C_{Z_\alpha}\alpha + \frac{c}{V_t}(C_{Z_q} q) + C_{Z_{\delta_e}} \delta_e\right] \tag{B.16}$$

For a steady non-manoeuvring flight, $q = 0$, and for small angles, $\alpha = W/U$,

$$\overset{\circ}{X}_u = \rho U S C_X - \bar{q} S \left[2 C_{x2} C_Z - C_{x1}\right] C_{Z_\alpha} \frac{\partial}{\partial U} \left[\frac{W}{U}\right] \tag{B.17}$$

Taking partial derivatives w.r.t U and simplifying the above expression yields,

$$\overset{\circ}{X}_u = \rho U S C_X + \frac{\bar{q} S}{U} \left[2 C_{x2} C_Z - C_{x1}\right] \left[C_{Z\alpha}\alpha\right] \tag{B.18}$$

whereas the terms U, C_X, C_Z and α are defined for trim conditions and C_{x1}, C_{x2} are constants used in the expression for axial force coefficient. The remaining X derivatives were obtained in a similar fashion and are given as,

$$\overset{\circ}{X}_w = -\frac{\bar{q} S}{U} [2 C_{x2} C_Z - C_{x1}] C_{Z_\alpha} \tag{B.19}$$

$$\overset{\circ}{X}_q = -\bar{q} S [2 C_{x2} C_Z - C_{x1}] C_{Z_q} \tag{B.20}$$

$$\overset{\circ}{X}_{\dot{w}} = 0 \tag{B.21}$$

$$\overset{\circ}{X}_{\delta_e} = -\bar{q} S [2 C_{x2} C_Z - C_{x1}] C_{Z_{\delta_e}} \tag{B.22}$$

B.1.2 Side Force (Y) Derivatives

Y force derivative w.r.t side velocity, $(\overset{\circ}{Y}_v)$

$$\overset{\circ}{Y}_v = \frac{1}{V_t} \frac{\partial Y}{\partial \beta} = \frac{1}{V_t} \frac{\partial}{\partial \beta} (\bar{q} S C_Y)$$

Substituting for C_Y,

$$\overset{\circ}{Y}_v = \frac{\bar{q} S}{V_t} \frac{\partial}{\partial \beta} (C_{Y_\beta}\beta + \frac{b}{V_t}\left(C_{Y_r} r + C_{Y_p} p\right) + C_{Y_{\delta_r}} \delta_r)$$

Substituting $p = r = 0$ for steady level flight and taking partial derivatives w.r.t β,

$$\overset{\circ}{Y}_v = \frac{\bar{q}S}{V_t} C_{Y_\beta} \tag{B.23}$$

The remaining Y force derivatives are given as,

$$\overset{\circ}{Y}_r = \frac{\bar{q}Sb}{V_t} C_{Y_r} \tag{B.24}$$

$$\overset{\circ}{Y}_p = \frac{\bar{q}Sb}{V_t} C_{Y_p} \tag{B.25}$$

$$\overset{\circ}{Y}_{\dot{v}} = 0 \tag{B.26}$$

$$\overset{\circ}{Y}_{\delta_a} = \bar{q}SC_{Y_{\delta_a}} \tag{B.27}$$

$$\overset{\circ}{Y}_{\delta_r} = \bar{q}SC_{Y_{\delta_r}} \tag{B.28}$$

B.1.3 Normal Force (Z) Derivatives

Z force derivative w.r.t down velocity, ($\overset{\circ}{Z}_w$)

$$\overset{\circ}{Z}_w = \frac{\partial Z}{\partial W} = \frac{\partial}{\partial W}(\bar{q}SC_Z)$$

Taking partial derivatives, with reference area (S) as constant,

$$\overset{\circ}{Z}_w = C_Z S \frac{\partial}{\partial W}(\bar{q}) + \bar{q}S \frac{\partial}{\partial W}(C_Z) \tag{B.29}$$

Substituting for C_X, and dynamic pressure, $\bar{q}$, in Equation B.29 we get,

$$\overset{\circ}{Z}_w = C_X S \frac{\partial}{\partial W}\left[\frac{1}{2}\rho(U^2 + W^2)\right] - \bar{q}S \frac{\partial}{\partial W}\left[C_{Z_0} + C_{Z_\alpha}\alpha + \frac{c}{V_t}(C_{Z_q} q) + C_{Z_{\delta_e}}\delta_e\right]$$

Replacing $\alpha = W/U$ for small angles and taking partial derivatives we get,

$$\overset{\circ}{Z}_w = \rho S C_Z W + \frac{\bar{q}S}{U_1} C_{Z_\alpha} \tag{B.30}$$

The remaining Z derivatives are given as,

$$\overset{\circ}{Z}_u = \rho S C_Z U - \frac{\bar{q}S}{U} C_{Z_\alpha}\alpha \tag{B.31}$$

$$\overset{\circ}{Z}_q = \bar{q}SC_{Z_q}/(V_t/\bar{c}) \tag{B.32}$$

$$\overset{\circ}{Z}_{\dot{w}} = 0 \tag{B.33}$$

$$\overset{\circ}{Z}_{\delta_e} = \bar{q}SC_{Z_{\delta_e}} \tag{B.34}$$

Again terms U, W, C_Z, α now represent trim conditions.

B.1.4 Roll Moment (L) derivatives

Dimensional derivatives for the rolling moment (L) are expressed as,

$$\overset{\circ}{L}_v = \frac{\bar{q}Sb}{V_t} C_{l_\beta} \tag{B.35}$$

$$\overset{\circ}{L}_p = \frac{\bar{q}Sb^2}{V_t} C_{l_p} \tag{B.36}$$

$$\overset{\circ}{L}_r = \frac{\bar{q}Sb^2}{V_t} C_{l_r} \tag{B.37}$$

$$\overset{\circ}{L}_{\delta a} = \bar{q}SbC_{l_\delta a} \tag{B.38}$$

$$\overset{\circ}{L}_{\delta r} = \bar{q}SbC_{l_\delta r} \tag{B.39}$$

B.1.5 Pitching moment (M) derivatives

The pitching moment derivatives are,

$$\overset{\circ}{M}_u = \bar{q}Sc(2C_m - C_{m\alpha}\alpha) \tag{B.40}$$

$$\overset{\circ}{M}_w = \bar{q}ScC_{m\alpha} \tag{B.41}$$

$$\overset{\circ}{M}_q = \frac{\bar{q}Sc^2}{V_t} C_{mq} \tag{B.42}$$

$$\overset{\circ}{M}_{\delta e} = \bar{q}ScC_{m\delta e} \tag{B.43}$$

B.1.6 Yawing moment (N) derivatives

Similarly for the yaw axis we have,

$$\overset{\circ}{N}_v = \frac{\bar{q}Sb}{V_t} C_{n_\beta} \tag{B.44}$$

$$\overset{\circ}{N}_p = \frac{\bar{q}Sb^2}{V_t} C_{n_p} \tag{B.45}$$

$$\overset{\circ}{N}_r = \frac{\bar{q}Sb^2}{V_t} C_{n_r} \tag{B.46}$$

$$\overset{\circ}{N}_{\delta a} = \bar{q}SbC_{n\delta a} \tag{B.47}$$

$$\overset{\circ}{N}_{\delta r} = \bar{q}SbC_{n\delta r} \tag{B.48}$$

B.2 Linearization Results

A MATLAB program was written to evaluate the linear model using the formulation presented in the previous section. Following is a program output for linearization about a wings level flight at 400 kts and 10,000 ft altitude. Results from MATLAB's linearization utility `<linmod.m>` are also given at the end for comparison purposes.

```
================================================================================
.            B W B   L I N E A R   A I R F R A M E   R E S U L T S          .
================================================================================

RESULTS FOR: Vtrim  = 400 knots, Height = 3048 m
Date and Time: 19/2/2009  -   1:23pm

==============
1. INPUT DATA:
==============

Wing area         :S    =  841.700 m2
Wing span         :b    =   80.000 m
Mean chord        :c    =   12.310 m
Mass              :m    =   371280 kg
True Air Speed    :Vt   =  205.640 m/s
Off-Std Temp Inc  :DelT =   25.000 K
Air-density       :rho  =    0.850 kg/m3
Dynamic Pressure  :q1   = 17965.84 N/m2
Mach Number       :M1   =    0.597

Body axes moment of inertias:

Ixxb:  = 4.7032e+007 kg.m2
Iyyb:  = 2.5069e+007 kg.m2
Izzb:  = 9.9734e+007 kg.m2
Ixzb:  = 0 kg*m2

====================
2. TRIM PARAMETERS:
====================

Trim angle of Attack (alpha)        =     4.234 deg
Trim sideslip angle (beta)          =     0.000 deg
Trim aileron deflection (da)        =     0.000 deg
Trim elevator deflection (de)       =    -6.867 deg

Trim forward vel (body-axes):  U1b  =   205.079 m/s
Trim side vel    (body-axes):  V1b  =     0.000 m/s
Trim down vel    (body-axes):  W1b  =    15.184 m/s

Trim Roll rate   (body-axes):  P1   =     0.000 rad/s
Trim Pitch rate  (body-axes):  Q1   =     0.000 rad/s
Trim Yaw rate    (body-axes):  R1   =     0.000 rad/s
Trim Yaw angle   (body-axes):  PS1  =     0.000 deg
Trim Pitch angle (body-axes):  THE1 =     4.234 deg
Trim Roll angle  (body-axes):  PHI1 =    -0.000 deg
```

```
Trim lift co-eff.            (CL1)  =     0.238
Trim drag co-eff.            (CD1)  =     0.031
Trim side force co-eff.      (Cy1)  =     0.000
Trim Roll co-eff.            (Cl1)  =    -0.000
Trim pitch co-eff.           (Cm1)  =    -0.000
Trim yaw co-eff.             (Cn1)  =    -0.000
Trim Normal force co-eff     (CZ1)  =    -0.234
Trim x-thrust co-eff.        (CTx1) =     0.032
Trim thrust pitch mom co-eff.(CmT1) =     0.000

==============================
3. AERO DATA: NON-DIMENSIONAL
==============================


Longitudinal Non-dimensional derivatives:

CZu:          0.0000          Cmu:          0.0000
CZalf:       -5.4868          Cmalf:       -0.9950
CZalfdot:     0.0000          Cmalfdot:     0.0000
CZq:         -1.0787          Cmq:         -0.8799
CZde:        -1.2006          Cmde:        -0.9222
CZ0:          0.0217          Cm0:         -0.0370


Lateral Non-dimensional derivatives:

Cybet:       -0.2725          Clbet:       -0.0687          Cnbet:       -0.0054
Cybetdot:     0.0000          Clbetdot:     0.0000          Cnbetdot:     0.0000
Cyp:          0.0713          Clp:         -0.3508          Cnp:         -0.0511
Cyr:         -0.1557          Clr:          0.0706          Cnr:         -0.0251
Cyda:        -0.0088          Clda:        -0.0442          Cnda:         0.0014

==========================
4. AERO DATA: DIMENSIONAL
==========================


Longitudinal Dimensional derivatives:

Xu:           -912.84          Zu:         -5284.88          Mu:         66746.68
Xw:         -15351.53          Zw:       -407184.13          Mu:         66746.68
Xwdot:          0.00          Zwdot:          0.00          Mwdot:          0.00
Xq:         -36689.49          Zq:       -976463.77          Mq:       -9804961.3
Xde:       -682163.88          Zde:     -18155289.5          Mde:    -171668801.6
Xalf:      -3117521.9          Zalf:    -82970550.3          Malf:   -185218744.1
Xalfdot:        0.00          Zalfdot:        0.00          Malfdot:        0.00

Lateral Dimensional derivatives:

Yv:           -20041.55          Lv:        -404285.40          Nv:         -31732.88
Yvdot:            0.00          Lvdot:          0.00          Nvdot:          0.00
Yp:           419617.70          Lp:     -165081078.1          Np:       -24068908.6
Yr:          -915739.16          Lr:       33206434.8          Nr:       -11809994.7
Yda:         -133072.25          Lda:     -53470851.1          Nda:        1685965.9
Ydr:          706190.25          Ldr:      18872065.1          Ndr:      -13912099.2
Ybet:       -4121345.37          Lbet:    -83137249.7          Nbet:         -0.0654
Ybetdot:          0.00          Lbetdot:        0.00          Nbetdot:        0.00
```

```
================================================================================
5. State Space Matrices
                           [II]xdot = [AA]x + [BB]u
                               xdot = [A]x +  [B]u

                       where:   [A] = inv[II]  [AA]
                                [B] = inv[II]  [BB]
================================================================================

Longitudinal States Dynamics & Controls Matrix :
================================================

<linafm.m> Output
-----------------

State Vector:   x = [ u  w  q  theta  h ]
Control Vector: u = [ de dt ]

|udot  |  |-0.00246 -0.0413   -15.3   -9.77  5.38e-005 ||u  |   |-1.83     0|
|wdot  |  |-0.01420    -1.1     202  -0.723   0.000930 ||w  |   |-48.9     0|
|qdot  |= | 0.00266  -0.036  -0.391       0          0 ||q  | + |-6.84     0||de|
|thedot|  |       0       0       1       0          0 ||the|   |   0      0||dt|
|hdot  |  |  0.0738  -0.997       0     206          0 ||h  |   |   0      0|

<linmod.m> Output
-----------------

|udot  |  |-0.00244 -0.0411   -15.28   -9.77  5.39e-005 ||u  |   |-1.837 4.44|
|wdot  |  | -0.0145   -1.09    202.4  -0.723   0.000930 ||w  |   |-48.89    0|
|qdot  |= | 0.00265 -0.0358  -0.3911       0  9.65e-019 ||q  | + |-6.847    0||de|
|thedot|  |       0       0       1       0          0 ||the|   |     0    0||dt|
|hdot  |  |  0.0738  -0.997       0   205.6          0 ||h  |   |     0    0|

Lateral-Directional States Dynamics & Controls Matrix
=====================================================

<linafm.m> Output
-----------------

State Vector:   x = [ v  p  r  psi  phi ]
Control Vector: u = [ da dr ]

|uvot  |  | -0.05400     16.3    -208  9.77   0 ||v  |   | -0.358  1.902|
|pdot  |  | -0.00860    -3.51   0.706     0   0 ||p  |   | -1.137  0.401|
|rdot  |= | -0.00031   -0.241  -0.118     0   0 ||r  | + |  0.017 -0.139||da|
|phidot|  |       0        1   0.074     0   0 ||phi|   |      0      0||dr|
|psidot|  |       0        0       1     0   0 ||psi|   |      0      0|

<linmod.m> Output
-----------------

|uvot  |  | -0.05398    16.31   -207.5  9.77   0 ||v  |  |-0.3584  1.9020|
|pdot  |  | -0.00859    -3.51    0.706     0   0 ||p  |  |-1.1369  0.4012|
|rdot  |= |-0.000318  -0.2413  -0.1184     0   0 ||r  | +| 0.0169 -0.1394||da|
|phidot|  |       0        1   0.0740     0   0 ||phi|  |      0       0||dr|
|psidot|  |       0        0        1     0   0 ||psi|  |      0       0|

< End of Output >
```

B.3 Validation of the Linear Airframe Model

The purpose of this section is to validate the linear airframe model obtained in the previous section with the help of a non-linear aircraft simulation. The longitudinal and the lateral-directional axis are considered separately.

B.3.1 Longitudinal Axis

The linearized equations of motion can be re-arranged in state space form as,

$$E\dot{x} = Ax + Bu \tag{B.49}$$

$$\begin{bmatrix} 1 & -\overset{\circ}{X}_{\dot{w}} & 0 & 0 \\ 0 & 1-\overset{\circ}{Z}_{\dot{w}} & 0 & 0 \\ 0 & -\overset{\circ}{M}_{\dot{w}} & 1 & 0 \\ 0 & 0 & 0 & 1 \end{bmatrix} \begin{bmatrix} \dot{u} \\ \dot{w} \\ \dot{q} \\ \dot{\theta} \end{bmatrix} = \begin{bmatrix} \overset{\circ}{X}_u & \overset{\circ}{X}_w & (\overset{\circ}{X}_q - W_1) & -g\cos\theta_1 \\ \overset{\circ}{Z}_u & \overset{\circ}{Z}_w & (\overset{\circ}{Z}_q + U_1) & -g\sin\theta_1 \\ \overset{\circ}{M}_u & \overset{\circ}{M}_w & \overset{\circ}{M}_q & 0 \\ 0 & 0 & 1 & 0 \end{bmatrix} \begin{bmatrix} u \\ w \\ q \\ \theta \end{bmatrix} +$$

$$\begin{bmatrix} \overset{\circ}{X}_{\delta_e} & \overset{\circ}{X}_{\delta_t} \\ \overset{\circ}{Z}_{\delta_e} & \overset{\circ}{Z}_{\delta_t} \\ \overset{\circ}{M}_{\delta_e} & \overset{\circ}{M}_{\delta_t} \\ 0 & 0 \end{bmatrix} \begin{bmatrix} \delta_e \\ \delta_t \end{bmatrix} \tag{B.50}$$

In the above equation, the dimensional derivatives $(\overset{\circ}{X}_{\dot{w}}, \overset{\circ}{Z}_{\dot{w}}, \overset{\circ}{M}_{\dot{w}})$ that are dependent on rate of change of Z-axis body velocity, $\dot{w}$, are assumed zero. Hence the matrix, E, on the left hand side of the above equations becomes identity. The subscripted variables $[U_1, W_1, \theta_1]$ represent the state variables at trim conditions and the perturbation in state variables from the trim condition is $[u, w, q, \theta]$. Note that the height state has been omitted as it couples weakly into the longitudinal dynamics, on account of variation in density with altitude.

Using the linearization program, the dimensional derivatives in Equation (B.50) were obtained for a straight and level trim condition at an airspeed of $V_t = 400$ kts, altitude of $h = 10,000$ ft and a stable CG position of $x_{cg} = 29.4$ m. The resulting state and controls matrix for elevator control are,

$$\begin{bmatrix} \dot{u} \\ \dot{w} \\ \dot{q} \\ \dot{\theta} \end{bmatrix} = \begin{bmatrix} -0.0024398 & -0.041124 & -15.283 & -9.7705 \\ -0.014527 & -1.0908 & 202.45 & -0.72339 \\ 0.0026528 & -0.035831 & -0.39112 & 0 \\ 0 & 0 & 1 & 0 \end{bmatrix} \begin{bmatrix} u \\ w \\ q \\ \theta \end{bmatrix} + \begin{bmatrix} -1.8373 \\ -48.899 \\ -6.8479 \\ 0 \end{bmatrix} \begin{bmatrix} \delta e \end{bmatrix}$$

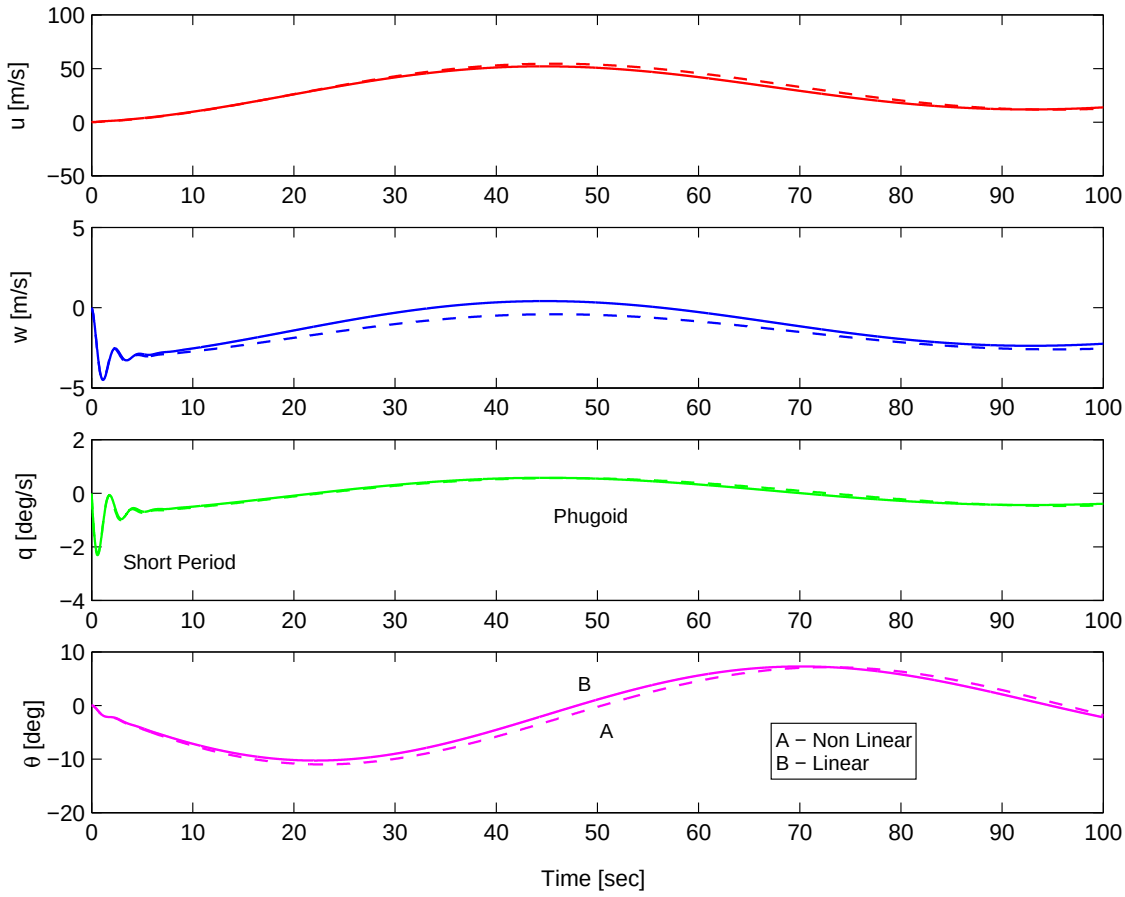

Figure B.1: Longitudinal response for +1.0° step elevator : Open loop

Longitudinal Transfer functions - Using the above linear model, transfer functions for each of the output variables (u, w, q, θ) with respect to elevator control (δ_e) were obtained.

$$\frac{u}{\delta e} = \frac{-1.8373(s - 58.42)(s + 1.509)(s + 0.3438)}{(s^2 + 0.01122s + 0.004312)(s^2 + 1.473s + 7.703)} \tag{B.51}$$

$$\frac{w}{\delta e} = \frac{-48.8992(s + 28.74)(s^2 + 0.002047s + 0.001582)}{(s^2 + 0.01122s + 0.004312)(s^2 + 1.473s + 7.703)} \tag{B.52}$$

$$\frac{q}{\delta e} = \frac{-6.8479s(s + 0.8362)(s + 0.001885)}{(s^2 + 0.01122s + 0.004312)(s^2 + 1.473s + 7.703)} \tag{B.53}$$

$$\frac{\theta}{\delta e} = \frac{-6.8479(s + 0.8362)(s + 0.001885)}{(s^2 + 0.01122s + 0.004312)(s^2 + 1.473s + 7.703)} \tag{B.54}$$

The generic open loop pitch rate to elevator (q/δ_e) transfer function is given as

$$\frac{q}{\delta e} = \frac{Ks(s + 1/T_{\theta 1})(s + 1/T_{\theta 2})}{(s^2 + 2\omega_{sp}\zeta_{sp}s + \omega_{sp}^2)(s^2 + 2\omega_{ph}\zeta_{ph}s + \omega_{ph}^2)} \tag{B.55}$$

Hence the short period damping and natural frequency are $\omega_{sp} = 2.78$ rad/s, $\zeta_{sp} = 0.265$ respectively, and the corresponding parameters for the phugoid are $\omega_{ph} = 0.0854$ rad/s, $\zeta_{ph} = 0.0657$. The response of the output variables $[u, w, q, \theta, h]$ to a +1.0 deg step elevator are shown in Figure B.1. At a forward CG location ($x_{cg} = 29.4$ m) and high speed ($V = 400$ kts) the short period dynamics are fast but poorly damped, whereas the phugoid dynamics are slow, stable and oscillatory. These time histories show conventional dynamics for the BWB and are for one particular combination of flight speed, altitude and CG position. Both linear and non-linear results are plotted for comparison.

B.3.2 Lateral-Directional Axis

For the lateral directional axis, the east position state, p_E, was omitted while aileron, δ_a, and rudder, δ_r, controls were retained. The linear model for the uncoupled lateral directional dynamics can be expressed as,

$$E\dot{x} = Ax + Bu \tag{B.56}$$

$$\begin{bmatrix} 1-\overset{\circ}{Y}_{\dot{v}} & 0 & 0 & 0 \\ -\overset{\circ}{L}_{\dot{v}} & 1 & -I_{xz}/I_{xx} & 0 \\ -\overset{\circ}{N}_{\dot{v}} & -I_{xz}/I_{zz} & 1 & 0 \\ 0 & 0 & 0 & 1 \end{bmatrix} \begin{bmatrix} \dot{v} \\ \dot{p} \\ \dot{r} \\ \dot{\phi} \end{bmatrix} = \begin{bmatrix} \overset{\circ}{Y}_{v} & (\overset{\circ}{Y}_{p} + W_1) & (\overset{\circ}{Y}_{r} - U_1) & g\cos\theta_1 \\ \overset{\circ}{L}_{v} & \overset{\circ}{L}_{p} & \overset{\circ}{L}_{r} & 0 \\ \overset{\circ}{N}_{v} & \overset{\circ}{N}_{p} & \overset{\circ}{N}_{r} & 0 \\ 0 & 1 & \tan\theta_1 & 0 \end{bmatrix} \begin{bmatrix} v \\ p \\ r \\ \phi \end{bmatrix} + \begin{bmatrix} \overset{\circ}{Y}_{\delta a} & \overset{\circ}{Y}_{\delta r} \\ \overset{\circ}{L}_{\delta a} & \overset{\circ}{L}_{\delta r} \\ \overset{\circ}{N}_{\delta a} & \overset{\circ}{N}_{\delta r} \\ 0 & 0 \end{bmatrix} \begin{bmatrix} \delta a \\ \delta r \end{bmatrix} \tag{B.57}$$

Since the derivatives $(\overset{\circ}{Y}_{\dot{v}}, \overset{\circ}{L}_{\dot{v}}, \overset{\circ}{N}_{\dot{v}})$ and the cross inertia term I_{xz} are assumed zero, the E matrix becomes identity. The terms U_1, W_1 are steady state X and Z body velocities, whereas θ_1 is the trim pitch angle. Using the linearization program, the above aerodynamic derivatives were obtained for a straight and level trim condition at an airspeed of $V_t = 400$ kts and altitude of $h = 10,000$ ft. The resulting state and controls matrices were

$$\begin{bmatrix} \dot{v} \\ \dot{p} \\ \dot{r} \\ \dot{\phi} \end{bmatrix} = \begin{bmatrix} -0.05398 & 16.314 & -207.55 & 9.77 \\ -0.00859 & -3.51 & 0.7060 & 0 \\ -0.00031 & -0.241 & -0.1184 & 0 \\ 0 & 1 & 0.07403 & 0 \end{bmatrix} \begin{bmatrix} v \\ p \\ r \\ \phi \end{bmatrix} + \begin{bmatrix} -0.358 & 1.902 \\ -1.137 & 0.401 \\ 0.0169 & -0.139 \\ 0 & 0 \end{bmatrix} \begin{bmatrix} \delta a \\ \delta r \end{bmatrix} \tag{B.58}$$

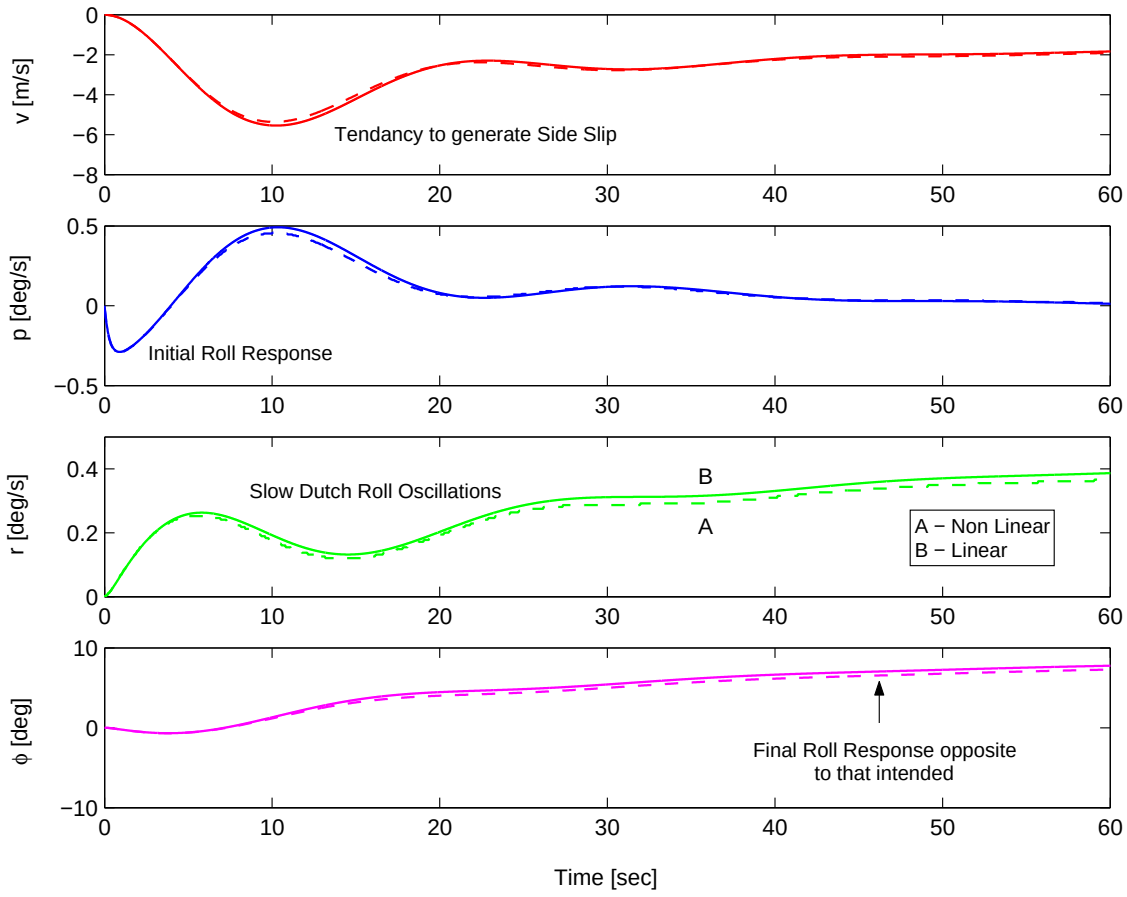

Figure B.2: Lateral-directional response for +1.0° step aileron : Open loop

Lateral-Directional Transfer functions w.r.t Aileron

Using the above linear model, transfer functions were obtained for each of the output variables $[v, p, r, \phi]$ with respect to aileron and rudder controls $[\delta_a, \delta_r]$. Transfer functions w.r.t to aileron are listed below.

$$\frac{v}{\delta_a} = \frac{-0.35841(s+61.42)(s+3.739)(s+0.01163)}{(s+3.463)(s+0.03715)(s^2+0.1824s+0.08898)} \tag{B.59}$$

$$\frac{p}{\delta_a} = \frac{-1.1369(s+0.3867)(s-0.2238)(s-0.003729)}{(s+3.463)(s+0.03715)(s^2+0.1824s+0.08898)} \tag{B.60}$$

$$\frac{r}{\delta_a} = \frac{0.016905(s+19.72)(s^2+0.07705s+0.01486)}{(s+3.463)(s+0.03715)(s^2+0.1824s+0.08898)} \tag{B.61}$$

$$\frac{\phi}{\delta_a} = \frac{-1.1357(s+0.3748)(s-0.2372)}{(s+3.463)(s+0.03715)(s^2+0.1824s+0.08898)} \tag{B.62}$$

From Figure B.2 it may be seen that the dutch roll mode is slow and poorly damped [$\omega_{dr} = 0.306$ rad/s, $\zeta_{dr} = 0.298$]. The roll mode time constant is $\tau_r = 0.289$sec, which indicates fast roll dynamics at this flight speed. The spiral mode is stable and slow with a time constant $\tau_s = 26.88$ sec.

It should be noted that for the roll rate to aileron transfer function (p/δ_a), the static loop sensitivity is negative, i-e positive aileron deflection shall generate a negative roll rate. At the same time the static loop sensitivity of yaw rate to aileron transfer function (r/δ_a) is positive. Thus positive aileron deflections will generate positive yaw rates. Positive roll rates with negative yaw rates are counteracting and indicate adverse yaw tendency. Figure B.2 shows the step response plots for the output variables $[v, p, r, \phi]$ to a +1.0 deg step aileron.

Note that the bank angle (ϕ) has developed opposite to the direction intended. The initial negative roll rate (p) response to positive aileron input is in the correct direction, however soon after the slow and poorly damped dutch roll dominates and the roll rate goes in the opposite direction and starts a dutch roll oscillation. Similar oscillations are observed in the yaw rate response. Large side-velocities (v) also appear in the response, indicating a tendency to side slip.

Lateral-Directional Transfer functions w.r.t Rudder

The open loop transfer functions in response to rudder control are as below,

$$\frac{v}{\delta_r} = \frac{1.902(s+18.76)(s+3.534)(s-0.007312)}{(s+3.463)(s+0.03715)(s^2+0.1824s+0.08898)} \tag{B.63}$$

$$\frac{p}{\delta_r} = \frac{0.40126(s-0.8933)(s+0.7829)(s-0.00342)}{(s+3.463)(s+0.03715)(s^2+0.1824s+0.08898)} \tag{B.64}$$

$$\frac{r}{\delta_r} = \frac{-0.161(s+4.735)(s^2+0.08652s+0.02114)}{(s+3.463)(s+0.03715)(s^2+0.1824s+0.08898)} \tag{B.65}$$

$$\frac{\phi}{\delta_r} = \frac{0.39093(s-0.9751)(s+0.7457)}{(s+3.463)(s+0.03715)(s^2+0.1824s+0.08898)} \tag{B.66}$$

The yaw rate to rudder transfer function (r/δ_r) shows negative loop sensitivity, thus positive rudder deflection (trailing edge towards port) generates negative yaw rate or positive side slip velocities. This is confirmed by the (v/δ_r) transfer function.

The roll rate to rudder transfer function (p/δ_r) has a non-minimum phase zero and hence the step response goes initially in the positive direction before settling down to negative values, this behavior leads to adverse roll behavior which is undesirable and difficult to control. The open loop time histories in Figure B.3 with respect to rudder control show similar dutch roll oscillations. The dynamics for the BWB show conventional behavior except that the dutch roll oscillations are unacceptably slow. This is due to the absence of conventional rudders that provide directional stiffness into the aircraft design.

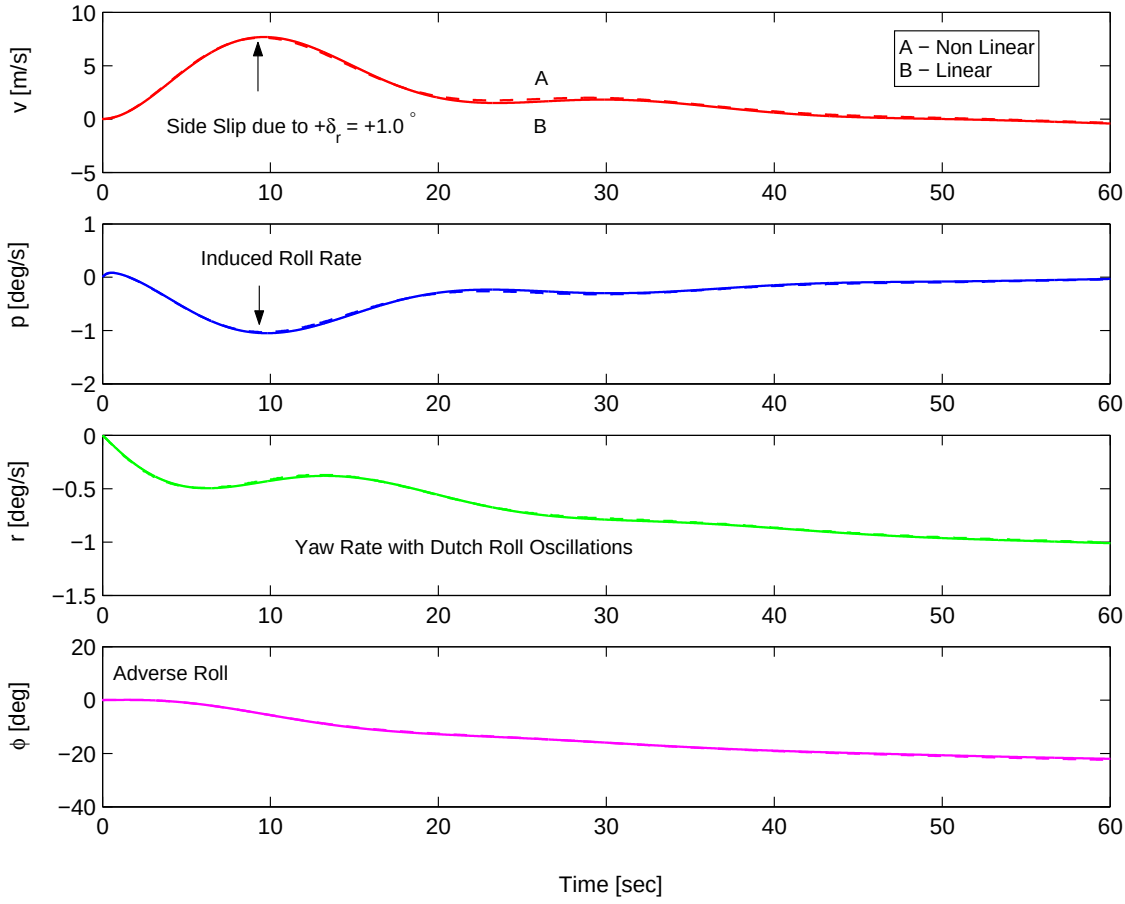

Figure B.3: Lateral-directional response for +1.0° step rudder : Open loop

Appendix C

BWB - Flight Control System Design

A Flight Control System (FCS) was designed as an integral part of this research. It proved valuable in system simulation and handling qualities assessment. The FCS had inner loops for stability augmentation and outer loops for attitude and flight path control. Both longitudinal and lateral-directional controls were designed separately. The flight controls design program files are available as <`BWBLongFCS.m`> and <`BWBLatDirFCS.m`> respectively. The longitudinal FCS is considered first.

C.1 Control of Longitudinal Axis

The longitudinal control system architecture is shown in Figure C.1. The inner most loop with pitch rate and alpha feedback places the short period poles at the desired locations on the s-plane. The pitch angle loop provides control of the pitch attitude and also damps the phugoid mode. The outer loops control airspeed and altitude.

C.1.1 Longitudinal Stability Augmentation

Requirements - The MILSPEC 8785C Level 1 requirements on ω_{sp} and ζ_{sp} are,

Flight Phase	Damping (ζ_{sp})	CAP (ω_{sp}^2/N_α)
Category A (rapid maneuvering)	0.35 - 1.30	0.280 - 3.6
Category B (gradual maneuvers)	0.30 - 2.00	0.085 - 3.6
Category C (take-off and landing)	0.25 - 1.30	0.160 - 3.6

Table C.1: MILSTD 8785C - short period mode requirements

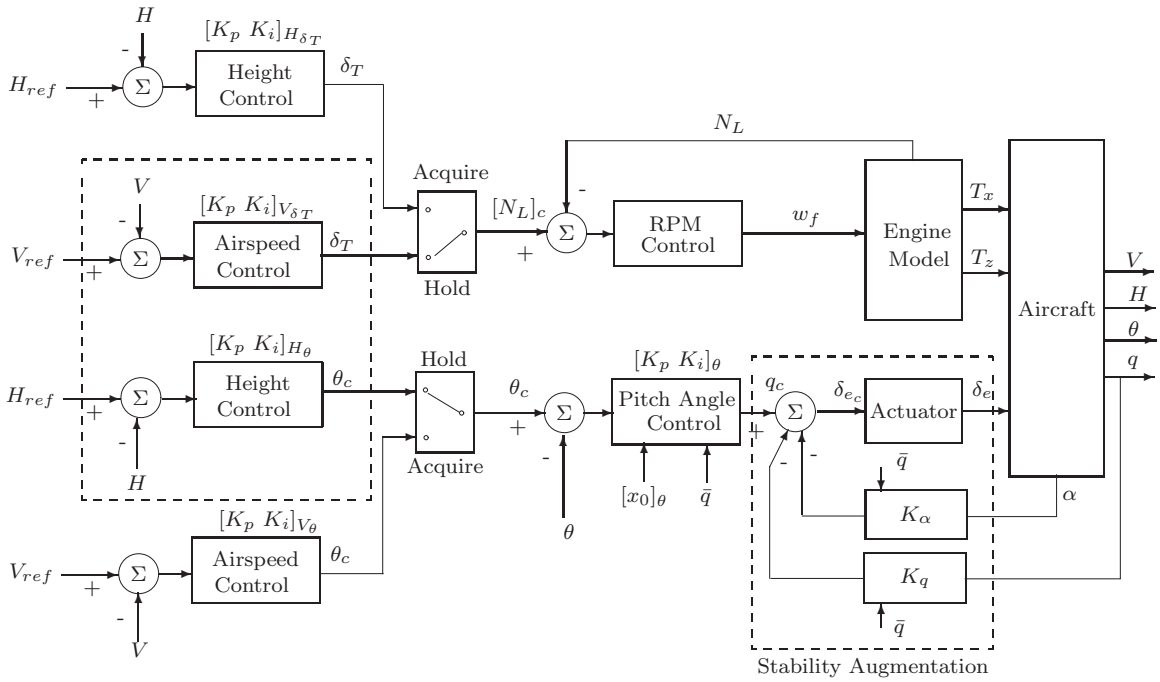

Figure C.1: Longitudinal flight control system architecture

Consider a low speed category-C flight case (V = 200 kts, Alt = 5000 ft). The reduced order short period dynamics (using the short period approximation) are given by,

$$\begin{bmatrix}\dot{\alpha}\\ \dot{q}\end{bmatrix} = \begin{bmatrix}-0.5960 & 0.9874\\ -1.1816 & -0.2007\end{bmatrix}\begin{bmatrix}\alpha\\ q\end{bmatrix} + \begin{bmatrix}-0.1304\\ -1.7745\end{bmatrix}\begin{bmatrix}\delta_e\end{bmatrix}$$

The corresponding angle of attack and pitch rate to elevator transfer functions are,

$$\frac{\alpha}{\delta e} = \frac{-0.13042(s+13.64)}{(s^2+0.7968s+1.286)} \tag{C.1}$$

$$\frac{q}{\delta e} = \frac{-1.7745(s+0.5092)}{(s^2+0.7968s+1.286)} \tag{C.2}$$

From the above we have,

$$\begin{aligned}\omega_{sp} &= 1.139 \text{ rad/s}\\ \zeta_{sp} &= 0.384\\ T_{\theta 2} &= 1.72 \text{ sec}\\ \text{CAP} &= 0.216\end{aligned}$$

From Table C.1 the Control Anticipation Parameter (CAP) requirements for category-C flight phase are 0.16 to 3.6. The requirements on short period natural frequency can be then be derived from these CAP limits as,

$$\omega_{sp} = \sqrt{\frac{\text{CAP}V_0}{gT_{\theta_2}}} \tag{C.3}$$

This results in a desired short period frequency range of 0.98 to 4.68 rad/s. At the flight condition considered, the BWB aircraft has a short period frequency, $\omega_{sp} = 1.13$ rad/s, and therefore just satisfies the short period frequency requirements. The short period damping, $\zeta_{sp} = 0.384$, also satisfies the minimum MIL-SPEC 8785C damping ratio limit of $\zeta_{sp} = 0.3$. However, for a second order system a short period damping of 0.6 to 0.7 is considered more adequate. To satisfy the MIL-SPEC 8785C requirements, it was decided to increase the short period frequency from 1.13 to 1.5 rad/s and damping from 0.384 to 0.9. This high value of damping reduces the close loop resonance magnitude in the Neil Smith criteria, and the slight increase in short period natural frequency greatly helps in the reducing the amount of phase compensation required from the pilot.

Alpha Feedback - Both short period frequency and damping could be improved by angle of attack and pitch rate feedback respectively. To improve the short period frequency, angle of attack feedback was necessary.

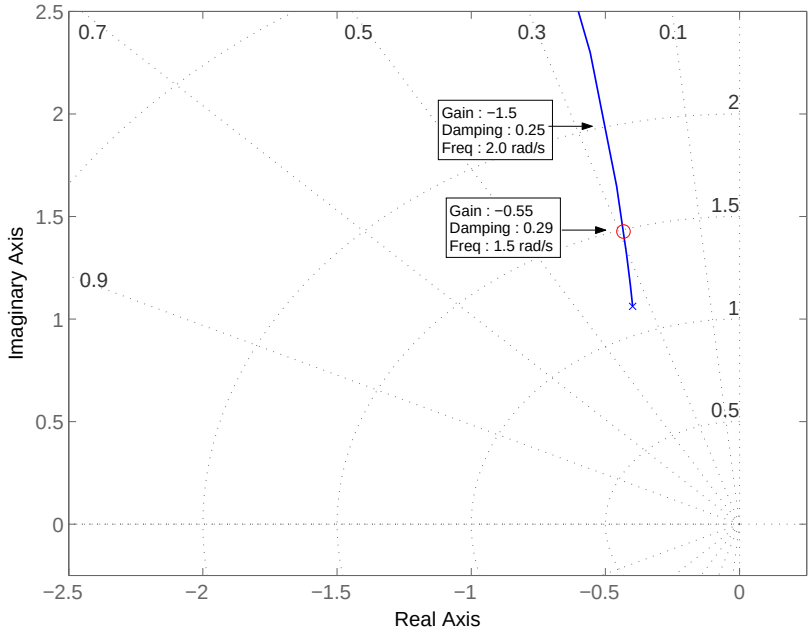

Figure C.2: Effect of angle of attack feedback on short period poles

Figure C.2 shows the effect of the alpha feedback on the short period poles. The short period frequency increases and damping decreases as the poles move out along the imaginary axis. Feedback gain of $K_\alpha = -0.55$ corresponding to a short period natural frequency of $\omega_{sp} = 1.5$ rad/s was selected. The short period damping, ζ_{sp}, decreased from 0.384 to 0.29. It can be noted that sign of feedback gain, K_α, is negative. Thus a sudden increase in angle of attack due to a disturbance results in positive elevator displacement, $\delta e > 0$. A positive elevator displacement generates a nose down moment thus reducing the angle of attack, which is a stabilizing effect. The pitch rate to elevator transfer with alpha feedback is,

$$\frac{q}{\delta e} = \frac{-1.7745(s + 0.5092)}{(s^2 + 0.8655s + 2.223)} \tag{C.4}$$

When (C.4) is compared with the open loop transfer function in (C.2), the effect of alpha feedback become apparent. The short period mode is now faster as desired but poorly damped, this reduction in short period damping is improved using pitch rate feedback.

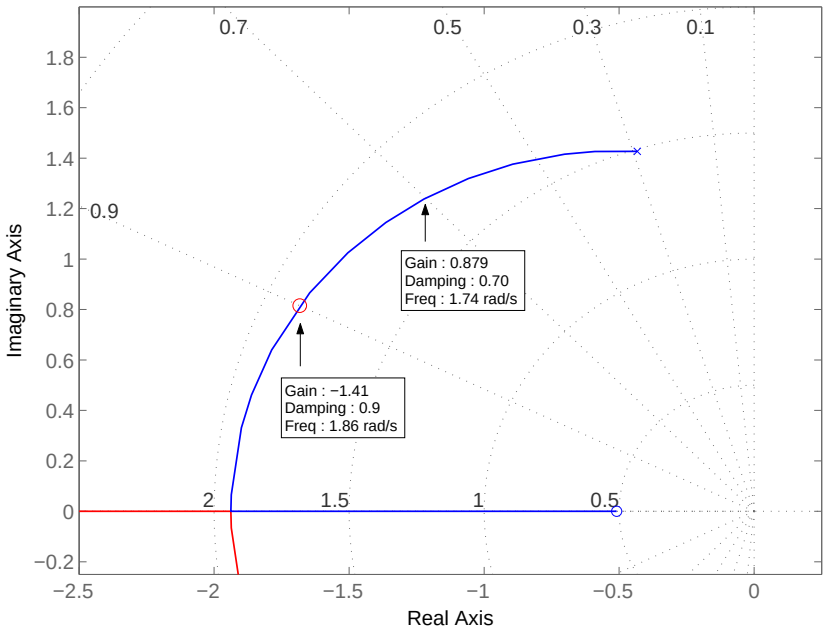

Figure C.3: Effect of pitch rate feedback on short period damping

Pitch Rate Feedback - To improve the short period damping, a pitch rate loop is closed with a feedback gain K_q. The corresponding root locus is shown in Figure C.3. A pitch rate feedback gain of $K_q = -1.41$ is selected to provide a short period damping of 0.9. The pitch rate feedback also had the beneficial effect of increasing the short period frequency from 1.5 to 1.86 rad/s. The new state space matrix with alpha and pitch rate feedback can be expressed as

$$A_n = A - BKC \tag{C.5}$$

where the gain matrix K is

$$K = \begin{bmatrix} K_\alpha & K_q \end{bmatrix} \tag{C.6}$$

The step response is plotted in Figure C.4 and shows the improvement in pitch rate damping by use of pitch rate feedback. Finally it is observed that if the open loop dynamics had an adequate short period natural frequency then alpha feedback could have been avoided. However in this case alpha feedback was necessary to speed up the short period mode to meet the handling qualities requirements.

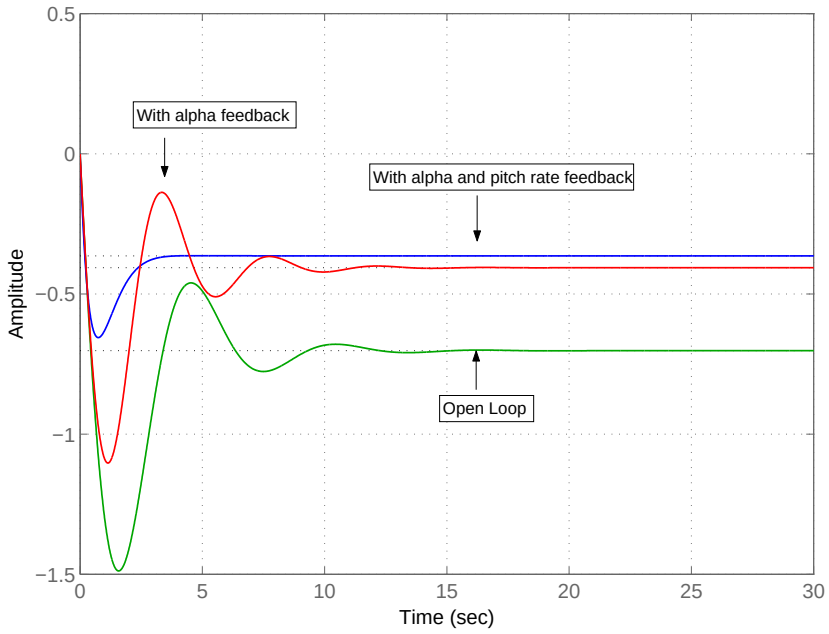

Figure C.4: Step response with alpha and pitch rate feedback

C.1.2 Control of Airspeed and Altitude

Reference is made to Figure C.1. Control of airspeed and altitude is further subdivided into acquire climb/descent and cruise phases.

Climb/Descent Phase - During climbs or descents it was required to maintain the speed of the aircraft constant. Therefore the height was controlled with throttle and airspeed with pitch angle/elevator. Such a control scheme was devised to allow the aircraft not to stall during climbs or over-speed during descents. The required pitch angle to maintain a given airspeed is automatically determined by the control system. As soon as the aircraft reaches the desired altitude window (± 500 ft of reference altitude) the control switches to the cruise phase.

Cruise Phase - In the cruise phase, the airspeed is maintained with throttle and the height is controlled with pitch angle. For the control of height, either with throttle or pitch angle, phase lead compensation was required to bring the stability margins to the required level. The inner/attitude control loop gains were scheduled with respect to dynamic pressure and are presented in Figure C.5. The dynamic pressure range was restricted from 10,000 to 35,000 Pa.

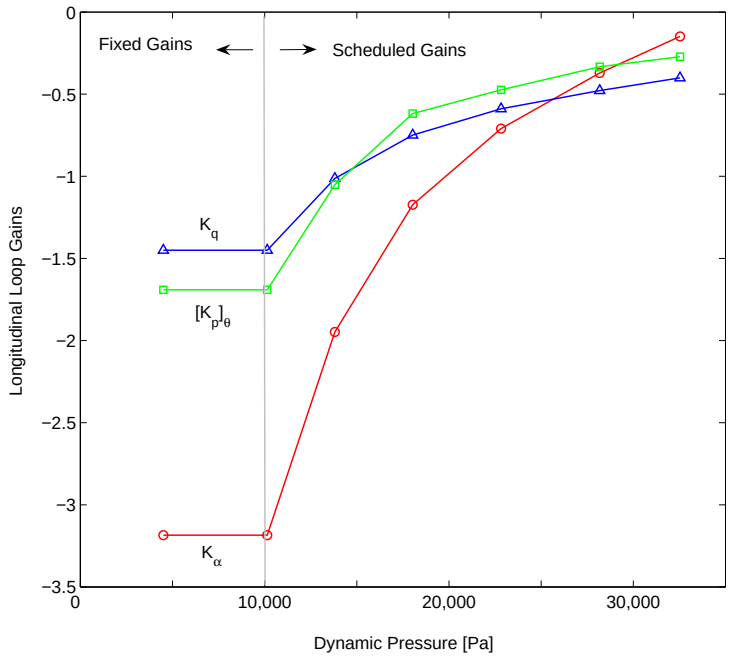

Figure C.5: Gain schedule for longitudinal control

The pitch loop integral gain, $[K_i]_\theta$, was kept at 10% of the proportional gain, $[K_p]_\theta$. The outer loop gains (airspeed and altitude control) were not scheduled and were

kept fixed. These are presented in the following table.

Airspeed control				Height control			
With throttle		With elevator		With throttle		With elevator	
$[K_p]_{V_{\delta_T}}$	$[K_i]_{V_{\delta_T}}$	$[K_p]_{V_{\delta_e}}$	$[K_i]_{V_{\delta_e}}$	$[K_p]_{H_{\delta_T}}$	$[K_i]_{H_{\delta_T}}$	$[K_p]_{H_{\delta_e}}$	$[K_i]_{H_{\delta_e}}$
-0.05	-0.00125	0.00125	0.0000625	0.1	0.005	0.001	0.0005

Table C.2: Longitudinal controller gains

The controllers in Figure C.1 had a PI loop structure and had an integral state associated with it. For example the PI state associated with the pitch angle loop is x_θ. It was important to initialize this state each time the controller boots up or switches from acquire to hold mode and vice versa. For example the control equation for the pitch angle loop is

$$\delta_{e_c} = [K_p]_\theta \theta_{err} + [K_i]_\theta x_\theta - (K_\alpha \alpha + K_q q) \tag{C.7}$$

From the above, the initial state $[x_0]_\theta$ is easily given by setting $\delta_{e_c} = \delta_e$,

$$[x_0]_\theta = \frac{1}{[K_i]_\theta} \left(\delta_e - [K_p]_\theta \theta_{err} + (K_\alpha \alpha + K_q q)\right) \tag{C.8}$$

The remaining longitudinal controllers were initialized using a similar approach.

C.2 Control of Lateral-Directional Axis

The lateral-directional control system provides control of the bank and heading angles along with suppression of sideslip with rudder. The loop structure is shown in Figure C.6. The innermost stability augmentation uses washed out yaw rate feedback, roll rate feedback and an aileron to rudder interconnect. The lateral directional gains were scheduled with respect to dynamic pressure, however at low dynamic pressures (< 10,000 Pa), the required gains to hold the bank angle were very high and had to be limited.

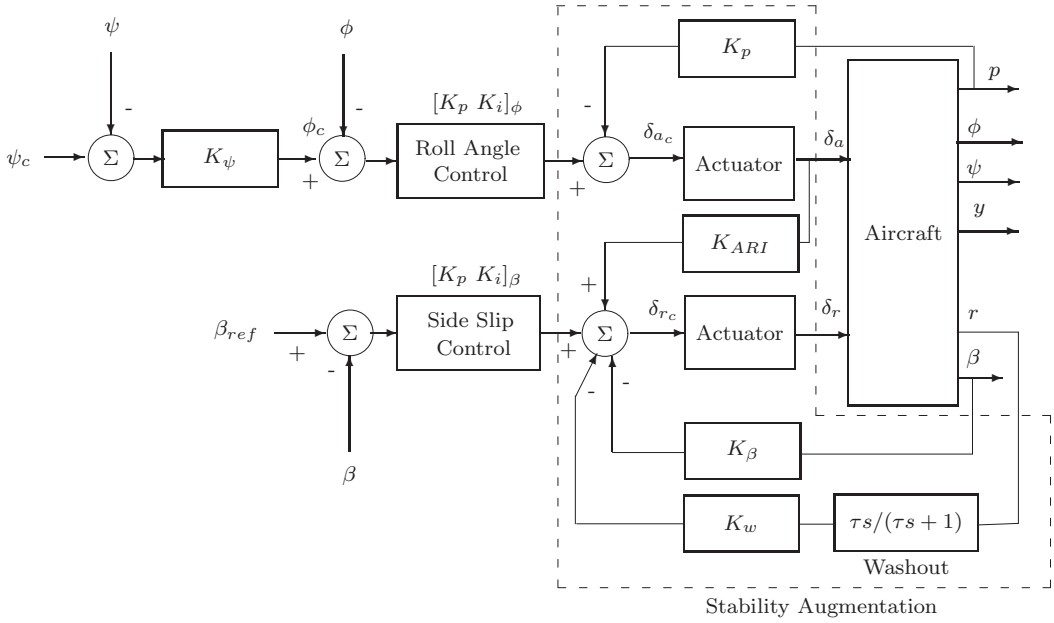

Figure C.6: Lateral-directional FCS architecture

C.2.1 Lateral-Directional - (SAS)

The purpose of the lateral directional stability augmentation system is to increase the dutch roll natural frequency while maintaining good dutch roll damping. The BWB aircraft has poor lateral-directional characteristics, therefore the design of the lateral-directional SAS is considered in slightly greater detail for future reference. To meet Level 1 requirements, a dutch roll frequency ($\omega_{dr} > 0.5$ rad/s) was considered appropriate. This was achieved by sideslip feedback while a washed out yaw rate feedback ensured good dutch roll damping ($\zeta_{dr} > 0.6$).

The system dynamics after addition of aileron and rudder actuators and a washed out yaw rate are given by Equation (C.2.1). The aileron, rudder and washout states are $[x_{\delta_a}, x_{\delta_r}, x_w]$ respectively. The actuator poles are placed at 15 rad/s and the washout time constant, τ_w, is set at 2.5 sec.

$$\begin{bmatrix} \dot{v} \\ \dot{p} \\ \dot{r} \\ \dot{\phi} \\ \dot{x}_{\delta_a} \\ \dot{x}_{\delta_r} \\ \dot{x}_w \end{bmatrix} = \begin{bmatrix} \overset{\circ}{Y}_v & (\overset{\circ}{Y}_p + W_1) & (\overset{\circ}{Y}_r - U_1) & g\cos\theta_1 & \overset{\circ}{Y}_{\delta_a} & \overset{\circ}{Y}_{\delta_r} & 0 \\ \overset{\circ}{L}_v & \overset{\circ}{L}_p & \overset{\circ}{L}_r & 0 & \overset{\circ}{L}_{\delta_a} & \overset{\circ}{L}_{\delta_r} & 0 \\ \overset{\circ}{N}_v & \overset{\circ}{N}_p & \overset{\circ}{N}_r & 0 & \overset{\circ}{N}_{\delta_a} & \overset{\circ}{N}_{\delta_r} & 0 \\ 0 & 1 & \tan\theta_1 & 0 & 0 & 0 & 0 \\ 0 & 0 & 0 & 0 & -1/\tau_{\delta_a} & 0 & 0 \\ 0 & 0 & 0 & 0 & 0 & -1/\tau_{\delta_r} & 0 \\ 0 & 0 & 0 & 0 & 0 & 0 & -1/\tau_w \end{bmatrix} \begin{bmatrix} v \\ p \\ r \\ \phi \\ x_{\delta_a} \\ x_{\delta_r} \\ x_w \end{bmatrix} + \begin{bmatrix} 0 & 0 \\ 0 & 0 \\ 0 & 0 \\ 0 & 0 \\ 1/\tau_{\delta_a} & 0 \\ 0 & 1/\tau_{\delta_a} \\ 0 & 0 \end{bmatrix} \begin{bmatrix} \delta_{a_c} \\ \delta_{r_c} \end{bmatrix} \tag{C.9}$$

The output equation included the washed out yaw rate, r_w, and angle of sideslip, β.

$$\begin{bmatrix} \beta \\ p \\ r \\ \phi \\ r_w \end{bmatrix} = \begin{bmatrix} 1 & 0 & 0 & 0 & 0 & 0 & 0 \\ 0 & 1 & 0 & 0 & 0 & 0 & 0 \\ 0 & 0 & 1 & 0 & 0 & 0 & 0 \\ 0 & 0 & 0 & 1 & 0 & 0 & 0 \\ 0 & 0 & 0 & 0 & 0 & 0 & -1/\tau_w \end{bmatrix} \begin{bmatrix} v \\ p \\ r \\ \phi \\ x_{\delta_a} \\ x_{\delta_r} \\ x_w \end{bmatrix} \tag{C.10}$$

At a low speed flight condition of V=200 kts, Alt = 5000 ft and a nominal CG position, $x_{cg} = 29.4$m, the sideslip to rudder transfer function is,

$$\frac{\beta}{\delta_r} = \frac{0.080225(s+12.69)(s+2.075)(s-0.03938)}{(s+15)(s+1.775)(s+0.07272)(s^2+0.2117s+0.1051)} \tag{C.11}$$

From above the roll pole is at 1.775 rad/s and the dutch roll frequency is at 0.324 rad/s, justifying the selection of washout out pole time constant. The spiral pole is at 0.072 rads/s. The system is non-minimum phase indicating adverse sideslip tendency.

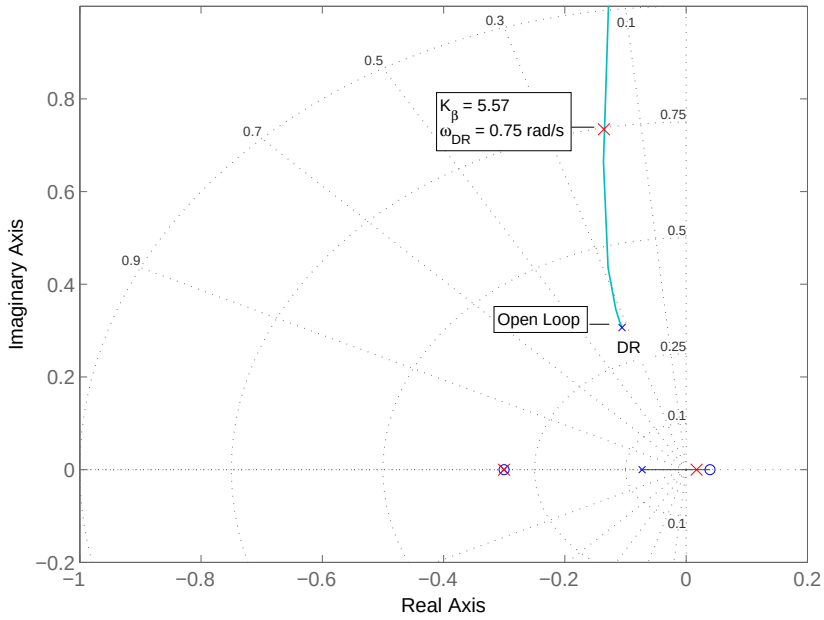

Figure C.7: Effect of sideslip feedback on dutch roll poles

Sideslip Feedback - In Figure C.7, sideslip feedback causes an increase in dutch roll frequency and decrease in damping as the poles move out along the imaginary axis. Feedback gain of $K_\beta = 5.56$ corresponding to a dutch roll natural frequency of $\omega_{dr} = 0.75$ rad/s was selected. The dutch roll damping decreased to 0.175 from its open loop value. It can be noted that sign of feedback gain, K_β, is positive, thus a sudden increase in sideslip due to any disturbance results in a negative rudder displacement ($\delta r < 0$) causing a reduction in sideslip. The effect of sideslip feedback on the directional stability is therefore stabilizing, however it comes at the cost of reduction in dutch roll damping.

Yaw Rate Feedback - The dutch roll damping was improved by a using a washed out rate feedback on the rudder control. Figure C.8 shows the results. The washout feedback gain was increased till a dutch roll damping of $\zeta_{dr} = 0.6$ was achieved. For the low speed flight condition considered, the washout gain is very high ($K_w = -8.37$) and can easily lead to control saturation.

Figure C.9 shows the yaw rate impulse response with sideslip and washed out yaw rate feedback. The effect of sideslip feedback is to improve the dutch roll frequency however the damping is reduced. Washed out yaw rate feedback improves the dutch roll damping to the desired level. A well damped and fast dutch roll mode also has a beneficial effect on the roll rate and angle response. Figure C.10 compares the significant improvement before and after a stability augmentation system (SAS).

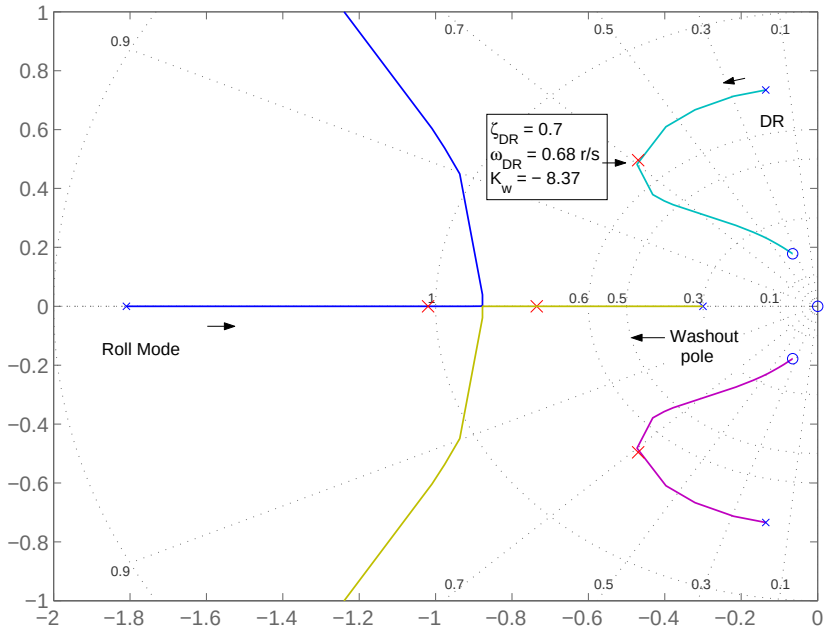

Figure C.8: Effect of yaw rate feedback on lateral dynamics

With the SAS, the roll rate and angle are in the direction intended. The roll angle approximates a pure integrator, but still far away from it. The roll angle response needs to be improved further.

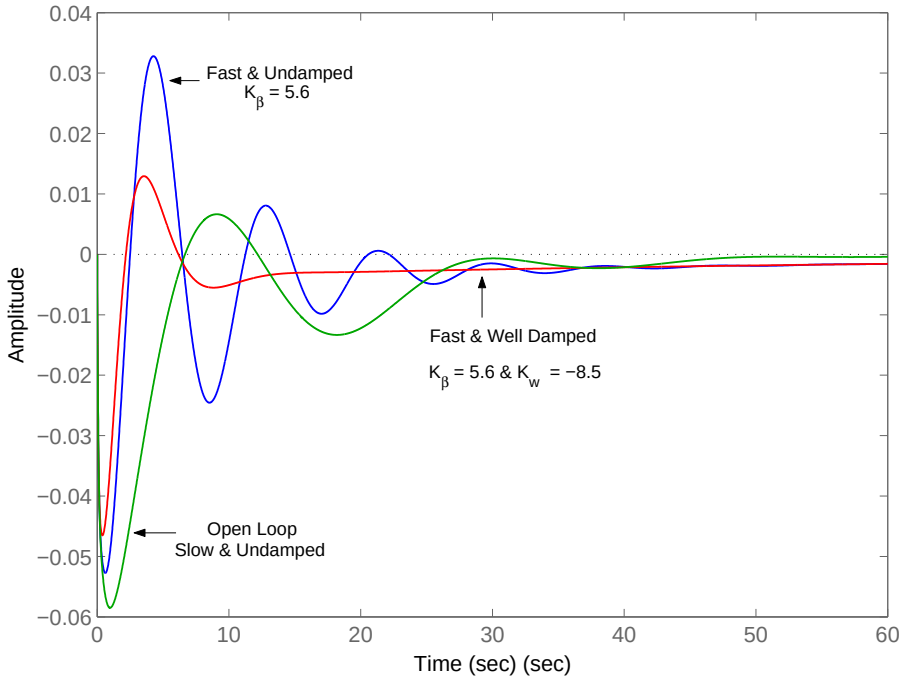

Figure C.9: Yaw rate to rudder (r/δ_r) impulse response with SAS

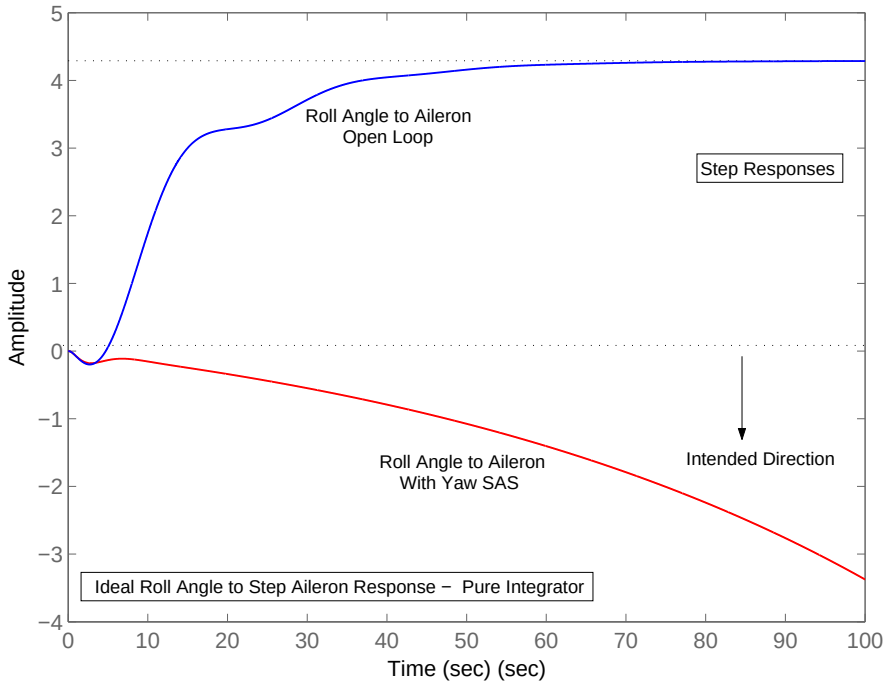

Figure C.10: Roll angle to aileron (ϕ/δ_a) response with yaw SAS

Roll Rate Feedback and Aileron to Rudder Interconnect - To maintain a consistent roll response throughout the flight envelope, it is desired to speed up the roll rate response using roll rate feedback. At higher airspeeds, the roll mode is fast and minimal roll rate feedback is necessary, however at lower airspeeds, the roll mode is sluggish and higher gains are required. The roll rate feedback gain was set at $K_p = -2.26$ to achieve a fast roll mode while still keeping the dutch roll frequency high, $\omega_{dr} > 0.5$ rad/s. However even after roll rate feedback, the roll angle response was not too much different than Figure C.10 and turn coordination through an aileron to rudder interconnect had to be used. To incorporate the aileron to rudder interconnect, the aileron actuator state was added into the output matrix,

$$y = Cx = \begin{bmatrix} \beta \\ p \\ r \\ \phi \\ r_w \\ \delta_a \end{bmatrix} = \begin{bmatrix} 1 & 0 & 0 & 0 & 0 & 0 & 0 \\ 0 & 1 & 0 & 0 & 0 & 0 & 0 \\ 0 & 0 & 1 & 0 & 0 & 0 & 0 \\ 0 & 0 & 0 & 1 & 0 & 0 & 0 \\ 0 & 0 & 0 & 0 & 0 & 0 & -1/\tau_w \\ 0 & 0 & 0 & 0 & 1 & 0 & 0 \end{bmatrix} \begin{bmatrix} v \\ p \\ r \\ \phi \\ x_{\delta_a} \\ x_{\delta_r} \\ x_w \end{bmatrix} \tag{C.12}$$

The control equation including the aileron to rudder interconnect is

$$u = -Ky = -\begin{bmatrix} 0 & 0 & K_p & 0 & 0 & 0 \\ K_\beta & 0 & 0 & 0 & K_w & -K_{ari} \end{bmatrix} \begin{bmatrix} \beta \\ p \\ r \\ \phi \\ r_w \\ \delta_a \end{bmatrix} \tag{C.13}$$

and the system dynamics can now conveniently be expressed as,

$$A_c = A - BKC \tag{C.14}$$

Where A and B represent the open loop system dynamics including actuators. The following close loop roll rate to aileron transfer function was obtained from the above matrix formulation,

$$\frac{p}{\delta_a} = \frac{-4.9401(s+14.64)(s+0.60)(s-0.018)(s^2+0.147s+0.028)}{(s+1.57)(s+0.722)(s-0.0156)(s^2+0.838s+0.3574)(s^2+29.24s+219.3)} \tag{C.15}$$

Equation C.15 shows the roll rate to aileron (p/δ_a) transfer function with an ARI gain ($K_{ari} = 1.0$) and roll rate loop engaged. The following can be observed.

- The actuator pole now forms an oscillatory pair, but is fast and well damped.
- The ARI causes the roll subsidence pole to slow down to 1.573 rad/s from its open loop value of 1.775 rad/s. This also justifies the use of roll rate feedback, otherwise the roll mode slows down to below Level 1, when ARI is engaged.
- The aileron to rudder interconnect speeds up the dutch roll mode, which is almost canceled by numerator zeros, hence a less oscillatory roll rate response.
- A slow but unstable spiral is almost canceled by a numerator zero.

The roll response to aileron control for a flight speed of 200 knots is shown in Figure C.11. The beneficial effect of aileron to rudder interconnect is evident.

C.2.2 Lateral-Directional Gain Schedule

With the lateral directional stability augmentation in place, the bank angle and heading control loops were formulated using standard methods, however the final gains actually used in the non-linear simulation had to be reduced/limited to prevent controls saturation. Figure C.12 presents the gain schedule.

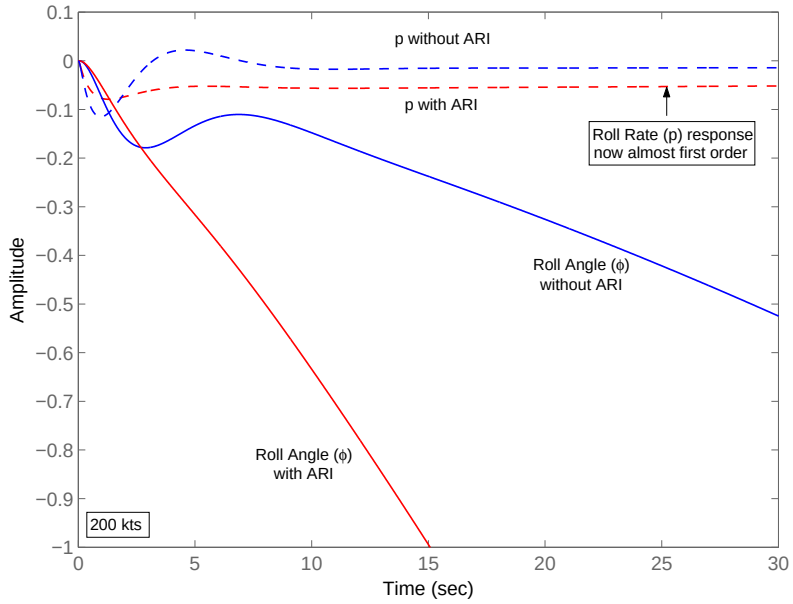

Figure C.11: Roll rate/angle response at 300 knots with and without ARI

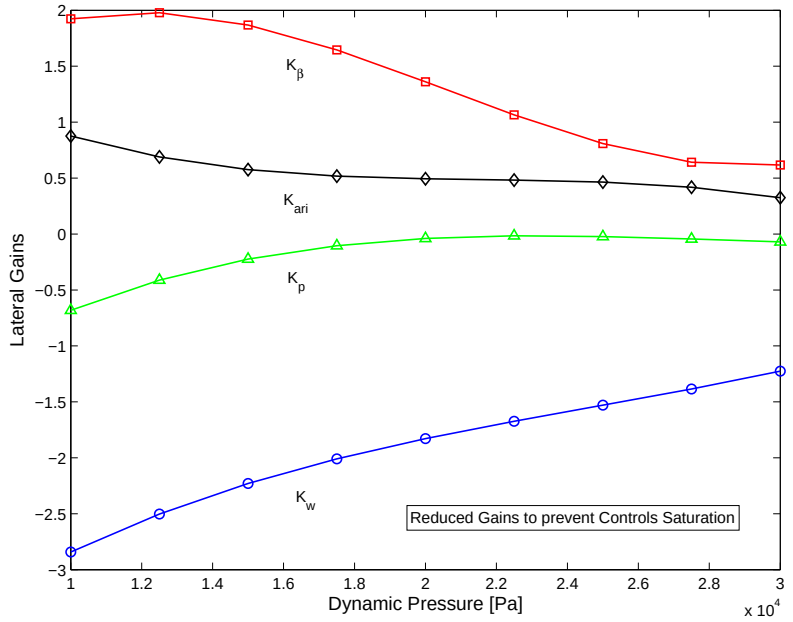

Figure C.12: Gain schedule for lateral-directional control

C.2.3 Conclusions

The above exercise clearly illustrates the difficulties in augmenting the lateral-directional dynamics of the BWB aircraft. A slow dutch roll, poor directional stiffness and adverse yaw are some of the troublesome factors. Besides inherently poor dynamics, the rudder control is severely limited in control authority especially at lower airspeeds and gains had to be restricted to avoid controls saturation.

Appendix D

Implementation Details - BWB Model with Blown Flaps

This section briefly describes the ESDU model subroutines written initially in MATLAB for trim and linear analysis and then in C Language for non-linear simulation implementation. The C language code for the ESDU aerodynamic model has 76 strips and runs in real time along with the hybrid engine model. The development of this model was greatly facilitated by Cooke's model of the NFLC Jetstream [59] which uses the ESDU methods for aerodynamic estimation and by Amrane [60] which discusses the development of a sail plane model using a strip element approach. A listing of the subroutines is presented in Table D.1 along with their brief description.

The user needs to initialize the model by first calling the `<init_geometry.m>` function, this will load the `<geom>` structure with appropriate airfoil geometry profile parameters along the span. If the user requires to make changes to the BWB planform or airfoil geometry, it will be required to make appropriate changes in this geometry initialization file. The next step is to call the function, `<get_aero_wing.m>`, with appropriate inputs such as the values of the current state vector, control inputs and CG position. This function then returns X, Y, Z body forces and moments L, M, N about the centre of gravity or the moment reference point. In a similar fashion, the function `<get_aero_fin.m>` returns contributions of the vertical fin to these aerodynamic forces and moments in body axis. The wing and fin contributions are then added up to get the net forces and moments in body axis.

Program listings are available in soft form in a CD accompanying this thesis.

No	Subroutine	Description	ESDU
1.0	init_geometry.m	Sets up the static geometry parameters for the BWB wing in a `<geom>` global structure. Loads the airfoil profiles, defines number of sections, allocates control, calculates strip areas and defines some of the fixed airfoil geometrical parameters.	-
2.0	get_aero_wing.m	Main subroutine to calculate wing forces and moments in body axis. Calls the following subroutines.	-
2.1	get_controls.m	Updates the dynamic part of the `<geom>` structure by assigning control deflections to each strip element.	-
2.2	atmos_AK.m	An atmospheric model routine by Dr. Alistair Cooke.	-
2.3	airdata_y.m	Calculates spanwise air data parameters such as angle of attack, sideslip, airspeed etc.	-
2.4	CL_y.m	Calculates spanwise lift coefficient with blown flaps.	
2.4.1	CLa_inviscid.m	Calculates $a_{1i}, \alpha_0, C_{m0_i}, x_{ac}$	72024
2.4.2	CLa_viscid.m	Calculates a_{1v}	97020
2.4.3	CL_max.m	Calculates $C_{L_{max}}$	84026
2.4.4	CL0_CLmax.m	Calculates $\Delta C_{L0_{flap}}, \Delta C_{L_{max_{flap}}}$	94028
2.5	CD_y.m	Calculates spanwise drag coefficient.	
2.5.1	CD0_airfoil.m	Calculates C_{D0} for the airfoil section	00027
2.5.2	CD0_flap.m	Calculates $\Delta C_{D0_{flap}}$ due to flap deflection	87005
2.6	Cm_y.m	Calculates spanwise pitch moment coefficient.	03017 98017
3.0	get_aero_fin.m	Vertical fin forces and moments	
		Y_v, L_v, N_v derivatives due to side velocity (v)	82010
		Y_r, L_r, N_r derivatives due to yaw rate (r)	32017
		Y_p, L_p, N_p derivatives due to roll rate (p)	83006
		$Y_{\delta_r}, L_{\delta_r}, N_{\delta_r}$ derivatives due to rudder deflection (δ_r)	87008
3.1	CLa_wing.m	To calculate the vertical fin lift curve slope $a_{1_{fin}}$	70011

Table D.1: Description of ESDU strip element model subroutines

Appendix E

Implementation Details - Hybrid Turbofan Model

This section covers some additional details of the 3 spool turbofan hybrid engine model discussed in Chapter 4. Specifically it entails, (i) a brief summary of the model sub-routines, (ii) a graphical illustration of the compressor and turbine maps used in the simulation and (iii) some code listings for the iterative part of the program. The turbofan model was implemented in MATLAB/Simulink as <`RR500.mdl`> and consists of the following subroutines.

No	Subroutine	Description
1	RR500_init.m	Specifies the design point inputs for the compressors and the turbines. It also sets up values for rotor inertias, component volumes, nozzle areas and values for the initial state vector.
2	inlet_calcs.m	Performs inlet calculations, establishes inlet exit conditions.
3	cmap_LPC.m	On the first call, this subroutine loads a reference Fan/LPC map and scales it according to the design point inputs specified in <`RR500_init.m`>. On subsequent calls, it uses the search routine <`search.m`> to get compressor mass flow and efficiency, given compressor speed and pressure ratio.
4	cmap_IPC.m	Performs a similar function as above, for the IP compressor.
5	cmap_HPC.m	Loads, scales and searches the high pressure compressor.
6	thcomp.m	Iterative subroutine for compressor thermodynamics. It establishes exit conditions of specific enthalpy, h, temperature, T, pressure, P and entropy, S.

Some of the above subroutines, specifically those for iterative solution of compressor

No	Subroutine	Description
7	comb_calcs.m	Performs combustor calculations.
8	cmap_HPT.m	On the first call, this subroutine loads a reference high pressure turbine map and scales it according to the turbine design point inputs specified in <RR500_init.m>. On subsequent calls, it uses the search routine <search.m> to get turbine mass flow and efficiency given turbine speed and pressure ratio. It may be noted that the reference turbine maps were obtained from the DYNGEN program [12], which uses enthalpy work function ($\Delta H/T$) instead of turbine pressure ratios. These maps are therefore internally converted to the turbine pressure ratio vs mass flow form for use in this simulation.
9	cmap_IPT.m	Performs a similar function as above for the IP turbine.
10	cmap_LPT.m	Loads, scales and searches the low pressure turbine.
11	thturb.m	Iterative subroutine for turbine thermodynamics. It establishes exit conditions of specific enthalpy, h, temperature, T, pressure, P and entropy, S.
12	therm.m	Calculates thermodynamic conditions for a fuel to air mixture using either temperature or enthalpy. Uses <gasprop.m>.
13	gasprop.m	Calculates the basic gas properties of air alone or fuel/air mixture based on JP4.
14	search.m	Compressor/turbine map linear interpolation search routine.

Table E.1: Description of 3 spool turbofan model subroutines

and turbine thermodynamics are discussed in a greater detail later in this chapter.

E.1 Components Maps

In this section, a graphical illustration of the compressor and turbine maps scaled to their respective design points is presented. Lines of constant efficiencies and the design point values are identified on the maps. These maps are automatically generated by specified design point values in <RR500_init.m> file and may be considered representative of the Trent 500. The actual component maps are however usually proprietary and therefore may be different than those presented here. The design points have been placed at an area of maximum compressor or turbine efficiency.

E.1.1 Compressor Maps

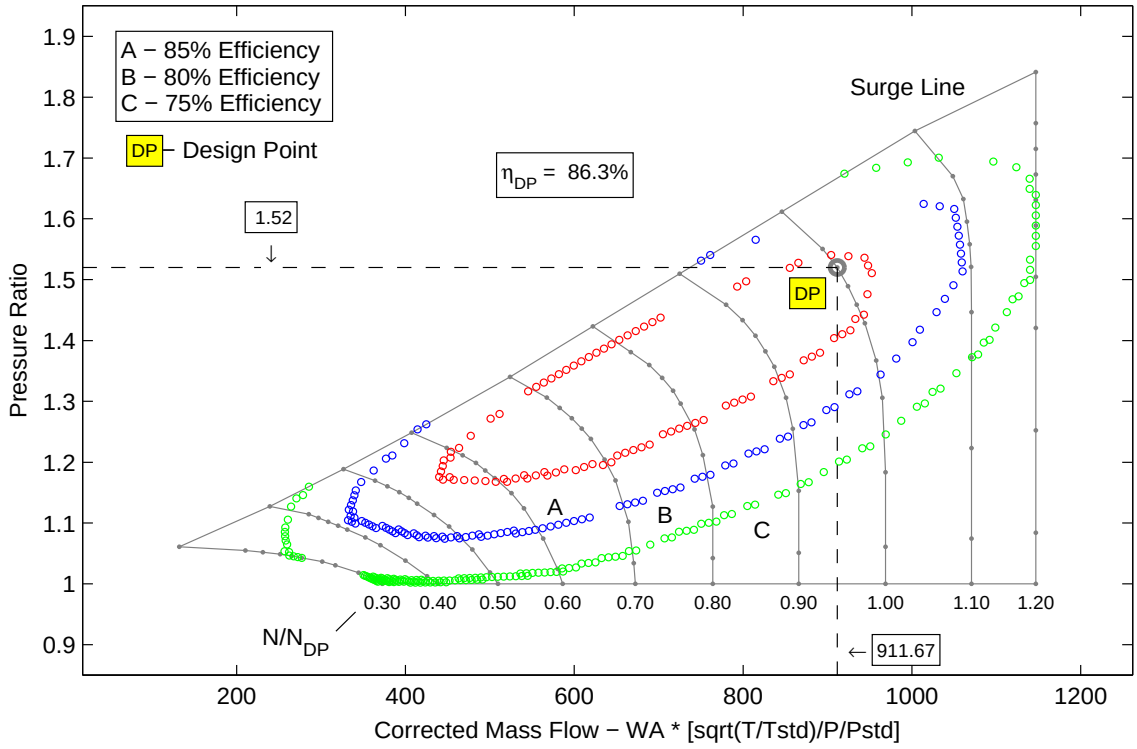

Figure E.1: Low Pressure Compressor (LPC/Fan) map and design point

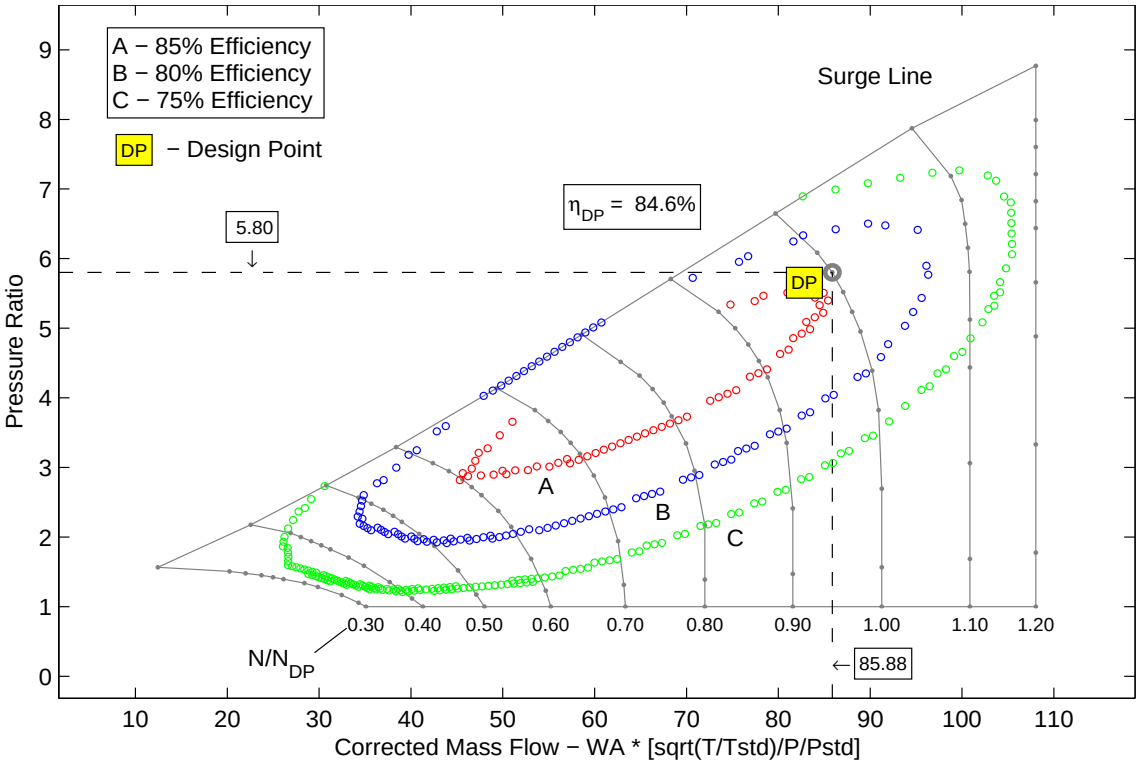

Figure E.2: Intermediate Pressure Compressor (IPC) map and design point

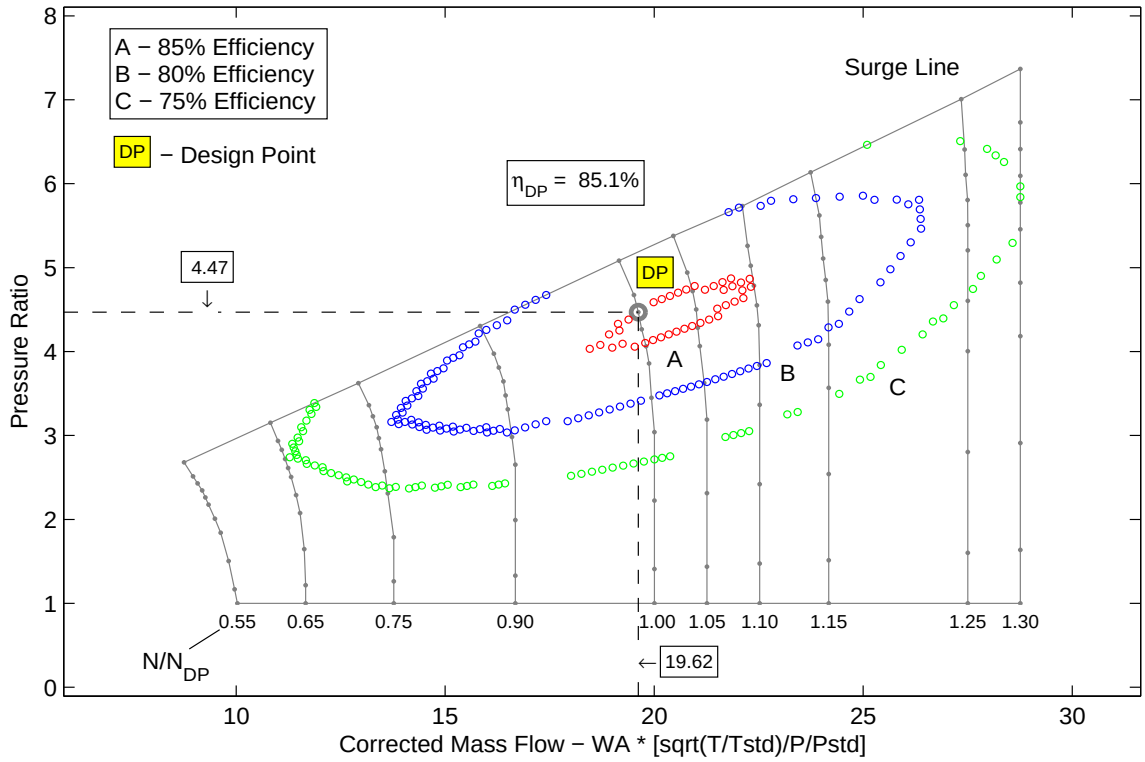

Figure E.3: High Pressure Compressor (HPC) map and design point

E.1.2 Turbine Maps

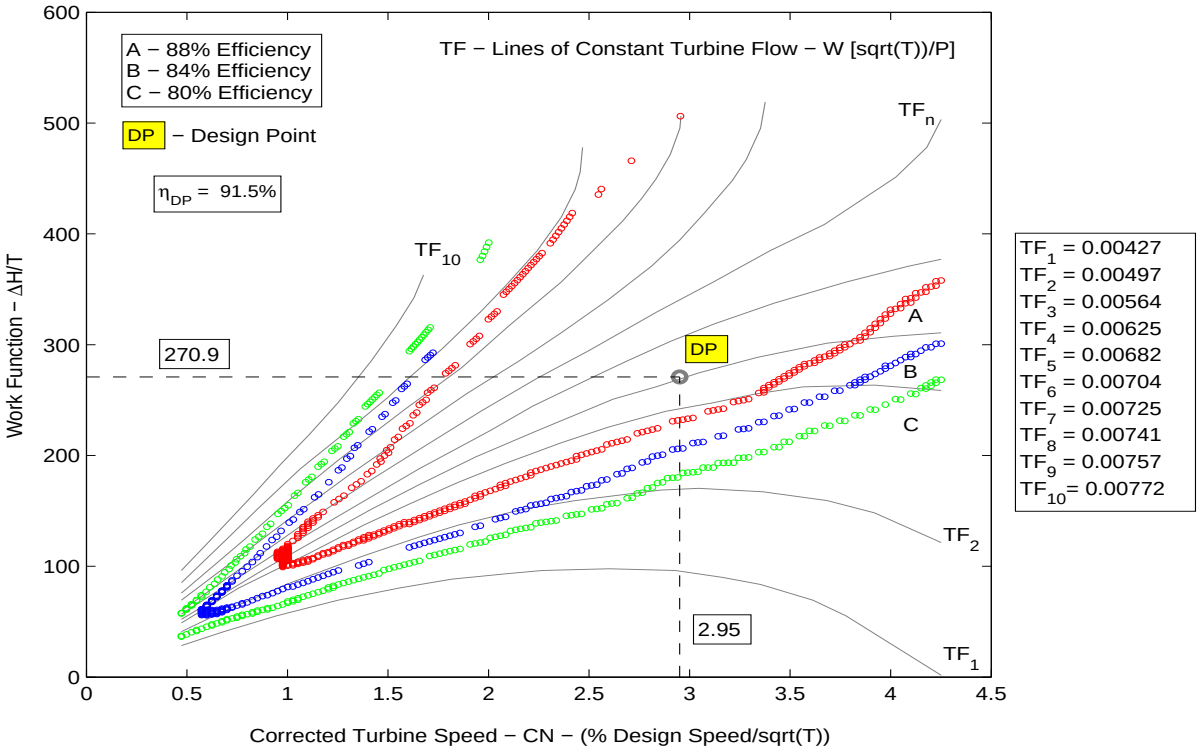

Figure E.4: Low Pressure Turbine (LPT) map and design point

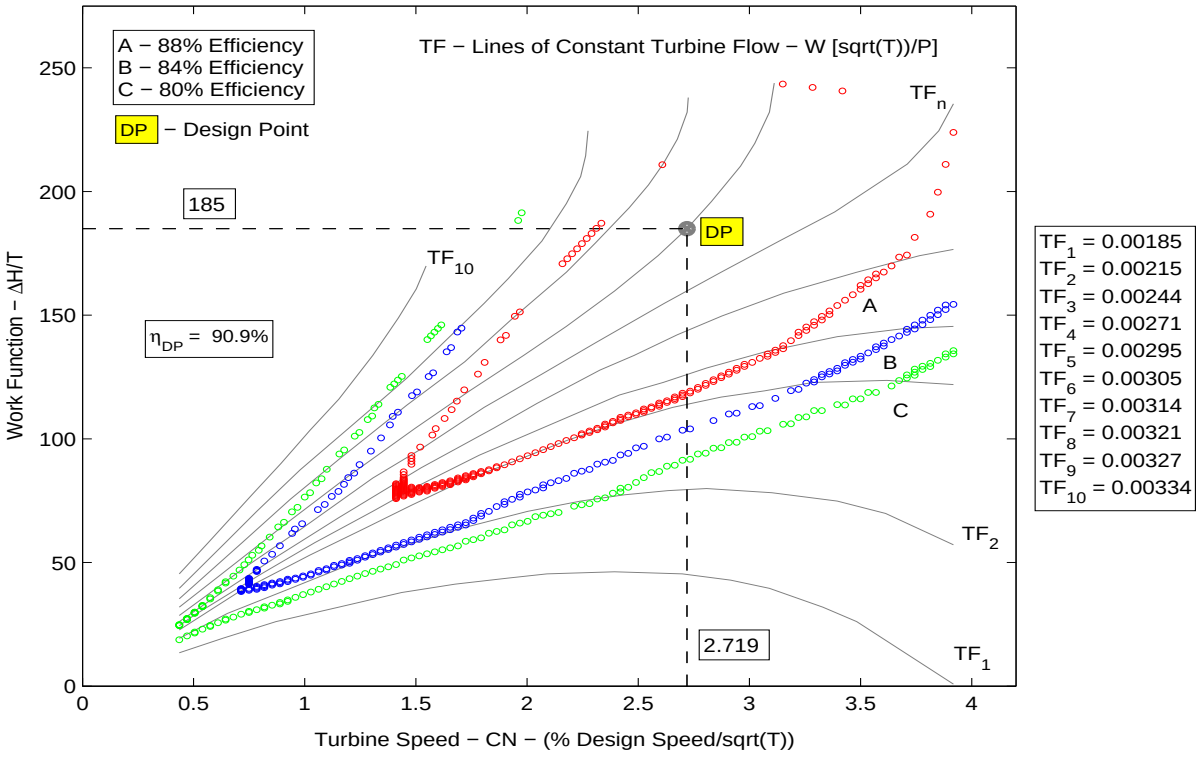

Figure E.5: Intermediate Pressure Turbine (IPT) map and design point

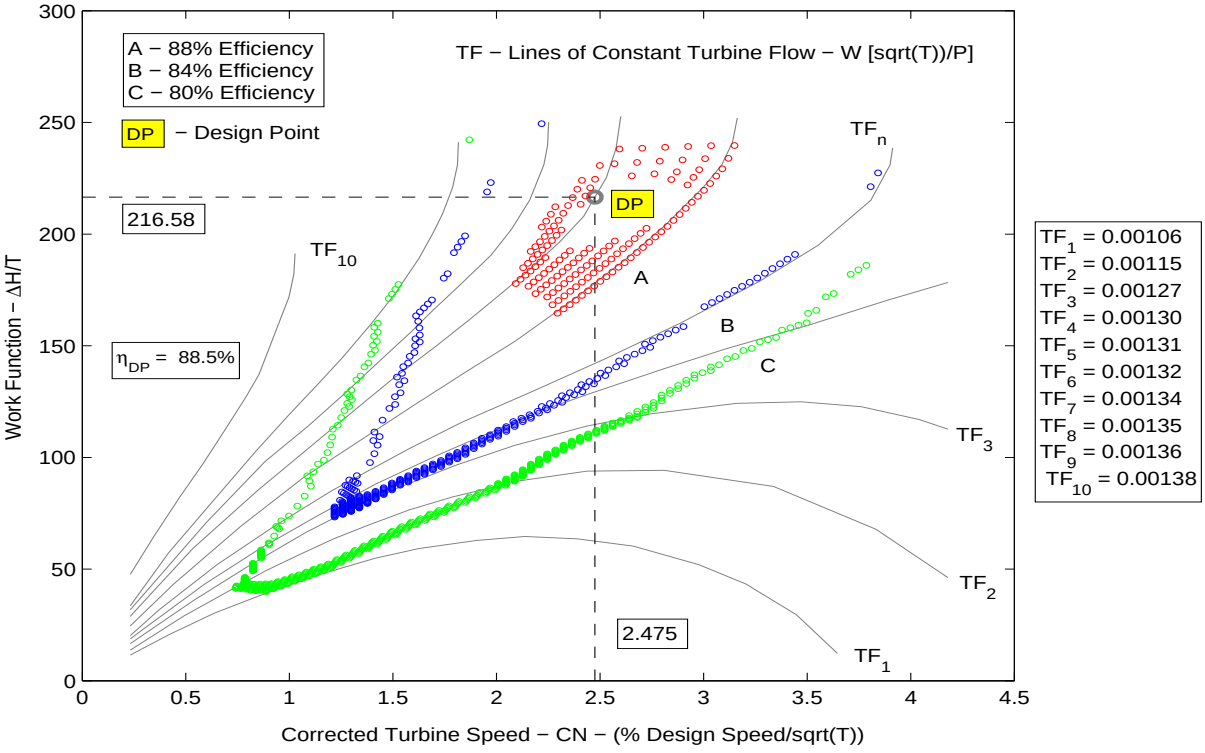

Figure E.6: High Pressure Turbine (HPT) map and design point

E.2 Code Listings

E.2.1 Iterative Routine for Compressor Calculations

In Chapter 4, a hybrid scheme was adopted for engine simulation, in which the compressor and turbine thermodynamic conditions are calculated using an iterative procedure and the pressure derivatives and hence exit pressures using the component volume technique. Whereas, other details of the method have been covered earlier, it was considered important for future reference to list here the subroutines used for iterative compressor/turbine calculations. The iterative subroutine for the compressor as listed below is a modified version from the open source reference, DYNGEN [12]. Figure E.7 shows a Simulink block diagram for the HP compressor that uses this iterative subroutine to perform stage calculations. The IP and the LP compressor stages were implemented using a similar procedure.

```
% ================================================================================
%            COMPRESSOR ITERATIVE THERRMODYNAMIC CALCULATIONS                    .
% ================================================================================
%
% Function Name : [TO,HO,SO,PO] = thcomp(PR,ETA,T,H,S,P,FAR,SI)
% Purpose       : Calculates Thermodynamic conditions for the compressor.
%
%     Inputs to the program:
%
%     PR        = Compressor Pressure Ratio                        [-]
%     ETA       = Compressor Efficiency                            [-]
%     T         = Temperature at Inlet                             [K]
%     H         = Specific Enthalpy at Inlet                   [J/Kg/s]
%     S         = Entropy at Inlet                             [J/Kg-C]
%     P         = Pressure at Compressor Inlet                     [Pa]
%     FAR       = Fuel to Air Ratio at Compressor Inlet            [-]
%
%     Outputs of the program:
%
%     TO        = Temperature at Compressor Exit                   [K]
%     HO        = Specific Enthalpy at Compressor Exit         [J/Kg/s]
%     SO        = Exit Entropy                                 [J/Kg-C]
%     PO        = Pressure at Compressor Exit                      [Pa]
%
% Subroutines used :
%
% thermo()      : Calculates gas thermodynamic conditions using temperature
%                 or enthalpy.
%
% Modified From Original reference : DYNGEN[]
% ================================================================================

function [TO,HO,SO,PO] =  thcomp(PR,ETA,T,H,S,P,FAR,SI)

CPG = 1048.0;  % Specific Heat for Air...[J/Kg/K]
```

```
% Pressure at Compressor Exit
% ---------------------------

PO = P*PR;

% Initial Guess for Exit Temperature
% ----------------------------------

TP = T * PR^0.28572;

% Step 1. Find Exit Enthalpy (H) iteratively, assuming Process to be Isentropic
% ------------------------------------------------------------------------------

for (I=1:25)

    % Thermodynamic gas calculations
    % ------------------------------

    % Inputs - PO, TP (Actual Exit Pressure    , Guessed Exit Temperature)
    % Output - SP, HP (Exit Entropy Isentropic , Exit Enthalpy Isentropic)

    XX1 = 0.0;  % Dummy Input
    FLAG =  0;  % (0) - Use Temperauture for Gas Thermo Calculations

    [SP,YY1,HP,YY2] =  therm(PO,XX1,TP,FAR,FLAG);

    % Difference in Inlet and Exit Entropy
    DELS = SP-S;

    % Check convergence (Exit Entropy ~ Inelt Entropy)
    if (abs(DELS) <= (0.00005 * S)) break; end

    % New Guess for Exit Temperature
    TP = TP / exp(DELS/CPG);

    if (I==25)
     disp('Error - Iterations exceeded in THCOMP');
    end
end

% Step 2. Now Use Compressor Efficiency to find actual exit Enthalpy (HO)
% ------------------------------------------------------------------------

% Note if ETA = 1.0, then HO = HP and process will be isentropic
HO = H + (HP-H)/ETA;

% Step 3. Use Exit Enthalpy (HO) to Calculate Exit Temperature (TO) and Entropy (SO)
% -----------------------------------------------------------------------------------

% Inputs - PO, HO (Exit Press  , Exit Enthalpy after including ETA effect)
% Output - SO, TO (Exit Entropy, Exit Temperature)

FLAG =  1;  % (1) - Use Enthalpy for Gas Thermo Calculations

[SO,YY1,YY,TO] =  therm(PO,HO,XX1,FAR,FLAG);

% <End of File>
```

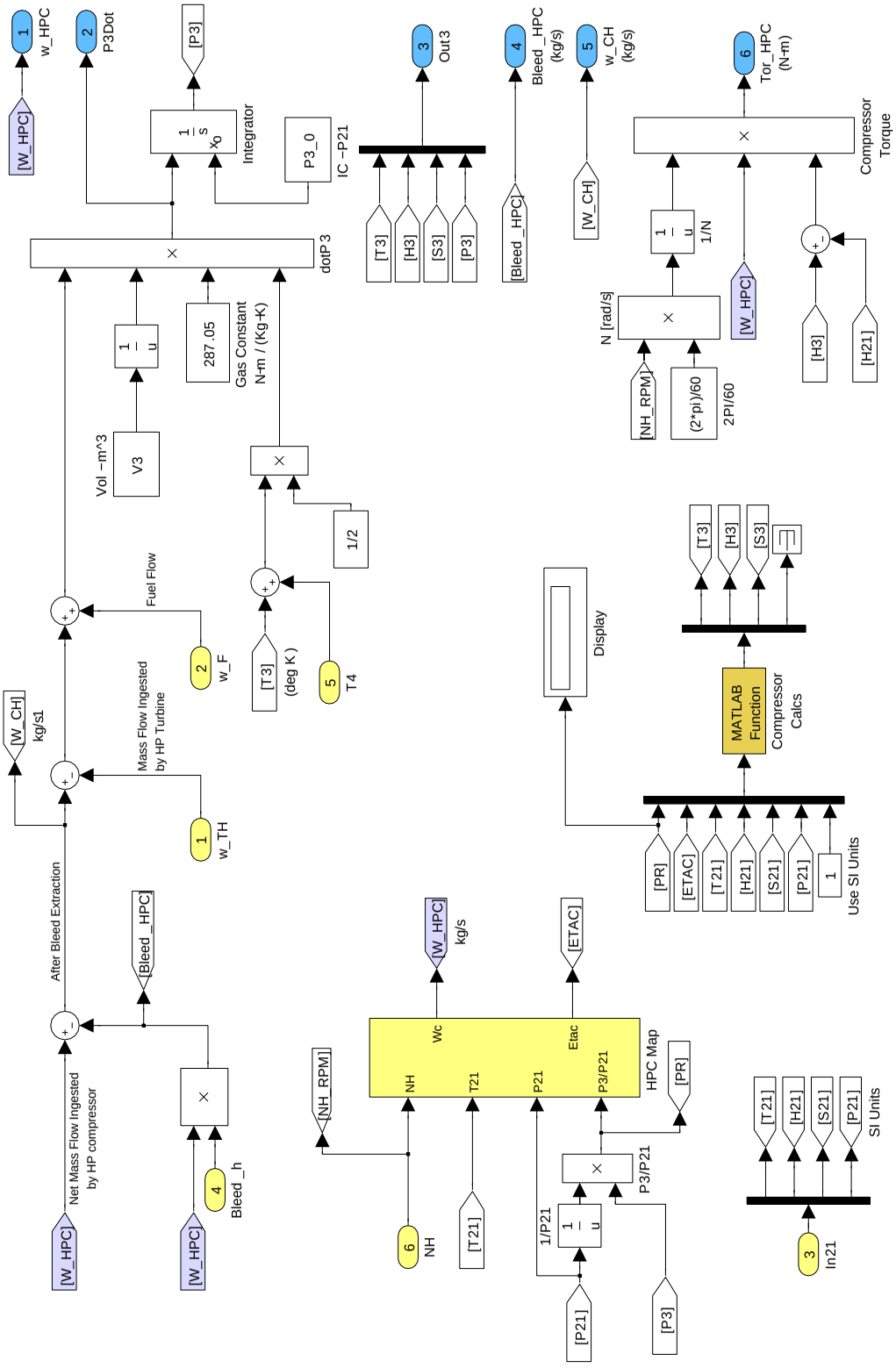

Figure E.7: HP Compressor calculations and pressure derivatives

E.2.2 Iterative Routine for Turbine Calculations

The turbine calculations were performed using an iterative procedure similar to compressors, however in this case the input pressure ratio (PR) is less than 1.0, whereas for the compressor it was greater than 1.0. However, this makes no difference in the calculations procedure, only the corresponding exit temperatures are less as the turbine extracts energy from the flow. In addition, the exit enthalpy is calculated differently than for the compressor stage, specifically if h_i is the inlet enthalpy, and h_p is the enthalpy at the turbine exit assuming the process to be isentropic, then the actual exit enthalpy is

$$h_o = h_i - \eta\Delta_h = h_i - \eta(h_p - h_i) \tag{E.1}$$

where η is the turbine efficiency. Thus if $\eta = 1.0$, then the exit enthalpy would be the same as that for an isentropic process and the turbine would be able to extract greater energy from the flow. A MATLAB/Simulink subsystem that implements the turbine calculations is shown in Figure E.8 and the code listing is presented below.

```
% ================================================================================
%                   TURBINE ITERATIVE THERRMODYNAMIC CALCULATIONS                .
% ================================================================================
%
% Function Name : [TO,HO,SO,PO] = thturb(PR,ETA,T,H,S,P,FAR)
% Purpose       : Calculates Thermodynamic conditions for the turbine.
%
%     Inputs to the program:
%
%     PR        = Turbine Pressure Ratio                          [-]
%     ETA       = Turbine Efficiency                              [-]
%     T         = Temperature at Inlet                            [K]
%     H         = Specific Enthalpy at Inlet                  [J/Kg/s]
%     S         = Entropy at Inlet                            [J/Kg-C]
%     P         = Pressure at Turbine Inlet                       [Pa]
%     FAR       = Fuel to Air Ratio at Turbine Inlet              [-]
%
%     Outputs of the program:
%
%     TO        = Temperature at Turbine Exit                     [K]
%     HO        = Specific Enthalpy at Turbine Exit           [J/Kg/s]
%     SO        = Exit Entropy                                [J/Kg-C]
%     PO        = Pressure at Turbine Exit                        [Pa]
%
% Subroutines used :
%
% thermo()      : Calculates gas thermodynamic conditions using temperature
%                 or enthalpy.
% ================================================================================

function [TO,HO,SO,PO] = thturb(PR,ETA,T,H,S,P,FAR)

CPG = 1048.0;  % Specific Heat for Air...[J/Kg/K]
```

```
% Pressure at Compressor Exit
PO = P*PR;

% Initial Guess for Exit Temperature
% ----------------------------------

TP = T * PR^0.28572;

% Step 1. Find Exit Enthalpy (H) iteratively, assuming Process to be Isentropic
% ------------------------------------------------------------------------------

for (I=1:25)

    % Thermodynamic gas calculations
    % ------------------------------

    % Inputs - PO, TP (Actual Exit Pressure    , Guessed Exit Temperature)
    % Output - SP, HP (Exit Entropy Isentropic , Exit Enthalpy Isentropic)

    XX1 = 0.0;  % Dummy Input
    FLAG =  0;  % (0) - Use Temperauture for Gas Thermo Calculations

    [SP,YY1,HP,YY2] =  therm(PO,XX1,TP,FAR,FLAG);

    % Difference in Inlet and Exit Entropy
    DELS = SP-S;

    % Check convergence (Exit Entropy ~ Inelt Entropy)
    if (abs(DELS) <= (0.00005 * S)) break; end

    % New Guess for Exit Temperature
    TP = TP / exp(DELS/CPG);

    if (I==25) disp('Error - Iterations exceeded in THTURB'); end
end

% Step 2. Now Use Turbine Efficiency to find the new Enthalpy
% -----------------------------------------------------------

DELH_i = H - HP;  % isentropic drop in enthalpy

% Note if ETA = 1.0, Then HO = HP and process will be isentropic
HO = H - ETA * DELH_i;

% Step 3. Use Exit Enthalpy (HO) to Calculate Exit Temperature (TO) and Entropy (SO)
% -----------------------------------------------------------------------------------

% Inputs - PO, HO (Exit Press  , Exit Enthalpy after including ETA effect)
% Output - SO, TO (Exit Entropy, Exit Temperature)

FLAG =  1;  % (1) - Use Enthalpy for Gas Thermo Calculations

[SO,YY1,YY,TO] =  therm(PO,HO,XX1,FAR,FLAG);

% <End of File>
```

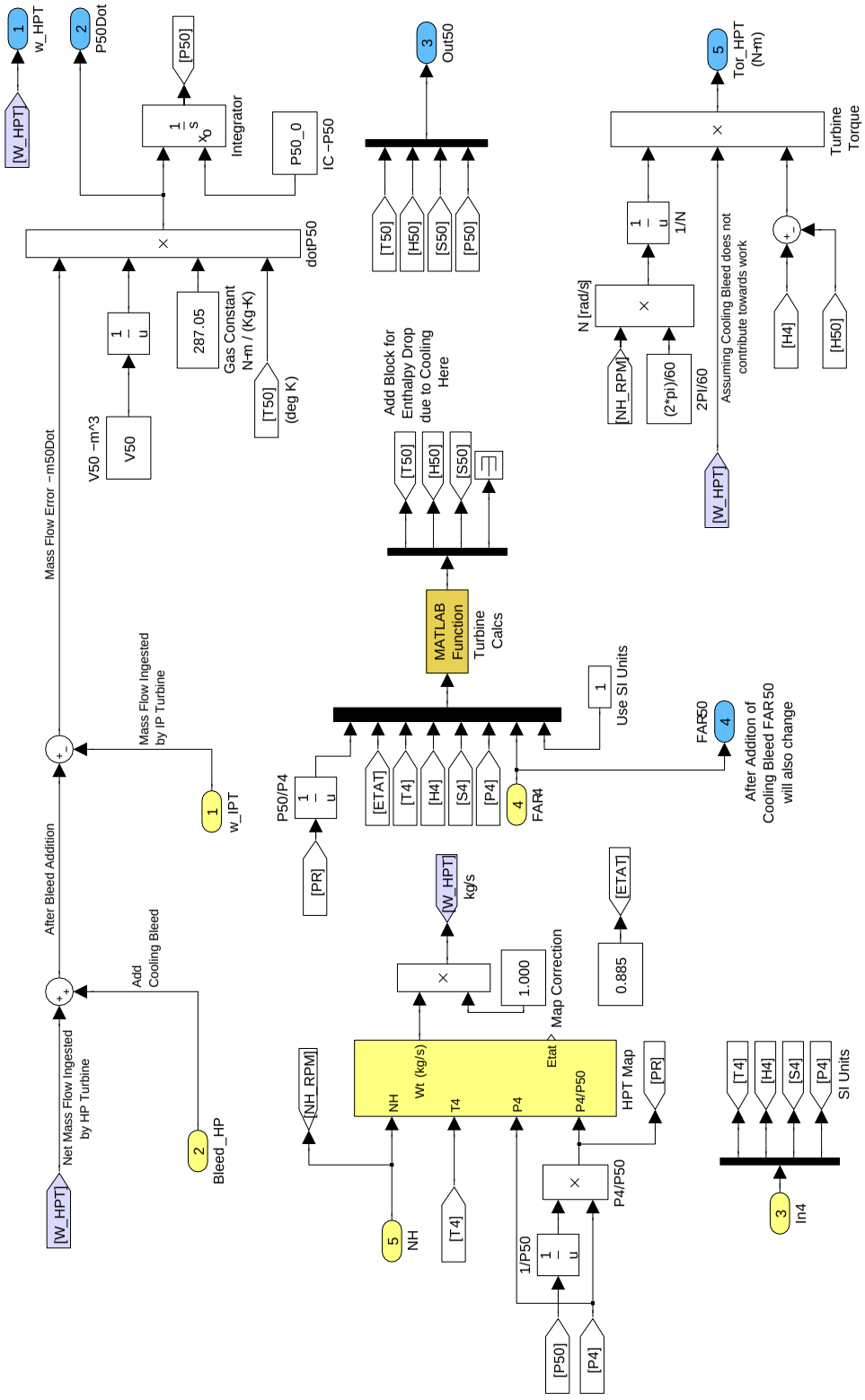

Figure E.8: HP Turbine calculations and pressure derivatives

E.2.3 Calculation of Thermodynamic properties of Gas

An important subroutine <therm.m> that was used in the compressor and the turbine calculations is listed here. This subroutine calculates temperature, given enthalpy or enthalpy given temperature for a given fuel to air mixture. If the state of enthalpy is specified for the gas, then the corresponding temperature has to be found through an iterative procedure. From reference [56], enthalpy, h, is defined as,

$$h = f(c_p(T), T) \tag{E.2}$$

Thus if enthalpy, h, is known and $c_p(T), T$ are not known, then the value of temperature, T, is found by an iterative method, which satisfies the above equation. An initial guess for temperature ($T_g = h/c_p$) is made by assuming a nominal value for c_p, and a corresponding guess enthalpy, h_g, is calculated using the <gasprop.m> function. The difference in enthalpy ($\Delta h = h - h_g$) is used to find a new and better guess for the temperature. This process is repeated till a temperature value is found so that error, Δh, is below a specified tolerance, the procedure normally converges in a few iterations.

If the temperature value is specified, then an iterative procedure is not required and corresponding enthalpy can be found directly using gas tables or the <gasprop.m> routine. This subroutine also returns the state of entropy for the gas. These subroutines may be considered as standard and can be found in engine simulation programs such as DYNGEN [12], however they are listed here for reference.

```
% ================================================================================
%               THERMOYDNMAIC PROPERTIES FOR FUEL AND AIR MIXTURE                .
% ================================================================================
%
% function [SX,AMX,HX,TX] =  therm(P,H,T,FAR,FLAG)
%
% Purpose  : Provides Thermodynamic conditions for a fuel to air mixture using
%            either temperature or enthalpy.
%
%     Input to the program is:
%            P    =  Pressure
%            H    =  Enthalpy    or
%            T    =  Temperature
%            FAR  =  Fuel to Air Ratio
%            FLAG =  1, Use Input H, for Gas Properties Calcs
%                    0, Use Input T, for Gas Properties Calcs
%
%     Output of the program is:
%            SX   =  Entropy
%            AMX  =  Speed of Sound
```

```
%            TX   =  Temperature (IF H is input, FLAG = 1)
%            HX   =  Enthalpy    (if T is input, FLAG = 0)
%
% Subroutines used :
%
% gasprop()  : Calculates gas thermodynamic conditions using temperature
%              or enthalpy.
% Modified From Original reference : DYNGEN[]
% ==========================================================================

function [SX,AMX,HX,TX] =  therm(P,H,T,FAR,FLAG)

DEM  = 8316.41;
CPG  = 1048.00;    % Specific Heat of Gas      [J/Kg-k]
PSTD = 101325.0;   % Standard Pressure             [Pa]
FX   = FAR;        % Fuel to Air Ratio

if (FLAG == 1) % USE H

HX = H;

    % Calculate TX (Temperature) Given HX (Enthalpy)
    % ---------------------------------------------

    % Initial Guess for Temperature
    TX = HX/CPG;

    for (I=1:15)

        % Gas Properties at FX and TX
        % ---------------------------

        [CS,AK,CP,R,PHI,H] = gasprop(FX,TX);
        DELH = HX-H;

        if (abs(DELH) <= (0.00001*HX))
            break; end

        % New Guess for Temperature
        TX = TX + DELH/CPG;

        if (I==15)
            disp('Error - Iterations Exceeded in Therm');
        end
    end
else % (FLAG = 0)

    % Calculate HX (Enthalpy) Given TX (Temperature)
    % ---------------------------------------------

    TX = T;
    [CS,AK,CP,R,PHI,HX] = gasprop(FX,TX);
end

SX  = PHI - R * log(PX/PSTD);   % Entropy
AMX = DEM/R;                    % Speed of Sound

% <End of File>
```

<gasprop.m>

The function <gasprop.m> calculates the basic gas properties based on temperature and a given fuel to air mixture. From reference [56], for a perfect gas, the properties (h, c_p, ϕ) are a function of gas temperature (T) alone and are given by,

$$c_p = A_0 + A_1T + A_2T^2 + A_3T^3 + A_4T^4 + A_5T^5 + A_6T^6 + A_7T^7$$
$$\phi = \phi_{ref} + A_0 log_e(T) + A_1T + A_2T^2 + A_3T^3 + A_4T^4 + A_5T^5 + A_6T^6 + A_7T^7$$
$$h = h_{ref} + A_0T + \frac{A_1}{2}T^2 + \frac{A_2}{2}T^3 + \frac{A_3}{2}T^4 + \frac{A_4}{2}T^5 + \frac{A_5}{2}T^6 + \frac{A_6}{2}T^7 + \frac{A_7}{2}T^8$$

The values of h, c_p, ϕ for air and combustion products can be calculated independently given coefficients A_0 to A_7. For a combined fuel to air mixture (f), the values of c_p, h and ϕ are given by [56],

$$c_p = \frac{c_{p_{air}} + f c_{p_{prod}}}{1 + f}$$
$$h = \frac{h_{air} + f h_{prod}}{1 + f}$$
$$\phi = \frac{\phi_{air} + f \phi_{prod}}{1 + f}$$

The implementation of the above formulation is as follows,

```
% ========================================================================
%                BASIC GAS PROPERTIES FOR AIR and FUEL & AIR MIXTURE              .
% ========================================================================
%
% Function Name : [A,GAMMA,CP,R,PHI,H] = gasprop(FAR,T,SI)
%
% Purpose       : Calculates Thermodynamic properties of Air or Fuel
%                 Air Mixture based on JP4.
%
%     Input to the program is:
%            FAR = Fuel to Air Ratio - JP4                    [-]
%            T   = Temperature of Air or Fuel Air Mixture     [K]
%
%     Output of the program in: [SI Units]
%            A     = Speed of Sound                          [m/s]
%            GAMMA = Ratio of Specific Heats
%            CP    = Specific Heat at Constant Pressure   [J/Kg/K]
%            R     = Gas Constant                         [J/Kg/K]
%            PHI   = integral( cp dT/T)                   [J/Kg/K]
%            H     = integral( cp dT  ) (Enthalpy)          [J/Kg]
% ========================================================================

function [A,GAMMA,CP,R,PHI,H] = gasprop(FAR,T)

% Max Value of FAR is 0.0676 for hydrocarbon fuels of type (CH2)n
% ---------------------------------------------------------------
```

```
if (FAR > 0.067623) FAR = 0.067623; end;

% T must be in degree Rankine for Gas tables
% ------------------------------------------

T = T * 9.0/5.0;  % Convert to degree Rankine (R)

if (T  < 300.0   ) T  = 300.0;  end;
if (T  > 4000.0  ) T  = 4000.0; end;

% AIR PATH - INLET AND COMPRESSOR
% -------------------------------

CPA = (((((( 1.0115540E-25 *T - 1.4526770E-21)*T + 7.6215767E-18)*T -...
             1.5128259E-14)*T - 6.7178376E-12)*T + 6.5519486E-08)*T -...
             5.1536879E-05)*T + 2.5020051E-01;
HEA =(((((((  1.2644425E-26 *T - 2.0752522E-22)*T + 1.2702630E-18)*T -...
             3.0256518E-15)*T - 1.6794594E-12)*T + 2.1839826E-08)*T -...
             2.5768440E-05)*T + 2.5020051E-01)*T - 1.7558886E+00;
SEA =(((((((  1.4450767E-26 *T - 2.4211288E-22)*T + 1.5243153E-18)*T -...
             3.7820648E-15)*T - 2.2392790E-12)*T + 3.2759743E-08)*T -...
             5.1576879E-05)*T + 4.5432300E-02) + 2.5020051E-01 *log(T);

% FUEL AIR PATH - PRODUCTS OF COMBUSTION
% --------------------------------------

if (FAR > 0.0)

CPF = (((((( 7.2678710E-25 *T - 1.3335668E-20)*T + 1.0212913E-16)*T -...
             4.2051104E-13)*T + 9.9686793E-10)*T - 1.3771901E-06)*T +...
             1.2258630E-03)*T + 7.3816638E-02;
HEF =(((((((  9.0848388E-26 *T - 1.9050949E-21)*T + 1.7021525E-17)*T -...
             8.4102208E-14)*T + 2.4921698E-10)*T - 4.5906332E-07)*T +...
             6.1293150E-04)*T + 7.3816638E-02)*T + 3.0581530E+01;
SEF =(((((((  1.0382670E-25 *T - 2.2226118E-21)*T + 2.0425826E-17)*T -...
             1.0512776E-13)*T + 3.3228928E-10)*T - 6.8859505E-07)*T +...
             1.2258630E-03)*T + 6.4833980E-01)   + 7.3816638E-02 *log(T);
end

CP    = (CPA + FAR*CPF)/(1.0+FAR);
H     = (HEA + FAR*HEF)/(1.0+FAR);
PHI   = (SEA + FAR*SEF)/(1.0+FAR);
R     = 1.986375/(28.97 - 0.946186 * FAR);       % Gas constant
GAMMA = CP/(CP - R);                             % Specific Heat Ratio
A     = sqrt(GAMMA * R * T * 25031.37);          % Speed of Sound [ft/sec]

% Convert to SI Units
% -------------------

CP   = CP  * 4185.7666; % Specific Heat [J/Kg-K]
PHI  = PHI * 4185.7666; %               [J/Kg-K]
R    = R   * 4185.7666; % Gas Constant  [J/Kg-K]
H    = H   * 2325.4259; % Enthalpy        [J/Kg]
A    = A   * 0.3048;    % Speed of sound   [m/s]
T    = T   * 5.0/9.0;   % Temperature    [deg K]

% < End of File>
```

Appendix F

Single Spool Turbojet Model and Investigation of Bleed Effects

During the initial part of this research, a single spool turbojet engine model was developed to investigate the affects of engine bleed on its performance. Although later on for the BWB, a three spool turbofan model was used for propulsion and flight controls integration, the single spool turbojet model proved to be very valuable in validation of the numerical simulation, as real engine bleed data was available for this purpose [79]. The single spool turbojet engine model is therefore presented here for future reference. It is a simpler model than the hybrid engine model discussed earlier and uses the inter-component volume approach.

F.1 Introduction

This section presents dynamic modeling of a single spool turbojet engine and its overall performance under variable bleed conditions. The approach followed is to model various engine subsystems using performance maps and then interlink each individual component to get an overall engine performance model. Two approaches were considered, the inter component volume method [48] and the constraint satisfaction iterative method [53]. However the inter-component volume method was eventually selected due to its real time performance and simplicity. Both open loop (fuel flow demand defined by user) and closed loop (fuel flow demand set by RPM control) responses were simulated. The AMT Olympus single spool turbojet engine [50] was selected as a test case. The simulation results were validated with data from bleed experiments conducted on the AMT Olympus engine at University of Manchester [79].

F.2 The Engine Model

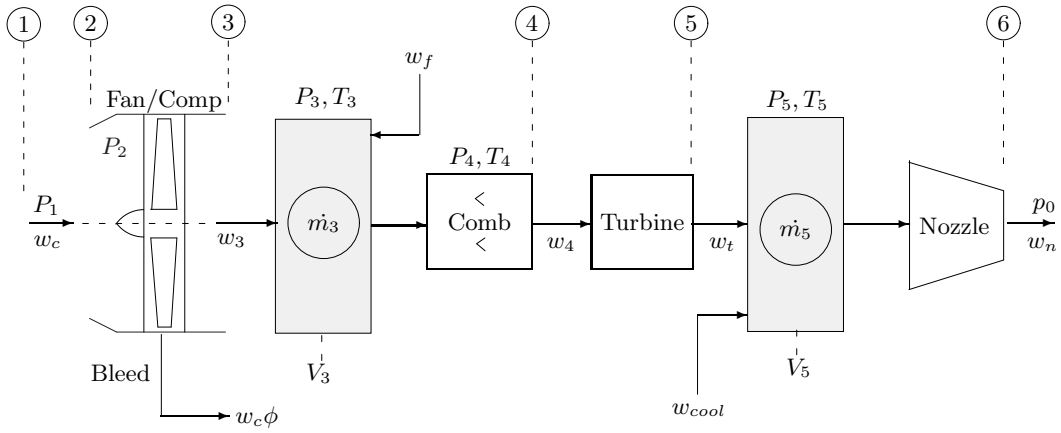

Figure F.1: Single spool turbojet schematic with inter-component volumes

In order to simulate a dynamic system it is important to specify a set of minimum number of variables or states, X, that completely define the system dynamics. An input vector, u, establishes a means of controlling or changing the state of the system. For a single spool turbojet system as shown in Figure F.1, the compressor and turbine exit pressures $[P_3, P_5]$ are important system states. If component efficiencies and exit pressures are known, then temperatures at various engine stages of the engine can be calculated using thermodynamic relationships. Shaft rotational speed, N, is another important parameter that forms part of the state vector. The fuel flow rate, w_f, and nozzle area, A_n, were used to control the state of the system. Thus,

$$X = (P_3, P_5, N)$$
$$u = (w_f, A_n)$$

F.2.1 Intake Model

In this work, a static intake model was incorporated and the flow process was assumed to be adiabatic. With the free stream static pressure and temperature as p_0, t_0 and Mach number, M, the total conditions (T_1, P_1) at the intake face can be calculated from reference [55],

$$\frac{T_1}{t_0} = \left(1 + \frac{\gamma - 1}{2} M^2\right) \tag{F.1}$$

$$\frac{P_1}{p_0} = \left(\frac{T_1}{t_0}\right)^{\frac{\gamma}{\gamma - 1}} \tag{F.2}$$

The total temperature, T_1, represents the rise in temperature by bringing air molecules traveling at Mach number, M, to rest at the intake face. The total pressure at the intake face is a function of temperature ratio and is given by Equation (F.2). Since no energy is added in the intake, the total temperature remains constant [80]. However there is a loss in total pressure as the flow passes through the intake and this pressure loss is a measure of intake efficiency, η_I. The intake exit conditions are

$$T_2 = T_1 \tag{F.3}$$

$$P_2 = \eta_I(P_1) \tag{F.4}$$

For the AMT Olympus the intake efficiency is assumed to be 1.0.

F.2.2 The AMT Olympus Compressor Model

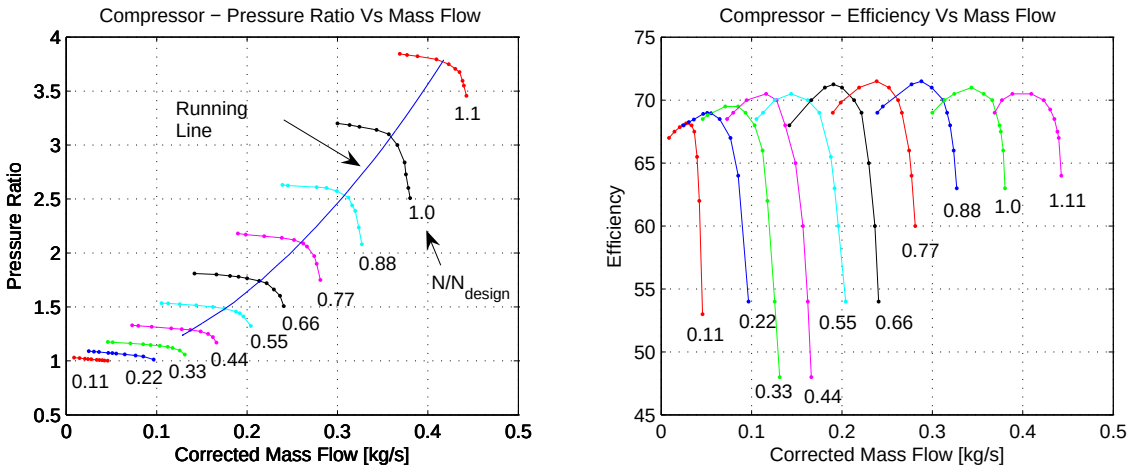

Figure F.2: Compressor map for the AMT Olympus engine

Representative AMT Olympus engine compressor maps from [81] are shown in Figure F.2. These maps are a function of non-dimensional compressor speed ($N_c^* = N/\sqrt{T_2/T_{std}}$) and the corrected mass flow ($w_c^* = w_c\sqrt{T_2/T_{std}}/(P_2/P_{std})$). Using these definitions, the compressor pressure ratio and corrected speed ($P_3/P_2, N_c^*$) were calculated using the compressor inlet conditions (T_2, P_2) and the knowledge of the state vector, $X = (P_3, P_5, N)$. A 2D interpolation routine was used to get the corrected mass flow and efficiency (w_c^*, η_c) from the compressor maps. From [55] the compressor temperature rise is,

$$\Delta T_{23} = \frac{1}{\eta_c} T_2 \left(\left(\frac{P_3}{P_2} \right)^{\frac{\gamma-1}{\gamma}} - 1 \right) \tag{F.5}$$

therefore the total temperature at the compressor exit is,

$$T_3 = T_2 + \Delta T_{23} \tag{F.6}$$

If a fraction of bleed ($\phi = w_b/w_c$) is taken from the compressor at a non-dimensional axial location (x/l) along the compressor, then the exit mass flow is

$$w_3 = w_c(1 - \phi) \tag{F.7}$$

and with a bleed location of x/l, the torque required by the compressor is

$$\tau_{comp} = \frac{w_c c_p \Delta T_{23}}{N_{rad/s}} \left((1 - \phi) + \phi \frac{x}{l} \right) \tag{F.8}$$

The above set of equations was used to calculate compressor exit conditions (w_3, T_3, P_3) and compressor torque, with inlet exit conditions (T_2, P_2) and the state vector, $X = (P_3, P_5, N)$ as inputs.

F.2.3 The AMT Olympus Combustor Model

The AMT Olympus engine uses an annular type combustion chamber. The amount of energy imparted to the pressurized air depends upon the fuel to air ratio and the heating value (HV) of the fuel. Not all the fuel is burnt and a burner efficiency, η_b, is associated with the fuel burning process. A typical value for burning efficiency is 0.98. Reference [57] gives an expression for combustor temperature rise,

$$\Delta T_{34} = \eta_b \left(\frac{w_f}{w_3} \right) \frac{HV_{fuel}}{c_p} \tag{F.9}$$

The combustor exit temperature is therefore

$$T_4 = T_3 + \Delta T_{34} \tag{F.10}$$

and the net mass flow from combustor,

$$w_4 = w_f + w_3 \tag{F.11}$$

With a pressure loss, ΔP_{loss}, the combustor exit pressure will be

$$P_4 = P_3(1 - \Delta P_{loss}) \tag{F.12}$$

This establishes the combustor exit conditions (w_4, T_4, P_4).

F.2.4 The AMT Olympus Turbine Model

Like the compressor, the turbine model for the AMT Olympus was also based on performance maps. The first map relates the corrected turbine mass flow ($w_t^* = w_t\sqrt{T_4}/P_4$) with turbine pressure ratio and the second map gives a measure of turbine efficiency. Representative turbine maps for the AMT Olympus turbojet engine from [81] are shown in Figure F.3. The speed line corresponding to lowest non-dimensional turbine speed ($N_t^* = N/\sqrt{T_4}$) is highlighted.

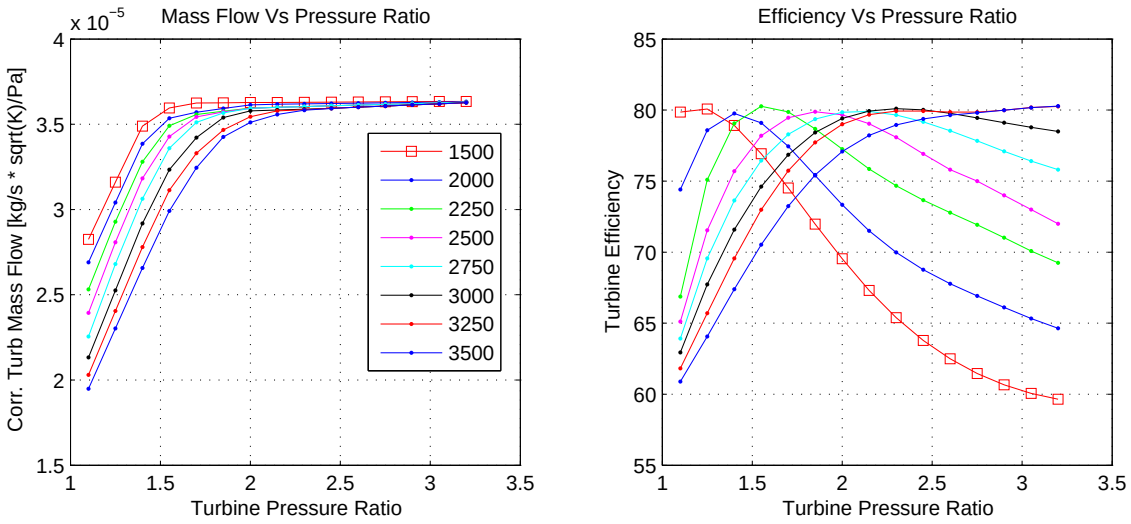

Figure F.3: Turbine map for the AMT Olympus engine

Using the state vector $X = (P_3, P_5, N)$ and 2D interpolation, the non-dimensional turbine mass flow and turbine efficiency (w_t^*, η_t) are calculated from the turbine maps. From [55], the temperature drop across the turbine is

$$\Delta T_{45} = \eta_t T_4 \left(1 - \left(\frac{P_5}{P_4}\right)^{\frac{\gamma-1}{\gamma}}\right) \tag{F.13}$$

The turbine exit temperature is therefore

$$T_5 = T_4 - \Delta T_{45} \tag{F.14}$$

and the torque generated by the turbine at a given rotational speed is expressed as

$$\tau_{turb} = \frac{w_5 c_p \Delta T_{45}}{N_{rad/s}} \tag{F.15}$$

It should be noted that the turbine and compressor speeds are taken as equal since

they are connected on a common shaft. The turbine exit conditions (w_5, T_5, P_5) are now established.

F.2.5 The AMT Olympus Convergent Nozzle

The ambient pressure outside the nozzle is taken as, p_0, the nozzle pressure ratio is hence

$$P_{r_{noz}} = \frac{P_5}{p_0} \tag{F.16}$$

The pressure ratio for which the nozzle exit speed reaches the speed of sound is called the critical pressure ratio and is a sole function of ratio of specific heats [56].

$$P_{r_{crit}} = \left(\frac{2}{1+\gamma}\right)^{\frac{\gamma}{1-\gamma}} \tag{F.17}$$

If the nozzle pressure ratio $P_{r_{noz}} > P_{r_{crit}}$, the nozzle will choke and the nozzle pressure ratio will be limited to $P_{r_{crit}}$. For a convergent nozzle with exit area, A_n, the mass flow through the nozzle is given by the following expression from [56].

$$w_n = \frac{A_n P_5}{R} P_r^{\frac{-1}{\gamma}} \sqrt{\frac{2gc_p}{T_5}\left(1 - P_r^{\frac{-R}{c_p}}\right)} \tag{F.18}$$

In the above equation, P_r represents the limited value of nozzle pressure ratio which is less than or equal to the critical pressure ratio $P_{r_{crit}}$. The nozzle jet velocity is a function of nozzle pressure ratio and total nozzle temperature.

$$V_{jet} = \sqrt{2gc_pT_5\left(1 - P_r^{\frac{-R}{c_p}}\right)} \tag{F.19}$$

The net thrust is a sum of momentum and pressure components,

$$F = w_n(V_{jet} - V_0) + A_n(P_6 - p_0) \tag{F.20}$$

where V_0 is the aircraft speed and P_6 is the pressure at the face of nozzle exit.

F.2.6 Evaluation of Pressure Derivatives $(\dot{P}_3, \dot{P}_5)$

Figure F.4 shows two control volumes for the AMT Olympus single spool turbojet. The first control volume is associated between the compressor and combustor. The mass storage in this volume is used to calculate rate-of-change of compressor exit

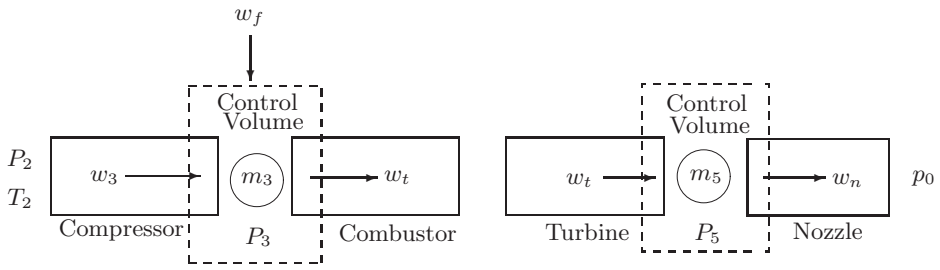

Figure F.4: Control volumes on a single spool turbojet

pressure, $\dot{P}_3$. The second control volume is between the turbine and nozzle and shall provide derivative of turbine exit pressure, $\dot{P}_5$. For the volume associated with the combustor chamber and the compressor, the rate of accumulation of mass is

$$\dot{m}_3 = w_3 + w_f - w_t \tag{F.21}$$

and similarly for the volume between the turbine and the nozzle the rate of change of mass is

$$\dot{m}_5 = w_t - w_n \tag{F.22}$$

Taking the time derivative of the ideal gas law and neglecting the temperature derivative term ($m\dot{T}$) as suggested Bates and Fawke [48], gives

$$\dot{P} = \frac{RT}{V}(\dot{m}) \tag{F.23}$$

which was used to calculate the pressure derivatives ($\dot{P}_3, \dot{P}_5$) inside each control volume.

F.2.7 Evaluation of Rotational Acceleration ($\dot{N}$)

The rotational acceleration derivative, $\dot{N}$, is evaluated by calculating the difference in torque generated by the turbine and that required by the compressor.

$$\dot{N} = \frac{dN}{dt} = \frac{(\eta_m \tau_{turb} - \tau_{comp})}{I_{spool}} \tag{F.24}$$

This expression was integrated to get shaft rotational speed as a function of time. Using the above formulation a dynamic model for the AMT Olympus engine was implemented in MATLAB/Simulink and is shown in Figure F.5.

F.2.8 RPM Controller

To run the above engine simulation model and test various bleed cases at different throttle/RPM settings, an RPM control system was designed. The control scheme is shown in Figure F.6. The controller uses a proportional + integral architecture, with the maximum fuel limit set by either the maximum allowable fuel flow or the turbine entry temperature (T_4). An anti-windup was used for the integral element and the input RPM demand was slew rate limited for both engine acceleration and deceleration. The slew rate limit was set to $\pm 10\%$ of the max RPM. Gain values for the proportional and integral were set at $K_p = 0.05$ and $K_i = 0.0075$ respectively. The initial integral state (x_0) in the RPM controller was set to 50% of maximum fuel flow rate.

F.3 AMT Olympus Turbojet Engine

The simulation method described above was validated on the AMT Olympus [50] turbojet engine. It is a small engine that generates up to 190 N of thrust. The engine has a single stage centrifugal compressor and single stage axial turbine. The combustor chamber is of annular type. An electronic engine control unit (ECU) controls the RPM and limits the maximum exhaust gas temperature (EGT). The basic engine specifications as derived from [50] are presented in Table F.1.

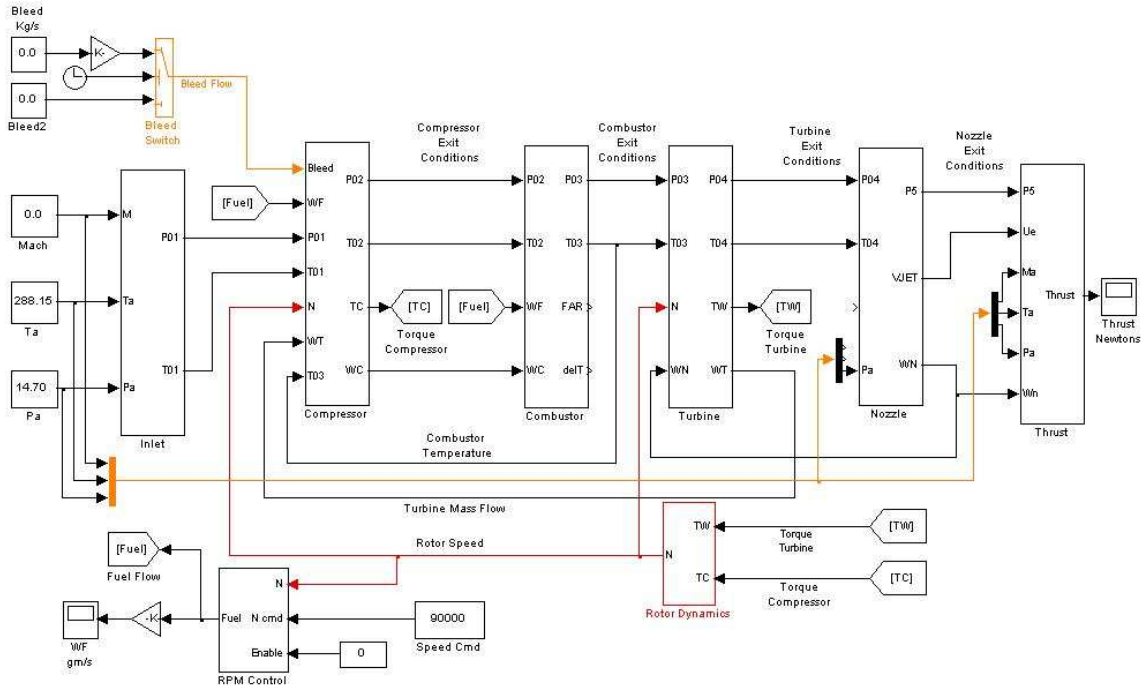

Figure F.5: Simulink model for the AMT Olympus turbojet

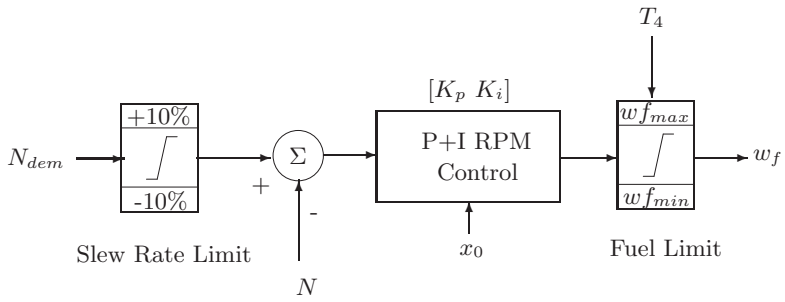

Figure F.6: RPM control system architecture

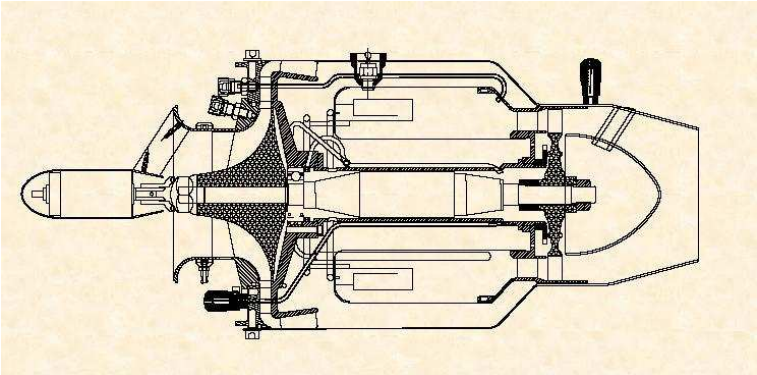

Figure F.7: AMT Olympus single spool turbo jet engine [81]

Besides the component map data, certain other engine parameters were required to complete the engine model. These were adjusted to match the experimental results. A combustion burner efficiency of 0.88 was used, together with combustion chamber pressure loss of 5%. The intake and mechanical transmission efficiencies were set at 1.0 and 0.92 respectively. A rotor inertia of 0.0004 kg-m^2 was assumed. An exact value of rotor inertia was not available so this was adjusted by observing the time to reach maximum RPM. An effective nozzle area which is 95% of the geometrical nozzle area was used to cater for the effect of boundary layer growth in the nozzle. Two control volumes were needed to calculate the pressure derivatives, these were selected as 1.0 ft^3 and 0.75 ft^3 for the volumes associated with compressor/combustor and turbine/nozzle respectively. The initial state vector was set at

$$X_0 = [P_3, P_5, N] = [2.2P_2, 1.5P_2, 88000] \tag{F.25}$$

which places the engine operating point at a reasonable location on the compressor and turbine maps.

Engine Parameter	Value	Units
Diameter	130	mm
Length	270	mm
Maximum thrust	190	N
Pressure ratio	4:1	
Mass flow	0.4	kg/sec
Maximum rotational speed	112,500	RPM
Nominal EGT	923	° K
Maximum EGT	973	° K
Maximum fuel consumption	0.4	kg/min

Table F.1: Technical data AMT Olympus

F.4 Simulation Description

The engine simulation was divided into pre-transient and transient phases.

F.4.1 Pre-Transient

Keeping a fixed value of fuel inflow, the simulation runs till it reaches a state when $\dot{X} = 0$ and there is no accumulation of mass in any control volume. This phase is called the pre-transient and with the control vector $u = [w_f, A_n]$ fixed, the simulation converges to a steady state condition. The pre-transient phase can be avoided by using the last known converged or steady state values of, X_0 and control input, u_0 respectively. On Figure F.8, the line from point A to B shows the path followed by the engine as it settles down to a steady state condition in the pre-transient phase. Point A represents the initial condition, X_0, on the compressor map as specified at start of the simulation and point B corresponds to a steady state condition reached, according to the fuel setting specified in u_0.

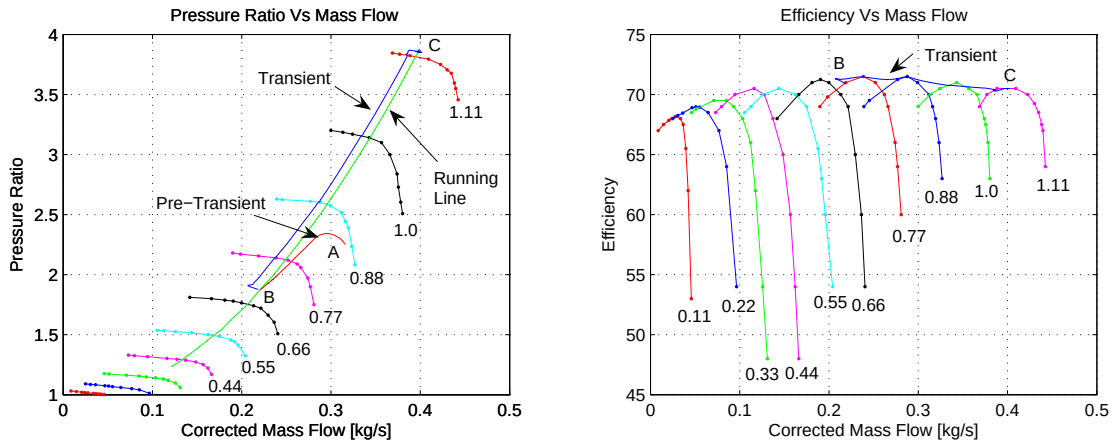

Figure F.8: Transients on the AMT Olympus compressor map

F.4.2 Transient

Once the engine has reached a steady state condition at point B, the control vector $u = [w_f, A_n]$ consisting of fuel flow rate and nozzle area can be varied to initiate a transient. During a transient, it takes a finite amount of time for the rotor to spool up or down but the mass flow and therefore pressure changes inside the engine can be quite rapid. The effect of a sudden increase in fuel flow is to move the compressor operating point up along the speed line toward surge. A sudden reduction in fuel flow causes the reverse action and the compressor operating point moves down toward the choking point. Path B to C on Figure F.8, shows the transient response of the AMT Olympus engine to a slew rate limited RPM demand. The transient was run with RPM control engaged. The engine settles down at point C corresponding to maximum speed demand of 112,500 RPM.

F.5 Simulation Results and Validation

F.5.1 Steady State Results

The steady state experimental values under zero compressor bleed were compared at maximum speed with RPM control engaged. Values of fuel flow, thrust, compressor pressure ratio and mass flow were noted. Table F.2, summarizes the steady state results at maximum engine RPM.

Engine Parameter	Exper.	Sim	% Error
Maximum Thrust, N	193	189.5	+1.81
Pressure ratio	3.55	3.47	+2.25
Maximum fuel, gm/sec	9.10	8.85	+2.75
EGT at max RPM, ° K	1035	970	+6.28

Table F.2: AMT Olympus engine steady state comparison at 112,500 RPM

It is evident from above that there is a good match between the experimental and the simulated values. The percentage errors are less than 3% for most of the parameters except the exhaust gas temperature (EGT) error, which is approx 6%. The simulation predicts lesser values of exhaust gas temperature at max RPM, however as will be discussed later, at lower RPM values the EGT correlation was much better.

Figure F.9 presents a correlation between static experimental and simulated engine thrust as a function of RPM. Besides the engine setting, various environmental

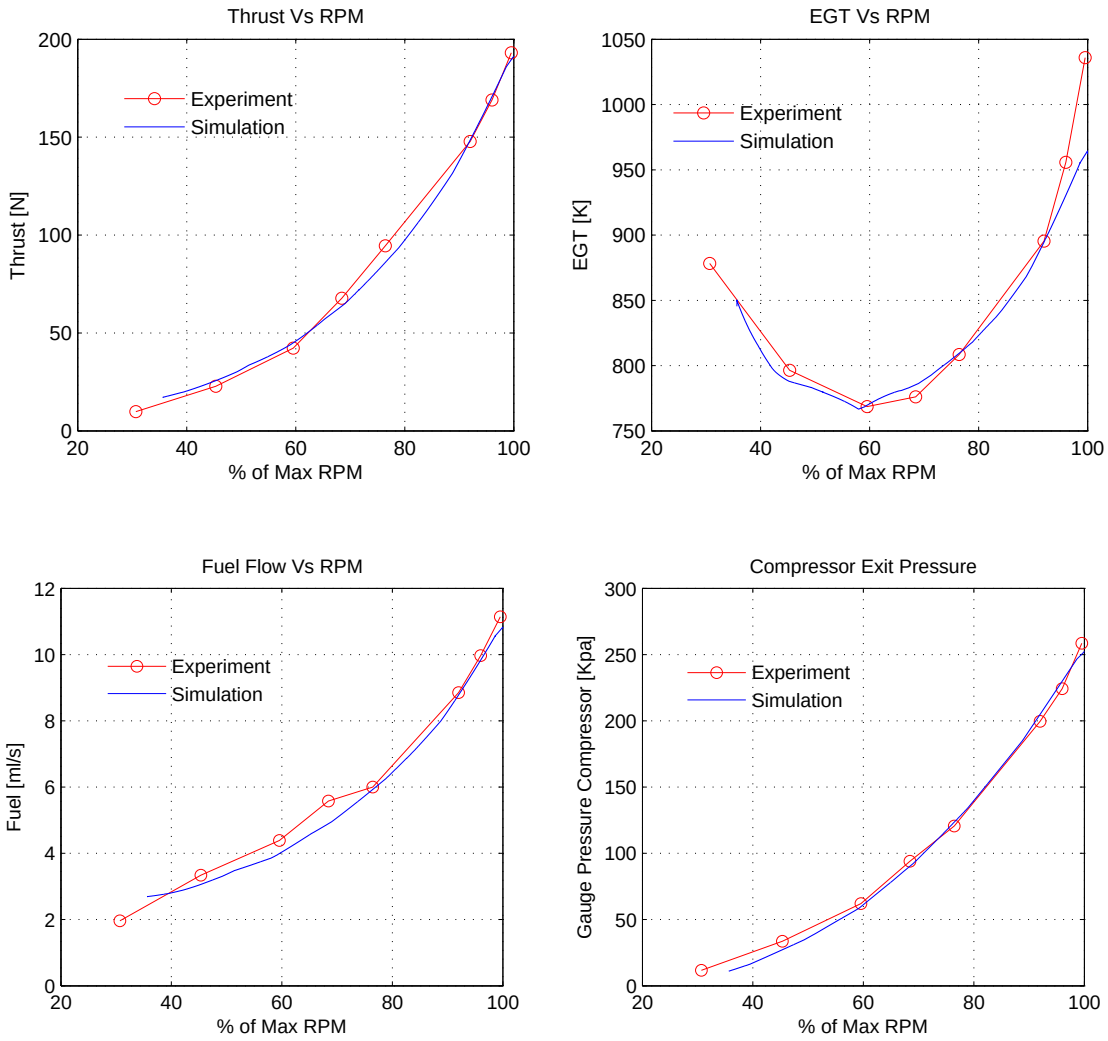

Figure F.9: Validation : Thrust, EGT, fuel and compressor exit pressure

factors affect engine thrust. A higher ambient temperature results in a drop in thrust and rise in exhaust gas temperature. Whereas a lower ambient pressure results in a loss in the compressor delivery pressure and thrust. The mean static correlation for thrust under zero bleed conditions was within 5.0% of experimental values. The engine mechanical transmission efficiency was adjusted from 0.99 to 0.92 to match the EGT values of the experiments. With higher mechanical efficiency the simulation predicted lower values of exhaust gas temperature. From Figure F.9, the EGT correlation is quite good at lower speeds but degrades at higher RPM values, suggesting that the mechanical efficiency (η_m) may not be constant over the whole RPM range. The fuel burning efficiency was decreased from 0.98 to 0.88 to match the excessive fuel consumed by the engine. This could also be attributed to the fact that the manufacturer uses 5% oil in the fuel for lubrication purposes [50] and a relatively simple combustor model was used. The fuel consumption as function of RPM as well as compressor exit pressure is also presented in Figure F.9.

F.5.2 Bleed Experimentation

The bleed experiments [79] were conducted at the University of Manchester's Jet Engine Test Facility. These experiments were done as part of FLAVIIR (Flapless Aerial Vehicle Integrated Interdisciplinary Research) project which aims at developing novel technologies for control of future aircraft. The bleed air was extracted from thirty (30) radially symmetric holes on the AMT Olympus engine's centrifugal compressor. The amount of bleed was controlled by a bleed valve and various engine parameters were recorded by a data acquisition system. At a given throttle setting, as the amount of bleed is varied the electronic engine control adjusts the fuel flow in an attempt to keep the RPM constant. However in nearly all bleed cases, the EGT limit is hit as the bleed reaches approximately 30% of compressor mass flow. This bleed air from the engine is used to power a (i) Circulation control actuator and a (ii) Fluidic thrust vectoring system [79]. Experimental testing was considered necessary to quantify the effect of engine bleed on its performance and to identify the boundaries of safe engine operation.

F.5.3 Bleed Simulation and Validation

Bleed extraction from the compressor has a degrading effect on engine performance. It alters the work and mass flow balance on engine components. Pilidis [77] states that upon bleed extraction the turbine will have to operate with a lower mass flow to produce the work required by the compressor. This will result in a higher turbine entry temperature (T_4) and therefore higher exhaust gas temperature (T_5). The turbine is designed to operate choked even at relatively reduced mass flows, therefore the non-dimensional mass flow ($w_t\sqrt{T_4}/P_4$) through the turbine is constant. To keep the non-dimensional mass flow constant, the turbine entry pressure (P_4) will drop. This implies that compressor pressure ratio will fall. The steady state running line will shift towards choke with a corresponding reduction in compressor efficiency. Pilidis [77] suggests that when the non-dimensional bleed (ϕ) is small, the decrease in compressor pressure ratio due to bleed extraction can be approximated as

$$\left(\frac{P_3}{P_2}\right)_{bleed} \approx \left(\frac{P_3}{P_2}\right)_{nobleed} \sqrt{1-\phi} \tag{F.26}$$

and the corresponding increase in turbine entry temperature (T_4) is

$$(T_4)_{bleed} \approx (T_4)_{nobleed} \frac{1}{(1-\phi)} \tag{F.27}$$

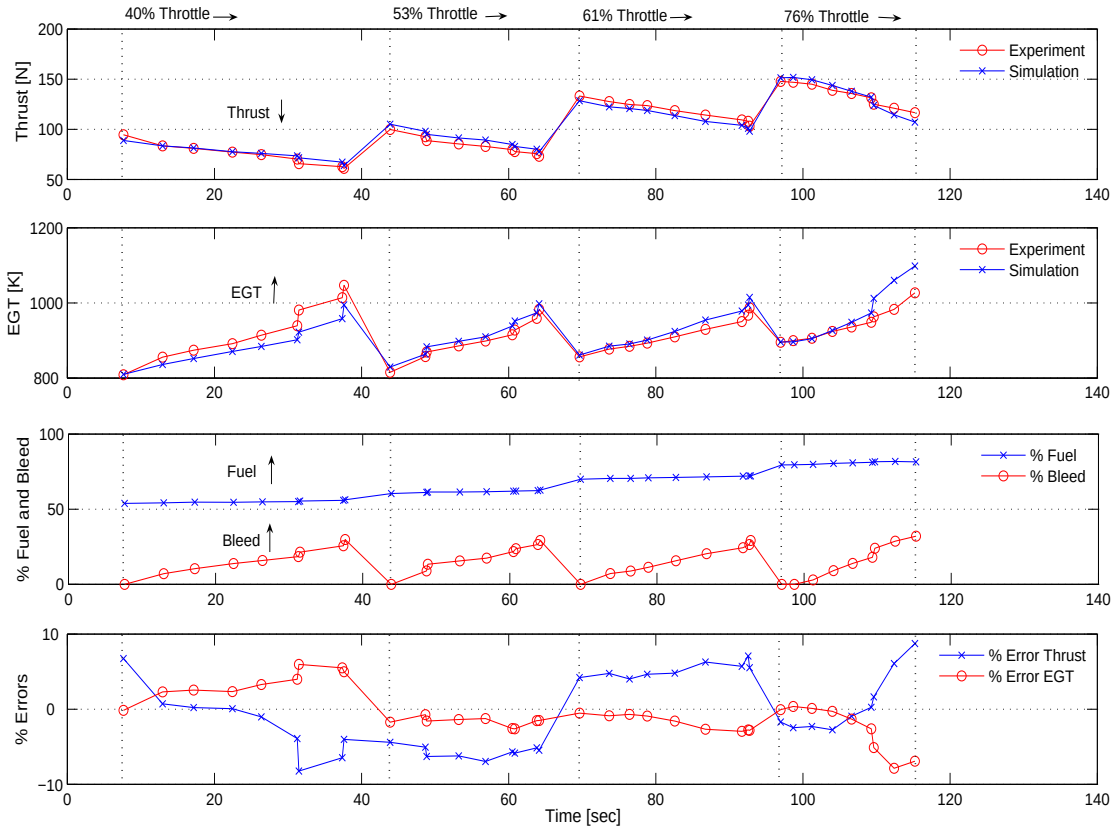

Figure F.10: Validation : Drop in thrust due to bleed at different throttle settings

Mass Flow	% Bleed	Fuel Flow	Thrust(N)			EGT (K)		
(gm/s)		(gm/s)	Exp.	Sim.	% Error	Exp.	Sim.	% Error
336.29	0.00	6.36	133.17	127.57	+4.2	856.51	861.0	-0.5
347.75	7.17	6.41	127.57	121.49	+4.8	877.19	884.9	-0.9
350.05	08.79	6.41	124.79	119.78	+4.0	884.43	890.6	-0.7
354.68	11.29	6.44	123.67	117.91	+4.7	892.92	901.0	-0.9
359.50	15.64	6.47	118.56	112.87	+4.8	909.49	923.9	-1.6
363.92	20.39	6.51	114.18	107.01	+6.3	929.45	954.3	-2.7
370.47	24.33	6.55	109.38	103.14	+5.7	950.21	978.3	-3.0
372.60	26.47	6.56	108.00	100.37	+7.1	967.38	994.1	-2.8
374.95	29.13	6.56	103.05	97.37	+5.5	986.73	1014.6	-2.8

Table F.3: Validation of bleed results - 61% throttle setting

Bleed simulation was performed using the engine simulation program and compared with experimental results. Four throttle settings were simulated, 40%, 53%, 61% and 76%. The input for the bleed simulation is the actual experimental fuel and bleed flow rates. This sets the engine operating point. Once the engine reaches a steady state for a given fuel and bleed flow the input is changed to the next value. In this way all the bleed cases were tested in a single simulation run.

Figure F.10 shows that as the bleed flow is increased the thrust decreases and the

EGT increases. Even at lower throttle settings as the bleed flow is increased, the EGT hits the upper limit. At this point the fuel or bleed flow cannot be increased further. Hence there is an upper limit on the amount of bleed that can be extracted at any given throttle setting or engine RPM. The percentage errors for thrust and exhaust gas temperature are within 5-10% of experimental values. This variation is expected since the compressor characteristics change with the amount of bleed flow, and only steady state compressor maps under no bleed conditions were used for the simulation. It may also be noted that as the engine bleed is increased the electronic Engine Control Unit (ECU) tries to adjust the corresponding drop in speed by increasing the value of fuel flow. Each step in the fuel flow setting corresponds to a different value of throttle setting. Table F.3 summarizes the experimental and simulated results for the 61% throttle case.

F.6 Summary

A gas turbine simulation program was written in MATLAB/Simulink and performance was compared with experimental values. The results were accurate to within 5.0% for the nominal or zero bleed case and within 10.0% for excessive bleed cases. The increase in error upon bleed extraction can be attributed to two factors. Firstly, the location where the bleed is extracted affects the amount of work required by the compressor and this may also vary non-linearly for the radial compressor of the AMT Olympus engine. Secondly, the bleed extraction itself may adversely influence the performance of the compressor and the compressor characteristics may change. Further work will be required to more accurately model the compressor map with bleed extraction and improve upon the accuracy of the overall simulation. The compressor/turbine maps were obtained from [81] and the experimental data from [79]. Although both sources refer to the same AMT Olympus engine, the possibility of statistical variation between the available component maps and the actual engine under test exists. It is possible to further adjust the component efficiencies in order to match the experimental results, however this was not considered further. The simulation method runs in real time and therefore can easily be integrated with aircraft and active flow control simulation codes.

Bibliography

[1] R. Leibeck. Design of blended wing body subsonic transport. *Journal of Aircraft*, Vol 41, pp. 10-25, 2004.

[2] A. Diedrich, J. Hileman, D. Tan, K. Wilcox, and Z. Spakovsky. Multidisciplinary design and optimization of the silent aircraft. In *44th AIAA Aerospace Sciences Meeting and Exhibit, Nevada, AIAA Paper 2006-1323*, 2006.

[3] A. Agarwal and A. Dowling. A ray tracing approach to calculate acoustic shielding by the silent airframe. In *44th AIAA Aerospace Sciences Meeting and Exhibit, Nevada, AIAA Paper 2006-2618*, 2006.

[4] M.A. Sargeant, J.I. Hileman, S. Spakovszky, and M. Drela. Airframe design for silent aircraft. In *45th AIAA Aerospace Sciences Meeting and Exhibit, Nevada, AIAA Paper 2007-0453*, 2007.

[5] J.I. Hileman, T.R. Reynolds, E. de la Rosa Blanco, and T. Law. Development of approach procedures for silent aircraft. In *45th AIAA Aerospace Sciences Meeting and Exhibit, Nevada, AIAA Paper 2007-0456*, 2007.

[6] E. de la Rosa Blanca, C. Hall, and D. Crichton. Challenges in silent aircraft engine design. In *45th AIAA Aerospace Sciences Meeting and Exhibit, Nevada, AIAA Paper 2007-0454*, 2007.

[7] H.V. Castro. *Flying and Handling Qualities of a Fly by Wire Blended Wing Body Civil Transport Aircraft*. PhD thesis, Cranfield University, Cranfield UK, 2003.

[8] J.V. Decken. Aerodynamics of pneumatic high lift devices. In *AGARD Lecture Series, AGARD-LS-43*, April, 1970.

[9] R.J. Englar. Development of circulation control technology for application to advanced subsonic transport aircraft. *Journal of Aircraft*, Vol 31, pp. 1160-1177, 1994.

[10] G.S Jones. Pneumatic flap performance for a two dimensional circulation control airfoil. In *Applications of Circulation Control Technology, Progress in Aeronautics and Astronautics, AIAA, Vol 214*, 2005.

[11] Department of Power and Propulsion, Cranfield University, UK. *Cranfield University Design and Off Design Engine Simulation Code,* TURBOMATCH.

[12] J.F. Sellers and C.J. Daniele. DYNGEN a program for calculation of steady state and transient performance of turbojet and turbofan engines, NASA TN-D7901. Technical report, NASA, 1975.

[13] Department of Aeronautics, KTH, Sweden. *User's Guide, Reference Manual,* TORNADO 1.0.

[14] D.A. Spence. The lift coefficient of a thin jet-flapped wing. *Proceedings of the Royal Society of London*, Vol 251, pp. 407-425, 1959.

[15] J. Williams and A.J. Alexander. Some exploratory jet flap experiments. *Aero. Quarterly*, Vol 8, pp. 21-30, 1957.

[16] www.cite.monash.edu.au.

[17] B. Casey. Flying qualities and control of a blended wing body transport aircraft. Master's thesis, Cranfield University, Cranfield UK, 2005.

[18] www.secondworldwarhistory.com.

[19] J.K. Northrop. The development of all wing aircraft. *Journal of the Royal Aeronautical Society*, Vol 51, pp. 481-510, 1941.

[20] northrop.host.sk.

[21] Aerospace America, October 2006 Issue. pp 28-33.

[22] C.A. Hall and D. Crichton. Engine and installation configurations for silent aircraft. In *ISABE 2005-1164*, 2005.

[23] D. Crichton, E. de la Rosa Blanco, T. Law, and J.I. Hileman. Design and operation for ultra low noise at take-off. In *45th AIAA Aerospace Sciences Meeting and Exhibit, Nevada, AIAA Paper 2007-0451*, 2007.

[24] B.W. McCormick. *Aerodynamics, Aeronautics and Flight Mechanics.* John Wiley, New York, 1995.

[25] R.T. Jones. Notes on the stability and control of tailless airplanes NACA Report 837. Technical report, NACA, 1941.

[26] C.J. Donlan. An interim report on the stability and control of tailless airplanes, NACA Report No 796. Technical report, NACA, 1944.

[27] C.M. Fremaux. Effect of geometry static stability and mass distribution on the tumbling characteristics of generic flying wing models. In *Proceedings of the AIAA Atmospheric Flight Mechanics Conference, AIAA-93-3615*, 1993.

[28] A.W. Thorpe. Note on longitudinal stability and trim of tailless aircraft, RAE-TN-AERO 1021. Technical report, Royal Aircraft Establishment, 1942.

[29] D.D. Mclean. *Automatic Flight Control Systems*. Prentice Hall International, 1990.

[30] I.M. Davidson. The jet flap. *Journal of the Royal Aeronautical Society*, Vol 60, pp. 25-50, January, 1956.

[31] B.S. Stratford. Early thoughts on the jet flaps. *Aero. Quarterly*, Vol 7, pp, 85-105, 1956.

[32] N.A. Dimmock. Some early jet-flap experiments. *Aero. Quarterly*, Vol 8, pp. 331-345, 1957.

[33] K.D. Harris. The Hunting H-126 jet flap research aircraft. In *AGARD Lecture Series, AGARD-LS-43*, April, 1970.

[34] S.P. Frith and N.J. Wood. The use of circulation control for flight control. In *Proceedings of the NASA's Circulation Control Workshop*, 2004.

[35] J.D. Anderson. *Fundamentals of Aerodynamics*. McGraw Hill, 2001.

[36] J.A. Hooper. Lift augmentation devices and their effect on the engine. In *AGARD Lecture Series, AGARD-LS-43*, April, 1970.

[37] J.M. Williams, S.F.J. Butler, and M.N. Wood. The aerodynamics of jet flaps. In *2nd International Congress of Aeronautical Sciences, Zurich*, Sept, 1960.

[38] J.J. Burken. Longitudinal emergency control system using thrust modulation demonstrated on the MD-11 airplane. In *32nd Joint Propulsion Conference, AIAA 93-3062*, 1996.

[39] M. Hareförs and D.G. Bates. Integrated propulsion based flight control system design for civil transport aircraft. In *Proceedings of the 2002 IEEE International Conference on Control Applications*, 2002.

[40] F.W. Burcham. Development and flight evaluation of an emergency digital flight control system using only engine thrust on an F-15 airplane NASA-TP-3627. Technical report, NASA, 1996.

[41] G.S. Jones and R.J. Englar. Advances in pneumatic controlled high lift systems through pulsed blowing. In *21st AIAA Applied Aerodynamics Conference*, June, 2003.

[42] D.H. Kim and D.J. Saunders. Embedded wing propulsion conceptual study, NASA TM-2003-212696. Technical report, Glenn Research Center, 2003.

[43] M.V. Cook. *Flight dynamics principles*. Arnold publishers, 1997.

[44] MIL-F-8785C. Military specification, flying qualities of piloted airplanes. Technical report, USAF, 1980.

[45] ESDU 94028. A background to the handling qualities of aircraft. Technical report, ESDU International, London, 1992.

[46] T.P Neal and R.J. Smith. A flying qualities criterion for the design of fighter flight control systems. *Journal of Aircraft*, Vol 8, 1971.

[47] M.D. McLaughlin and J.B. Whitten. Pilot evaluation of dynamic stability characteristic of a supersonic transport in cruising flight using a fixed base simulator. Technical report, Langley Research Center, 1964.

[48] A.J. Fawke. *Digital Computer simulation of Gas Turbine Dynamic Behavior*. PhD thesis, University of Bristol, Bristol UK, 1970.

[49] A. Behbahani. Modeling diagnostics and prognostics of a two spool turbofan engine. In *Proceedings of the 41st AIAA/ASME/SAE/ASEE Joint Propulsion Conference and Exhibit, AIAA 2005-4344*, 2005.

[50] Advanced Micro Turbines (AMT) Netherlands. *AMT Olympus Engine User's Manual Serial No 112171*.

[51] N.U. Rahman and J.F. Whidborne. A numerical investigation into the effect of engine bleed on performance of a single-spool turbojet engine. *Journal of Aerospace Engineering*, Vol 222, IMECHE Part G, pp. 939-949, 2008.

[52] E.T. Whittaker and G. Robinson. *The Calculus of Observations: A Treatise on Numerical Mathematics*. Dover publishers, New York: Dover, 4th ed., 1967.

[53] K. Parker and T.H. Guo. Development of turbofan engine simulation in a graphical simulation environment NASA-TM-2003-212543. Technical report, NASA, 2003.

[54] AS755D. Aircraft propulsion system performance station designation and nomenclature, aerospace standard AS755D. Technical report, SAE, 20 Aug 2004.

[55] H.I.H. Saravanamuttoo, G.F.C. Rogers, and H. Cohen. *Gas Turbine Theory*. Longman, 1996.

[56] J.D. Mattingly. *Elements of Gas Turbine Propulsion*. McGraw Hill, 1996.

[57] P.P. Walsh and P. Fletcher. *Gas Turbine Performance*. Blackwell publishing, 1999.

[58] K. Seldner. Generalized simulation technique for turbojet engine system analysis, NASA-TND-6610. Technical report, NASA, 1972.

[59] A.K. Cooke. Simulation model of NFLC Jetstream 31. Technical report, Cranfield University, Reports CU/COA-2006/0402, 2006.

[60] A.R. Amrane. Flight dynamics model of a high performance sailplane. Master's thesis, Cranfield University, Cranfield UK, 2005.

[61] Z. Spakovszky, D. Pilczer, and A. Manneville. Preliminary evaluation of noise reduction approaches for a functionally silent aircraft. *AIAA Journal*, Vol 43, No.3, pp. 836-840, 2006.

[62] A.P. Plas, V. Madani, M.A. Sargant, E.M. Greitzer, C.A. Hall, and T.P. Hynes. Performance of a boundary layer ingestion propulsion system. In *45th AIAA Aerospace Sciences Meeting and Exhibit, Nevada, AIAA Paper 2007-0450*, 2007.

[63] N. Qin and A. Vavalle. Aerodynamic considerations on blended wing body aircraft. *Progress in Aerospace Sciences*, Vol 40, pp. 321-343, 2004.

[64] ESDU 72024. Aerodynamic characteristics of aerofoils in compressible inviscid airflow at sub-critical mach numbers. Technical report, ESDU International, London, With Amendments A to D, January 1999.

[65] ESDU 97020. Slope of aerofoil lift curve for subsonic two dimensional flow. Technical report, ESDU International, London, Issued, September, 1997.

[66] ESDU 96028. VGK method for two dimensional aerofoil sections part 1, principles and results. Technical report, ESDU International, London, With Amendments A and B, April 2004.

[67] ESDU 94028. Increments in aerofoil lift coefficient at zero angle of attack and in maximum lift coefficient due to deployment of plain trailing-edge flap, with or without high lift devices at low speeds. Technical report, ESDU International, London, Issued, December 1994.

[68] ESDU 00027. Aerofoil profile drag for mach numbers below the drag rise condition. Technical report, ESDU International, London, With Amendments A, January 2006.

[69] ESDU 87005. Increment in aerofoil profile drag coefficient due to deployment of a single slotted flap. Technical report, ESDU International, London, With Amendments A to D, November 2008.

[70] ESDU 98017. Aerofoil and wing and pitching moment coefficient at zero angle of attack due to deployment of trailing edge plain flaps at low speeds. Technical report, ESDU International, London, With Amendment A, August 2003.

[71] ESDU 03017. Pitching moment curve for wing with leading edge and trailing edge high lift devices deployed at low speeds. Technical report, ESDU International, London, With Amendment A, August 2007.

[72] ESDU 82010. Contribution of fin to side-force, yawing moment and rolling moment derivatives due to side slip, $(Y_v)_f$,$(N_v)_f$, $(L_v)_f$ in presence of body, wing and tail plane. Technical report, ESDU International, London, With Amendment A to C, April 1993.

[73] ESDU 70011. Lift curve slope and aerodynamic center position of wings in inviscid subsonic flow. Technical report, ESDU International, London, With Amendments A to I, 1996.

[74] ESDU 82017. Contribution of fin to side-force, yawing moment and rolling moment derivatives due to rate of yaw, $(Y_r)_f$,$(N_r)_f$, $(L_r)_f$. Technical report, ESDU International, London, With Amendment A, 1983.

[75] ESDU 83006. Contribution of fin to side-force, yawing moment and rolling moment derivatives due to rate of roll, $(Y_p)_f$,$(N_p)_f$, $(L_p)_f$ in presence of body, wing and tail plane. Technical report, ESDU International, London, With Amendment A, 1985.

[76] ESDU 87008. Rudder side-force, yawing moment and rolling moment control derivatives at low airspeeds, Y_{δ_r},N_{δ_r}, L_{δ_r}. Technical report, ESDU International, London, With Amendment A to G, April 1994.

[77] P. Pilidis and J.R. Palmer. Gas turbine theory and performance. MSc Thermal Power Course Notes, 2006.

[78] A.H. Cesare and C. Daniel. Engine design studies for silent aircraft. *Journal of Turbomachinery*, Vol 129, pp. 479-487, July 2007.

[79] W.J. Crowther, K. Gill, P. Wilde, and R. Gueroult. Development of an integrated propulsion and pneumatic power supply system for flapless uavs. In *AIAA Aviation Technology, Integration and Operations Conference, AIAA 2007-7726, Belfast UK*, 18-20 Sept, 2007.

[80] R.L. Daughtery, B. Joseph, and E.J. Franzini. *Fluid Mechanics with Engineering Applications*. McGrawHill, 1997.

[81] M. Lichtsinder and Y. Levy. Jet engine model for control and real time simulations. *Journal of Engineering for Gas Turbine and Power*, Vol 128, pp. 745-753, 2006.